

# Radio Occultation Data Analysis for Climate Change Monitoring and First Climatologies from CHAMP

Andreas Gobiet

December 2005

financially supported by



Wegener Center  
[www.wegcenter.at](http://www.wegcenter.at)



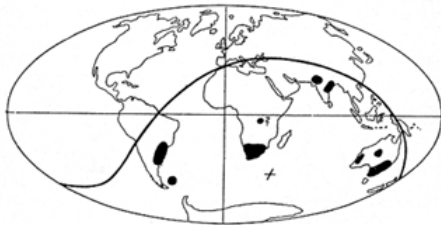
**FWF**

Der Wissenschaftsfonds.



The **Wegener Center for Climate and Global Change** combines as an interdisciplinary, internationally oriented research center the competences of the University of Graz in the research area „Climate, Environmental and Global Change“. It brings together, in a dedicated building close to the University central campus, research teams and scientists from fields such as geo- and climate physics, meteorology, economics, geography, and regional sciences. At the same time close links exist and are further developed with many cooperation partners, both nationally and internationally. The research interests extend from monitoring, analysis, modeling and prediction of climate and environmental change via climate impact research to the analysis of the human dimensions of these changes, i.e, the role of humans in causing and being effected by climate and environmental change as well as in adaptation and mitigation. The director of the center, hosting about 30 researchers, is the geophysicist Gottfried Kirchengast, the lead partner and deputy director is the economist Karl Steininger. (more informationen at [www.wegcenter.at](http://www.wegcenter.at))

The present report is the result of a PhD thesis work completed in October 2005.



**Alfred Wegener** (1880-1930), after whom the Wegener Center is named, was founding holder of the University of Graz Geophysics Chair (1924-1930) and was in his work in the fields of geophysics, meteorology, and climatology a brilliant, interdisciplinary thinking and acting scientist and scholar, far ahead of his time with this style. The way of his ground-breaking research on continental drift is a shining role model — his sketch on the relationship of the continents based on traces of an ice age about 300 million years ago (left) as basis for the Wegener Center Logo is thus a continuous encouragement to explore equally innovative scientific ways: *ways emerge in that we go them* (Motto of the Wegener Center).

## Wegener Center Verlag • Graz, Austria

© 2005 All Rights Reserved.

Selected use of individual figures, tables or parts of text is permitted for non-commercial purposes, provided this report is correctly and clearly cited as the source. Publisher contact for any interests beyond such use: [wegcenter@uni-graz.at](mailto:wegcenter@uni-graz.at).

ISBN 3-9502126-3-9

December 2005

Contact: Dr. Andreas Gobiet  
[andreas.gobiet@uni-graz.at](mailto:andreas.gobiet@uni-graz.at)

Wegener Center for Climate and Global Change  
University of Graz  
Leechgasse 25  
A-8010 Graz, Austria  
[www.wegcenter.at](http://www.wegcenter.at)

# Radio occultation data analysis for climate change monitoring and first climatologies from CHAMP

Dissertation

zur Erlangung des akademischen Grades  
eines Doktors der Naturwissenschaften  
vorgelegt von

Mag. Andreas Gobiet

Wegener Center for Climate and Global Change (WegCenter)  
und  
Institutsbereich für Geophysik, Astrophysik und Meteorologie (IGAM)/ Institut für Physik  
Universität Graz



# Acknowledgments

I want to express my gratitude and respect to my supervisor Prof. G. Kirchengast whose mentorship reached far beyond excellent scientific advice. Above that he is, as founder and head of the Atmospheric Remote Sensing and Climate System (ARSCliSys) Research Group, also responsible for the fruitful and challenging atmosphere building the framework of this thesis.

Thanks are expressed to my colleagues of the ARSCliSys Research Group for their great support and many scientific discussions, especially to S. Tschürtz, Dr. A. K. Steiner, Dr. J. M. Fritzer, and Dr. U. Foelsche. Many parts of this work would not have been possible without the heritage from their work and their support in many regards. For fruitful cooperation during the last year of this thesis I thank my colleague Mag. M. Borsche.

Thanks also to the staff at the Institute for Geophysics, Astrophysics, and Meteorology, especially the system administrators Ing. R. Maderbacher and Mag. K. Huber, but to all others as well for unbureaucratic support.

A lot of the work of this thesis is based on code from the End-to-end GNSS Occultation Performance Simulator (EGOPS), especially on parts written by S. Syndergaard (University Corporation for Atmospheric Research, UCAR, Boulder, CO) and M. Gorbunov (Institute for Atmospheric Physics, Russian Academy of Sciences, Moscow). Thanks for this heritage and discussions related to it.

My colleagues at GeoForschungsZentrum (GFZ) Potsdam enabled access to CHAMP data. In this regard, and on top of that for many fruitful discussions and common studies and publications, I especially thank Dr. J. Wickert and Dr. T. Schmidt.

Other institutions contributing data and advice for this work include the European Centre for Medium-Range Weather Forecasts (ECMWF) and the Institut für Meteorologie und Klimaforschung (IMK) in Karlsruhe. Special thanks are expressed to Dr. A. Simmons (ECMWF) and Dr. D.-Y. Wang (IMK).

Furthermore, I gratefully acknowledge financial support from the START research award of G. Kirchengast funded by the Austrian Ministry for Education, Science, and Culture and managed under Program No. Y103-N03 of the Austrian Science Fund and from CHAMPCLIM project of G. Kirchengast funded by the Austrian Ministry for Traffic, Innovation, and Technology within the Austrian Space Applications Programme (ASAP) and managed under Project ASAP-CO-004/03 of the Austrian Space Agency (since 2005: Aeronautics and Space Agency).



# Table of Contents

<b>INTRODUCTION</b> .....	<b>1</b>
<b>1 THE CLIMATE SYSTEM AND CLIMATE MONITORING</b> .....	<b>3</b>
1.1. THE CLIMATE SYSTEM .....	3
1.2. RADIATIVE ENERGY BALANCE .....	5
1.3. NATURAL CLIMATE VARIABILITY AND CHANGE .....	6
1.4. PAST ANTHROPOGENIC CLIMATE CHANGE.....	6
1.5. CLIMATE MODELING AND PROJECTED CLIMATE CHANGE.....	7
1.6. CLIMATE MONITORING.....	8
<b>2 THE RADIO OCCULTATION TECHNIQUE</b> .....	<b>11</b>
2.1. BASIC CONCEPT.....	11
2.2. HISTORY, CURRENT ACTIVITIES, AND FUTURE PERSPECTIVES .....	11
2.3. THE GNSS AND ITS SIGNALS .....	13
2.4. GNSS SIGNALS IN THE ATMOSPHERE .....	14
2.4.1. Neutral Atmosphere .....	15
2.4.2. Ionosphere.....	16
2.4.3. Geometric Optics and Single Ray Approximation .....	17
2.5. THE RECEIVED SIGNAL.....	18
2.6. THE GROUND SEGMENT - CALIBRATION.....	19
2.7. SPATIAL AND TEMPORAL COVERAGE .....	20
2.8. RADIO OCCULTATION FOR CLIMATE MONITORING AND NWP .....	22
2.9. CHAMP — THE CHALLENGING MINISATELLITE PAYLOAD RADIO OCCULTATION EXPERIMENT .....	23
<b>3 RADIO OCCULTATION RETRIEVAL</b> .....	<b>27</b>
3.1. RETRIEVAL OF BENDING ANGLES.....	27
3.1.1. Retrieval of Total Atmospheric Bending Angles .....	27
3.1.2. Ellipsoid Correction .....	30
3.1.3. Ionospheric Correction.....	30
3.2. RETRIEVAL OF ATMOSPHERIC PARAMETERS .....	33
3.2.1. Retrieval of Refractivity.....	33
3.2.2. Retrieval of Dry Density, Pressure, Geopotential Height, and Temperature (“Dry Retrieval”)....	35
3.2.3. The Temperature - Humidity Ambiguity .....	36
<b>4 HIGH ALTITUDE INITIALIZATION AND STATISTICAL OPTIMIZATION</b> .....	<b>39</b>
4.1. REVIEW OF HIGH ALTITUDE INITIALIZATION AND STATISTICAL OPTIMIZATION METHODS.....	39
4.2. IMPROVEMENT OF HIGH ALTITUDE INITIALIZATION AND STATISTICAL OPTIMIZATION.....	42
4.2.1. The Basic IGAM High Altitude Retrieval Scheme .....	42
4.2.2. The Enhanced IGAM High Altitude Retrieval Scheme .....	43
4.3. EVALUATION OF THE IGAM RETRIEVAL SCHEMES .....	45
4.3.1. Systematic Case Study Setup .....	46
4.3.2. Large Ensemble Study Setup .....	50
4.3.3. Results of the Systematic Case Study .....	51
4.3.4. Results of the Large Ensemble Study.....	53
4.3.5. Conclusions From the Evaluation Studies.....	55
<b>5 DEVELOPING A ROBUST RETRIEVAL SYSTEM FOR CHAMP DATA – CCRV2</b> .....	<b>57</b>
5.1. INTERFACE TO GFZ LEVEL 2 DATA AND TECHNICAL ROBUSTNESS .....	57
5.2. QUALITY CONTROL .....	58

5.2.1.	Internal Quality Control .....	58
5.2.2.	External Quality Control .....	60
5.3.	STABLE IONOSPHERIC CORRECTION .....	60
5.4.	STATISTICAL OPTIMIZATION OF CHAMP BENDING ANGLES .....	63
5.4.1.	Observation Error Estimation .....	63
5.4.2.	Climatological Background Information and Bias Correction .....	64
5.4.3.	ECMWF Background Information .....	65
5.5.	CHAMPCLIM RETRIEVAL (CRR) VERSION 2 OVERVIEW .....	65
<b>6</b>	<b>CHAMP RETRIEVAL PERFORMANCE STUDIES .....</b>	<b>67</b>
6.1.	VALIDATION SETUP AND DATA .....	67
6.1.1.	Methodology .....	67
6.1.2.	CHAMP Data for the CCR – GFZ Retrieval Intercomparison .....	68
6.1.3.	CHAMP Data for Comparison with ECMWF Analyses .....	69
6.1.4.	CHAMP Data for Comparison with MIPAS and GOMOS .....	69
6.1.5.	ECMWF Correlative Data .....	70
6.1.6.	ENVISAT/MIPAS and ENVISAT/GOMOS Correlative Data .....	71
6.2.	VALIDATION RESULTS .....	74
6.2.1.	IGAM – GFZ Retrieval Intercomparison .....	74
6.2.2.	Validation with Independent Data Sources .....	78
6.3.	SUMMARY OF THE CCR VALIDATION .....	85
<b>7</b>	<b>RADIO OCCULTATION BASED CLIMATOLOGIES .....</b>	<b>87</b>
7.1.	THE CHAMPCLIM PROJECT .....	87
7.2.	FIRST CLIMATOLOGIES FROM CHAMP .....	87
7.2.1.	Sampling Strategies – Sampling Errors .....	87
7.2.2.	Quality of Seasonal RO-Based Climatologies .....	93
7.3.	CHAMP RO CLIMATOLOGIES FOR MODEL VALIDATION .....	97
7.3.1.	Relevance of ECMWF Operational Analysis and its Validation .....	97
7.3.2.	ECMWF and CHAMPCLIM Data Used .....	97
7.3.3.	Validation Methodology .....	98
7.3.4.	Results and Discussion .....	98
7.3.5.	Concluding Remarks .....	102
	<b>CONCLUSIONS .....</b>	<b>103</b>
	<b>REFERENCES .....</b>	<b>105</b>
	<b>LIST OF SYMBOLS .....</b>	<b>113</b>
	<b>LIST OF ACRONYMS .....</b>	<b>117</b>
	<b>APPENDIX JJA2003 CHAMPCLIM RESULTS .....</b>	<b>119</b>
A.1	CAMPCLIM AND ECMWF REFRACTIVITY AND DRY TEMPERATURE .....	120
A.1.1	Refractivity: 18 Latitude Bands (10 Degree Zonal Means) .....	120
A.1.2	Dry Temperature: 18 Latitude Bands (10 Degree Zonal Means) .....	121
A.1.3	Dry Temperature: 18 Latitude x 24 Longitude Bins .....	122
A.2.	REFRACTIVITY AND DRY TEMPERATURE SAMPLING ERROR ESTIMATE .....	125
A.2.1	18 Latitude Bands (10 Degree Zonal Means) .....	125
A.2.2	18 Latitude x 24 Longitude Bins .....	126
A.3	REFRACTIVITY AND DRY TEMPERATURE MEASUREMENT BIAS (VS. ECMWF) .....	129
A.3.1	18 Latitude Bands (10 Degree Zonal Means) .....	129
A.3.2	18 Latitude x 24 Longitude Bins .....	130
A.4	REFRACTIVITY AND DRY TEMPERATURE MEASUREMENT RANDOM ERROR (VS. ECMWF) .....	133
A.4.1	18 Latitude Bands (10 Degree Zonal Means) .....	133
A.4.2	18 Latitude x 24 Longitude Bins .....	134
A.5	REFRACTIVITY AND DRY TEMPERATURE CLIMATOLOGICAL TOTAL ERROR (VS. ECMWF) .....	137
A.5.1	18 Latitude Bands (10 Degree Zonal Means) .....	137
A.5.2	18 Latitude x 24 Longitude Bins .....	138

# Introduction

The framework for this thesis is the broad field of climate research. Like many studies in this field, it is basically motivated by the concern about the state and the development of the Earth's climate and its impact on the human society. The Intergovernmental Panel on Climate Change (IPCC) states in its third assessment report (TAR):

“The global average surface temperature has increased over the 20th century by about 0.6°C.” [IPCC, 2001]

“There are new estimates of the climate response to natural and anthropogenic forcing, and new detection techniques have been applied. Detection and attribution studies consistently find evidence for an anthropogenic signal in the climate record of the last 35 to 50 years.” [Mitchell et al., 2001]

These statements show us that the Earth's climate is changing and that the human society has influence on it. Other statements, like the preface of a recent report of the International Task Force on Climate Change, a political high-level cooperation of three internationally renowned think tanks (The Australia Institute, the Institute for Public Policy Research in London, and the Center for America Progress in Washington, D.C.) summarize the motivation why political actions are necessary:

“Beyond the 2°C level, the risks to human societies and ecosystems grow significantly. It is likely, for example, that average temperature increases larger than this will entail substantial agricultural losses, greatly increased numbers of people at risk of water shortages, and widespread adverse health impacts. Exceeding a global average increase of more than 2°C could also imperil a very high proportion of the world's coral reefs and cause irreversible damage to important terrestrial ecosystems, including the Amazon rainforest. Above the 2°C level, the risks of abrupt, accelerated, or runaway climate change also increase. The possibilities include reaching climatic tipping points leading, for example, to the loss of the West Antarctic and Greenland ice sheets (which, between them, could raise sea levels more than ten meters over the space of a few centuries), the shutdown of the thermohaline ocean circulation (and, with it, the Gulf Stream), and the transformation of the planet's forests and soils from a net sink of carbon to a net source of carbon. Climate science is not yet able to specify the trajectory of atmospheric concentrations of greenhouse gases that corresponds precisely to any particular global temperature rise. Based on current knowledge, however, it appears that achieving a high probability of limiting global average temperature rise to 2°C will require that the increase in greenhouse-gas concentrations as well as all the other warming and cooling influences on global climate in the year 2100, as compared with 1750, should add up to a net warming no greater than what would be associated with a CO<sub>2</sub> concentration of about 400 parts per million (ppm). Concentrations of CO<sub>2</sub> alone (standing at 379 ppm in March 2004 compared to the pre-industrial level of 280 ppm) are likely to rise above 400 ppm in coming decades and could rise far higher under a business-as-usual scenario.” [International Climate Change Task Force, 2005]

Impacts of climate change include the increased risk of flooding and droughts, generally increased probability of extreme weather events, regionally decreased water availability and crop yields potentially resulting in mass starvation in risk regions (e.g., southern Africa). Furthermore we are potentially facing severely rising sea levels causing many low-lying islands to disappear and threatening many densely populated regions on the globe. Rising atmospheric CO<sub>2</sub> concentrations enhance the acidity of the oceans and reduce their capacity as a carbon-sink and affect the entire marine food chain. Rising global temperatures can

exacerbate the spread of diseases. Even the probability of singular irreversible events to occur during the recent century is recently not regarded to be negligible any more and estimated to be in the range of 10 % – 50 %.

One example for such an event is the breakdown of the thermohaline circulation which would cause a cooling of the whole northern hemisphere with especially strong cooling around the North Atlantic. Another example is the disintegration of the Greenland and West-Antarctic ice sheets which could raise the global sea level by ~ 6 m and ~ 5 m, respectively (International Symposium on the Stabilisation of Greenhouse Gases, report of the steering committee and presentations given at the symposium, Exeter, UK, 2005, <http://www.stabilisation2005.com/>).

“If one wishes to understand, detect and eventually predict the human influence on climate, one needs to understand the system that determines the climate of the Earth and of the processes that lead to climate change.“ [Baede et al., 2001]

The above quotations from the TAR of IPCC and from Task Force on Climate Change together with consideration of recent results from climate impact research summarize the motivation for this work and many other works in the field of climate research. The aim of the scientific community to understand the Earth’s climate system is not only driven by scientific curiosity but also by the growing awareness of the potentially devastating impacts of climate change and by realizing that human beings are standing in mutual interaction with other parts of the climate system and have the ability to influence and change the climate on global scale.

Understanding the climate system is a prerequisite for successfully coping with the responsibility for it and this work aims at adding to our knowledge and understanding in a very basic way, by describing and advancing a method for climate monitoring, i.e., by helping to build up a high-quality reference database describing fundamental climate variables of the three-dimensional global atmosphere as a basis for climate research and the development and enhancement of climate models.

The thesis first gives a very brief overview of the climate system, elaborates the idea behind climate monitoring (Chapter 1), and subsequently focuses on a method particularly useful for climate monitoring, the satellite-based radio occultation (RO) technique which has the potential to become a reference method in this field. Its basic characteristics and techniques are explained in Chapters 2 and 3, while the enhancements of the technique worked out during the work for this thesis and its application to data from the first satellite providing RO data on a longer term, the CHALLENGING Minisatellite Payload (CHAMP), are described in Chapters 4 and 5. Chapter 6 is dedicated to the validation of the performance of the elaborated methods and finally, in Chapter 7, first climatologies based on CHAMP data and one application of these climatologies are presented.

# 1 The Climate System and Climate Monitoring

## 1.1. The Climate System

Weather events, such as mid-latitude low and high pressure systems and their associated frontal zones, can be regarded as single realizations of a set of climate variables. In this respect, climate is the statistics of weather describing its mean state, its variability, and other statistical properties like the frequency of the occurrence of extremes. Significant variations of the statistical parameters persisting for decades or longer are referred to as “climate change”, while the term “climate variability” denotes variations on all temporal and spatial scales beyond that of individual weather events. Both, climate change and variability may be due to internal dynamic of the climate system or variations in the external forcings like volcanic eruptions, solar variations, human induced changes of the composition of the atmosphere, and anthropogenic land-use change. To understand the terms “internal” and “external” one has to be aware of the components of the climate system and its system boundaries. A schematic overview is given in Figure 1.1a.

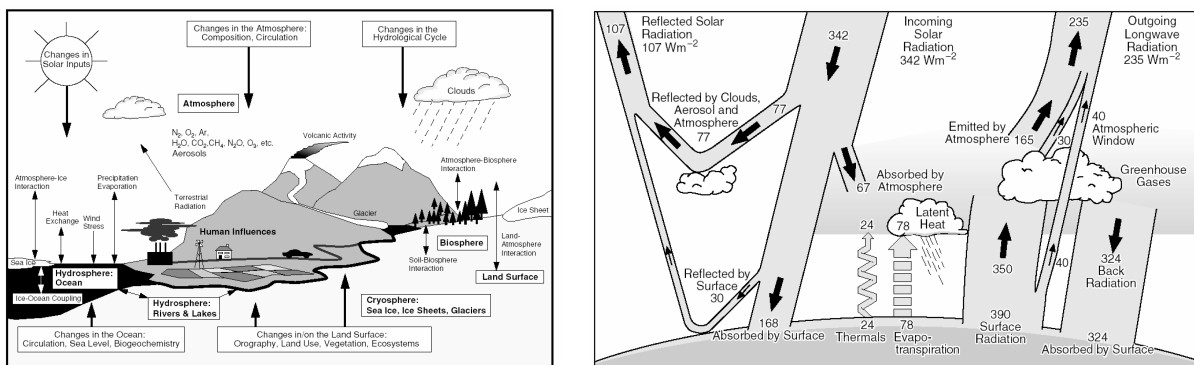


Figure 1.1: a) Schematic view of the climate system’s components (bold text in boxes), their processes and interactions (text associated with thin arrows), and selected aspects of each component that may change (text in boxes associated with bold arrows) Source: *Baede et al.* [2001]. b) The Earth’s annual global mean energy budget. Source: *Kiehl and Trenberth* [1997].

The *atmosphere* is, due to its relatively large compressibility and low specific heat and density, the most rapidly changing part of the climate system with a relaxation time (in its lowest compartment, the troposphere) of days to weeks. It is the central component of the climate system and shows great spatial and temporal variability. 99 % of the mass of the atmosphere is found below an altitude of only 30 km compared to its horizontal extension in the order of 20,000 km. The temporal, horizontal, and vertical atmospheric structure is closely related to dynamics, energy transport, and radiative properties and therefore of key importance for the climate system.

According to the vertical temperature gradient, the atmosphere can be divided into four main layers: The troposphere ranging from ground to  $\sim 7$  km at the poles and  $\sim 17$  km near the Equator, the stratosphere above it up to  $\sim 50$  km, the mesosphere up to  $\sim 90$  km and the thermosphere above. The transition zones between the different spheres are (roughly) defined to be at the altitudes where the sign of the temperature gradient changes and are called “pauses”. However, there is no representative global mean vertical temperature structure but very significant spatial and temporal variability (see Figure 7.7 for an example of the atmospheric temperature structure) and the detailed knowledge of this variability is a key to the understanding of atmospheric dynamics and the climate system.

The troposphere is the part of the atmosphere with the highest variability, the shortest relaxation time, and is the stage for virtually all weather phenomena. The stratosphere shows less pronounced variability, longer relaxation time (in the order of months), and its direct impact on life on earth (apart from its role as shield against biological harmful short wave radiation) is much smaller than that of the troposphere. Nevertheless, climatic changes in the stratosphere are important because of their effect on stratospheric chemistry, on the radiation budget, and since stratospheric temperature trends and changes in tropopause heights are indicators for climate change [e.g., *Shine and Forster, 2002; Santer et al., 2002, Hare et al., 2004*] which is particularly interesting from the climate monitoring point of view (see section 1.4).

The atmosphere is composed of nitrogen ( $N_2$ , 78.1 % volume mixing ratio), oxygen ( $O_2$ , 20.9 % volume mixing ratio) and Argon (Ar, 0.93 % volume mixing ratio), and trace gases. Due to their atomic configuration the main constituents don't interact with infrared radiation emitted from the Earth but many trace gases, the so-called “greenhouse gases” do so and play an essential role in the Earth's energy budget. They are responsible for the natural and anthropogenic (or “additional”) greenhouse effect. Most important in this respect are  $H_2O$ ,  $CO_2$ ,  $CH_4$ ,  $N_2O$ ,  $O_3$ , and some other trace gases like halogenated hydrocarbons. The atmospheric concentration of some of them is strongly influenced by the human activities and contributes to global warming (see section 1.4) with  $CO_2$  being the most prominent. Besides trace gases, aerosols and clouds interact with incoming and outgoing radiation in a complex way leading to many feedback loops in the climate system. Water (in all three phases) plays a key role in the climate system due to the energy involved in phase changes and as the strongest greenhouse gas in its gaseous form. Comprehensive information about the physical and chemical properties of the atmosphere and its role in the climate system can be found in the textbooks of, e.g., *Andrews [2000], Finlayson-Pitts and Pitts [2000], and Peixoto and Oort [1992]*.

The *hydrosphere* comprises surface and subterranean liquid water and is strongly coupled to the atmosphere through mass- and heat exchange (water vapor). The salient parts of the hydrosphere are the oceans: They cover about 2/3 of the Earth's surface, possess large specific heat and transport huge amounts of energy from south to north. Due to the ocean's thermal inertia (relaxation times being in the order 100 to 1000 years), the oceans function as a damping regulator for the climate system, particularly for the troposphere which is directly coupled to the ocean via large amounts of heat and mass transfer. On a longer timescale, the oceans are a source of natural climate variability. Additionally, they play a crucial role as sink and source for atmospheric  $CO_2$ .

The *cryosphere* includes the polar ice sheets, glaciers, and all surface snow and ice in general. Its importance for the climate system is a strong influence on the radiation budget due to its high reflectivity for solar radiation (albedo), an important role in the surface-atmosphere and hydrosphere-atmosphere heat and mass exchange due its low thermal conductivity and insulating properties, and its role in driving deep ocean circulation. Since the cryosphere stores large amounts of water, it is a source of sea level variations.

The *land surface* system comprises the continents and controls (together with the hydrosphere and cryosphere) how solar energy is absorbed by the Earth and transferred to the atmosphere by latent heat (water vapor), sensible heat, and long wave radiation and dynamically influences the atmosphere through the transfer of angular momentum and dissipation of kinetic energy by friction in the planetary boundary layer.

The *biosphere* includes all continental and oceanic flora and fauna. It plays a central role in the budget of many trace gases, in particular in the carbon-cycle for the CO<sub>2</sub> concentrations (respiration and photosynthesis), influences the water input to the atmosphere through evapotranspiration, and is, e.g., tightly connected with the land surface by influencing its radiative properties and surface roughness.

Processes in the individual components and interaction processes between them occur on a wide range of spatial and temporal timescales making the system extremely complex. As demonstrated in some examples above, all components are tightly interconnected via fluxes of mass, heat and momentum.

Processes not covered by the five components but influencing the climate system like solar variations, volcanic eruptions, or anthropogenic CO<sub>2</sub> emissions and land use changes are called external forcings and play, besides the internal variability of the system, a crucial role in climate variability and change.

## 1.2. Radiative Energy Balance

The only significant source of energy for the climate system is radiation from the Sun. According to its blackbody temperatures, the Sun (~ 5770 K) provides virtually all of its energy at wavelengths between 100 nm and 2 μm in the ultraviolet, visible, and near infrared region of the electromagnetic (EM) spectrum while the Earth (~ 255 K) emits most of its radiation between 4 μm and 60 μm in the infrared region.

The global annual mean temperature near the Earth's surface is the result of a radiative equilibrium of incoming solar and outgoing terrestrial radiation and strongly influenced by the composition of the atmosphere since trace gases, aerosols, and clouds strongly interact with radiation. Figure 1.1b gives a schematic overview of this system: Of 342 Wm<sup>-2</sup> solar radiation ~ 31 % is immediately reflected back into space by clouds, aerosols, gases, and the surface (Albedo). The rest serves as energy input to the system and is absorbed by the surface and a minor part by the atmosphere. The earth surface returns that energy as sensible or latent heat to the atmosphere and emits infrared radiation which is mainly absorbed in the atmosphere by greenhouse gases and reemitted into all directions including towards Earth's surface. This process increases the tropospheric temperature and reduces the amount of energy emitted to space (outgoing long wave radiation). Since the imbalance between incoming and outgoing radiation heats up the atmosphere and since higher temperatures result in (super-proportional) more emitted long wave radiation, the temperature increases until a new radiative equilibrium is reached on a higher temperature level compared to an atmosphere with less greenhouse gases. This process is called greenhouse effect and is responsible for a global annual mean surface temperature of + 14°C compared to the Earth's effective emission temperature of - 19° C. More detailed elaboration of the Earth's radiative energy equilibrium can be found in the textbook of *Peixoto and Oort* [1992] and the article of *Kiehl and Trenberth* [1997].

In an equilibrium state, the net radiation at the top of the atmosphere is zero. In practice, the top of the troposphere can be taken as top of atmosphere for this purpose because the stratosphere adjusts to changes in the radiative balance much quicker (in the order of month) than the troposphere-ocean part of the system. Radiative imbalances at the

tropopause (net irradiance other than zero) are called radiative forcing and can be caused by internal or external processes, being of natural or anthropogenic origin, and having warming or cooling impact on Earth's near surface climate and drive climate variability and change. A comprehensive description of the radiative forcing concept is given by *Ramaswamy et al.* [2001] and references therein.

### 1.3. Natural Climate Variability and Change

Climate variations may be caused by external radiative forcings, such as variations in the solar radiation, or aerosols from volcanic eruptions but also from internal interactions of components of the climate system such as the El Niño-Southern Oscillation (ENSO) resulting from ocean-atmosphere interaction in the tropical Pacific. The response of the climate system to internal variations and external forcings is complicated by feedbacks and non-linear mechanisms.

Natural climate variations occur on all time-scales. During the last million years glacial periods and interglacials have alternated due to variations of the Earth's orbital parameters and the related changes in incoming solar radiation. During these long periods, also large and rapid changes occurred like warming and cooling of many degrees within one human lifetime. The last 10,000 years have been relatively stable and the last 1000 years are characterized by an irregular but steady cooling. A review on the current knowledge about the Earth's past climate is given by *Folland et al.* [2001] in the TAR.

More recent studies are in conflict with some temperature reconstructions in the TAR, particularly those presented by M.E. Mann and his co-authors [*Mann et al.*, 1998; *Mann and Bradley*, 1999] and show higher natural variability in the Northern Hemispheric temperatures of the past two millennia [*Moberg et al.*, 2005]. But apart from the higher natural variability found by these studies, they are consistent with older studies in their finding that there is no evidence for any earlier period in the past two millennia with warmer conditions than in the post-1990 period.

On the regional scale, climate variability is much larger than on global scale since often variations in one region are compensated by opposite variations in other regions. Closer inspections shows that regional climate variations are often related to large-scale spatially anchored quasi-oscillatory patterns, the most prominent being the ENSO and the North Atlantic Oscillation (NAO) influencing the climate in Europe.

### 1.4. Past Anthropogenic Climate Change

It's only since the beginning of the industrial revolution in the mid-18<sup>th</sup> century that human activities started to have impact beyond the direct human vicinity and surrounding regions and became important on continental on global scales. In respect to climate change, the most important human activities are the combustion of fossil fuels and land-use changes. The amount of CO<sub>2</sub> in the atmosphere has increased by 34 % since pre-industrial times from 280 ppm in 1750 to 376 ppm in 2003 and is currently increasing by ~ 0.5 % per year (Conway et al., NOAA Climate Monitoring and Diagnostics Laboratory, presentation at the 2004 ANNUAL Meeting of the NOAA Climate Monitoring and Diagnostics Laboratory, [http://www.cmdl.noaa.gov/publications/pdf\\_2004/conway.pdf](http://www.cmdl.noaa.gov/publications/pdf_2004/conway.pdf)). About 2/3 of this increase is due to combustion of fossil fuels and the rest due to land-use change, mostly deforestation [*Prentice et al.*, 2001].

The best estimate of the near-surface warming since the late 19<sup>th</sup> century up to the end of the 20<sup>th</sup> century is  $0.6^{\circ}\text{C} \pm 0.2^{\circ}\text{C}$  which is likely to be the largest in the last millennium [Folland *et al.*, 2001]. Up-to-date global temperature analyses show an increase by  $0.7^{\circ}\text{C} - 0.8^{\circ}\text{C}$  until today (2005) (e.g., Goddard Institute for Space Studies, online material, <http://data.giss.nasa.gov/gistemp/>).

Most of the recent temperature increase occurred between 1910 and 1945 and since 1976 with a current warming rate of  $0.17^{\circ}\text{C}$  per decade. Regional examination of the data showed more warming over the continents than over the oceans with largest warming over the northern winter high-latitudes. In parallel to the near surface temperature increase, the free tropospheric temperatures also increased (but slower), the diurnal temperature range decreased, the stratospheric temperature strongly decreased ( $0.5^{\circ}\text{C} - 2.5^{\circ}\text{C}$  per decade since 1979), the sea level rose by 10 cm – 20 cm, and precipitation strongly changed regionally. IPCC's third assessment report (TAR) concludes that most of the observed warming during the last 50 years is likely due to the increase of greenhouse gas concentrations in the atmosphere [IPCC, 2001].

More recently, many of the numbers and conclusions presented in the TAR have been updated pointing towards even stronger climate change and more severe impacts (e.g., International Symposium on the Stabilisation of Greenhouse Gases, report of the steering committee and presentations given at the symposium, Exeter, UK, 2005, <http://www.stabilisation2005.com/>).

## 1.5. Climate Modeling and Projected Climate Change

Due to the complexity of the climate system the only tools that provide quantitative estimates of future climate change are complex numerical models. Climate models or “general circulation models” (GCMs) are simplified mathematical representations of the climate system. The growing complexity of GCMs, the inclusion of more and more climate system components in addition to the atmosphere (such as the ocean, the carbon cycle, land-surface processes, sea- and land-ice processes, atmospheric chemistry, and aerosols), and the simplified representation of many subgrid-scale processes, the so-called physical parameterization, makes it inevitable to evaluate and tune the models by simulating past periods and comparing the results to observational data. This is, besides the necessity to describe the state of the climate for the purpose of gaining better understanding, one major objective of climate monitoring (see also section 1.6).

Climate projections are based on future scenarios of different climate forcing agents (predominately  $\text{CO}_2$  and other greenhouse gases, aerosols, and solar radiation) [e.g., IPCC, 2000] and are afflicted with uncertainties in these scenarios, uncertainties due to the partly chaotic behavior of the climate system, and uncertainties in the models' ability to properly describe the climate system. These uncertainties must be quantified to be able to judge the outcome of climate projections. One current approach for uncertainty estimation is to build ensembles of models containing models driven by different forcing scenarios, models initialized differently, and different models (or different sets of physical parameterization in one model). Assuming that climate predictions produced by such an ensemble spans the range of scenario- and model-uncertainties as well the non-predictable chaotic variability of the climate system, the uncertainty of the predictions can be estimated to some degree. More than that, it has been shown that the ensemble mean of such simulations generally has more skill in describing climate parameters than any single model in the ensemble [e.g., Gates *et al.*, 1999].

For the TAR, various GCMs have been gathered to build an ensemble that projected the Earth's climate for the current century. According to the results of this ensemble, the global mean surface temperatures will rise by 1.4° C to 5.8° C in the period from 1990 to 2100, including the full range of uncertainty mentioned above, approximately half of it due to scenario uncertainty and half due to model sensitivity (which contains model uncertainty and sensitivity due to chaotic climate variability). The temperature trend is more pronounced over continents than over oceans and strongest in the northern high latitudes in winter. Increased temperatures intensify the water cycle and atmospheric water vapor content and precipitation is projected to increase globally, but with large regional differences (and uncertainties): In northern Europe, the winter precipitation is likely to increase and in the Mediterranean the summer precipitation is likely to decrease. A decrease of summer precipitation is also predicted for Australia and southern Africa. The global snow and ice-cover will further decline (partially) causing the global sea level to rise by 9 cm – 88 cm. As for the extreme events, increasing frequency of heat-waves, droughts, and more intense precipitation events is estimated to be likely or very likely over many areas. For a comprehensive review of the projected climate change according to IPCC, the reader is referred to the Chapters 9 and 10 of the TAR by *Cubasch et al.* [2001] and *Giorgi et al.* [2001].

Some figures of the TAR, particularly those about sea-level rise, are currently under discussion due to new data indicating that the West-Antarctic ice sheet previously assumed to be stable might already be starting to disintegrate. The possibility of a total collapse can not be neglected any more and would cause the sea level to rise by ~ 5 m (C. Rapley, British Antarctic Survey, presentation at the International Symposium on the Stabilisation of Greenhouse Gases, Exeter, UK, 2005, <http://www.stabilisation2005.com/>).

Also the TAR's range of uncertainty in the global surface temperatures is under discussion as a recent study investigated the response of a "grand" GCM ensemble (2017 simulations) to doubling CO<sub>2</sub> concentration compared to pre-industrial concentrations and found the global mean surface temperature response spanning from 1.9° C to 11.5° C with a median at 3.4° C. This range doesn't only represent model uncertainty but to big degree also natural (chaotic) climate variability since no indication was found that models giving extreme responses were less realistic than models giving "normal" responses [*Stainforth et al.*, 2005].

## 1.6. Climate Monitoring

The need for a global climate monitoring system for the purpose of understanding the climate system is self-evident for most climate scientists, but that objective (based on scientific curiosity) is not sufficient to raise funding for such an expensive undertaking. Additionally to the scientifically-driven motivation, there are societal objectives to fulfill because impacts of climate change on human society are significant as pointed out in the Introduction to this thesis.

On one hand, the documentation of current climate is important for many direct users in the field of agriculture, renewable energy production, insurances, disaster management, policy, and many other (partly commercial) activities. Data for this kind of users is usually provided by the national weather services. But apart from that there is need for reliable projections of climate into the future under certain forcing scenarios enabling to quantify impacts, to attribute climate change to forcings that can be influenced by society, to find prevention and adaptation strategies, and to give reliable information to society and policy makers.

These goals can be only reached by interconnecting the two major strategies of climate research, namely monitoring and modeling. Monitoring is essential to analyze the recent and past climate, to evaluate and improve modeling and, at the same time, the act of assimilating observed data to improve model performance provides criteria for improving the monitoring program [e.g., *Goody et al.*, 2002].

For model validation, additionally to surface data, upper air data is increasingly important and apart from that, needed climate variables are often non-conventional because the model input (natural and anthropogenic forcings) has to be evaluated as well.

One of the leading international bodies concerned with global climate monitoring, the Global Climate Observing System (GCOS), defined, in cooperation with IPCC, the basic requirements of systematic climate monitoring. Following the definitions in the relevant GCOS report [*WMO*, 2003], climate observations are required to:

- Characterize the state of the global climate system and its variability;
- Monitor the forcing of the climate system, including both the natural and anthropogenic contributions;
- Support the attribution of the causes of climate change;
- Support the prediction of global climate change;
- Project global climate change information down to regional and national scale; and
- Characterize extreme events important in impact assessment and adaptation, and to assess risk and vulnerability.

GCOS identified the climate variables listed in Table 1.1 to have high impact with respect to these requirements and are currently feasible for global implementation and concluded that achieving global coverage and climate quality observations of these variables is essential.

Table 1.1: Essential climate variables currently feasible for global implementation. Source: *WMO* [2003].

Domain	Essential Climate Variables
<b>Atmospheric</b> (over land, sea and ice)	<p><b>Surface:</b> Air temperature, Precipitation, Air pressure, Surface radiation budget, Wind speed and direction, Water vapour.</p> <p><b>Upper-air:</b> Earth radiation budget (including solar irradiance), Upper-air temperature (including MSU radiances), Wind speed and direction, Water vapour, Cloud properties.</p> <p><b>Composition:</b> Carbon dioxide, Methane, Ozone, Other long-lived greenhouse gases<sup>5</sup>, Aerosol properties.</p>
<b>Oceanic</b>	<p><b>Surface:</b> Sea-surface temperature, Sea-surface salinity, Sea level, Sea state, Sea ice, Current, Ocean colour (for biological activity), Carbon dioxide partial pressure.</p> <p><b>Sub-surface:</b> Temperature, Salinity, Current, Nutrients, Carbon, Ocean tracers, Phytoplankton.</p>
<b>Terrestrial</b>	River discharge, Water use, Ground water, Lake levels, Snow cover, Glaciers and ice caps, Permafrost and seasonally-frozen ground, Albedo, Land cover (including vegetation type), Fraction of absorbed photosynthetically active radiation (FAPAR), Leaf area index (LAI), Biomass, Fire disturbance.

Table 1.1 addresses the entire climate system including physical, chemical and biological properties, and atmospheric, oceanic, hydrologic, cryospheric, and terrestrial processes which is one main difference to the requirements of operational meteorological monitoring systems.

The second major difference is addressed by the phrase “climate quality” in the GCOS conclusion mentioned above. The quality requirements on climate data are basically induced by the need for information on changes and rates of changes in the climate system. These requirements imply that data sets covering long periods with the option of easily expanding them into the future are necessary. Such data sets must be homogeneous without extraneous and undocumented instrument or observing-system changes.

An third important point (though equally required for advancing numerical weather prediction (NWP) as for climate research) is the claim for global coverage.

In recent years, satellite remote sensing became increasingly important for climate monitoring and many coverage problems imminent to in-situ monitoring systems could be resolved using satellite data. Additionally, entirely new and important surface and upper air data became available. However, particularly for satellite data that primarily rely on the measurement of broadband radiances, the claim for homogeneity is not easy to fulfill. In such measurements the data records of different instruments are biased relative to each other and sometimes have drifts. Homogeneity can only be reached if overlapping datasets are available. But even if it is possible to homogenize the datasets, they are still calibrated relative to some other dataset and can therefore not be used as independent reference or “climate benchmark” (datasets of key climate variables valid for all time, i.e. possessing high precision, accuracy, and stability and being absolutely calibrated based on irrefutable standards with broad laboratory base) which would be desirable for model calibration and the detection of trends.

As will be demonstrated in the subsequent Chapters of this thesis, the RO method fits perfectly into the requirements for upper air climate benchmark data and is a feasible method with unique potential for global climate monitoring.

## 2 The Radio Occultation Technique

### 2.1. Basic Concept

The radio occultation (RO) technique is an active satellite-to-satellite limb sounding concept exploiting the global navigation satellite system (GNSS) signals. The phase and amplitude of the EM waves transmitted by GNSS satellites are observed by a high precision receiver onboard a satellite in low Earth orbit (LEO). Due to the measurement geometry (Figure 2.1) the GNSS-LEO link scans the Earth's ionosphere and neutral atmosphere near-vertically while, viewed from the LEO satellite, the transmitting GNSS satellite is setting or rising behind the Earth's limb.

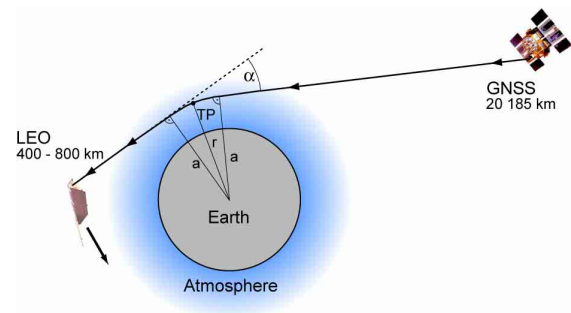


Figure 2.1: Geometry of a setting radio occultation event. TP: tangent point,  $a$ : impact parameter,  $r$  tangent point distance from Earth's center,  $\alpha$ : bending angle.

From the received signal's phase delay (relative to the vacuum phase) bending angles and the atmosphere's refractive index can be derived. In a further step, vertical profiles of basic atmospheric parameters like electron density, neutral density, pressure, temperature, geopotential height, and, if background information is added, humidity can be derived (see Chapter 3 for details on the retrieval and the review article by *Kursinski et al.*, [1997] for a comprehensive overview of the RO technique).

### 2.2. History, Current Activities, and Future Perspectives

The RO technique was originally developed and successfully applied to the study of our solar system's planetary atmospheres when scientists noticed that the radio link to a spacecraft passing behind a planet was systematically refracted by the planetary atmosphere. The technique was first applied to the atmospheres of Mars and Venus in the 1960's and subsequently also to the atmospheres of the outer planets. Accounts on these early applications of radio occultation are given in the reports of *Melbourne et al.* [1994] and *Steiner* [1998] and in the review article on RO history by *Yunck et al.* [2000].

The application of the RO technique to the Earth's atmosphere (Figure 2.1) became possible with the arrival of the U.S. Global Positioning System (GPS) in the early 1980's. Together with the Russian GLONASS system and the emerging European GALILEO system there is now a multitude of transmitter platforms available to be used for sounding Earth's atmosphere with high temporal and spatial resolution. The first suggestions to apply the RO technique to the Earth's atmosphere go back to the 1960's [*Fishbach*, 1965; *Lusignan et al.*, 1969], but the feasibility of the method was not recognized until the late 1980's [*Gurvich and*

*Krasil'nikova*, 1987; *Yunck et al.*, 1988]. Finally, the first RO mission dedicated to the Earth's atmosphere was launched in April 1995 under the conduction of the University Cooperation for Atmospheric Research (UCAR) in Boulder, Colorado. This "proof-of-concept" experiment under the name GPS/MET was an unqualified success and demonstrated the unique characteristics and performance of RO measurements applied to the Earth's atmosphere [e.g. *Ware et al.*, 1996; *Kursinski et al.*, 1996; *Rocken et al.*, 1997; *Steiner et al.*, 1999]: High vertical resolution (0.5 km – 1.5 km), high accuracy (< 1 K in the upper troposphere and lower stratosphere), all-weather capability, global coverage, and long-term stability (< 0.1 K drift per decade expected).

In 1999, two mini-satellite missions, the Danish Ørsted and the South-African SUNSAT, carried the GPS/MET-type RO receiver (TRSR-1) but the RO data of these missions which were not primarily designed for RO experiments, were of minor quality.

The first major steps forward since GPS/MET are the U.S.-Argentinean SAC-C and the German-U.S. CHAMP (see section 2.9) satellites. Both are equipped with new generation receivers (TRSR-2 and TRSR-3) developed at the NASA's Jet Propulsion Laboratory (JPL). These missions are not only more mature from a technical point of view but particularly the CHAMP mission offers the first longer continuous time series of RO data. While these lines are written, more than 3 year continuous data from CHAMP are available and SAC-C delivers additional data in some periods. Particularly CHAMP can therefore be seen as a starting point for RO-based climate monitoring. The CHAMP successor GRACE (launched in 2002) is carrying the TRSR-2 receiver as well and successfully delivered first RO data from which atmospheric profiles could be derived [*Wickert et al.*, 2005] but since the RO-experiment onboard GRACE has low priority in the overall GRACE mission concept it is yet unclear if GRACE will ever provide a continuous RO data stream.

GRACE and SAC-C carry, additional to the usual aft looking RO antennas recording setting occultation events, front looking antennas that enable to record rising events. This technique has not been technically demonstrated yet and would, if operationally feasible, double the yield of each RO satellite.

In near future, two big steps towards an operational RO-based monitoring system will be done: Europe's Meteorological Satellite Organisation EUMETSAT will soon launch Europe's first operational polar orbiting satellite (MetOp-1, launch scheduled in 2005) carrying, among other instruments, the GNSS Receiver for Atmospheric Sounding (GRAS). This satellite is the first of three in the MetOp-series which is planned to be operational until at least 2019. Also in 2005, the launch of the first RO satellite constellation is planned: The Constellation Observing System for Meteorology (COSMIC) [*Lee et al.*, 2001], a Taiwan-U.S. mission that will set up a constellation of 6 micro-satellites (each weighing less than 70 kg) carrying the Integrated GPS Occultation Receiver (IGOR). This constellation will provide some 2000 occultation events per day (depending on the realization of rising events and other hardware, software, and retrieval advancements made since CHAMP, a range of 900 to 3000 events is imaginable) and potentially a daily global coverage with a mean horizontal spacing in the sub-1000 km range. From 2007 on, the Brazilian EQUARS satellite, equipped with the IGOR receiver as well, will provide additional RO data in near equatorial LEO.

The further future perspectives of the RO technique are on one hand the extension of the measurement concept including higher frequencies to obtain independent information on water vapor [e.g., *Kirchengast and Hoeg*, 2005; *Schweitzer*, 2004]. On the other hand, there are convincing ideas to use the simplicity of the method and the technical possibility to build small low-cost RO receivers to launch a fleet of nano-satellites (each weighting only a few kilograms) as secondary payloads on other launches (i.e., very cheap). Miniature RO receivers could also be added at minimal costs to any other LEO mission [*Yunck et al.*, 2000]. The result would be an entirely new view on our atmosphere with unprecedented resolution and

accuracy offering to greatly improve the performance of NWP, climate models, and generally give us new possibilities to study atmospheric processes and climate.

From today's point of view, one can be optimistic that the continuous RO data stream that started with CHAMP will not run dry in near future. The recent results and the promise and simplicity of the method indicate the RO receivers might soon be standard instruments on operational meteorological and other LEO satellites.

### 2.3. The GNSS and its Signals

The source of signals used by the RO technique, the Global Navigation Satellite System (GNSS), currently consists of the U.S. Global Positioning System (GPS) and the Russian Global Navigation Satellite System (GLONASS). In 2008 a further constellation, the European Satellite Navigation System GALILEO will start operation. Currently, only the signals of the GPS system are actually used by RO missions.

The GPS constellation consists of 28 (originally 24) operating satellites arranged in six, almost circular, orbital planes. The planes have a nominal inclination relative to the equator of 55.0 degree, a height of 20,185 km, and a period of 11 hours and 58 minutes [e.g., *Hofmann-Wellenhof et al.*, 1992].

GPS satellites transmit EM signals on two carrier frequencies in the *L*-band ( $\sim 1$  GHz – 2 GHz), both of them being multiples of a precisely controlled atomic clock frequency ( $f_0 = 10.23$  MHz). The two signals, known as Link-1 (*L1*) and Link-2 (*L2*), are 154 and 120 multiples of this fundamental frequency, respectively (*L1*:  $f_1 \equiv 154 f_0 = 1575.42$  MHz; *L2*:  $f_2 \equiv 120 f_0 = 1227.60$  MHz). They are modulated by three binary pseudo random noise (PRN) sequences: The coarse acquisition (*CA*) PNR code modulates the *L1* signal with a frequency of  $f_0/10$  and the precise (*P*) code modulates both, the *L1* and the *L2* signals, with a frequency of  $f_0$ . These codes are known to the GPS receivers and are the basis for phase matching in most conventional GPS receivers. Clock offset data (the calibration signal) and ephemeris data is sent along with the signal in another modulation, the navigation message.

The transmit times for each bit of the PRN sequences are precisely known relative to the clock onboard the GPS transmitter. This is fundamental for the RO technique since it enables to exclusively use a calibration standard which is more accurate than necessary for the RO technique, the clock calibration. This property, together with the fact that only the short-term clock stability has impact on the accuracy of the method (see section 3.1), is a fundamental advantage of the method and justifies to refer to it as “self calibrating” and highly stable on the long term.

The operator of the GPS, the U.S. Department of Defense (DoD), limits the access of civil users to the full accuracy of the GPS by two techniques: The selective availability (SA) superimposing random noise on the ephemeris data and the satellite clock frequency, and anti-spoofing (AS) encrypting the high-frequency (more precise) *P*-code which is then referred to as *Y*-code. Both strategies can be largely, but not entirely, counterbalanced by double differencing techniques and codeless carrier phase tracking [e.g., *Ware et al.*, 1996; *Wickert*, 2002]. SA was preliminary deactivated in May 2000 by the U.S. government and not switched on since then but AS is still employed at random times. The future European GNSS GALILEO will be fully open to civilian use and not employ such signal degradation techniques.

The GPS *L1* and *L2* EM signals (electric field strength or magnetic induction) at the position of the transmitter antenna can be written as [*Spilker*, 1980]:

$$S_{L1}(t) = \sqrt{2C_{CA}}D(t)X(t)\sin(2\pi f_1 t + \theta_1) + \sqrt{2C_{P1}}D(t)P(t)\sin(2\pi f_1 t + \theta_1) \quad (2.1)$$

$$S_{L2}(t) = \sqrt{2C_{P2}}D(t)P(t)\sin(2\pi f_2 t + \theta_2) \quad (2.2)$$

$C_{CA}, C_{P1}$  ..... Power of the components of L1

$C_{P2}$  ..... Power of L2

$D(t)$  ..... Amplitude modulation containing navigation data

$X(t)$  ..... PRN sequence of  $\pm 1$  containing CA-code

$P(t)$  ..... PNR sequence of  $\pm 1$  containing P-code

## 2.4. GNSS Signals in the Atmosphere

Equations (2.1) and (2.2) represent an EM wave at one certain location. The propagation of these waves through the ionosphere and neutral atmosphere can be sufficiently described by means of classical electrodynamics based on Maxwell's macroscopic equations [e.g., *Jackson, 1982*]:

$$\begin{aligned} \nabla \cdot \mathbf{D} &= \rho & \nabla \times \mathbf{H} &= \mathbf{J} + \frac{\partial \mathbf{D}}{\partial t} \\ \nabla \times \mathbf{E} + \frac{\partial \mathbf{B}}{\partial t} &= 0 & \nabla \cdot \mathbf{B} &= 0 \end{aligned} \quad (2.3)$$

$\rho$  ..... charge density [ $\text{C m}^{-3}$ ]

$\mathbf{D}$  ..... dielectric displacement [ $\text{C m}^{-2}$ ]

$\mathbf{E}$  ..... electric field strength [ $\text{V m}^{-1}$ ]

$\mathbf{H}$  ..... magnetic field strength [ $\text{A m}^{-1}$ ]

$\mathbf{B}$  ..... magnetic induction [T]

$\mathbf{J}$  ..... current density [ $\text{A m}^{-2}$ ]

In order to solve Maxwell's equations and to constitute the relations to the specific properties of the medium (the atmosphere), a set of material equations describing the links between electric displacement and electric field, between magnetic induction and magnetic field, and the generalized Ohm's law giving the relation between the current density and the electric field are necessary (equations (2.4)). In other than ferroelectric or ferromagnetic media these relations are linear under the field strengths involved in RO measurements and can be written as:

$$\mathbf{D} = \varepsilon_0(1 + \vec{\chi}_e)\mathbf{E} \quad \mathbf{B} = \mu_0(1 + \vec{\chi}_m)\mathbf{H} \quad \mathbf{J} = \vec{\sigma}\mathbf{E} \quad (2.4)$$

$\varepsilon_0$  .....electric constant:  $8.854\,188 \dots \cdot 10^{-12} \text{ AsV}^{-1}\text{m}^{-1}$

$\vec{\chi}_e$  .....electric susceptibility tensor [1]

$\varepsilon_0(1 + \vec{\chi}_e)$  .....dielectric tensor [ $\text{AsV}^{-1}\text{m}^{-1}$ ]

$\mu_0$  .....magnetic constant:  $4\pi \cdot 10^{-7} \text{ VsA}^{-1}\text{m}^{-1}$

$\vec{\chi}_m$  .....magnetic susceptibility tensor [1]

$\mu_0(1 + \vec{\chi}_m)$  .....permeability tensor [ $\text{VsA}^{-1}\text{m}^{-1}$ ]

$\vec{\sigma}$  .....conductivity tensor [ $\Omega \text{ m}^{-1}$ ]

### 2.4.1. Neutral Atmosphere

For the neutral atmosphere, which is an electrical isotropic medium, the dielectric tensor degrades to a scalar, and the charge density, magnetic susceptibility, and conductivity can be set to zero (equations (2.5)). The resulting set of Maxwell equations (2.6) can be transformed into wave equations (2.7) with their well known solutions for plane waves at the position  $\mathbf{r}$  and time  $t$  given in equations (2.8).

$$\mathbf{D} = \varepsilon_0 \varepsilon_r \mathbf{E} \equiv \varepsilon \mathbf{E} \quad \rho = 0 \quad \tilde{\chi}_m = 0 \quad \vec{\sigma} = 0 \quad (2.5)$$

$\varepsilon_r$  ..... electric permittivity of medium [1]  
 $\varepsilon$  ..... electric permittivity [ $\text{AsV}^{-1}\text{m}^{-1}$ ]

$$\begin{aligned} \nabla \cdot \mathbf{E} &= 0 & \nabla \times \mathbf{H} &= \varepsilon_0 \varepsilon_r \frac{\partial \mathbf{E}}{\partial t} \\ \nabla \times \mathbf{E} &= -\mu_0 \frac{\partial \mathbf{H}}{\partial t} & \nabla \cdot \mathbf{H} &= 0 \end{aligned} \quad (2.6)$$

$$\Delta \cdot \mathbf{E} = \varepsilon_0 \varepsilon_r \mu_0 \frac{\partial^2 \mathbf{E}}{\partial t^2} \quad \Delta \cdot \mathbf{H} = \varepsilon_0 \varepsilon_r \mu_0 \frac{\partial^2 \mathbf{H}}{\partial t^2} \quad (2.7)$$

$$\mathbf{E}(\mathbf{r}, t) = \mathbf{E}_0 \exp\left[i\left(\frac{2\pi}{\lambda} \mathbf{nr} - 2\pi ft\right)\right] \quad \mathbf{H}(\mathbf{r}, t) = \mathbf{H}_0 \exp\left[i\left(\frac{2\pi}{\lambda} \mathbf{nr} - 2\pi ft\right)\right] \quad c = \lambda f \quad (2.8)$$

$\mathbf{n}$  .....unit vector pointing in the direction of wave propagation  
 $\mathbf{r}$  .....position vector  
 $\lambda$  .....wavelength [m]  
 $f$  .....frequency [ $\text{s}^{-1}$ ]  
 $c$  .....phase velocity [ $\text{ms}^{-1}$ ]

By combining equations (2.7) and (2.8) for the electric or magnetic field strengths we find the relation between the material- and wave properties:

$$\frac{1}{\lambda^2} \mathbf{E} = \varepsilon_0 \varepsilon_r \mu_0 f^2 \mathbf{E} \quad \lambda f \equiv c = \frac{1}{\sqrt{\varepsilon_0 \varepsilon_r \mu_0}} \quad (2.9)$$

A convenient way to describe the material properties in one number is the refractive index  $n$  given by the ratio of speed of EM waves in vacuum  $c_0$  ( $\varepsilon_r = 1$ ) and the actual phase velocity  $c$ . This relation (equation (2.10)) is known as the Maxwell relation for the neutral atmosphere:

$$n \equiv \frac{c_0}{c} = \sqrt{\varepsilon_r} \quad (2.10)$$

Generally,  $\varepsilon_r$  is a function of frequency but the frequencies involved are far away from molecular resonances and  $\varepsilon_r$  can therefore be considered as independent from frequency in RO applications. Furthermore,  $\varepsilon_r$  might be complex resulting in a complex refractive index and absorption of the EM waves' energy. Again, this is not the case for the atmosphere at wavelengths  $> \sim 1$  cm as used by the RO technique.

The relation between the refractive index and the macroscopic atmospheric properties like temperature, pressure, and water vapor pressure can be theoretically derived considering the atomistic theory of matter. For details, the interested reader is referred to the thesis of *Foelsche* [1999] and references therein. Considering the atmosphere as an ideal gas results in the Smith-Weintraub formula (equation (2.12)) [*Smith and Weintraub*, 1953]. This formula uses, instead of the refractive index, the more convenient quantity refractivity  $N$  (equation (2.11)) which will be used throughout the thesis from here on.

$$N \equiv (n - 1) \cdot 10^6 \quad (2.11)$$

$$N = k_1 \frac{p_d}{T} + k_2 \frac{e}{T} + k_3 \frac{e}{T^2} \quad (2.12)$$

$N$  .....refractivity  
 $k_1, k_2, k_3$  ..... constants (see below)  
 $p_d$  ..... pressure of dry air [hPa]  
 $T$  ..... temperature [K]  
 $e$  ..... pressure of water vapor[hPa]

The constants  $k_1$ ,  $k_2$ , and  $k_3$  can be theoretically derived using some simplifications [e.g., *Foelsche*, 1999], but generally, more precise experimental values suggested by *Bevis et al.* [1994] are used (equation (2.13)):

$$\begin{aligned} k_1 &= 77.60 \pm 0.05 \text{ K/hPa} \\ k_2 &= 70.4 \pm 2.2 \text{ K/hPa} \\ k_3 &= (3.739 \pm 0.012) \cdot 10^5 \text{ K}^2/\text{hPa} \end{aligned} \quad (2.13)$$

Equation (2.12) can be rearranged with little additional error to be dependent from total pressure  $p$  instead of dry air pressure introducing the new pseudo-constant  $k_4$ :

$$N = k_1 \frac{p}{T} + k_4 \frac{e}{T^2} \quad (2.14)$$

$$k_4 = (k_2 - k_1)T + k_3$$

$$k_4(273.15\text{K}) = 3.73 \cdot 10^5 \frac{\text{K}^2}{\text{hPa}} \quad (2.15)$$

Equation (2.14) with  $k_4$  as given in equation (2.15) has an error of  $< 0.5\%$  in wet atmospheres and  $< 0.02\%$  in dry atmospheres [*Smith and Weintraub*, 1953] and is widely used in RO data processing.

Equation (2.14) demonstrates that water vapor and temperature can not be separated using a single RO measurement. This ambiguity of refractivity measurements is of minor importance above the mid-troposphere because the water vapor signal is negligible there. At moist conditions near surface, however, background information is necessary to separate the temperature from the water vapor signal (see section 3.2.3).

## 2.4.2. Ionosphere

The situation is more complicated in the ionosphere where charged particles are interacting with EM waves and the Earth's magnetic field. Here, the magnetic susceptibility and conductivity can still be neglected, but the dielectric tensor does not degrade to a scalar since

the ionosphere is an anisotropic medium for EM waves due to the interaction of the Earth's magnetic field with the plasma. The ionosphere is, like the neutral atmosphere, transparent, but in contrary to it, dispersive for EM waves at GNSS frequencies. The relation for the ionospheric refractivity is generally given by the Appelton-Hartree formula [e.g., *Budden*, 1985]. For GPS signals, the ionospheric refractivity may be approximated to second order as [*Bassiri and Hajj*, 1993]:

$$N_k = -C \frac{N_e}{f_k^2} - K \frac{B_{par} N_e}{f_k^3} \quad (2.16)$$

$k$  ..... index denoting the signal number (1,2)

$C$  ..... constant:  $40.3 \text{ m}^3 \text{ s}^{-2}$

$N_e$  ..... electron density [ $\text{m}^{-3}$ ]

$f_k$  ..... carrier frequency of signal no.  $k$  [ $\text{s}^{-1}$ ]

$K$  ..... constant:  $1.13 \cdot 10^{-12} \text{ m}^3 \text{ T}^{-1} \text{ s}^{-3}$

$B_{par}$  ..... absolute value of the Earth's magnetic field parallel to wave propagation [T]

The frequency dependency of the ionospheric refractivity in equation (2.16) shows the dispersive nature of the ionosphere resulting in two independent measurements for  $L1$  and  $L2$ . In general, the second term on the right side can be neglected [*Syndergaard*, 2000] enabling to derive an ionosphere-free linear combination of the two signals for further retrieval of neutral atmospheric properties (see section 3.2).

### 2.4.3. Geometric Optics and Single Ray Approximation

For most parts of the atmosphere it is possible to work with the geometric optics (GO) approximation and treat the EM waves as rays. This is justified as long as the wavelengths are small compared to the spatial extension of the problem, or more specifically, as long as the bending of wave-fronts can be neglected in scales of the wavelength and waves can be regarded as plane.

GNSS signals are so-called “centimeter-waves” ( $L1$ :  $\lambda \sim 0.19 \text{ m}$ ,  $L2$ :  $\lambda \sim 0.24 \text{ m}$ ) which implies that the approximation is generally justified for the RO problem dealing with atmospheric structures in the  $> 100 \text{ m} - 1000 \text{ m}$  scale. However, in the lower troposphere and partially in the ionosphere, small-scale variability can perturb the performance of GO RO retrieval due to diffraction effects. Particularly water vapor in the lower troposphere in mid and low latitudes strongly contributes to the atmospheric refractivity field and causes strong gradients potentially resulting in multipath signal propagation which causes that traditional geometric optic RO retrieval technique to fail due to an ambiguous signal at the position of the receiver. To resolve this ambiguity radio holographic methods have been developed. The most advanced of these methods are the canonical transform method [*Gorbunov and Gurvich*, 1998; *Gorbunov et al.*, 2000; *Gorbunov* 2002a; 2002b; 2002d] and the full spectrum inversion technique [*Jensen et al.*, 2003]. These techniques are have been demonstrated to have positive impact on RO retrieval performance in the lower troposphere but it is not necessary to apply them elsewhere. For the means for this thesis, which focuses on the stratosphere rather than the lower troposphere, it is sufficient to use the single-ray GO approximation.

For EM waves, when regarded as rays, the optical path can be defined as given in equation (2.17). The actual ray path is, depending on the refractive properties of the medium, not straight but follows Fermat's principle of minimization of the optical path. In GPS applications the optical path is often called pseudo-range.

$$L_k = \int_{GNSS}^{LEO} n ds \quad (2.17)$$

$L_k$  .....optical path  
 $k$  .....index denoting the signal (1,2)  
 $n$  .....refractive index  
 $ds$  .....arc element

The refractive properties of the neutral atmosphere ( $n > 1$ ) lead to delays of the wave's phase compared to the vacuum-phase, i.e., a deceleration of the phase velocity ( $c = c_0/n$ ), elongation of the optical path, and bending of the ray towards the Earth center. In the ionosphere, where the refractive index is less than unity, phase acceleration and outward bending occurs.

## 2.5. The Received Signal

Basic properties of RO signals that theoretically can be measured and related to the Earth's refractive field are the bending angle of the ray and the phase (the number of cycles from transmitter to the receiver). While the direct measurement of bending angles would require huge antennas, the phase can be measured with much less effort and can be directly converted into additional range (or optical path) due to the refractive properties of the atmosphere if the orbits of the transmitter and receiver are well known. This information can subsequently be utilized to derive bending angles.

The RO technique uses high precision GNSS receivers mounted on satellite platforms in low Earth orbit (orbit height typically 400 km – 800 km). A properly equipped GPS receiver detects amplitude and phase measurements for each of the *CA*-code, *L1 P*-code, and *L2 P*-code signals. More precisely, the receiver measures the difference between the received phase and a reference phase generated onboard. Since the *L1 P*-code and *CA*-code essentially contain similar information and the *CA* code's power is stronger by 3 dB, the *CA*-code is generally preferred. The basic RO technique uses only phase, but no amplitude information, so the observables of a RO experiment are the *CA* and *L1 P* phase measurements. The measured phase delay is equivalent to the EM wave's extra time or, in a more convenient representation, to the optical path  $L_k$ . It can be modeled as follows [Hajj *et al.*, 2002]:

$$L_k \equiv -\frac{c_0}{f_k} \Phi_k = \gamma^V + \gamma_k + C^G + C^L + \nu_k \quad (2.18)$$

$L_k$  .....measured optical path of signal  $Lk$  [m]  
 $k$  .....index denoting the signal number (1 for *L1* and 2 for *L2*)  
 $c_0$  .....speed of light in vacuum (299,792,458 m/s)  
 $\Phi_k$  .....recorded phase in cycles  
 $f_k$  .....carrier frequency of signal  $Lk$  [ $s^{-1}$ ]  
 $\gamma^V$  .....optical path corresponding to the signal travel time in vacuum [m]  
 $\gamma_k$  .....extra optical path caused by neutral atmospheric and ionospheric refraction [m]  
 $C^G, C^L$  .....extra optical path caused by transmitter and receiver clock errors [m]  
 $\nu_k$  .....extra optical path caused by receiver noise (thermal noise and local multi-path effects) [m]

From the RO point of view, the neutral atmospheric contribution to the term  $\gamma_k$  is of interest (as will be demonstrated in section 3.1.1, actually its time derivative is the important quantity). Precise satellite orbit information enables to remove the vacuum-length  $\rho$ . Clock errors  $C$  can be precisely removed using “differencing techniques” based on links to other GNSS satellites and to the GPS ground network (see section 2.6). The receiver noise term has to be dealt with in the retrieval of atmospheric parameters (see Chapter 3). Once having isolated the atmosphere-ionosphere term (plus noise), two measurements, one for each frequency ( $k = 1, 2$ ), are available. Since the neutral atmosphere is non-dispersive in the frequency range under consideration (1 GHz – 2 GHz) the two signals contain redundant information on the neutral atmosphere. The ionosphere, however, is dispersive and its influence on both signals is different. This enables to remove the first order of the ionospheric contribution by linearly combining the two signals (see section 3.1.2). Once having available the neutral atmospheric signal, the atmospheric parameters can be derived as described in some detail in Chapter 3.

## 2.6. The Ground Segment – Calibration

Beside the space segment described in the sections above, a ground infrastructure is necessary for operating RO missions. As an example, the infrastructure of the CHAMP RO experiment is depicted in Figure 2.2. It consists of the downlink station (“polar receiving station” in Figure 2.2) located near the pole to enable data download links to CHAMP (in near-polar orbit) each orbit. This is desirable in order to confine the memory requirements onboard the satellite or to avoid data loss, respectively.

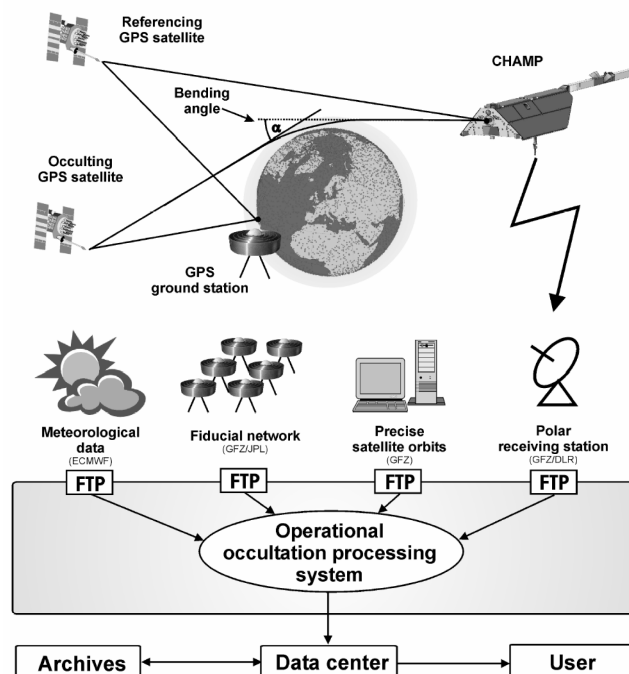


Figure 2.2: The CHAMP mission infrastructure exemplifying elements necessary to maintain a radio occultation experiment. Source: Wickert et al. [2004b].

The second part of the ground segment, the “fiducial network”, consists of several GPS ground stations (e.g., about 40 stations for the CHAMP mission) necessary for clock correction and precise orbit determination of the GPS and LEO satellite. Depending on the

GNSS and LEO clock qualities one needs or needs not to solve for one or two of the clock errors in equation (2.18). A common method correcting for  $C^{LEO}$  and  $C^{GPS}$  needs links between the RO receiver in LEO and two GPS satellites (one occulting and one as reference) and the link from each GPS satellite to a ground station (see Figure 2.2) and is described in the article of *Hajj et al.* [2002] and in the thesis of *Wickert* [2001].

Recently, methods exploiting the fact that AS is off and the improved accuracy of recent oscillators has been developed. These methods (“single differencing”, “space based single differencing”, “zero differencing”) need less (or none) reference links or a smaller ground station data acquisition rate, respectively. Generally, each inevitable link less is desirable since each link increases the requirements on the infrastructure (GNSS transmitters, ground stations, data transfer) and is sensitive to various sources of errors like technical failures or insufficient ionospheric correction. However, one has to be careful not to degrade quality and, in particular, the self calibrating nature the RO method by removing reference links.

Since this thesis focuses on the enhancement of the derivation of atmospheric parameters from the atmosphere term ( $\gamma_k$  in equation (2.18)) for climate monitoring, the clock correction (or “calibration”) procedure is not discussed in detail here. For a more detailed discussion of different calibration techniques the reader is referred to the paper of *Wickert et al.* [2004b] and references therein.

After the calibration process, the clock errors are removed (or sufficiently diminished to be ignored) and the observation equation (2.18) is reduced to:

$$L_k = \gamma^V + \gamma_k + \nu_k \quad (2.19)$$

- $L_k$  ..... measured optical path of signal  $Lk$  [m]
- $k$  ..... index denoting the signal number (1 for  $L1$  and 2 for  $L2$ )
- $\gamma^V$  ..... optical path corresponding to the signal travel time in vacuum [m]
- $\gamma_k$  ..... extra optical path caused by neutral atmospheric and ionospheric refraction [m]
- $\nu_k$  ..... extra range due to receiver noise (thermal and local multipath) [m]

In addition to the signal calibration described above, data from the GPS ground station network is necessary for generation of precise LEO and GNSS orbits [*König et al.*, 2002] to be able to account for the vacuum path ( $\gamma^V$  in equation (2.19)). The facility for rapid and precise generation the orbits is therefore an important part of the ground infrastructure (“precise satellite orbits” in Figure 2.2).

A link to an operational weather service (“meteorological data” in Figure 2.2) to access additional (background) information about the state of the atmosphere aiding RO data processing is very desirable as but not inevitable (see section 4).

Data from the components described above are transferred to the data processing facility (“operational occultation processing system” in Figure 2.2) where the information on atmospheric parameters is extracted.

A very important further component of the ground infrastructure is the data center managing the archival storage and the interface to the user which are scientists in general, other data centers that derive higher-level products from the basic measurements, and potentially operational weather services using the data for assimilating it in their models.

## 2.7. Spatial and Temporal Coverage

RO receivers are generally mounted on satellite platforms in low Earth orbit (300 – 1500 km altitude, typically 400 – 800 km) featuring orbital periods of 90 to 116 minutes. The orbit planes are often highly inclined relative to the Earth’s equator to obtain even

geographical distribution of measurements with one satellite. This is not necessarily the case for missions focused on low latitudes (neglecting the high latitudes) or constellations of several satellites.

Depending on the specifications of the antenna (the field of view) and the receiver software, each receiver can record some 250 – 300 occultation events per day (considering only the GPS but not the GLOANSS transmitter constellation). Each satellite can record occultation events in setting (aft-looking) and rising (fore-looking) mode, thus a maximum number of 600 events per satellite and day is possible. Currently, only setting events have been operationally demonstrated but rising events are feasible (though technically more demanding) and will be tested in near future missions (see section 2.1).

Due to a multitude of error sources (see section 5) not each recorded occultation event yields profiles of atmospheric parameters. The efficiency rate of current state-of-the-art retrieval schemes (considering the total retrieval chain from the observed signal to, e.g., profiles of temperature) amounts 60 % – 70 % resulting in some 180 atmospheric profiles per day and receiver.

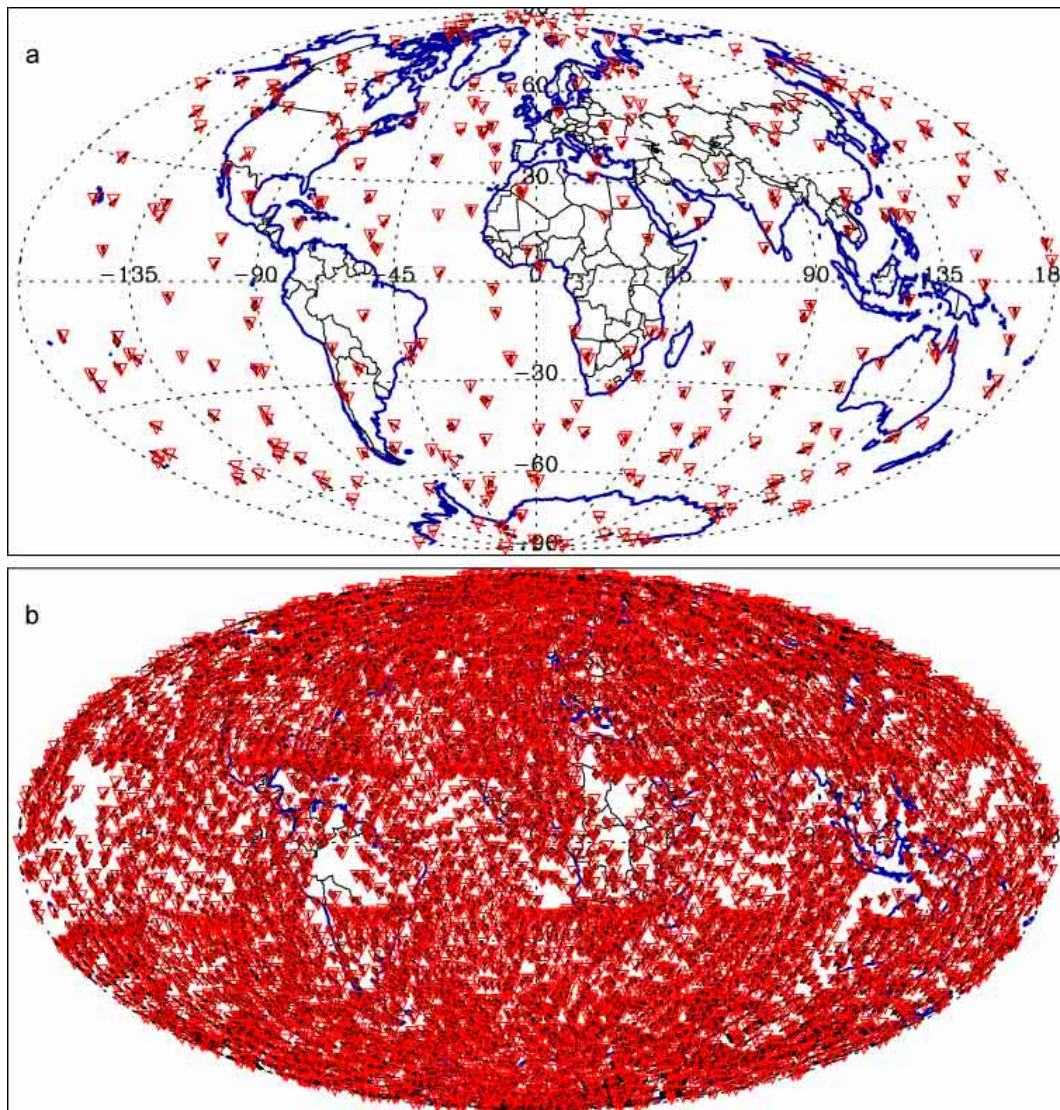


Figure 2.3: Geographical distribution of occultation events recorded with one receiver (only setting occultation events) rising mode. a) one day, 279 events. b) one month, 8649 events.

For demonstration, the geographical distribution of occultation events recorded from an ideal (assuming 100 % retrieval efficiency) one-satellite RO mission with highly inclined orbit is displayed in Figure 2.3 (only setting events considered). The simulation is based on

the orbit parameters of the METOP mission (98.7 degree inclination to the equator, see section 2.2) and a 24-satellite GPS constellation and was conducted with the End-to-end GNSS Occultation Performance Simulator (EGOPS) [Kirchengast *et al.*, 2002]. The upper panel shows the coverage for one day (279 events) and the lower panel for one month (8649 events).

This simulation demonstrates the near-even global distribution of measurements and the fact that one single satellite is able to provide dense sampling of the atmosphere for monthly or seasonal means, but not for a diurnal resolution. It can also be seen in the monthly distribution that some regions, particularly near the Equator, remain coarsely sampled.

However, the near future COSMIC mission with its six-satellite constellation and lower inclined orbits will ideally complement the highly inclined METOP orbit (regarding the low measurement density in low latitudes) and multiply the availability of RO events by six to twelve (depending on the performance of the not yet demonstrated acquisition of rising occultation events).

A more detailed and realistic overview of the geographical distribution of occultation events and resulting sampling errors will be given in section 7.2.1 using data from the CHAMP mission.

## 2.8. Radio Occultation for Climate Monitoring and NWP

The RO technique can provide unique contributions to a global climate monitoring system as the proposed Global Climate Observation System (GCOS) by the WMO (see section 1.6 and the report by the *WMO* [2003]) mainly because of the following unique characteristics:

- Absolute calibration and long term stability (the RO technique is based on timing measurements using atomic clocks);
- Global and even coverage over both, land and ocean;
- Diurnal cycle coverage (if satellite constellations are deployed);
- All-weather capability (insensitive to clouds);
- High accuracy temperature, pressure, and geopotential height measurements (e.g., climatological temperature accuracy 0.1 – 0.5 K, see section 6.3)
- Large vertical range spanning from the lower troposphere to the mid-upper stratosphere;
- High vertical resolution ( $\sim 1$  km to  $\sim 100$  m depending on the retrieval technique), including the capability to observe fine atmospheric structures such as the tropopause temperature globally;
- Cost effectiveness.

The characteristics specified above fulfil all criteria to establish a climate benchmark dataset as defined by *Goody et al.* [1998]: RO data are relevant for climate research (sensitive to ill-constrained feedbacks in the climate system by providing vertically resolved temperature data), global, precise, and calibratable against absolute standard measurement (in the case of radio occultation, that standard is the second, the most precisely defined unit of the International System of Units (SI)). The RO technique provides long-term stable “self-calibrating” data and is insensitive to instrument changes. It therefore solves the major problem of state-of-the-art passive remote sensing systems, namely the inter-calibration problem, and can be used as absolute reference for calibration of such and other observation systems.

RO data are ideally suited to monitor climate variations and trends in temperature and geopotential height. Dependent on the scientific purpose this can be realized either

independent of any model or by employing modern data assimilation techniques, i.e. combining RO with model data. An important application climate of benchmark observations like RO data is testing climate models. This is indispensable to establish credibility and reduce the uncertainty in long term climate predictions. In this context, it is of importance that climate models are validated not only with respect to the observed climate, but also against known external forcings. In such cases, the observed data must be assimilated into the atmospheric model and the model parameters have to be varied in such a way that the forcing errors are minimized. This technique is already now used in a range of projects but a major obstacle when using data from currently available sources, such as radiosondes and vertical profiling from present satellites, is either their coarse spatial and temporal resolution and/or lack of sufficient accuracy and/or long-term stability and vertical coverage. Additionally to model parameter estimation, the technique of forcing error estimation can provide valuable guidelines for construction of new and improved physics parameterisation algorithms. For more details on this topic, the reader is referred to article of *Goody et al.* [1998] and the overview description of the proposed Atmosphere and Climate Explorer (ACE+) mission, a mission that would even extent the RO concept [*Kirchengast and Høeg, 2004*].

Apart from the utility in climate research it has been demonstrated that RO data has significant impact on the weather forecast quality when assimilated into NWP models, especially in the Southern Hemisphere where high-quality observations are rare [*Healy et al., 2005*]. In section 7.3 of this thesis, an example will be given how RO data can reveal deficiencies in current NWP systems.

## 2.9. CHAMP — The Challenging Minisatellite Payload Radio Occultation Experiment

All measured RO data processed and analyzed in this thesis originate from the German-U.S. CHALLENGING Minisatellite Payload (CHAMP). This section gives an overview of the RO experiment onboard CHAMP and is based on the thesis of *Wickert* [2002] and several articles by *Wickert et al.* [2001, 2004a, 2004b, 2005].

The CHAMP mission emerged 1994 from a project proposal of GeoForschungsZentrum (GFZ) Potsdam [*Reigber et al., 1995*] and was realized in cooperation with the German Aerospace Center (DLR) and an industry consortium under the conduction of GFZ.

The satellite has a total mass of 522 kg and a length of 8.33 m (including a 4.04 m boom). Figure 2.4 shows the CHAMP platform at the cleanroom before it was transported to the launch site (a) and an artistic impression of the satellite in orbit (b).

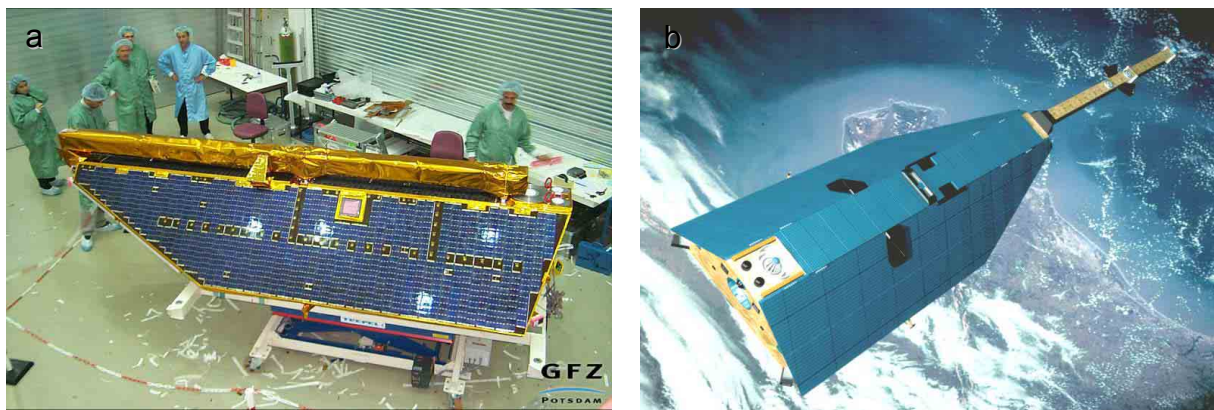


Figure 2.4: a) CHAMP in the cleanroom before it was transported to the launch site. Source GFZ. b) Artistic impression of CHAMP in orbit. Source: Astrium.

The principal CHAMP mission objectives are to determine the Earth's gravity and magnetic fields and to perform global limb soundings of the Earth's ionosphere and neutral atmosphere using the GNSS RO technique. CHAMP carries the so-called “Black Jack” (TRSR-2) GPS flight receiver developed at NASA’s Jet Propulsion Laboratory (JPL) in combination with a aft looking high gain helix antenna resulting in substantially improved signal quality compared to the GPS/MET experiment (+ 5 dB). Besides GPS receiver located at the rear of the satellite (see Figure 2.5), CHAMP carries several other scientific instruments (magnetometer, accelerometer, star sensor, laser retro reflector, ion drift meter) mainly designed to measure the Earth’s gravity and magnetic field. More detailed information on the CHAMP payload and the gravity-magnetosphere experiments can be found at the CHAMP homepage at GFZ (<http://www.gfz-potsdam.de>).

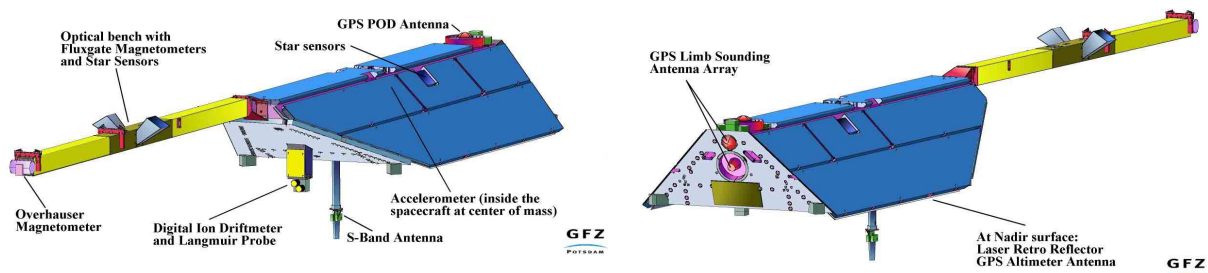


Figure 2.5: The physical layout of the CHAMP spacecraft with the location of instruments and subsystems. Source: GFZ Potsdam.

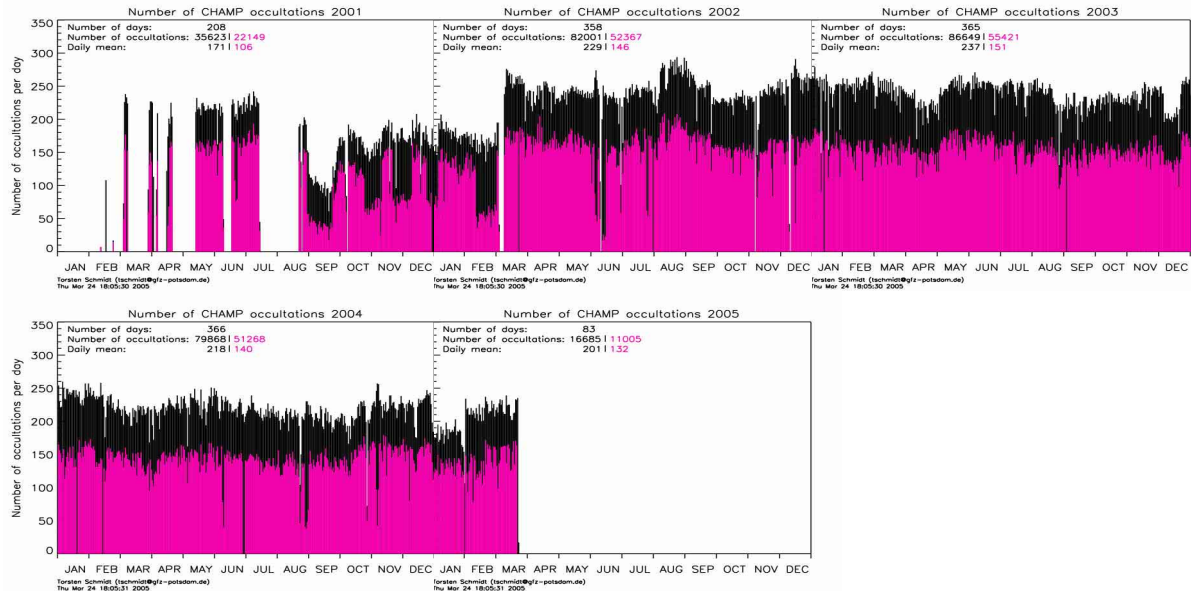


Figure 2.6: Number of daily CHAMP occultation events (duration link longer than 20 seconds, black bars) and atmospheric profiles retrieved by the operational CHAMP retrieval scheme at GFZ, Source: GFZ Potsdam.

The satellite was launched with a Russian COSMOS rocket on July 15, 2000 into an almost circular, near polar orbit (87.2 degree inclination relative to equatorial plane) with an initial altitude of 454 km and was originally scheduled for a mission lifetime of five years until the atmospheric drag would have lowered the orbit altitude below 300 km. In 2002 two orbit lifting maneuvers have been carried out to maximize the mission lifetime. As of October 2004 the altitude is about 370 km and a lifetime until end 2007 is expected.

The first RO measurements were carried out in February, 2001 showing good quality. Since August 2001 CHAMP provides a virtually continuous RO data stream reaching its full yield in March 2002 (~ 240 occultations from which ~ 65 % atmospheric profiles can be operationally derived per day). Figure 2.6 depicts the occultation number statistic for the entire mission until March 24, 2005 demonstrating the reliability of the RO measurements.

The operational GFZ RO ground infrastructure performs data analysis and allows an average delay of 5 hours between the measurement and the provision of corresponding atmospheric profile. This is an important demonstration leading towards the future assimilation of GPS radio occultation data in NWP models that generally need a delay between measurement and data availability of not more than 3 hours. The measurement error of temperature profiles operationally derived from CHAMP RO data is less than 0.5 K bias and 1 K – 3 K random error between 10 km and 35 km altitude. More detailed information on the quality of CHAMP data processed with different retrieval schemes is given in Chapter 6.



# 3 Radio Occultation Retrieval

In the following Chapters, the RO retrieval chain starting with the calibrated phase delays and ending in profiles of temperature and humidity is described. Section 3.1 elaborates the retrieval of bending angles including ellipsoid correction (section 3.1.2) and ionospheric correction (section 3.1.3). Section 3.2 describes the transition from bending angles to profiles of atmospheric parameters, followed by Chapter 4 giving an overview of high altitude initialization and statistical optimization techniques. Though Chapters 3 and 4 include some technical details, the specific application of the described methods on CHAMP data and retrieval enhancements predominantly focusing on statistical optimization at high altitudes, creation of a stable (operational applicable) retrieval chain, and quality control is described in Chapter 5.

As already described, the optical path (proportional to the measured phase delay) after clock calibration can be modeled as follows:

$$L_k = \gamma^V + \gamma^N + \gamma_k^I + v_k \tag{3.1}$$

- $L_k$  ..... measured optical path of signal  $Lk$  [m]
- $k$  ..... index denoting the signal number (1 for  $L1$  and 2 for  $L2$ )
- $\gamma^V$  ..... optical path corresponding to the signal travel time in vacuum [m]
- $\gamma^N$  ..... extra optical path caused by neutral atmosphere [m]
- $\gamma_k^I$  ..... extra optical path caused by the ionosphere (negative) [m]
- $v_k$  ..... extra optical path due to receiver noise (thermal and local multi-path) [m]

Since we are interested only in the properties of the neutral atmosphere, the ionospheric contribution  $\gamma_k^I$  is addressed separately in equation (3.1). Methods to remove the ionospheric contributions are discussed in section 3.1.3. To derive profiles of atmospheric parameters from the phase delay, we first have to remove the vacuum length  $\rho$  which is accomplished by combining geometrical considerations with the measurement as explained in the next section.

## 3.1. Retrieval of Bending Angles

### 3.1.1. Retrieval of Total Atmospheric Bending Angles

From the geometry of an occultation event as depicted in Figure 3.1 the following relation (equation (3.2)) between the bending angle  $\alpha$  and the ray directions as seen from the satellites  $\theta_L$  and  $\theta_G$  (see Figure 3.1) can be established:

$$\alpha = \gamma + \theta_L + \theta_G - \pi \tag{3.2}$$

- $\alpha$  ..... total bending angle of the ray
- $\gamma$  ..... angle between the two lines connecting the center of refraction with the satellites
- $\theta_L$  ..... angel between the center to LEO-satellite line and the ray direction
- $\theta_G$  ..... angel between the center to GPS-satellite line and the ray direction

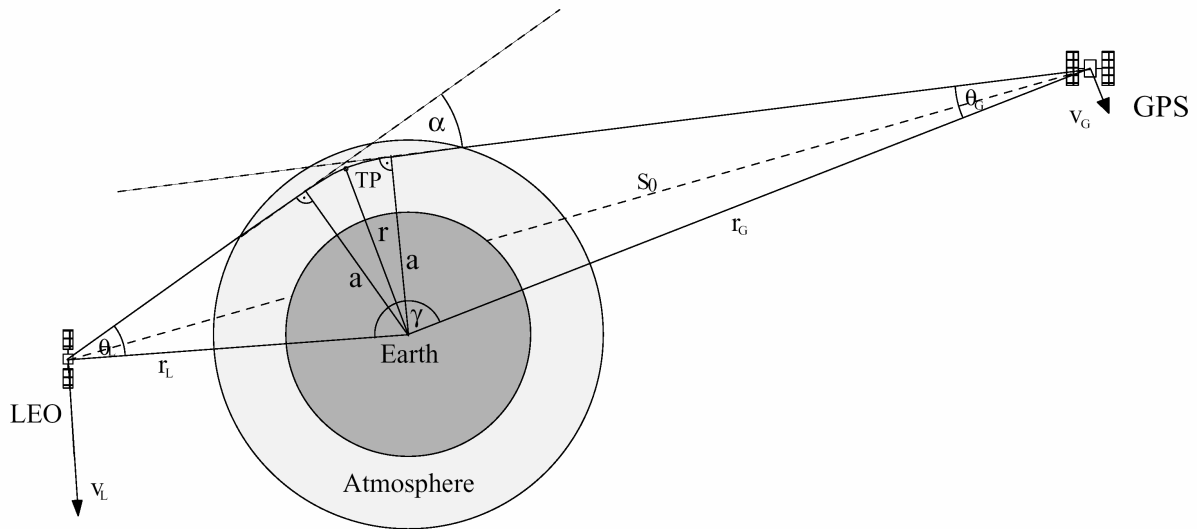


Figure 3.1: Geometry of an occultation event. Source: *Foelsche* [1999]

The three unknown quantities in equation (3.2) require two further equations in order to solve for  $\alpha$ . The first of them, the formula of Bouguer (equation (3.5)), can be derived from the principles of geometric optics as described in the following two paragraphs:

In geometric optics the path of a ray penetrating a refractive medium is represented by the differential equation (3.3) [e.g., *Born and Wolf*, 1999]. This equation can be strongly simplified by introducing a fundamental simplification of the RO technique: The assumption of local (in the region of the occultation event) spherical symmetry. By regarding the variation of quantity  $\mathbf{r} \times n(\mathbf{r})\mathbf{s}$  ( $\mathbf{s}$  being the unit vector in direction of the ray) along the ray one finds that this quantity is constant for a spherical symmetric refractivity field: The first term on the right hand side of equation (3.4) vanishes since  $d\mathbf{r}/ds = \mathbf{s}$ . The second term can be expressed as  $\mathbf{r} \times \nabla n$  using equation (3.3). If we now introduce a spherical symmetric refractivity field ( $n = n(r)$  and  $\nabla n(r) = \mathbf{r}/r \cdot dn/dr$ ) we find that the second term vanishes as well and thus  $\mathbf{r} \times n(r)\mathbf{s}$  is constant.

Equation (3.5) is called the formula of Bouguer and represents Snell's law in a spherical symmetric refractive medium. The constant term  $a$  is called impact parameter and can be geometrically interpreted as normal distance of the ray to the center of refraction as depicted in Figure 3.1.

At the positions of the satellites (which can be considered as being outside of the atmosphere for our purposes) the refractive index is unity and, since the impact parameter is constant along the ray path, the two formulas of Bouguer for the positions of both satellites can be equated (equation (3.6)). Given the orbit altitudes of the satellites this equation directly relates the two unknown angles.

$$\frac{d}{ds} \left( n \frac{d\mathbf{r}}{ds} \right) = \nabla n \quad (3.3)$$

$$\frac{d}{ds} (\mathbf{r} \times n\mathbf{s}) = \frac{d\mathbf{r}}{ds} \times n\mathbf{s} + \mathbf{r} \times \frac{d}{ds} (n\mathbf{s}) \quad (3.4)$$

$$\mathbf{r} \times n\mathbf{s} = \text{constant} \equiv a \quad \text{in scalar form: } nr \sin \varphi = a \quad (3.5)$$

$$r_L \sin \theta_L = r_G \sin \theta_G \quad (= a) \quad (3.6)$$

$n$  ..... refractive index  
 $\mathbf{r}$  ..... position vector  
 $\mathbf{s}$  ..... unit vector in ray direction  
 $ds$  ..... arc element  
 $a$  ..... impact parameter  
 $\varphi$  ..... angle between  $\mathbf{r}$  and  $\mathbf{s}$   
 $r$  ..... radius (distance to the center of refraction)  
 $r_L$  ..... distance of the LEO satellite to the center of refraction  
 $r_G$  ..... distance of the GPS satellite to the center of refraction  
 $\theta_L$  ..... angel between the center to LEO-satellite line and the ray direction.  
 $\theta_G$  ..... angel between the center to GPS-satellite line and the ray direction.  
 $a$  ..... impact parameter

The last equation necessary to derive  $\alpha$  is based on the measured phase delay (represented by the optical path) and the deviation of the observed from the transmitted frequency, the Doppler shift: Neglecting a small relativistic effect (see *Vorob'ev et al.* [1994], for the formulae including the first-order relativistic effect), the Doppler shift  $f_D$  is proportional to the time derivative of the optical path (equations (3.7) – (3.9)). Thus the Doppler shift is proportional to the satellite velocities projected on the ray path (equation (3.10)). This relates, when resolved into radial and tangential components, the measured quantity to the unknown angles (equation (3.11)).

$$f_D = f_L - f_G \quad (3.7)$$

$$f_L = f_G + \frac{dL/dt}{c_0} f_G \quad (3.8)$$

$$f_D = \frac{f_G}{c_0} \frac{dL}{dt} \quad (3.9)$$

$$f_D = \frac{f_G}{c_0} (\mathbf{v}_L \mathbf{s}_L + \mathbf{v}_G \mathbf{s}_G) \quad (3.10)$$

$$f_D = \frac{f_G}{c_0} (v_L^r \cos \theta_L - v_L^t \sin \theta_L + v_G^r \cos \theta_G + v_G^t \sin \theta_G) \quad (3.11)$$

$f_L$  ..... frequency at the receiver [ $s^{-1}$ ]  
 $f_G$  ..... frequency at the transmitter [ $s^{-1}$ ]  
 $f_D$  ..... Doppler shift [ $s^{-1}$ ]  
 $c_0$  ..... speed of light in vacuum [ $ms^{-1}$ ]  
 $L$  ..... optical path [m]  
 $v_L^r$  ..... radial velocity of the satellite in LEO (carrying the receiver)  
 $v_L^t$  ..... tangential velocity of the satellite in LEO (carrying the receiver)  
 $v_G^r$  ..... radial velocity of the GPS satellite (carrying the transmitter)  
 $v_G^t$  ..... tangential velocity of the GPS satellite (carrying the transmitter)  
 $\theta_L$  ..... angel between the center to LEO-satellite line and the ray direction.  
 $\theta_G$  ..... angel between the center to GPS-satellite line and the ray direction.

The three equations (3.2), (3.6), and (3.11) fully determine the bending angle. Given the transmitter and receiver position and velocity vectors, transmitter frequency, and the Doppler shift,  $\alpha$  can easily be derived numerically by using a standard iterative algorithm. The corresponding impact parameter is then defined by equation (3.6).

The Doppler shift is normally derived from the measured phase delay after smoothing it in order to allow stable numerical differentiation. In the retrieval algorithm used in this thesis, this is accomplished by an approach implemented for RO retrieval by S. Syndergaard which uses regularization applying a third differences operator with a regularization parameter of  $10^5$  on the observed phase delays provided by the CHAMP receiver with a sampling rate of 50 Hz. Following this filtering, simple three-point differentiation scheme can be applied without amplifying high frequency noise or introducing numerical instabilities [Syndergaard, 1999].

### 3.1.2. Ellipsoid Correction

Since the Earth is not a sphere, the assumption of local spherical symmetry is not only violated by eventual small-scale structures in the atmosphere but also by the oblateness of the refracting atmosphere. Syndergaard [1998] showed that the neglect of the Earth's oblateness can cause errors in the retrieved temperatures near the Earth's surface up to 6 K and proposed a correction scheme assuming spherical symmetry tangential to an ellipsoid approximation of the shape of the Earth. This is accomplished by moving the origin of the framework describing the satellite positions and velocities to the center of a sphere tangential to the Earth ellipsoid using the ellipsoid's radius of curvature in the occultation plane as radius of the sphere. By applying this simple correction scheme the earth-shape related errors can be reduced to less than 0.1 K near the surface and virtually zero above  $\sim 8$  km.

All data processed in this thesis were corrected by the scheme of Syndergaard [1998] using the global ellipsoid of the World Geodetic System of 1984 as reference [WGS, 1998].

### 3.1.3. Ionospheric Correction

Close to the surface the bending angle amounts typically 1 degree – 2 degree and is predominately caused by refraction in the neutral atmosphere. Following the decrease in atmospheric density with height the bending angle decreases exponentially. However, above some 30 km the influence of the ionosphere becomes remarkable and starts to dominate the total bending angle above  $\sim 45$  km (these statements are based on similar considerations for the Doppler shift by Hocke [1997] and the fact that the relation between the bending angle and the Doppler shift is near-linear within 2 % error [Melbourne *et al.*, 1994]).

The ionosphere has much more severe and lower reaching impact on, e.g., retrieved temperatures as it might seem since during the retrieval chain information (including information stemming from the ionosphere) numerically propagates downwards as will be explained in section 3.2.

Ionospheric refractivity can be described by the Appelton-Hartree formula (see section 2.4.2). For RO retrieval, higher than second order terms can be neglected [Hardy *et al.*, 1994; Melbourne *et al.*, 1994] resulting in a second order approximation (equation (3.12)) [Bassiri and Hajj, 1993]. More than that, the second order term, proportional to the inverse cube of the carrier frequency, has virtually no influence under most conditions and very little influence during daytime and high solar activity [Syndergaard, 1999] and is disregarded in all state-of-the art ionospheric correction schemes. The remaining first order term

(equation (3.12), right) is proportional to the inverse square of the carrier frequency and can efficiently be removed by a linear combination of the two measured signals ( $L_1$  and  $L_2$ ).

$$N_k^{IO} = -C \frac{N_e}{f_k^2} - K \frac{B_{par} N_e}{f_k^3} \approx -C \frac{N_e}{f_k^2} \quad (3.12)$$

$N_k^{IO}$  ..... ionospheric refractivity  
 $k$  ..... index denoting the signal (1,2)  
 $C$  ..... constant:  $40.3 \text{ m}^3 \text{ s}^{-2}$   
 $N_e$  ..... electron density [ $\text{m}^{-3}$ ]  
 $f_k$  ..... carrier frequency of signal  $L_k$  [ $\text{s}^{-1}$ ]  
 $K$  ..... constant:  $1.13 \cdot 10^{-12} \text{ m}^3 \text{ T}^{-1} \text{ s}^{-3}$   
 $B_{par}$  ..... absolute value of the Earth's magnetic field parallel to wave propagation [T]

Combining equations (2.17), (3.1), and (3.12) and combining the neutral atmospheric and ionospheric refractivity to give the total refractive index ( $n = 1 + (N^{NE} + N^{IO}) \cdot 10^{-6}$ ) the optical path can be written containing the ionospheric contribution proportional to the inverse square of the carrier frequency (equation (3.13)). By combining (subtracting) the two versions of equation (3.13) for the two signals  $L_1$  and  $L_2$  at time  $t$  and assuming that the two rays are traveling along the same paths ( $S_1 = S_2$ ) we find an expression for the ionospheric contribution to the optical path (either for  $L_1$  or  $L_2$ ) solely dependent on the carrier frequencies and the measured optical paths (equation (3.14)). This expression can be subtracted from the total optical path of the respective signal (e.g.,  $L_1$  in equation (3.15)) to yield the ionosphere corrected optical path  $L_C$  solely dependent on the carrier frequencies and the measured optical paths (equation (3.16)).

$$L_k(t) = \int_{S_k} \left( 1 + \frac{N_k^{IO} + N^{NE}}{10^6} \right) ds$$

$$L_k(t) = S_k - \frac{A_{S_k}}{f_k^2} + \frac{1}{10^6} \int_{S_k} N^{NE} ds, \quad \text{with : } A_{S_k} = \frac{C}{10^6} \int_{S_k} N_e ds \quad (3.13)$$

$$\frac{A}{f_1^2} = \frac{(L_1(t) - L_2(t))}{f_1^2} \left( \frac{1}{f_2^2} - \frac{1}{f_1^2} \right)^{-1}, \quad \text{with : } A_{S_1} = A_{S_2} (\equiv A) \quad (3.14)$$

$$L_C(t) = L_1(t) - \frac{A}{f_1^2} \quad (3.15)$$

$$L_C(t) = \frac{L_1(t) f_1^2 - L_2(t) f_2^2}{f_1^2 - f_2^2} \quad (3.16)$$

$L_k$  ..... measured optical path of signal  $L_k$  [m]  
 $t$  ..... time [s]  
 $k$  ..... index denoting the signal number (1 for  $L_1$  and 2 for  $L_2$ )  
 $S_k$  ..... (length of) ray path of signal  $L_k$   
 $N_k^{IO}$  ..... ionospheric refractivity  
 $N^{NE}$  ..... neutral atmospheric refractivity  
 $f_k$  ..... carrier frequency of signal  $L_k$  [ $\text{s}^{-1}$ ]  
 $C$  ..... constant:  $40.3 \text{ m}^3 \text{ s}^{-2}$   
 $L_C$  ..... ionosphere corrected optical path [m]

This traditional method of ionospheric correction is called the linear correction of phase delays [e.g., *Spilker*, 1980] and is widely used in navigation and geodetic applications of GPS.

The advantage of this method is that the assumption of local spherical symmetry which can be severely violated by the highly variable ionosphere is not needed. On the other hand, the method contains important simplifications: First, the higher order terms in equation (3.12) are neglected contributing to an ionospheric residual after correction. Second, the implicit assumption of identical ray paths of  $L1$  and  $L2$  is not fulfilled due to the dispersive nature of the ionosphere. This dispersion residual can dominate the total ionospheric residual at daytime conditions during solar maximum [Syndergaard, 2000].

In recent applications, the method of linear correction of bending angles [Vorob'ev and Krasil'nikova, 1994] has been applied more successfully. Similar to the optical path, the ionospheric contribution to the total bending angle at a certain impact height can be written proportional to the inverse square of the carrier frequency with high accuracy [Ladreiter and Kirchengast, 1996]. This enables to apply a formally similar linear correction scheme to the bending angles (equation (3.17)). The linear correction of bending angles has the advantage that it accounts for the different  $L1$  and  $L2$  ray paths since the correction is applied at same impact parameters instead of times. Furthermore it exploits the fact that most of the bending information is accumulated near the ray's perigee resulting in a higher neutral atmosphere-to-ionosphere signal ratio.

$$\alpha_c(a) = \frac{f_1^2 \alpha_1(a) - f_2^2 \alpha_2(a)}{f_1^2 - f_2^2} \quad (3.17)$$

$\alpha_c$  ..... ionosphere corrected angle  
 $a$  ..... impact parameter  
 $\alpha_1, \alpha_2$  ..... bending angles of the signals  $L1$  and  $L2$   
 $f_1, f_2$  ..... carrier frequencies of signals  $L1$  and  $L2$

In addition to the two methods described above, several other ionospheric correction schemes exist but none of them has proved to be more accurate than the simple linear correction of bending angles so far. For a review of model independent correction schemes (i.e., pure observational methods needing no background information about the state of the ionosphere) and the discussion of an interesting enhancement of the linear correction of phase delays, the interested reader is referred to the article of Syndergaard [2000].

A major enhancement of the ionospheric correction can only be expected by including a priori information about the ionosphere [Gorbunov, 1996; Ladreiter and Kirchengast, 1996; Syndergaard, 2000 and references therein]. Since this information is not available in sufficient quality and with manageable effort, these methods were only demonstrated in modeling studies but not applied to measured RO data so far in an operational way.

The linear ionospheric correction of bending angles (equation (3.17)) cannot correct for effects of small scale structures in the ionosphere and higher order terms in the formula describing ionospheric refractivity (equation (3.12)). These effects, together with measurement noise and technically corrupted data (leisurely called 'noise' thereafter), are amplified by the original linear correction of bending angles: Calculating error propagation in equation (3.17) shows that noise is amplified by the factor of 3 if noise in the  $L1$  and  $L2$  signals are of comparable size or by the factor of 1.5 if  $L2$  noise is dominant. I.e., the corrected signal carries at least 1.5 times more noise than the noisier of the two observed signals, which is not satisfying. More than that, technically corrupted data often lead to unphysical (negative) bending angles after correction causing the subsequent retrieval steps to fail. Hocke et al. [2003] describe a modification of the linear ionospheric correction of bending angles aiming at more stability and at reducing the noise-amplification (equation (3.18)). This modified scheme uses low-pass filtered bending angle profiles assuming that highly varying signatures can not be corrected for anyway since they are either not present in both signals (due to the fact that even if the correction is applied at a common

impact parameter-level, the ray path still slightly differ) or represent higher order terms not covered by the linear correction.

$$\alpha_c(a) = \frac{f_1^2 \bar{\alpha}_1(a) - f_2^2 \bar{\alpha}_2(a)}{f_1^2 - f_2^2} + \delta\alpha_1(a), \quad \delta\alpha_1(a) = \alpha_1(a) - \bar{\alpha}_1(a) \quad (3.18)$$

$\alpha_c$  ..... ionosphere corrected angle  
 $a$  ..... impact parameter  
 $\alpha_1, \alpha_2$  ..... bending angles of the signals  $L1$  and  $L2$   
 $\bar{\alpha}_1, \bar{\alpha}_2$  ..... low-pass fractions of bending angles  
 $\delta\alpha_1, \delta\alpha_2$  ..... high-pass fractions of bending angles  
 $f_1, f_2$  ..... carrier frequencies of signals  $L1$  and  $L2$

The advantage of this scheme is that noise amplification is reduced and that the formula is more robust against technically corrupted data. Since some of the small scale features filtered out can also be related to structures in the neutral atmosphere, the high-pass fraction of the  $L1$  bending angles is added to the signal again after correction ( $\delta\alpha_1(a)$ ) disregarding the high-pass fraction of the more noisy  $L2$  bending angles. This has the advantage that the ionospheric corrected bending angle profile is less sensitive to the low  $L2$  signal to noise ratio (SNR) without losing information about the non-dispersive neutral atmosphere. However, careful selection of filter width is necessary to avoid introducing biases. More details on the application of this method to CHAMP data and on its performance can be found in section 5.3.

## 3.2. Retrieval of Atmospheric Parameters

This section gives an overview on retrieval techniques to derive profiles of atmospheric parameters from bending angles. Starting with the derivation of refractivity (section 3.2.1) it describes how to retrieve density, pressure, geopotential height, and “dry” temperature (section 3.2.2), and briefly elaborates techniques to resolve the temperature-water vapor ambiguity of RO measurements (section 3.2.3).

### 3.2.1. Retrieval of Refractivity

The relation between bending angle and refractivity can be established using the optical ray equation (equation (3.3)) and Bouguer’s rule (equation (3.5)), i.e., assuming local spherical symmetry. The change in ray direction along the ray is given by  $d\mathbf{s}/ds$ ,  $\mathbf{s}$  being the unit vector in ray direction. Since  $d\mathbf{r} = \mathbf{s}ds$  the ray equation (3.3) can be written as:

$$\frac{d\mathbf{s}}{ds} = \frac{1}{n} \left( \nabla n - \mathbf{s} \frac{dn}{ds} \right) = \frac{1}{n} \nabla_{\perp \mathbf{s}} n \quad (3.19)$$

$n$  ..... refractive index  
 $\mathbf{r}$  ..... position vector  
 $\mathbf{s}$  ..... unit vector in ray direction  
 $ds$  ..... arc element  
 $\nabla_{\perp \mathbf{s}} n$  ..... gradient of  $n$  perpendicular to the ray direction

Equation (3.19) demonstrates that the change in ray direction (i.e., bending) is due to the proportion the refractivity gradient perpendicular to the ray direction. Since  $\mathbf{s}$  is a unit vector its variation is only directional and the differential bending angle along the ray is given by the norm of  $d\mathbf{s}$  (equation (3.20)). Considering local spherical symmetry of the refractivity field ( $n(\mathbf{r}) = n(r)$ ) this equation can be simplified and written in scalar form as given in equation (3.21). Considering the formula of Bouguer (equation (3.5)) it can be further simplified (equation (3.22)) and the total bending angle of a ray with impact parameter  $a$  is then given by integrating two times from outside the atmosphere ( $r = \infty$ ) to the point nearest to the center of refraction, the tangent point ( $r = a/n$ ) (equation (3.23)). The result is an Abel integral transform that can be inverted using standard mathematical techniques [Fieldbo et al., 1971]. The inverse Able transform (equation (3.24)), allows us to derive the refractive index from bending angles. From this equation refractivity as a function of height,  $N(z)$ , is obtained via  $N(a) = 10^6(n(a)-1)$  and  $z(a) = a/n(a) - R_C$ .  $R_C$  is the radius of curvature of the ellipsoidal Earth at the occultation location along the occultation plane ( $\sim$  Earth’s radius, see section 3.1.2). Since equation (3.24) contains a singularity at  $a' = a$ , generally a different form, that can be derived via integrating by parts, is used (equation (3.25), [e.g., Steiner, 1998; Ahmad and Tyler, 1999]).

$$d\alpha = \frac{1}{n} |\nabla_{\perp s} n| ds \tag{3.20}$$

$$d\alpha = \frac{1}{n} \frac{dn}{dr} \sin\phi ds = \frac{d(\ln n)}{dr} \frac{\sin\phi}{\cos\phi} dr = \frac{d(\ln n)}{dr} \frac{\sin\phi}{\sqrt{1-\sin^2\phi}} dr \tag{3.21}$$

$$d\alpha = \frac{d(\ln n)}{dr} \frac{a}{\sqrt{n^2 r^2 - a^2}} dr \tag{3.22}$$

$$\alpha(a) = -2a \int_{a/n}^{\infty} \frac{d(\ln n)}{dr} \frac{1}{\sqrt{n^2 r^2 - a^2}} dr \tag{3.23}$$

$$n(a) = \exp \left[ \frac{1}{\pi} \int_a^{\infty} \frac{\alpha(a')}{\sqrt{a'^2 - a^2}} da' \right] \tag{3.24}$$

$$n(a) = \exp \left[ -\frac{1}{\pi} \int_a^{\infty} \ln \left\{ \frac{a'}{a} + \sqrt{\left(\frac{a'}{a}\right)^2 - 1} \right\} \frac{d\alpha}{da'} da' \right] \tag{3.25}$$

$$N(z) = 10^6(n(z + R_C) - 1) \tag{3.26}$$

- $\alpha$  ..... bending angle (ionosphere corrected)
- $a$  ..... impact parameter
- $n$  ..... refractive index
- $\nabla_{\perp s} n$  ..... gradient of  $n$  perpendicular to the ray direction
- $ds$  ..... arc element
- $\phi$  ..... angle between point vector ( $\mathbf{r}$ ) and ray direction ( $\mathbf{s}$ )
- $z$  ..... height [m]
- $R_C$  ..... local radius of curvature [m]

The inversion of bending angles is a crucial link in the RO retrieval chain. Due to the fact that the refractivity at each level is dependent on the entire half room of bending angles above that layer, the inverse Abel transform (equation (3.24)) propagates high altitude bending angle information downwards. This is not only true for “regular” information about the atmosphere (the signal) but also for erroneous information (thermal and receiver noise, local multipath

errors, residuals from the ionospheric correction, and technically corrupt data). It is thus vital to use adequate bending angle information above any height of interest. Due to the fairly localized kernel  $(a'^2 - a^2)^{-1/2}$  of the inverse Abel transform (i.e., the weight given to a piece of information decreases with increasing distance from the height of interest), the vertical correlation is limited in  $N(z)$  but further vertical propagation of information occurs in a subsequent link of the retrieval chain (see section 3.2.2).

### 3.2.2. Retrieval of Dry Density, Pressure, Geopotential Height, and Temperature (“Dry Retrieval”)

The refractivity field  $N(z)$  is related to atmospheric state variables as elaborated in section 2.4.1. In current RO retrieval applications, the relation given in equation (2.14) is most frequently applied. Assuming that the contribution of humidity can be neglected, which is appropriate for the mid- to upper troposphere and above, it can be written as equation (3.27) and is the basis for the retrieval of “dry” atmospheric parameters (subsequently the expressions dry pressure, dry temperature, and dry density refer to the corresponding atmospheric parameters retrieved from RO data using this simplification). For the atmospheric boundary layer and in the tropical moist troposphere sometimes up to about 8 km this assumption leads to cold biased temperatures, a problem that is treated in section 3.2.3 in more detail.

$$N(z) = k_1 \frac{p(z)}{T(z)} + k_4 \frac{e(z)}{T^2(z)} \quad (2.14)$$

$$N(z) = k_1 \frac{p_{dry}(z)}{T_{dry}(z)} \quad (3.27)$$

$z$ .....	height [m]
$N$ .....	refractivity [N-units]
$k_1$ =	77.60 K/hPa,
$k_4$ =	$3.73 \cdot 10^5$ K <sup>2</sup> /hPa
$p_{dry}, p$ .....	(dry) pressure [hPa]
$T_{dry}, T$ .....	(dry) temperature [K]
$e$ .....	partial pressure of water vapor [hPa]

Combining the ideal gas law (equation (3.28)) with equation (3.27) shows that atmospheric density is directly proportional to refractivity (equation (3.29)). Hence, the hydrostatic integral can be written in terms of refractivity which enables do directly derive dry pressure from refractivity (equation (3.30)). Dry temperature is then given by equation (3.27).

Since the RO method delivers retrieval of both, height and pressure (i.e., height is not derived from the observed pressure but a directly observed quantity), these data can also be used to calculate geopotential height on pressure levels (see equation (3.31)).

From equation (3.30) it is apparent that vertical correlation in retrieved pressure (and temperature) profiles is much stronger than in refractivity profiles since no localized kernel is involved. This means that erroneous information is transported downwards without mitigation and can significantly disturb the retrieval results. Due to the measurement geometry and the influence of the ionosphere, errors at high altitudes can be very significant making it particularly important to control high altitude data above the actual region of interest. This issue is treated separately in Chapter 4.

$$\rho(z) = \frac{1}{RM_d} \frac{p(z)}{T(z)} \quad (3.28)$$

$$\rho_{dry}(z) = \frac{M_d}{k_1 R} N(z) \quad (3.29)$$

$$p_{dry}(z) = \frac{M_d}{k_1 R} \int_z^{\infty} g(\phi, z') N(z') dz' \quad (3.30)$$

$$\text{with: } g(\phi, z) = \left( \frac{R}{R+z} \right)^2 g(\phi)$$

$$g(\phi) = 9.7803(1 + 0.0053 \sin^2(\phi))$$

$$Z(p) = \frac{1}{g_{45}} \int_0^{z(p)} g(\phi, z') dz' \quad (3.31)$$

$\rho_{dry}, \rho$  ..... (dry) air density

$R$  ..... universal gas constant ( $8.3145 \cdot 10^3 \text{ JK}^{-1} \text{ kg}^{-1}$ )

$M_d$  ..... molar mass of dry air ( $28.964 \text{ kg kmol}^{-1}$ )

$g(\phi, z)$  ..... normal gravity as a function of latitude  $\phi$  and height  $z$  [ $\text{m s}^{-2}$ ]

$g(\phi)$  ..... normal gravity at the surface according to the international gravity formula [Moritz, 1980]

$g_{45}$  ..... normal gravity at  $\phi = 45^\circ$  ( $9.80665 \text{ ms}^{-2}$ )

$Z$  ..... geopotential height [gpm]

### 3.2.3. The Temperature – Humidity Ambiguity

The dry retrieval simplification is violated in the lowermost part of the atmosphere. Equation (2.14) shows that refractivity depends on both, temperature and water vapor. Since water vapor contribution to the signal amounts to some 30 % in the moist boundary layer (locally to over 50 %) [Kursinski *et al.*, 1997] the dry retrieval leads to systematic underestimation of retrieved temperatures in the order of several 10 K.

Figure 3.2 demonstrates the difference between dry temperature  $T_{dry}$  and the “moist” temperature  $T$  (corresponding to the physical temperature of the atmosphere) using simulated RO-derived temperature profiles retrieved with or without the dry retrieval assumption. The atmospheric state used in the forward model and as background information in the “moist” retrieval was extracted from Peixoto and Oort [1992; 1996] regarding humidity and from the MSISE-90 climatology [Hedin, 1991] regarding temperature and pressure.

Three cases were simulated: the polar (90 degree), mid-latitude (45 degree) and equatorial atmosphere (0 degree). In the moist equatorial atmosphere (specific humidity ( $q$ ) amounts  $\sim 18 \text{ g/kg}$  at the surface and  $\sim 0.5 \text{ g/kg}$  at 9 km) the cold bias at the surface is huge ( $> 60 \text{ K}$ ) and stays above the 1 K-level up to 10 km. In contrary, in the dry and cold polar atmosphere ( $q \sim 1.6 \text{ g/kg}$  at the surface and  $\sim 0.25 \text{ g/kg}$  at 4.5 km), the bias becomes negligible above 5 km. It has to be emphasized that these values are climate mean values and may not apply to specific atmospheric situations. According to the experience of the author based on comparison of RO-derived dry temperatures with other data sources (see section 6.2) the climatologically derived dry temperature errors slightly overestimate the real error and can be used as worst-case scenario and for the definition of cut-off altitudes above which dry temperatures are a precise measure for atmospheric temperature.

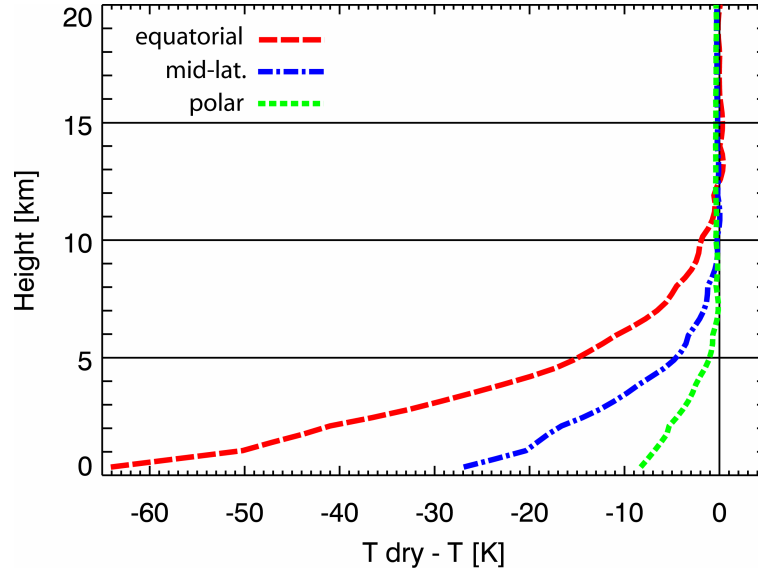


Figure 3.2: Simulated RO-derived dry temperature compared to retrieved temperatures using perfect background information on atmospheric humidity and pressure. The atmospheric state was extracted from the MSISE-90 climatology regarding temperature and pressure (September, 30 degree longitude; 0 degree latitude (equatorial), 45 degree latitude (mid-latitudes), 90 degree latitude (polar)) and extracted from *Peixoto and Oort* [1992, 1996] regarding specific humidity (see text for humidity values).

The temperature-humidity ambiguity of refractivity can only be resolved if some kind of a priori information (henceforth termed background information) either on humidity or temperature and pressure is available. Transformation of equation (2.14) gives the partial pressure of water vapor as a function of temperature, pressure, and refractivity (equation (3.32)). The simplest way to retrieve humidity is to use background information about tropospheric temperature and surface pressure which are by far better represented in numerical weather prediction (NWP) data assimilation systems than humidity. Humidity can then be derived directly from equation (3.32).

$$e(z) = \frac{T^2(z)N(z) - k_1 p(z)T(z)}{k_4} \quad (3.32)$$

*Kursinski et al.* [1995] and *Kursinski and Hajj* [2001] used this expression to calculate the retrieved humidity errors assuming typical RO retrieval error characteristics for refractivity and pressure and a temperature error estimate (RMS) typical for NWP analysis systems (1.5 K). The authors found humidity errors below 5 % (or 0.4 g/kg) in the moist regions of the atmosphere (near the surface at latitudes smaller than  $\sim 35$  degree) and up to 20 % (or 0.3 g/kg) towards the poles. Generally, the relative errors increase with decreasing water vapor pressure, i.e., with height and towards the poles.

Comparisons of humidity derived from CHAMP RO data with this method with various other data sources show, however, that the uncertainty is in the order of 20 % and above [e.g., *Hajj et al.*, 2004; *Wickert et al.*, 2004b]. These studies show that the major difficulty in the retrieval of water vapor is not the water vapor-temperature ambiguity, but the retrieval of refractivity in the lower troposphere [*Beyerle et al.* 2004; *Ao et al.*, 2003].

This problem also affects more sophisticated methods to solve the water vapor-temperature ambiguity: Optimal estimation algorithms like the one-dimensional variational data assimilation (1DVar) combine observed and background information considering their error characteristics in a statistically optimal way by minimizing the RMS error of the combined product. Since the focus of this thesis is not on the lower troposphere and the basic atmospheric parameters used here are refractivity and dry temperature, no detailed description

of these techniques is given here (see, however, section 4.1 for a brief discussion of the 1DVar method for high altitude initialization). The interested reader is referred to the works of *Eyre* [1994], *Healy and Eyre* [2000], *Palmer et al.* [2000], and *von Engeln et al.* [2003] for further information.

## 4 High Altitude Initialization and Statistical Optimization

As already mentioned in sections 3.2.1 and 3.2.2, noisy and erroneous information from high altitudes is transported downwards in the refractivity profile to some degree by the inverse Abel transform (equation (3.24)) and to a stronger degree by the hydrostatic integral (equation (3.30)) in the temperature profile. (A detailed discussion of RO retrieval error propagation is provided by *Rieder and Kirchengast* [2001]).

This vertical correlation of errors is the reason for the retrieval results at heights above 15 km – 30 km (depending on the quality of data at high altitudes) being sensitive to residual ionospheric noise (higher order terms), other noise (e.g., receiver thermal noise or local multipath effects), or technically corrupt data from altitudes far beyond the height of interest. Sensible use of RO data at high altitudes is necessary to cope with this problem.

Generally, background information about the atmosphere at high altitudes, i.e., in the stratopause region and above, to initialize the upper boundary of the Abel integration is necessary since its upper integration limit ranges to infinity and RO measurements don't deliver data with sufficient quality up to desirable altitudes (i.e. up to at least 100 km).

This section reviews recent methods of high altitude initialization of the Abel- and hydrostatic integral and statistical optimization techniques used to combine background information with observed data (section 4.1). Furthermore enhanced methods developed in the framework of this thesis at the Institute for Geophysics, Astrophysics, and Meteorology (IGAM) are described (section 4.2) and studies testing the performance of many of these methods are presented (section 4.3). Main results of this Chapter have been published by *Gobiet and Kirchengast* [2004] and *Steiner et al.* [2004].

### 4.1. Review of High Altitude Initialization and Statistical Optimization Methods

The simplest currently applied method to initialize the inverse Abel transform is to select an upper boundary height (UBH) at altitudes between 50–70 km above which an extrapolated exponential profile is used [e.g., *Kursinski et al.*, 1997]. This approach (“exponential extrapolation” and “no optimization” hereafter) features several weaknesses, the most important ones being the sensitivity of retrievals to the exact UBH setting and to extrapolation quality due to measurement noise as well as the intrinsic assumption of an isothermal (constant scale height) atmosphere above the UBH. The latter assumption leads to a systematic bias in any ensemble of retrieved profiles, which unfavorably is also UBH-dependent, since isothermality above 50 km – 70 km ignores the actual mesosphere/lower thermosphere temperature structure. In any application the author is aware of, this approach is combined with a second addition of background information, the initialization of the

hydrostatic integral a heights between 35 km and 45 km with information extracted from NWP analyses. As will be demonstrated later (see sections 4.3.3 and 4.3.4) the exponential extrapolation approach is very unstable without this additional piece of background information.

A more robust and sensible approach is statistical optimization, a form of optimal estimation [Turchin and Nozik, 1969; Rodgers, 2000]. It finds the most probable bending angle profile  $\alpha_{opt}$  by combining the observed profile with a background profile in a statistically optimal way [Sokolovskiy and Hunt, 1996; Rodgers, 2000].

Background profiles can be obtained from climatologic models or profile datasets or from NWP analyses or forecasts. Any work cited in this section use climatologic models like MSISE-90 [Hedin, 1991] or CIRA-86 [Fleming, 1988] which are closely similar in the height range 30 – 120 km.

The general effect of statistical optimization is that at higher altitudes, where the observation error exceeds the error of the background, the background determines  $\alpha_{opt}$ . At lower altitudes, where the background error becomes dominant, the observed data determine  $\alpha_{opt}$ . The transition zone between these two regimes lies typically between 40 km and 60 km, depending on the error characteristics of the observed and background data. Note that statistical optimization does not improve the quality of observed profiles themselves at high altitudes but rather delivers an improved combined profile thanks to the sensible inclusion of background information. The most important effect is that downward propagation of errors via the inverse Abel transform and the hydrostatic integral is reduced.

The full optimization formula which optimally combines, in a least-squares sense, observations and background reads (“inverse covariance weighting” optimization hereafter):

$$\alpha_{opt} = \alpha_b + \mathbf{B}(\mathbf{B} + \mathbf{O})^{-1}(\alpha_o - \alpha_b) \quad (4.1)$$

$\alpha_{opt}$ .....optimized bending angle profile [rad]  
 $\alpha_b$ .....background bending angle profile [rad]  
 $\alpha_o$ .....observed bending angle profile [rad]  
 $\mathbf{B}$ .....background error covariance matrix  
 $\mathbf{O}$ .....observation error covariance matrix

The assumptions of this approach are that unbiased (Gaussian) errors and a linear problem are assumed. Linearity is trivially fulfilled in the present case and the unbiased error assumption holds reasonably well for the observation error due to the self-calibrating nature of RO measurements. The background errors are likely to involve biases in addition to their random component, however. Consequently, biases in background data, which could partially leak into retrievals and thereby degrade the climate monitoring utility of retrieved profiles, are an important problem in the practical application of statistical optimization and are thus one key matter of this thesis.

Since it is difficult to obtain accurate error covariance matrices, Sokolovskiy and Hunt [1996] used a simpler form assuming vertically uncorrelated errors. This allows calculating the optimized bending angles ray-per-ray (“inverse variance weighting” optimization hereafter, equation (4.2)).

$$\alpha_{opti} = \alpha_{bi} + \frac{\sigma_{bi}^2}{\sigma_{bi}^2 + \sigma_{oi}^2}(\alpha_{oi} - \alpha_{bi}) \quad (4.2)$$

$\alpha_i$  ..... component of the bending angle vector.  $i$ : height index  
 $\sigma_{bi}, \sigma_{oi}$  ..... estimated standard deviations of background and the observed data [rad]

$\sigma_{bi}$  is typically assumed to be a constant fraction of the background bending angle profile (5 % – 20 %) and  $\sigma_{oi}$  is estimated, generally as a constant  $\sigma_o$ , from the root-mean-square (RMS) error of the observed profile compared to the background, or from the high frequency variations of the observed signal, within a high altitude range of 10 km – 15 km above 60 km, where noise dominates the signal [Gorbunov *et al.*, 1996; Gorbunov and Gurvich, 1998; Hajj *et al.*, 2002; Kuo *et al.*, 2003].

A modification of this “inverse variance weighting” is the “heuristic weighting” optimization [Hocke *et al.*, 1997; Hocke, 1997; Steiner *et al.*, 1999] as shown in equation (4.3).

$$\alpha_{opti} = \alpha_{bi} + \frac{\sigma_{bi}}{\sigma_{bi} + \sigma_{oi}} (\alpha_{oi} - \alpha_{bi}) \quad (4.3)$$

$\sigma_{bi}$  is again assumed to be a constant fraction of the background bending angle (typically 20 %) but  $\sigma_{oi}$  is defined to be the absolute difference between the observed profile and the background at each height  $i$ ,  $\sigma_{oi} = |\alpha_{oi} - \alpha_{bi}|$ . This approach effectively down-weights “outliers” and smoothes the profile at high altitudes, but is non-optimal in a formal statistical sense. It doesn’t produce the most probable solution and gives too much weight to the information with the larger error (see also Healy [2001]). Furthermore, the definition of observation error tends to produce a bias towards the background since eventual biases in the background information cause artificially enhanced higher observation errors.

Healy [2001] suggested to use the full inverse covariance weighting approach, equation (4.4), and demonstrated it with a simplified analytical background error covariance matrix of Gaussian shape.

$$B_{ij} = \sigma_{bi} \sigma_{bj} \exp \left[ - \frac{(a_i - a_j)^2}{L^2} \right] \quad (4.4)$$

$B_{ij}$ ..... element of the error covariance matrix **B**  
 $\sigma_{bi}, \sigma_{oj}$  ..... background standard errors at heights  $i$  and  $j$  [rad]  
 $a_i, a_j$  ..... the impact parameters at heights  $i$  and  $j$  [km]  
 $L$  ..... error correlation length [km]

The vertical error correlation length was set to 6 km and  $\sigma_{bi}$  again to 20 % of the background value. Regarding observation errors, a constant vertically uncorrelated error  $\sigma_o$  set to 5  $\mu$ rad was assumed.

A somewhat similar (applying inverse covariance weighting as well) but more general concept was introduced and discussed by Rieder and Kirchengast [2001], who generalized the treatment of the optimization problem to employ the full breath of the optimal estimation methodology detailed by Rodgers [2000]. In demonstrating the concept, the background bending angle errors  $\sigma_{bi}$  were set to linearly increase from 6 % to 18 % of the background profile between 30 km and 120 km; the background covariances were analytically derived according to equation (4.4). Though the demonstration started with phase delay observations the concept can be equally well used starting with bending angles.

Gorbunov [2002c] proposed a combined ionospheric correction and statistical optimization algorithm where the background is linearly fitted to the observations between 40 and 60 km to reduce the background bias, observation and background errors are assumed to be vertically uncorrelated, and both,  $\sigma_o$  and  $\sigma_b$ , are dynamically estimated:  $\sigma_o$  is estimated from the variance of the observation above 50 km and  $\sigma_b$  from the RMS deviation between background and observations between 12 km and 35 km.

The problem of high altitude initialization or statistical optimization can also be addressed by an alternative to the inversion approach described in section 3.2. This is the assimilation of observed (ionosphere-corrected) bending angle profiles with forward-modeled background data using one-dimensional variational (1DVar) data assimilation as proposed and described, e.g., by *Eyre* [1994], *Healy and Eyre* [2000], *Palmer et al.* [2000], and *von Engeln et al.* [2003]. Using this approach, the observed data is only processed to the bending angle level and no further inversion is applied. The main challenges using this approach are the adequate definition of the forward modeling operators (posing similar problems as the RO retrieval since the forward Abel transform needs, similar to the inverse transform, high altitude data which are generally not available with high quality from NWP models as well) and background error covariance matrices as well as the lack of a simple method to cope with biases in the background data.

## 4.2. Improvement of High Altitude Initialization and Statistical Optimization

This section describes two high altitudes retrieval schemes (including ionospheric correction and statistical optimization) aiming at the improvement of the methods reviewed in section 4.1. Both schemes were developed at IGAM using heritage from the End-to-end GNSS Occultation Performance Simulator (EGOPS) [*Kirchengast et al.*, 2002]. The first scheme (“Basic IGAM High Altitude Retrieval Scheme”) is part of the official EGOPS release and has been implemented by S. Syndergaard (University Cooperation of Atmospheric Research, UCAR, Boulder, CO) and G. Kirchengast (IGAM). The second scheme (“Enhanced IGAM High Altitude Retrieval Scheme”) has been developed by the author of this thesis and is implemented into an IGAM-internal version of EGOPS. Both schemes were developed and tested using simulated RO data produced in the framework of End-to-end simulation studies. Retrieval schemes tuned for the retrieval of observed data (from CHAMP) have been developed based on these schemes and will be described in Chapter 5.

### 4.2.1. The Basic IGAM High Altitude Retrieval Scheme

The basic high altitude retrieval scheme used at IGAM applies the linear ionosphere correction of bending angles, equation (3.17), followed by inverse covariance weighting, equation (4.1), using MSISE-90 bending angle profiles as background together with an analytical background error covariance matrix with an error correlation length of  $L = 6$  km. Different from *Healy* [2001], exponential decay of covariances was used which was found more adequate in an empirical error study by *Steiner and Kirchengast* [2004] (equation (4.5)).

$$B_{ij} = \sigma_{bi} \sigma_{bj} \exp \left[ -\frac{|a_i - a_j|}{L} \right] \quad (4.5)$$

Observation errors  $O_{ij}$  were specified in the same way as  $B_{ij}$ , but with a shorter correlation length ( $L = 1$  km) based as well on results of *Steiner and Kirchengast* [2004]. This short-range correlation accounts for the smoothing of the phase delays in an earlier step of the retrieval (see section 3.1.1). The background standard deviation  $\sigma_b$  is assumed to amount to 20 % of the background bending angle, which is a frequently used estimate of the strato-pause/mesosphere RMS uncertainty of the MSISE-90 climatology and is also based on

retrieval performance studies conducted at IGAM (not presented here). The observation errors  $\sigma_o$  are estimated from the RMS deviation of the observed bending angle profile compared to the background between 70 km and 80 km, where the bending angle signal is at the  $\leq 1 \mu\text{rad}$  level and ionospheric residual and measurement noise dominate. The optimization, equation (4.1), is applied from 120 km down to 30 km below which the SNR is high enough that statistical optimization is safely no longer required [e.g., *Rieder and Kirchengast, 2001*].

*Syndergaard* (UCAR, Boulder, CO, pers. communications, 1999) suggested to perform background search prior to statistical optimization, i.e., to fit the available ensemble of background profiles to the observed profile, and use the best-fit, instead of the co-located profile, as background in the statistical optimization process. We adopted this approach in the IGAM retrieval scheme, searching the global MSISE-90 climatology on a 5 degree latitude x 15 degree longitude grid through all months from January to December and using a least squares fit in the 45 km – 65 km height interval to determine the best-fit profile.

Besides this statistical optimization of bending angles no further background information is used in the IGAM scheme, different from most other retrieval schemes, which initialize the hydrostatic integral (equation (3.30)) as well using background data from NWP analyses or climatologies.

The scheme, which was tested in a systematic high altitude retrieval evaluation study [*Gobiet and Kirchengast, 2002*] and applied in a RO climate monitoring system simulation project designed to test the climate change detection capability of GNSS occultation sensors (GNSS-CLIMATCH; *Kirchengast et al. [2000]*; *Steiner et al. [2001]*; *Foelsche et al. [2003]*), already proved to be effective. However, it cannot cope with a situation where no unbiased data is available in the background climatology. As will be shown in section 4.3, for the MSISE-90 climatology this situation frequently occurs in the high-latitude winter region. Similar results were found by *Randel et al. [2003]* for the CIRA-86 climatology, which provided the basis for the MSISE-90 climatology below the thermosphere.

#### 4.2.2. The Enhanced IGAM High Altitude Retrieval Scheme

One of the most promising pathways to advance high altitude RO retrieval (besides enhancement of ionospheric correction) is to pay more attention to biases in background information used in the statistical optimization process. Since the method of statistical optimization is based on the assumption of Gaussian random errors any bias in the background information will introduce a bias into the retrieved profile at high altitudes.

The easiest way to avoid this would be to use unbiased background information climatologies but presently no such dataset is available. It has been shown that recent mesospheric climatologies such as MSISE-90 or CIRA-86 are biased in some regions of the atmosphere (section 4.3, *Randel et al. [2003]*).

Apart from climatologies, analyses from NWP systems can be used. Several reasons complicate the application such data: The quality of NWP analyses at high altitudes (above  $\sim 30$  km) is still questionable due to the sparseness of adequate assimilated observed data at these heights, NWP analyses generally do not reach above  $\sim 60$  km, RO-retrieved profiles may later be evaluated using these analyses, or they might be used in the data assimilation process to create these analyses.

For these reasons, we developed both, a “model-independent” optimization scheme using the MSISE-90 climatology combined with bias correction procedures as background information and a scheme using ECMWF-derived bending angles as background. The former approach, which is described here, is designed to be able to cope with partly inadequate background data as delivered by today’s climatologies and focuses on the correction of eventual biases in the background. The latter approach is described in section 5.4.3.

The main components of the enhanced algorithm are linear ionospheric correction of bending angles, equation (3.17), empirical background bias correction of bending angles (explanation below), and inverse covariance weighting statistical optimization of bending angles, equation (4.1). These main components involve the following ingredients:

*Background information.* Bending angle profiles derived from the MSISE-90 climatology.

*Empirical background bias correction, step 1.* Search the best-fit bending angle profile in the climatology using a least-squares criterion in the 45 km – 65 km interval. The optimal height interval depends on the noise level of the observations. For testing this scheme we used the GRAS error specifications [e.g., *GRAS-SAG*, 1998]. For more noisy observations (e.g., GPS/MET, CHAMP, or SAC-C) it is necessary to place the fit interval at lower altitudes.

*Empirical background bias correction, step 2.* Adjustment of the background profile by multiplying it with a fitting coefficient – a factor usually close to unity – derived from regression with respect to the observed profile at high altitudes (least-squares adjustment). A similar approach was suggested by *Gorbunov* [2002c], though that approach uses lower altitudes and was not combined with background search. Tests showed that the 55 km – 75 km interval is especially sensitive for detecting remaining background biases. The optimal height interval depends on the observation noise level and the error characteristics of the background. Regarding the resulting optimized profile it represents the region just above the transition zone from background-dominated to observation-dominated. GRAS error specifications were used when testing the correction. For more noisy observations (e.g., GPS/MET, CHAMP, or SAC-C) it is necessary to use a lower altitude range.

*Background error.* The standard deviation error is set to 15 % (instead of 20 %) of the background bending angle profile accounting for the bias reduction in empirical background bias correction, step 2 and determined in empirical tests. The background error covariance matrix is analytically defined according to equation (4.5) with a vertical error correlation over about a scale height ( $L = 6$  km).

*Observation error.* Standard deviation estimated from the RMS deviation of the observed bending angle profile compared to the background (after bias correction) within 70 km – 80 km. The observation error covariance matrix is analytically defined according to equation (4.5) and vertically correlated ( $L = 1$  km).

The key advancement of this scheme is its bias correction before the optimization, which is done in an empirical way by comparing the background to the observations within suitable altitude ranges. It combines the advantages of the near bias-free observations and the small statistical error of the background. Step 1 means that the climatology is used as a library of representative bending angle profiles and the best-fit profile is chosen as background. Step 2 means that if there is no well fitting profile in the library, there is the possibility to adjust the background profile towards the observed profile.

This can be regarded as an “emergency reserve” of the algorithm, as illustrated in Figure 4.1. It shows the relative bending angle error (upper row) and the temperature error (lower row) of two quasi-realistically simulated occultation events, each retrieved with or without the background bias correction step 2. In most cases, as demonstrated in the left panels, the effect of correction step 2 is small (adjustment of background bending angles within 55 km – 70 km by  $\sim 1$  % only) and thus the effect on retrieved temperature profiles below 40 km is negligible. In some cases, when no unbiased background can be found in the library, the adjustment amounts to up to 15 % and significantly improves the temperature retrieval down to  $\sim 20$  km. An example of this latter case is shown in the right panels of Figure 4.1.

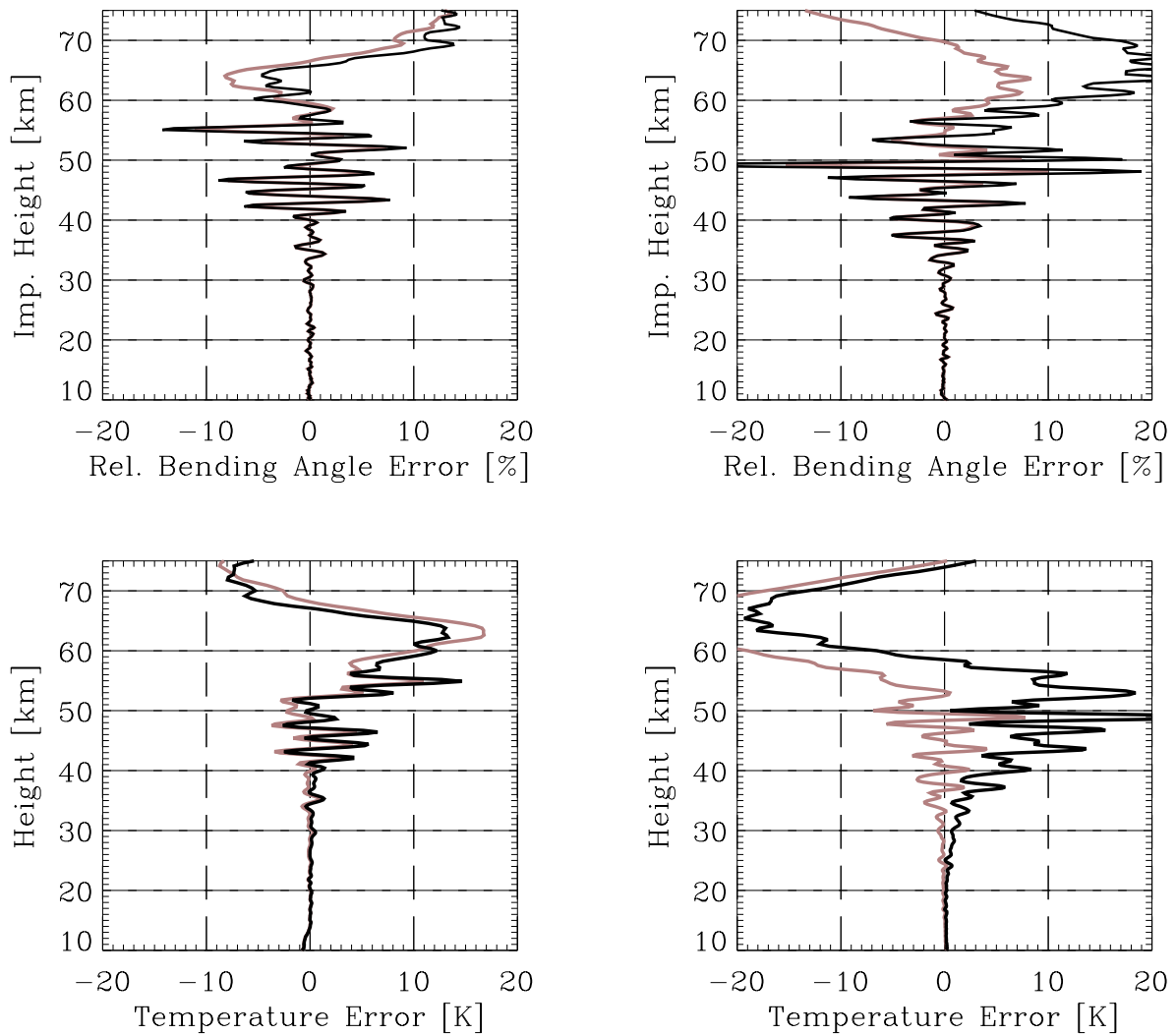


Figure 4.1: Retrieval without background bias correction step 2 (black line) and with correction step 2 (grey line). Upper row: rel. errors of bending angles; lower row: temperature errors; left column: typical case, virtually no effect; right column: critical case, large effect.

After searching and adjusting the background information and after estimation of  $\mathbf{B}$  and  $\mathbf{O}$ , the enhanced scheme continues similar to the basic scheme.

It has to be noted that, in contrary to all other retrieval schemes the author is aware of, the IGAM schemes produce optimized bending angles up to 120 km and don't need any further background information for the initialization of the hydrostatic integral later because any realistic contribution to the signal above 120 km can safely be neglected. For aesthetical reasons we generally initialize the hydrostatic integral with pressure derived from MSISE-90 at 120 km but simply setting the pressure to zero at that altitude gives the same retrieval results.

### 4.3. Evaluation of the IGAM Retrieval Schemes

The performance of high altitude RO retrieval schemes was evaluated in a twofold way: The first part was a systematic case study, which focused on individual occultation events and their error characteristics under different ionospheric conditions. The second part was a large-sample study focusing on sample error statistics and spatial (latitudinal) distribution of errors. Both parts were based on end-to-end simulations of RO events, which have the advantage that

the “true” state of the atmosphere is known and a detailed error analysis is possible (see Figure 4.2 for a schematic sketch of the end-to-end simulation setup).

The complete study, beginning with satellite geometry simulation and proceeding with modeling of GNSS signal propagation through the atmosphere/ionosphere, simulation of the observation system and the observables, and retrieval of the atmospheric profiles was performed by means of a study-tailored version of the EGOPS software tool (End-to-end GNSS Occultation Performance Simulator; *Kirchengast et al. [2002]*).

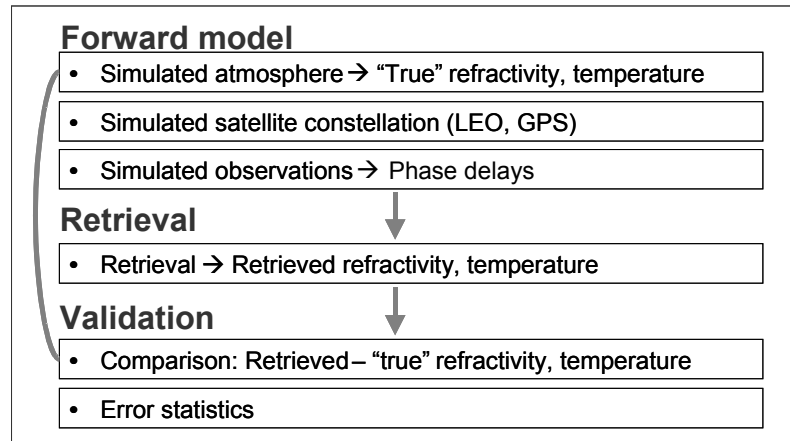


Figure 4.2: Schematic sketch of the end-to-end simulation study setup.

### 4.3.1. Systematic Case Study Setup

In order to study the effects of statistical optimization as a function of ionospheric state, three occultation events were chosen (out of a sample consisting of  $\sim 2100$  events) as base scenarios, each of them being representative for one type of symmetry or asymmetry of electron density distribution in the ionosphere. For the sake of brevity they are referred to as “Nice”, “Nasty 1”, and “Nasty 2” events hereafter. In the forward model provided by EGPOS the propagation of radio signals through the atmosphere without ionosphere (“no ionosphere” reference case) as well as at three different ionization levels, represented by the radio flux at 10.7 cm ( $F_{10.7}$  index) ranging from  $F_{10.7} = 70$  via  $F_{10.7} = 140$  to  $F_{10.7} = 210$  (low, mid, high solar activity) were simulated.

The ionosphere model utilized in the simulation was the NeUoG model [*Leitinger and Kirchengast, 1997a*]. NeUoG provides global 3D electron density distributions depending on local time, season, and solar activity. It features reasonably realistic climatological ionization conditions and has already proven to be useful in the past in occultation-related studies [e.g., *Leitinger and Kirchengast, 1997b*] but does not feature small-scale structures. This latter restriction should be kept in mind when interpreting the results of this study.

The “Nice” event (Figure 4.3) was chosen to be zonally oriented. By this and due to careful selection of the occultation event location, the spherical symmetry assumption is met as good as it is possible in a realistic ionosphere during daytime conditions. The two “Nasty” events (Figure 4.4 and Figure 4.5) were chosen to be meridionally oriented and probe through severe electron density gradients associated with the equatorial anomaly, each violating the spherical symmetry assumption in a specific distinct manner. The “Nasty 1” event exhibits relatively low electron densities at the in and out bounds of the occultation rays and a maximum in electron density above the occultation tangent point. The “Nasty 2” event exhibits low electron densities at the in bound and high electron densities at the out bound of the occultation rays.

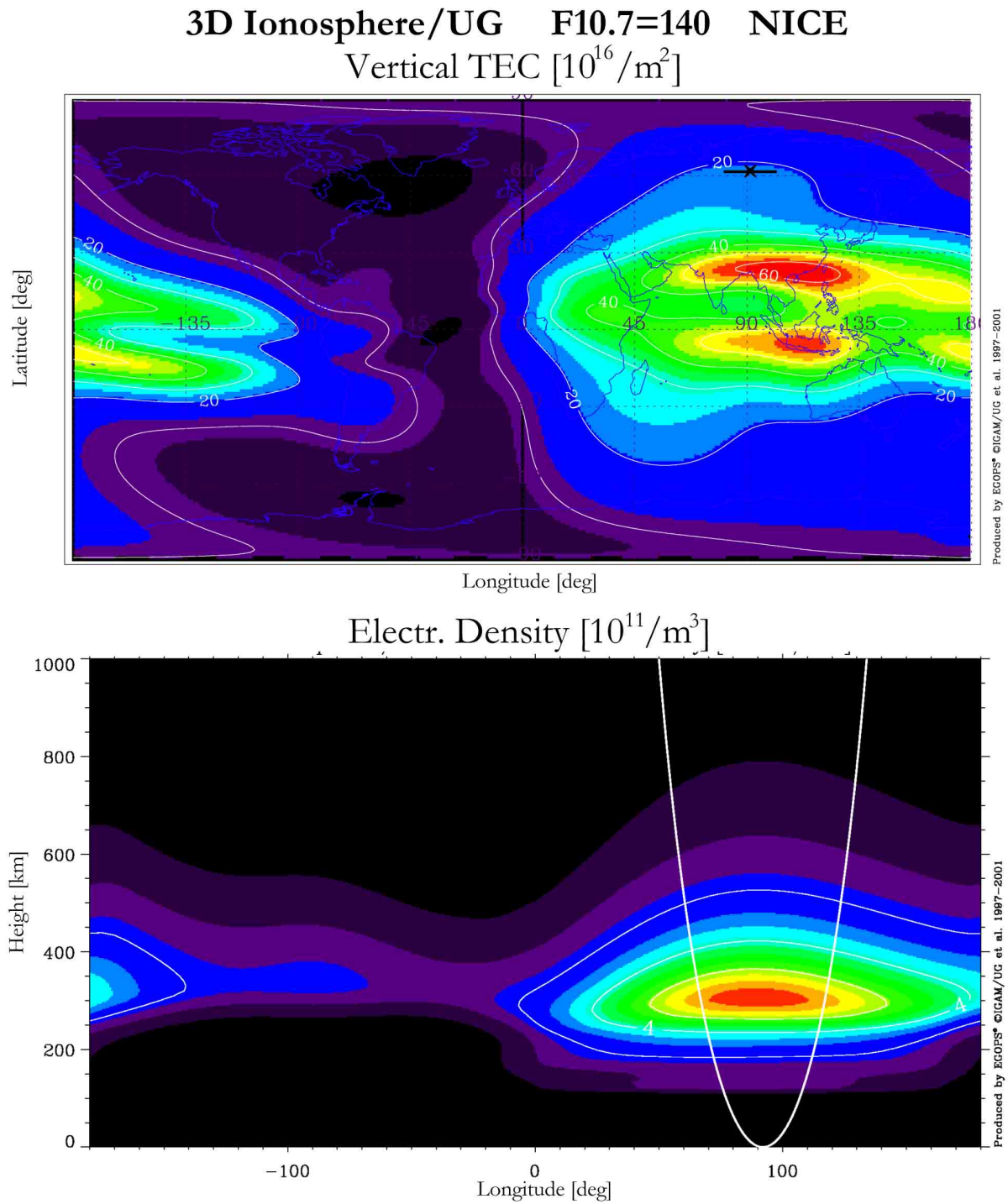


Figure 4.3: Ionospheric conditions during the “nice” occultation event. Vertical total electron content above the mean tangent point:  $\sim 20 \cdot 10^{16} \text{ m}^{-2}$ . The electron density varies less than  $1.5 \cdot 10^{11} \text{ m}^{-3}$  between in bound and out bound of the lowermost occultation ray.

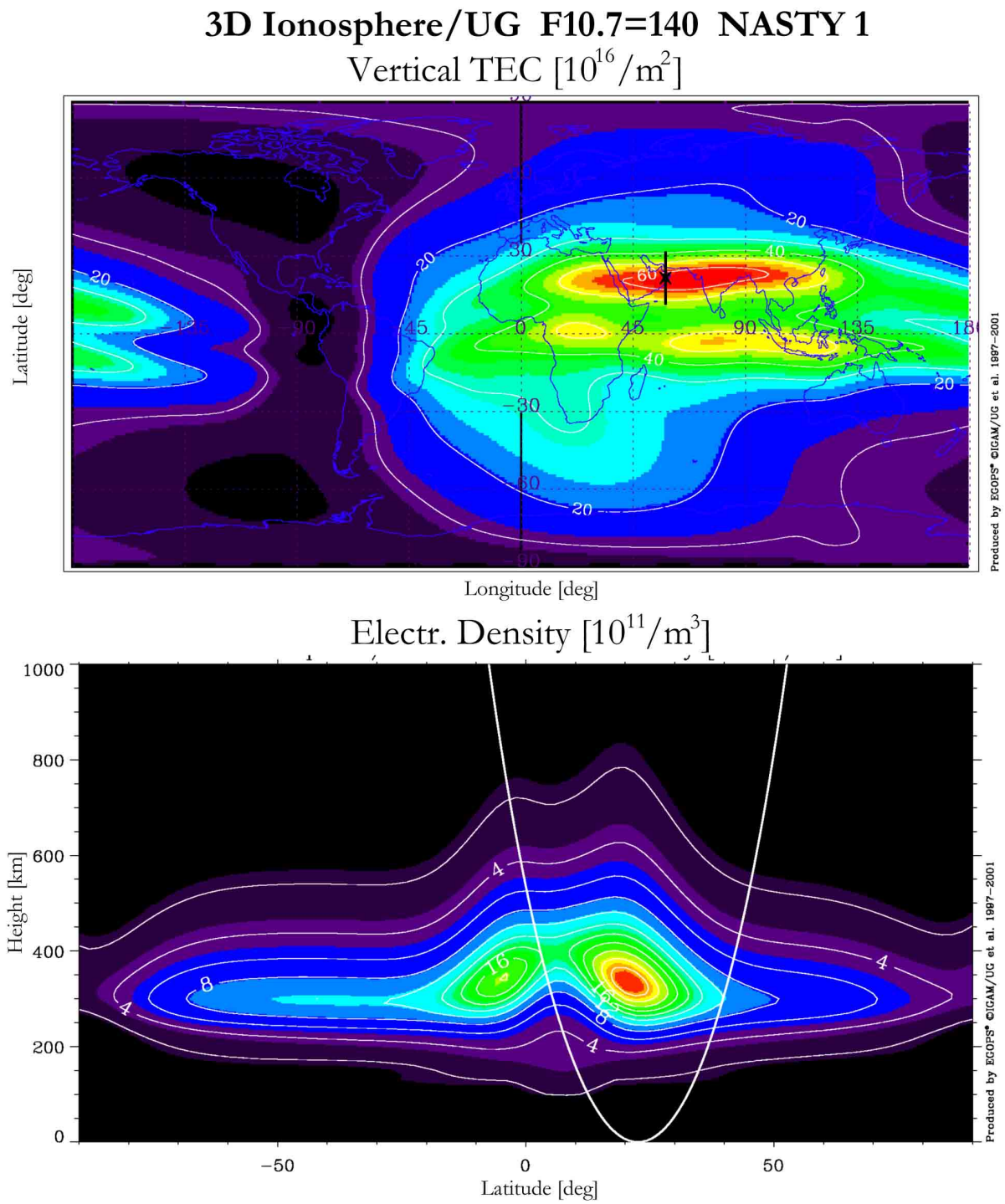


Figure 4.4: Ionospheric conditions during the “nasty 1” occultation event. Vertical total electron content above the mean tangent point:  $\sim 60 \cdot 10^{16} \text{ m}^{-2}$ . The electron density varies up to  $12 \cdot 10^{11} \text{ m}^{-3}$  between in bound and out bound of the lowermost occultation ray. The maximum electron density is located directly above the neutral atmosphere tangent point location of the occultation.

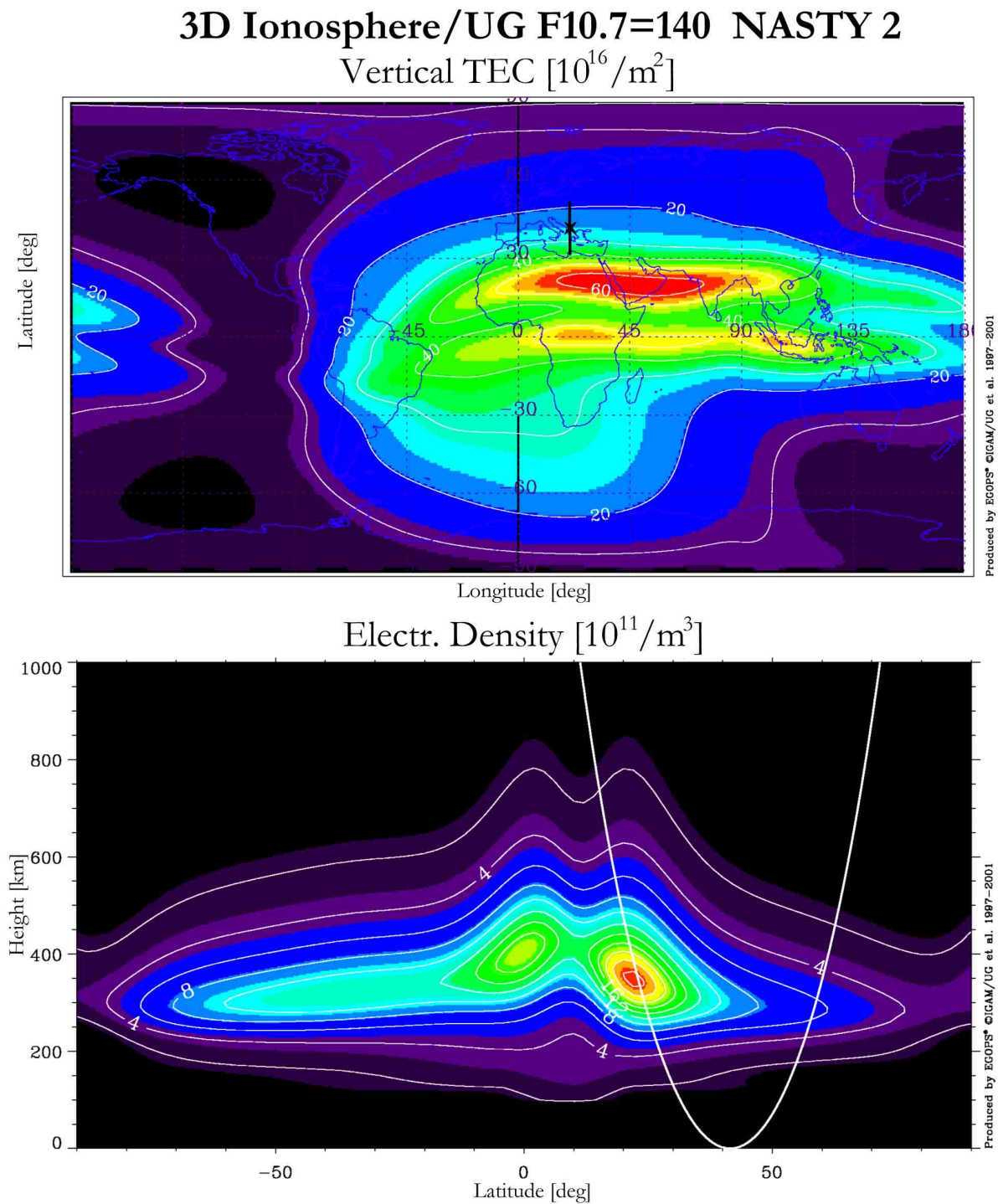


Figure 4.5: Ionospheric conditions during the “nasty 2” occultation event. Vertical total electron content above the mean tangent point:  $\sim 25 \cdot 10^{16} \text{ m}^{-2}$ . The electron density varies up to  $18 \cdot 10^{11} \text{ m}^{-3}$  between in bound and out bound of the lowermost occultation ray. The maximum electron density is found at the outbound of the lowermost ray.

Since the aim of this case study was to describe the effects of the ionospheric conditions and the method of high-altitude initialization on the RO retrieval products, rather than effects of error sources internal to the neutral atmosphere, the forward model was supplied with a simple neutral atmosphere in order to ensure that the errors in the subsequently retrieved atmospheric parameters would be fully traceable to ionospheric residuals and the method of

statistical optimization. A dry atmosphere, local spherical symmetry, and identical conditions for all three simulated occultation events were used. The neutral atmosphere employed this way was one selected vertical profile out of the MSISE-90 climatology, i.e., the same climatology that was used as background in the statistical optimization process. The profile chosen was co-located with the “Nice” event (63 degree N, 93 degree E; month September). This adds some interesting aspects to the interpretation of the results (section 4.3.3).

Additionally, two different receiving systems were modeled: an idealized, where observation system related errors were neglected, and a “realistic” one, which was based on the error specifications of the GRAS receiver [e.g., *GRAS-SAG*, 1998] and included the main receiving system related errors such as orbit uncertainties, receiver noise, local multi-path errors, and clock errors. Subsequently, the retrieval was performed using five different retrieval scheme settings.

The setup of the study is described in more detail in the report of *Gobiet and Kirchengast* [2002]. In the framework of this thesis it was expanded by two additional retrieval schemes. Results for no optimization (with observed profile exponentially extrapolated; section 4.1), heuristic weighting optimization, equation (4.3), inverse covariance weighting optimization without (basic IGAM-no search) and with (basic IGAM-search) background search (section 4.2), and inverse covariance weighting with enhanced background bias correction (enhanced IGAM; section 4.2). In total, 24 different scenarios were modeled (3 representative events x 4 ionization levels x 2 receiving system types), and each of these 24 scenarios evaluated using the 5 different retrieval schemes.

### 4.3.2. Large Ensemble Study Setup

Selected retrieval schemes were also tested statistically using a large ensemble of quasi-realistically simulated occultation events. In order to allow comparison to earlier results, a simulated occultation event ensemble which was originally produced in the framework of the GNSS-CLIMATCH study [*Kirchengast et al.*, 2000; *Steiner et al.*; 2001; *Foelsche et al.*; 2003] was used. It involves the simulation of a six-satellite constellation, each satellite equipped with a GRAS-type receiver. The neutral atmosphere modeling used a middle atmosphere-extended version (T42L39 resolution) of the ECHAM4 General Circulation Model [*Roeckner et al.*, 1999] with a horizontal resolution of  $\sim 2.8$  degree and 39 vertical levels up to 0.01 hPa ( $\sim 80$  km). Above about 80 km, the neutral atmosphere was extrapolated using the MSISE-90 climatology. While typical current GCM fields, including ECMWF analyses, do not reach beyond 0.1 hPa, the extend up to near the mesopause is important for the present assessment of retrieval schemes as it ensures that any search and best-fit estimates are performed at height ranges governed by the more variable GCM conditions rather than the climatological conditions. The ionosphere was modeled using the NeUoG model.

The ensemble consists of  $\sim 1000$  occultation events that characterize the northern summer/southern winter season 1997 (June, July, and August) and are evenly distributed in time and space in a latitudinal slice of the globe (see Figure 4.6). It was partitioned into 17 equal area latitude bins of 10 degree width (equatorial bin: 10 degree latitude x 15 degree longitude), each containing 50 – 60 occultation events [*Foelsche et al.*, 2003], and enables to analyze error statistics and the latitudinal dependency of errors. We used this ensemble to systematically test the performance of three different high-altitude retrieval schemes (no optimization, basic IGAM-search, and enhanced IGAM; see sections 4.1 and 4.2), with focus on the latitude-height distribution of biases.

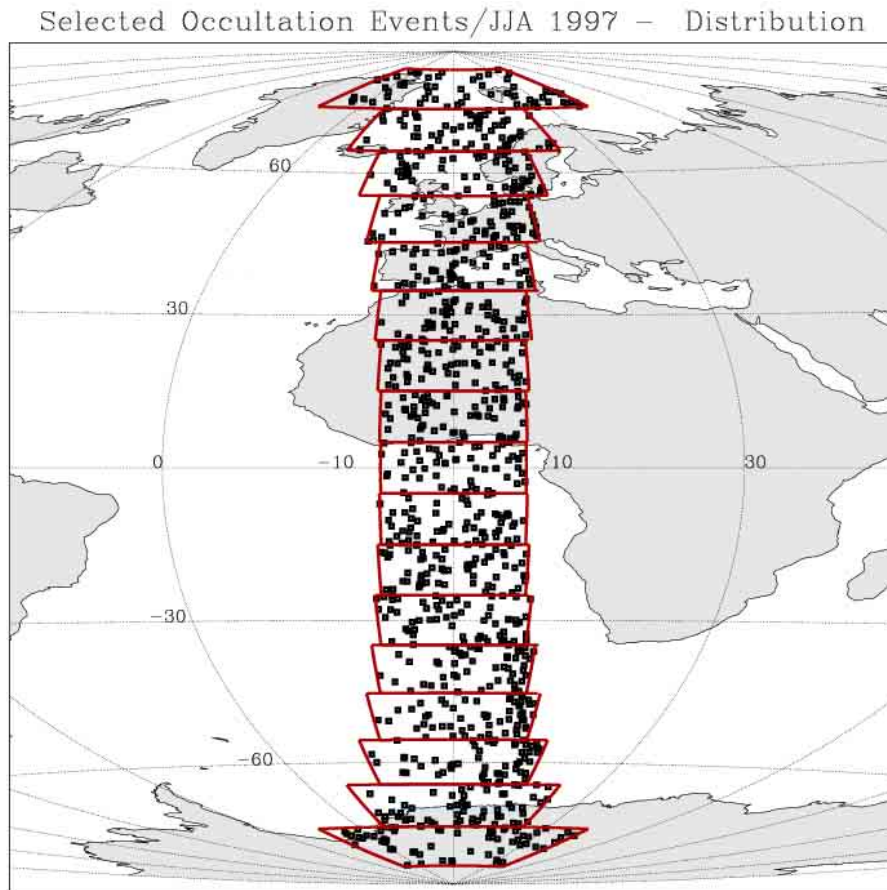


Figure 4.6: Distribution of 979 simulated occultation events comprising the validation ensemble in the large ensemble study. After: *Foelsche et al.* [2003].

### 4.3.3. Results of the Systematic Case Study

Figure 4.7 gives an overview of the performance of the no optimization retrieval and the inverse covariance weighting optimization retrieval with search in MSISE-90 applied to the 24 simulated scenarios. Each bar in Figure 4.7 represents the mean temperature error between 35 km and 45 km (“upper stratosphere bias” hereafter) of one specific scenario. At these altitudes, the RO-retrieved temperatures are heavily influenced by background information, thus the upper stratosphere bias indicates the bias in the background, or in the exponentially extrapolated bending angle profile, respectively.

The most salient result is the strong mitigation of the upper stratosphere bias by statistical optimization. Without optimization, the behavior of the retrieval above  $\sim 30$  km depends heavily on noise in the data. One and the same simulated occultation event can give different upper stratosphere biases of up to 20 K, depending on the starting value of the random number generator used in the simulation of receiver noise (not shown). Applying statistical optimization (in this case the basic IGAM scheme) strongly stabilizes the retrieval, makes it robust against random noise and residual ionospheric errors, and retains the upper stratosphere bias below 1 K in most cases.

Additionally, it is shown for the linear ionospheric correction of bending angles that neither highly asymmetric ionospheric conditions nor high ionization levels do significantly degrade the retrieval performance, especially when statistical optimization is applied, as one should expect as long as noise due to small-scale ionospheric structures is small [e.g., *Gorbunov* [2002c]; and references therein].

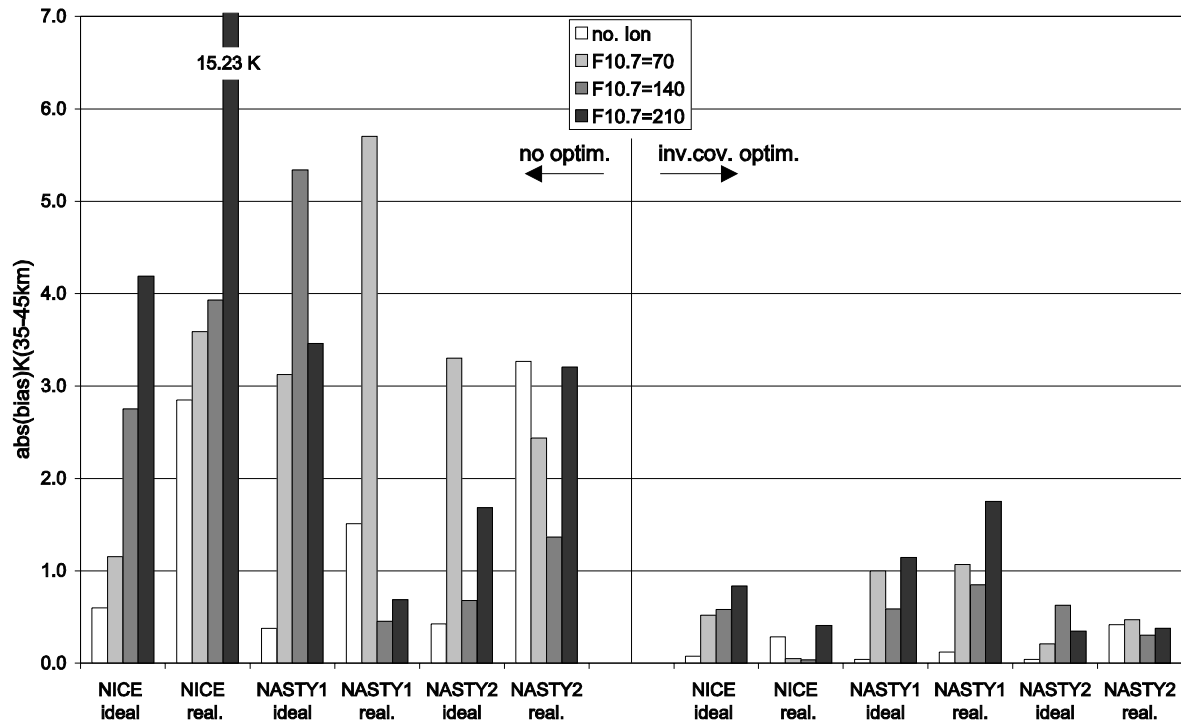


Figure 4.7: Mean error of the retrieved temperature between 35 km and 45 km (“upper stratosphere bias”) for all simulated occultation scenarios (3 events, 4 ionization levels, ideal and realistic receiving system). Left: no optimization retrieval. Right: basic IGAM-search retrieval.

A further result is the insensitivity of the statistically optimized retrieval to receiver noise: While the no optimization retrieval generally degrades as soon as receiver noise is added, the optimized retrieval keeps its performance. This effect demonstrates one of the key advantages of statistical optimization, its optimal treatment of random noise. The no optimization retrieval is over-sensitive to high altitude noise and responds to in a somewhat chaotic way. Since UBH selection and extrapolation are heavily influenced by noise, small variations in noise structure can have huge effects and random noise in the observation is often converted into a bias in the final retrieval product.

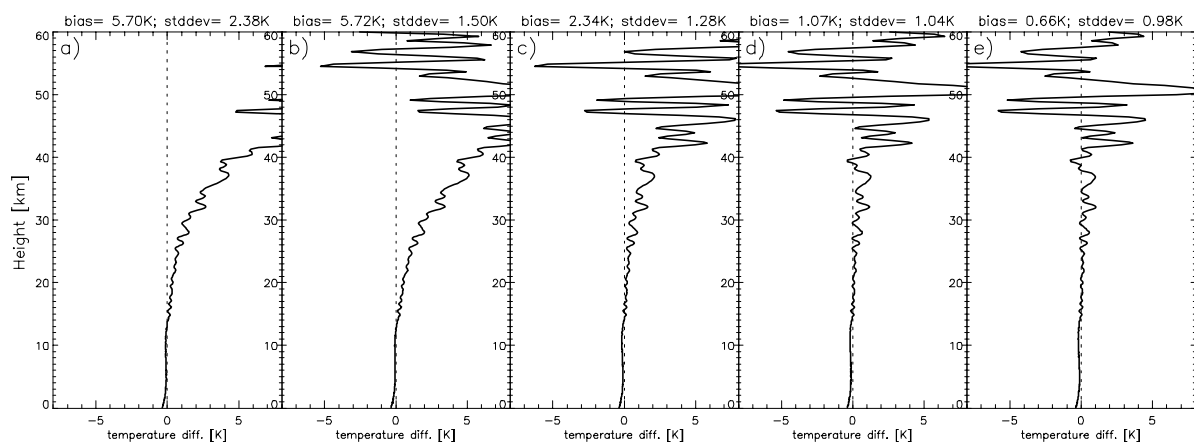


Figure 4.8: Temperature error profiles for the “Nasty 1” occultation event (asymmetric ionospheric conditions,  $F_{10.7} = 70$ , realistic receiver) retrieved with different high altitude retrieval schemes: no optimization (a), heuristic weighting optimization (b), basic IGAM-no search (c), basic IGAM-search (d), and enhanced IGAM (e).

Figure 4.8 shows the error profiles of temperature for one example occultation scenario (“Nasty 1”,  $F_{10.7} = 70$ , realistic receiving system) retrieved with five different high altitude retrieval schemes (no optimization, heuristic weighting optimization, basic IGAM-no search, basic IGAM-search, and enhanced IGAM). In this scenario, the co-located background information profile from MSISE-90 is biased, since we used a different neutral atmosphere profile (from the “Nice” event) in the forward modeling (see section 4.3.1). However, inspection shows that the background error is  $< 8\%$  in the strato- and mesosphere, which is clearly within the assumed uncertainty of  $15\% - 20\%$ . The example scenario can thus be considered representative for a real RO retrieval situation.

Figure 4.8, panels a and b (no optimization and heuristic weighting retrievals), show that errors due to deficient high altitude initialization can propagate down to below 20 km in the temperature profile. While this may be considered a “bad case”, error propagation down to  $< 30$  km will be common. Heuristic weighting optimization (panel b) stabilizes the retrieval, but it is strongly biased towards the background. The inverse covariance weighting optimization without search leads to much better results (panel c), but the temperature stays biased towards the background. The retrieval with search (panel d) is able to account for the biased background by finding an un-biased background profile in the search library. The retrieval result stays virtually unbiased up to 40 km. This demonstrates the situation, when a search library is adequate, i.e., when an unbiased profile is available in the library. In such a situation a second step of background bias reduction is not necessary and the enhanced IGAM retrieval (panel e) gives essentially the same result as the basic IGAM-search retrieval. In the example shown here (panel e), the enhanced IGAM retrieval is still slightly better than the basic retrieval with search, while in other cases it can also be slightly worse or closely the same, but never far away from the basic retrieval with search (difference in terms of upper stratosphere bias  $< 0.5$  K).

#### 4.3.4. Results of the Large Ensemble Study

The ECHAM4 model was used to create neutral atmospheric fields representing the summer season 1997 for the simulation of a large ensemble of occultation events ( $\sim 1000$  events; see section 4.3.2). In contrary to the systematic case study, this setup does not automatically ensure that unbiased background profiles are available for each observed profile since the forward model atmosphere is different from the MSISE-90 climatology used for background information. The MSISE-90 search library may thus be partially inadequate, which is a situation more realistic but also more demanding for the statistical optimization scheme.

Figure 4.9 shows latitude versus height slices of the retrieved dry temperature seasonal mean bias and standard deviation for the no optimization, basic IGAM-search, and enhanced IGAM retrieval schemes.

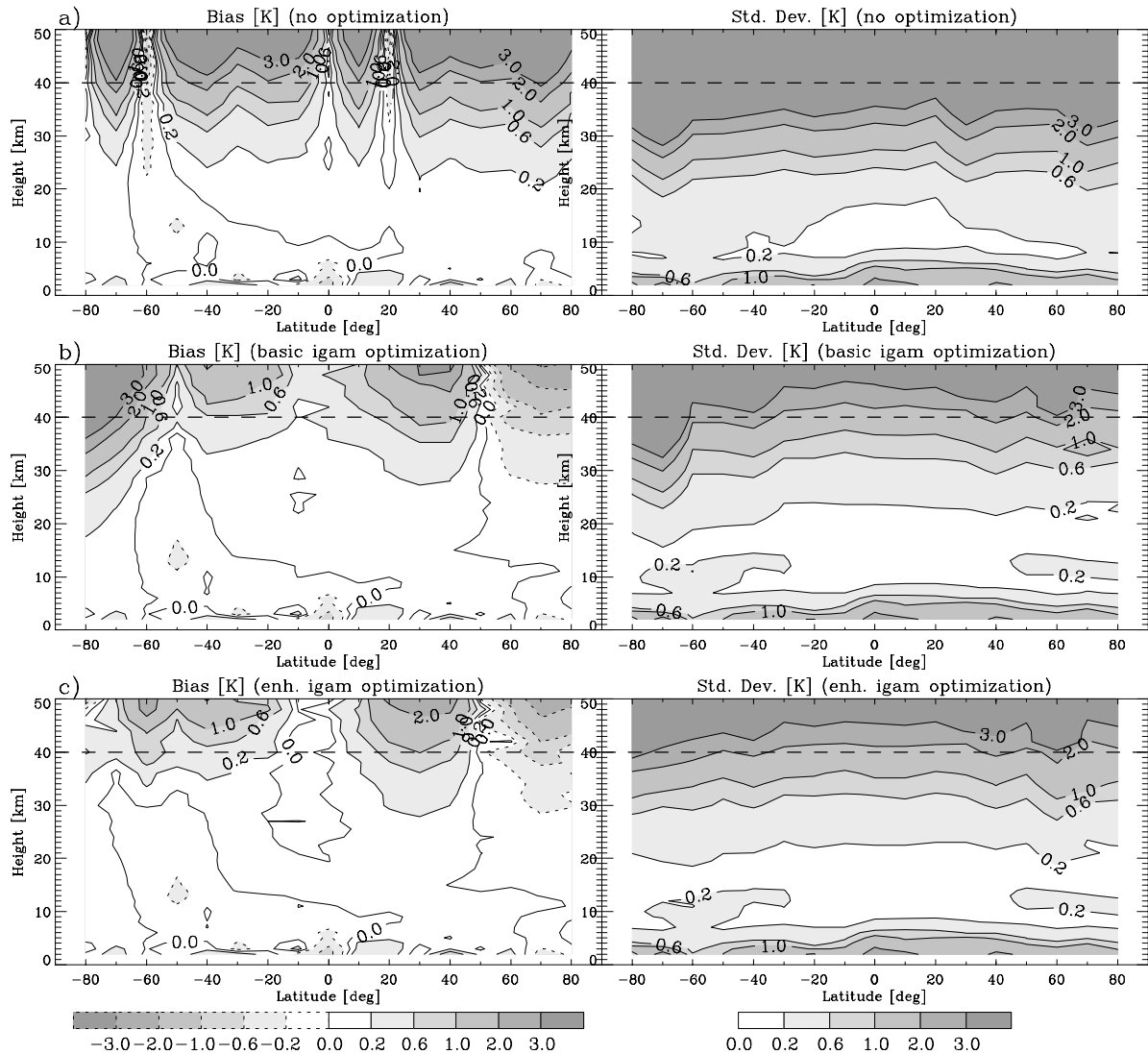


Figure 4.9: Seasonal mean bias (left) and standard deviation (right) of temperature retrieved from an ensemble of  $\sim 1000$  simulated occultation events. High altitude retrieval schemes: no optimization (a), basic IGAM-search (b), and enhanced IGAM (c).

The no optimization case (panels a) shows again a very unstable high altitude retrieval performance if the bending angle profile is simply exponentially extrapolated: The  $> 1$  K standard deviation region starts at  $\sim 25$  km, which is about 10 km lower than in the two optimization cases (panels b and c). In terms of high altitude bias this scheme is as well clearly inferior to the optimization schemes. The reasons for that have already been discussed in the previous section. Here, we demonstrate that the arguments we brought forward in the case study regarding single occultation events also apply in a statistical sense when a large ensemble of occultation events is examined and when a more realistic experimental setup is regarded.

The most salient improvement of the enhanced IGAM algorithm (panels c) over the basic IGAM-search algorithm (panels b) is the error reduction in the southern high latitude region, where the MSISE-90 search library is most inadequate. This demonstrates that the additional bias correction step of the enhanced IGAM scheme exhibits the behavior of an “emergency reserve”: In most cases, where the background library is adequate, the background bending angles are only slightly modified ( $\sim 1\%$ ) and the effect on the retrieved temperatures below 40 km is small. In the cases, however, when no unbiased background profile is found in the library, the modification reaches up to 15%, and significant improvement is achieved. For

these cases the MSISE-90 climatology is inadequate to supply profiles unbiased against the ECHAM4 model atmosphere used. The capability of the enhanced IGAM scheme to handle these conditions is important since also in case of real data existing climatologic libraries will not be able to supply adequate background profiles under all conditions.

Less salient than the improvements in the southern high latitudes, but robustly evident, is a global improvement of the retrieval quality above 30 km in terms of biases. Note that this statistical effect is rather due to better retrieval performance in individual cases than to gross retrieval enhancement as well (not shown).

#### 4.3.5. Conclusions From the Evaluation Studies

The evaluation studies showed that sensible statistical optimization of bending angles is vital to obtain results of good quality in the middle and upper stratosphere. In this context, it is shown for the linear ionospheric correction of bending angles that neither highly asymmetric ionospheric conditions nor high ionization levels do significantly degrade the retrieval performance, as one should expect as long as noise due to small-scale ionospheric structures (“ionospheric scintillations”) is small. The latter has been disregarded in this investigation; in the processing of real data it needs separate care in filtering before correction (see section 5.3).

Using statistical optimization, it is found that the retrieval performance can be significantly improved further if biases in the background information are corrected. Since the statistical optimization method fundamentally assumes unbiased errors, potential biases need to be removed before the optimization. The “enhanced IGAM scheme” incorporates an empirical background bias correction scheme that is particularly effective when background data are systematically inadequate, as was found for MSISE-90 data in the high-latitude winter atmosphere.



# 5 Developing a Robust Retrieval System for CHAMP Data – CCRv2

The retrieval schemes described in the preceding Chapter were so far applied to simulated data in the framework of a modified version of the EGOPS software. Starting from this point, a robust stand-alone retrieval system suited for application in an operational processing system for CHAMP data has been developed: the CHAMPCLIM Retrieval (CCR). The CCR-chain starts with atmospheric phase delay profiles from CHAMP (level 2 data provided by GeoForschungsZentrum Potsdam, GFZ) and returns profiles of the atmospheric parameters refractivity, density, pressure, geopotential height, dry temperature, temperature, and humidity.

In this Chapter the developments leading to the current stable version 2 of CCR (CCRv2) are described.

## 5.1. Interface to GFZ Level 2 Data and Technical Robustness

The creation of a flexible interface to the provider of CHAMP phase delay (level 2) data, the GeoForschungsZentrum (GFZ) Potsdam included data format conversion (GFZ to CCR/EGOPS format) and the modification of the retrieval algorithm's control structure. To reach maximum flexibility, the retrieval sequence in CCR is controlled by an occultation table containing the filenames of all GFZ level 2 data files to be processed. This enables to flexibly process any period or randomly selected level 2 files regardless of temporal or any other order. In consequence to the drop of a monotonous timeline inside the algorithm, the handling of date and time variables and the interface to background data had to be adapted.

After creating the interface to GFZ level 2 data, CCR was principally capable to retrieve CHAMP data using the retrieval schemes described in section 4.2 but in practice only few profiles could be processed without "repairing" input data manually in advance. Since this is not acceptable for an operational retrieval system, considerable effort was made to assure technical robustness of the algorithm. During this development phase more than 4500 CHAMP phase delay profiles were processed to assure robustness against any kind of input data including completely unphysical data, data gaps, outliers, and the like. At that stage, data was not modified in any way and we did not regard the quality of the retrieval results but only assured that CCR would not collapse from a technical point of view.

After technical robustness was reached, CCR's performance was still not comparable with results of leading RO retrieval centers like NASA's Jet Propulsion Laboratory (JPL), EUMETSAT's GRAS Satellite Application Facility, GFZ, or the University Corporation for Atmospheric Research (UCAR). Detailed inspection showed that most profiles could be retrieved properly by CCR but some were very far away from any reference data used for validation. These outliers are generally caused by corrupted or very noisy input data, most of the problems stemming from the uppermost part of the phase delay profiles. These data often led to failure of the ionospheric correction algorithm yielding negative (unphysical) ionosphere corrected bending angles and many subsequent problems in the retrieval chain like unrealistic observation error estimates and the downward propagation of severe high-altitude bending angle errors in the atmospheric profiles. For this reason, a combined strategy of

increasing the robustness against noisy data and quality control effectively sorting out unrecoverable corrupted data was developed as described in the following sections.

## 5.2. Quality Control

The quality control schemes described below are the most essential retrieval advancements compared to the retrieval schemes described in sections 4.1 and 4.2. They are strongly related to all further developments described in the subsequent sections and enable the CCR retrieval schemes to operationally cope with CHAMP data.

The quality control implemented in the CCRv2 algorithm can be subdivided into internal and external quality control. While external quality control is only applied to the retrieval results and uses background information about the atmosphere as reference, internal quality control only regards technical and consistency aspects of the data and modifies or rejects data during the retrieval process. From the data user's point of view it is important that quality control criteria are transparent and do not modify statistical properties of the "good" part of the data. Hence, it seems desirable to apply as few internal modifications of data as possible. Nevertheless, some data modifications are necessary to assure high delivery rate of the algorithm and to prevent the retrieval results from being biased towards atmospheric conditions favorable for RO retrieval performance.

In order to make the quality control mechanisms transparent for the user, suspect data is not simply rejected but flagged with a 2-digit integer value. Internal quality control affects the 1-decimal place (1, 2, ..., 9) of the quality flag while external quality control affects the 10-decimal place (10, 20, ..., 90). The overall quality flag is obtained by adding the two numbers.

### 5.2.1. Internal Quality Control

CCR applies the following internal quality control mechanisms. Depending on the findings of the internal quality control routines, data are flagged according to Table 5.1.

*Enforcement of positive phase delays.* Negative phase delays are often not related to the state of the atmosphere, but due to technical aspects of the RO receiver ('unphysical data'). In the case of CHAMP, they often indicate a known receiver clock malfunction. Therefore, negative values are replaced by 'pseudo-zero' ( $10^{-12}$ ) and subsequent quality control ensures that profiles severely disturbed by the enforcement of positive phase delays are sorted out. However, negative phase delays are not necessarily unphysical but can also be related to layers in the ionosphere that can be corrected for. In that case, it would be preferable not to artificially introduce pseudo-zero. For other RO experiments than CHAMP it might be possible to drop the enforcement of positive phase delays.

*3- $\sigma$  outlier rejection of phase delays.* Each one-second interval (in case of CHAMP 50 data points) of the phase delay profiles is checked for data points being 3 times the standard deviation away from the mean. If so, the data point is replaced by the interval's mean.

*Impact parameter consistency 1.* If impact parameters are rising with decreasing altitude for more than one second in the uppermost part of the impact parameter/bending angle profile, the entire profile is regarded as corrupt and rejected (quality flag 9).

*Impact parameter consistency 2.* If large impact parameter ambiguities occur below 15 km impact height, i.e., if the impact parameters rise by more than 0.2 km from one data point to the next downwards (for 50 Hz sampling rate), the profile is cut off. Data downwards are

regarded as non-retrievable because of receiver tracking failure or multipath conditions in the atmosphere. This check is necessary in a geometric optical retrieval as applied here. However, advanced lower tropospheric retrieval schemes based on wave optics exist and are capable of dealing with bending angle ambiguities to some degree (see section 2.4.3). Future versions of CCR will include data retrieved with one of these methods to obtain a lower mean cut-off altitude.

*Bending angle consistency.* If negative bending angles occur after ionospheric correction, these data are regarded to be unphysical and set to pseudo-zero. Pseudo-zero data above 50 km impact height and all data above are removed. If pseudo-zero data occur below 55 km (or 65 km in the “strict” mode, see section 5.3) the observation error is set to a very high value (50  $\mu$ rad) and the retrieval results are flagged to be “suspect above 25 km” (quality flag 2).

*Bending angle availability.* If the ionosphere corrected bending angle profile contains no data above 35 km or below 20 km impact height the entire profile is regarded as non-retrievable and rejected (quality flag 6).

*Consistency of estimated observation error 1.* The error of the observed bending angles is estimated from the variance of the observed profile in the impact height-interval from 65 to 80 km. If this estimation is not possible using at least 25 data points or if the estimated observation error is unrealistically small ( $< 0.5 \mu$ rad), the observation error is set to a very high value (50  $\mu$ rad) and the retrieval results are flagged to be “suspect above 25 km” (quality flag 2).

*Consistency of estimated observation error 2.* If the bias of the observed profile compared to the background profile is larger than the estimated observation error in the 65 to 85 km impact height interval or if the estimated observation error is larger than 50  $\mu$ rad, the data is regarded to be corrupt and is rejected (quality flags 7 and 8, respectively).

Table 5.1. Meaning of quality flags (QF) for internal quality control (EGOPS/CCR Version 2, June 2004).

Meaning	QF internal
No deficiencies found. Retrieval results may be used without restrictions.	0
The observation error could not be estimated from data and was set conservatively to 50 $\mu$ rad. Retrieval results may not be used above 25 km.	2
Not enough observed bending angle data available to perform statistical optimization. Retrieval results may not be used.	6
The bias (background compared to observation) is larger than estimated observation error. Retrieval results may not be used.	7
The estimated observation error is huge ( $> 50 \mu$ rad). Retrieval results may not be used.	8
The impact parameters are irrecoverably inconsistent at high altitudes. Retrieval results may not be used.	9

### 5.2.2. External Quality Control

CCR's external quality control compares the retrieval products to coinciding atmospheric profiles extracted from operational analyses of the European Centre for Medium-Range Weather Forecasts (ECMWF) in T42L60 resolution. This comparison is performed in height intervals where RO retrieval errors as well as the ECMWF analysis errors are regarded to be small and only retrieval results with deviations from reference data by far larger than the error characteristics of both dataset are rejected (outliers). This ensures that eventual errors in the reference datasets are not introduced to the statistical properties of the retrieval results.

In detail, retrieved refractivity profiles are compared to a coinciding refractivity profile extracted from ECMWF analysis in the 5 km – 35 km height interval and profiles featuring deviations larger than 10 % are rejected. Additionally, though only acting as a fallback, temperature profiles are checked in the interval between 8 km and 25 km for deviations larger than 20 K.

The external quality control criteria are listed in Table 5.2. Retrieved data not meeting the criteria are flagged as listed in Table 5.3.

Table 5.2. CCR's external quality control. Retrieval results containing data with larger deviations from the reference (operational ECMWF analyses, T42L60) than indicated by the threshold values are rejected (EGOPS/CCR Version 2, June 2004).

<b>Atmospheric Parameter</b>	<b>Height Interval</b>	<b>Threshold</b>
Refractivity	5 km – 35 km	10 %
Temperature	8 km – 25 km	20 K

Table 5.3. Meaning of quality flags (QF) for external quality control (EGOPS/CCR Version 2, June 2004).

<b>Meaning</b>	<b>QF external</b>
The temperature criterion is not met. Retrieval results may not be used.	10
The refractivity criterion is not met. Retrieval results may not be used.	20
The temperature and refractivity criteria are not met. Retrieval results may not be used.	30
No reference data is available. Retrieval results may not be used.	40
Not enough retrieved data is available to perform external quality control. Retrieval results may not be used.	50

## 5.3. Stable Ionospheric Correction

As mentioned in section 3.1.3, the original linear ionospheric correction of bending angles (equation (3.17)) cannot correct for effects of small scale structures in the ionosphere and higher order terms in the formula describing ionospheric refractivity. More than that, noise in

the  $L1$  and  $L2$  bending angles is amplified by a factor of 1.5 to 3 and technically corrupted data can lead to negative bending angles. This led to the development of an enhanced correction formula (equation (3.18)) based on smoothed bending angle profiles.

For the retrieval of simulated occultation data, the original formula is nearly as successful as the modified one, but for CHAMP data with its frequently minor data quality in high altitudes, and probably for measured RO data in general, it pays to apply the more stable algorithm.

The modified scheme described by *Hocke et al.* [2003] (equation (3.18)) provides the desired stability by low-pass filtering the  $L1$  and  $L2$  bending angles before ionosphere correction and adding the high-pass fraction of the stronger  $L1$  signal again after correction again.

Tests showed that the filter width has to be carefully selected since too broad filters introduce positive temperature biases above 30 km. Applied to CHAMP data we found, in agreement with *Hocke et al.* [2003], a 1 km boxcar filter applied to bending angles and impact parameters showing best performance.

The direct effect of the smoothed ionospheric correction is demonstrated in Figure 5.1 which shows the ionospheric corrected bending angles of 206 CHAMP profiles (measured on Jan. 1, 2003) including all outliers (black dashed lines). For comparison, the climatologic mean and standard deviation derived from the CIRA86 climatology is displayed. After the standard ionospheric correction hardly any profile contains physical information (positive bending angles) above 60 km (Figure 5.1, left panel). After smoothed correction the mean maximum altitude could be raised (Figure 5.1, right panel) which is favorable for the subsequent statistical optimization and background bias correction processes.

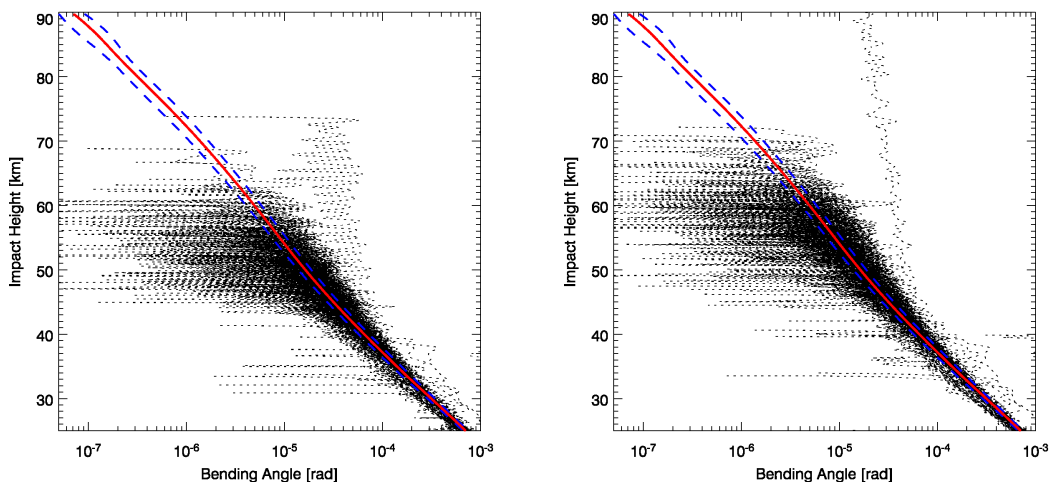


Figure 5.1: Ionospheric corrected bending angle profiles measured by CHAMP on Jan. 1, 2003. Sample-size: 206 events, no outliers were removed. The red and blue lines demonstrate the climatological mean and standard deviation, respectively (derived from CIRA86). Left panel: Standard ionospheric correction of bending angles. Right panel: Smoothed ionospheric correction of bending angles (1 km boxcar filter).

The effect of smoothed ionospheric correction on retrieved dry temperature profiles of the same CHAMP sample (Jan. 1, 2003) is demonstrated in Figure 5.2. Dry temperatures retrieved with the original (equation (3.17), upper left panel) and smoothed ionospheric correction (equation (3.18), upper middle and right panels, 1 km and 2 km boxcar filter, respectively) compared to operational ECMWF analyses are displayed showing mean difference (bold line) and standard deviation of differences (light lines). In exchange for a raised variance above 30 km, the variance in the altitude region between 15 km and 25 km is reduced and the delivery rate is raised by  $\sim 4\%$  (167 instead of 161 profiles) by applying the

1 km filter. Further broadening of the filter width to 2 km results in slightly further reduction of variance between 15 km and 25 km and yields one additional profile, but also modifies the bias above 30 km. Since our retrieval schemes aim at producing high-quality data for climate applications where bias-free data is most important, we decided to accept the slightly more pronounced variance of the 1 km filter in order to avoid high-altitude biases.

Besides the positive aspect of reducing the error standard deviation in the core RO altitude region, the main effect is a trade-off between a high delivery rate (including the danger to include some low-quality measurements resulting in high variance and potential biases at high altitudes) and restrictive external quality control.

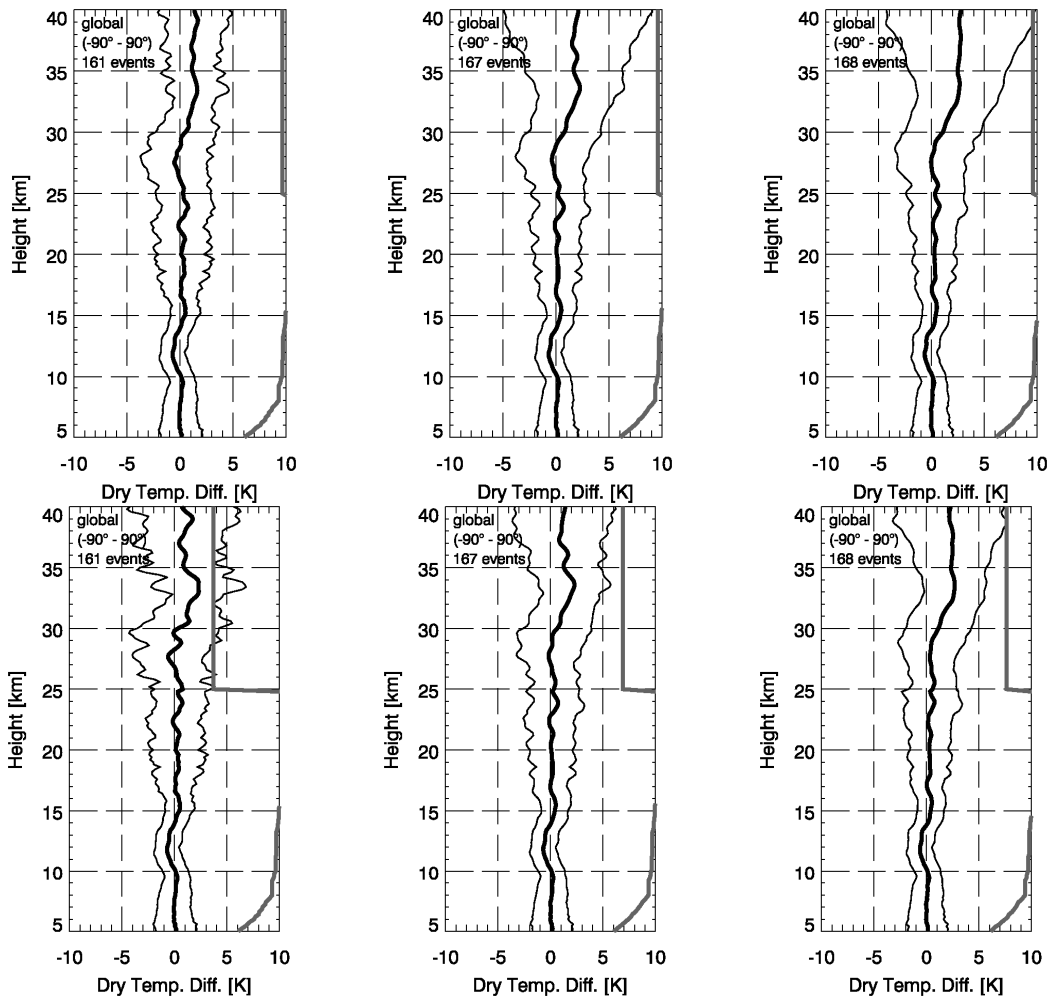


Figure 5.2: CHAMP dry temperature error statistics (Jan. 1, 2003, ~170 profiles) compared to ECMWF analyses. Bold line: bias. Light line: standard deviation. Grey line: percent number of data points contributing to each altitude's error statistic (10 K corresponds to 100 %). Upper left panel: standard ionospheric correction. Upper middle and upper right panels: smoothed ionospheric correction with 1 km and 2 km boxcar filter, respectively. Lower panels: same ionosphere correction schemes as above with stricter internal quality control for high altitude data.

If a high delivery rate and minimal systematic errors at high altitudes are not the prime objectives, broader filters combined with stricter external quality control could be applied which would result in combining low variance in the core-region with low variance at high altitudes. However, strict external quality control can introduce biases in direction of the reference data used and filters broader than 1 km are not guaranteed to operate bias-free since they interfere with scales covered by the ionospheric correction and are not recommended.

Another possibility is to carefully apply stricter internal quality control at high altitudes, i.e., to sort out more technically suspect profiles without comparing them to reference data. Figure 5.2 (lower panels) show the results of such a retrieval scheme: The same ionosphere correction schemes as in the upper panels are combined with stricter internal quality control of high altitude data (see section 5.2.1) resulting in  $\sim 25\%$  to  $60\%$  of the profiles sorted out above 25 km (quality flag 2) as indicated by the gray line. In this case, the smoothed ionosphere correction drastically increases the yield of the retrieval scheme and does not introduce additional variance above 30 km. Independent from internal quality control, this experiment as well indicates that filter widths greater than 1 km (right panel) should not be used to avoid high-altitude biases.

The current CCRv2 schemes apply moderately smoothed ionospheric correction (1 km boxcar) without strict internal high altitude quality control (Figure 5.2, upper middle panel). In applications not crucially dependent on high data density above 25 km the same scheme with stricter internal quality control (Figure 5.2, lower middle panel) is recommended.

## 5.4. Statistical Optimization of CHAMP Bending Angles

This section describes the adaptation of the IGAM statistical optimization schemes as described in section 4.2 to the retrieval of atmospheric profiles from CHAMP data and additionally the inclusion of an alternative source of background information.

### 5.4.1. Observation Error Estimation

The statistical optimization process needs an estimate about the error characteristics of the observed data. In current statistical optimization schemes most observation error estimates are based on comparisons with background information (see section 4.1). This technique is problematic and counterproductive since any large difference between background and observation, even if caused by biased background information, leads to large observation error estimates, gives the observation less weight in the statistical optimization process and overemphasizes background information, particularly when it is biased.

In the CCRv2 retrieval schemes, the observation error estimate is obtained independently from the background information by analyzing the altitudinal variance of the observed (ionosphere corrected) bending angle profile at high altitudes where the neutral atmospheric contribution to the signal is negligible.

The appropriate height interval for estimating the observation error should be above the altitude where the expected bending angle noise of CHAMP equals the bending angle caused by the neutral atmosphere. For a first estimate of the lowermost altitude applicable for this purpose, CHAMP-derived bending angle profiles are compared with profiles derived from climatology as depicted in Figure 5.1. It shows the mean (red line) and the standard deviation (blue dashed lines) of 1130 bending angle profiles derived from CIRA86 (globally equal distributed). Above some 70 km the neutral atmospheric bending angles amount less than  $\sim 10^{-6}$  rad which is approximately the lower bound for the CHAMP error resulting from instrument noise. The original interval for observation error estimation used for simulated data was 70 km – 80 km (see section 4.2). However, from CHAMP data hardly ever useful ionosphere corrected bending angles can be derived above 70 km which makes it necessary to set the interval as low as possible. Extensive empirical studies showed that an interval above 65 km still yields good results and drastically increases the number of profiles that allow

observation error estimation. For this reason we use the error estimation interval between 65 km and 80 km for CHAMP data.

Apart from that, the observation error estimates are also used for internal quality control: In the CCRv2 scheme, the main criteria to accept the error estimation is an upper (50  $\mu$ rad) and lower (0.5  $\mu$ rad) threshold value, a consistency check comparing the variance to the bias relative to the background data, and a minimum of 25 data points available for estimation. If one of these quality criteria is not met, the data is either marked as suspect at high altitudes or rejected entirely (see section 5.2 for details).

#### 5.4.2. Climatological Background Information and Bias Correction

It is crucial to use as good background information as possible in the statistical optimization process of RO retrieval. Apparently, analysis data from NWP systems describing the actual state of the atmosphere have advantages over climatologies describing the mean state at a certain location and month. However, the quality of NWP analyses at high altitudes (above  $\sim 30$  km) is still questionable due to the sparseness of adequate assimilated data at these heights. More than that, eventual biases in the analysis are not necessarily stable over long periods since NWP systems are under steady development and could possibly introduce artificial trends into the retrieval results at high altitudes.

Since the RO-retrieved profiles may later be evaluated using these analyses or even be used in the data assimilation process producing them and since, in the case of CCRv2, one major purpose of the derived datasets is to detect climate trends, it is desirable to have available model-independent retrieval results.

These considerations led to the decision to use of an independent search library for best-fit selection of background profiles (e.g., the MSISE-90 climatology) rather than coinciding NWP analysis profiles (e.g., from ECMWF operational analyses) as background information.

As described in section 4.2, two background correction steps are applied to bending angle profiles derived from the MSISE-90 climatology in advance to their use as background information in order to reduce eventual biases. This method proved to be successful applied to realistically simulated RO data. Applied to CHAMP data the methods had to be adjusted since the low quality of CHAMP high-altitude data enforced to use lower intervals found for searching and adjusting the background data. The intervals used for simulated data (45 km – 65 km and 55 km – 75 km) are not applicable and had to be displaced to 35 km – 55 km and 45 km – 65 km, respectively. The displacement had a negative effect on the performance of the background bias correction scheme and, no significant performance-gain compared to the usage of non-modified co-located profiles from climatology can be reached when retrieving from CHAMP data. However, the scheme (addressed as IGAM/MSIS scheme thereafter) still easily competes with other schemes using climatologic background data (see section 6.1.2 and *Gobiet et al.*, [2004]) and has a good potential when applied to data from RO missions using further developed RO receivers that yield better data quality at high altitudes like GRACE, GRAS/MetOp, or COSMIC. Additionally, improved search libraries (compared to the currently available MSISE-90 and CIRA-86 climatologies) should be built in the future (e.g., from middle atmosphere LIDAR data or ENVISAT/MIPAS data) in order to ensure that adequate background profiles are available for all the diverse strato- and mesosphere conditions of different locations and seasons.

### 5.4.3. ECMWF Background Information

As explained above, depending on the data user's intention it might be desirable to have available RO-data independent from NWP-models like data from the IGAM/MSIS retrieval scheme. On the other hand, it might be favorable to use the best-possible temperature data available and to accept a slight dependency from NWP-models at high altitudes. For these users, a second retrieval mode has been developed (addressed as IGAM/ECMWF scheme thereafter) using bending angle profiles derived from atmospheric fields of ECMWF operational analyses as background information in the statistical optimization process. This scheme is very similar to the IGAM/MSIS scheme with the main difference of making direct use of ECMWF data without any modification (no background bias correction).

The Integrated Forecasting System (IFS) of ECMWF operationally produces analyses 00, 06, 12, and 18 UT every day by dynamically combining a short-range forecast with observational data with a four-dimensional variational data assimilation system [ECMWF, 2004]. We used these analyses in their full vertical resolution (L60, 60 levels up to  $\sim 0.1$  hPa) but with reduced horizontal resolution (T42,  $\sim 300$  km grid spacing), roughly corresponding to the horizontal resolution of RO data. For each RO profile, a coinciding atmospheric profile were extracted from the analysis, i.e., spatially interpolated to the locations of the RO data using the nearest time layer of the analysis and expanded upwards to 120 km altitude using the MSISE-90 climatology. From this combined profile, a bending angle profile was derived and used in the statistical optimization process of the IGAM/ECMWF retrieval scheme (see Table 5.4 for details).

## 5.5. CHAMPCLIM Retrieval (CRR) Version 2 Overview

In order to give an overview, the main features of the two CCRv2 retrieval schemes are listed in Table 5.4. It also provides some additional information on aspects of the retrieval scheme not discussed in this thesis since they cannot be regarded as advancements but rather as state-of-the-art procedures and are equally implemented in the EGOPS software [Kirchengast *et al.*, 2002] which is the basis for CCRv2.

Table 5.4: Overview of the IGAM/MSIS and IGAM/ECMWF CHAMP-RO retrieval schemes (CCR Version 2, June 2004).

	IGAM/MSIS	IGAM/ECMWF
<b>Outlier Rejection</b>	“ $3\sigma$ ” outlier rejection on phase delays based on one second samples (50 data points)	Like IGAM/MSIS
<b>Phase Smoothing</b>	Smoothing of phase delay profiles using regularization (third order norm, regularization parameter = $10^5$ [Syndergaard, 1999]).	Like IGAM/MSIS
<b>Bending Angle Retrieval</b>	Geometric optics retrieval.	Like IGAM/MSIS
<b>Ionospheric Correction</b>	Linear combination of bending angles [Vorob'ev and Krasil'nikova, 1994]. Correction is applied to low-pass filtered bending angles (1 km sliding average), L1 high-pass contribution is added after correction [Hocke et al., 2003]. L2 bending angles < 15 km derived via L1-L2 extrapolation.	Like IGAM/MSIS
<b>Statistical Optimization of Bending Angles</b>	Statistical optimization of bending angles between 30 and 120 km. Vertical correlated background (corr. length $L = 6$ km) and observation ( $L = 1$ km) errors. Observation error estimated from observed variance of observed profile > 65 km. Background error: 15 %. Background information: MSISE-90 [Hedin, 1991] best fit-profile, bias corrected [Gobiet and Kirchengast, 2004].	Like IGAM/MSIS, but co-located bending angle profile derived from ECMWF operational analysis (T42L60) as background information (above ~ 60 km: MSISE-90). No further pre-processing.
<b>Hydrostatic Integral Initialization</b>	No initialization below 120 km. At 120 km: pressure = pressure(MSISE-90).	Like IGAM/MSIS
<b>Humidity Retrieval</b>	Optional: 1DVar using ECMWF analyses as background.	Like IGAM/MSIS
<b>Lower Cut-Off Altitude</b>	The lowermost altitude where data is delivered is set to the altitude where severe impact parameter ambiguities occur (impact parameter increase > 0.2 km from one data point to the next downwards).	Like IGAM/MSIS
<b>External Quality Control</b>	Refractivity 5 km – 35 km: $\Delta N/N < 10$ %; Temperature 8 km – 25 km: $\Delta T < 20$ K. Reference: ECMWF operational analysis (T42L60).	Like IGAM/MSIS

# 6 CHAMP Retrieval Performance Studies

This Chapter gives a summary of several studies for validating the IGAM/MSIS and IGAM/ECMWF retrieval schemes (CCRv2, see Chapter 5) applied to CHAMP data (GFZ level 2 data, version 2). Section 6.1 describes the validation methods applied and the CHAMP and correlative datasets involved, followed by the presentation of the results in section 6.2.

First, the CCRv2 results are compared to the operational CHAMP products from GFZ to give a basic view on the consistency of both schemes. Further, the CCRv2 results are compared to independent data, namely coinciding profiles derived from operational analysis fields of ECMWF and coinciding temperature profiles from ENVISAT instruments (MIPAS and GOMOS). Main results of this Chapter have been published by *Gobiet et al.* [2004].

## 6.1. Validation Setup and Data

### 6.1.1. Methodology

The validation is based on profiles of dry temperature and refractivity. These profiles were retrieved from operational GFZ CHAMP level 2 data (phase delays) with the CCRv2 schemes as described in Chapter 5 and validated against different correlative data as described in sections 6.1.2, 6.1.5 and 6.1.6. Three different validation periods were selected according to the availability of correlative data (see sections 6.1.2 to 6.1.4). For each period CCR and correlative data was collected forming a statistical sample (“validation sample”) from which error statistics derived.

The methodology is based on simple statistics of difference profiles. For each corresponding pair of profiles in a validation sample ( $\mathbf{x}^{CCR}$ , being an IGAM-retrieved CHAMP profile and  $\mathbf{x}^{refer}$  being a correlative profile), a difference profile is derived ( $\Delta\mathbf{x} = \mathbf{x}^{CCR} - \mathbf{x}^{refer}$ ). The calculation of the sample mean of  $\Delta\mathbf{x}$  leads to the bias profile  $\mathbf{b}$  and the subtraction of the bias from each difference profile in the sample gives the centered (or unbiased) difference profiles  $\Delta\mathbf{x}^{center}$ . From all centered difference profiles in one validation sample the variance profile (mean squared centered difference at each height level) and its square root, the standard deviation profile  $\mathbf{s}$  is derived.

All comparisons in this Chapter are based on biases  $\mathbf{b}$  and the standard deviations  $\mathbf{s}$ . These parameters were chosen since they separate the systematic from the random part of the more frequently used root mean square error which is a measure of the total error.

Temperature differences are given in absolute quantities [K] and refractivity differences in terms of relative quantities [%]. The relative quantities are derived by dividing the absolute quantities by the mean of the reference profiles  $\mathbf{x}^{refer}$  at each altitude and are indicated by the subscript *rel*.

In addition to the analysis of the total validation samples containing globally distributed measurements, the samples were separated into three sub-samples, each containing measurements from one of three latitude bands in order to account for the different mean state of the atmosphere and ionosphere at different latitudes: low latitudes ( $-30$  degree to  $+30$  degree), mid latitudes ( $\pm 30$  degree to  $\pm 60$  degree), and high latitudes ( $\pm 60$  degree to  $\pm 90$  degree). This is particularly important to judge the success of the ionospheric correction scheme which faces a more complicated situation at low latitudes (equatorial anomaly, spherical asymmetry, small-scale structures causing scintillations in the RO signal) than at mid- and high latitudes. Additionally, the dry and stable conditions in the high-latitude troposphere represent much easier conditions for the RO retrieval than the moist and highly variable equatorial troposphere.

Based on this latitudinal classification, the CHAMP occultation events are roughly equally distributed. However, if one refers to equal areas, the measurement density near the poles is much higher than at low latitudes. This is due to the high inclination ( $i = 87$  degree) of the CHAMP orbit relative to the equatorial plane and results in an increased observational coverage at high latitudes (Figure 6.1 to Figure 6.3).

### 6.1.2. CHAMP Data for the CCR – GFZ Retrieval Intercomparison

For the intercomparison of GFZ- and IGAM-derived (CCR version 2) atmospheric profiles from CHAMP, a 7-day period (January 1 – 7, 2003) was selected. The IGAM/MSIS and IGAM/ECMWF retrieval schemes applied to the GFZ level 2 data of this period yielded 1197 and 1187 atmospheric profiles, respectively, which corresponds to about 170 profiles per day on average. The geographical distribution of the occultation events is depicted in Figure 6.1. These profiles were compared to the operational GFZ atmospheric profiles (level 3, retrieval version 4 [e.g., Wickert *et al.*, 2004b]).

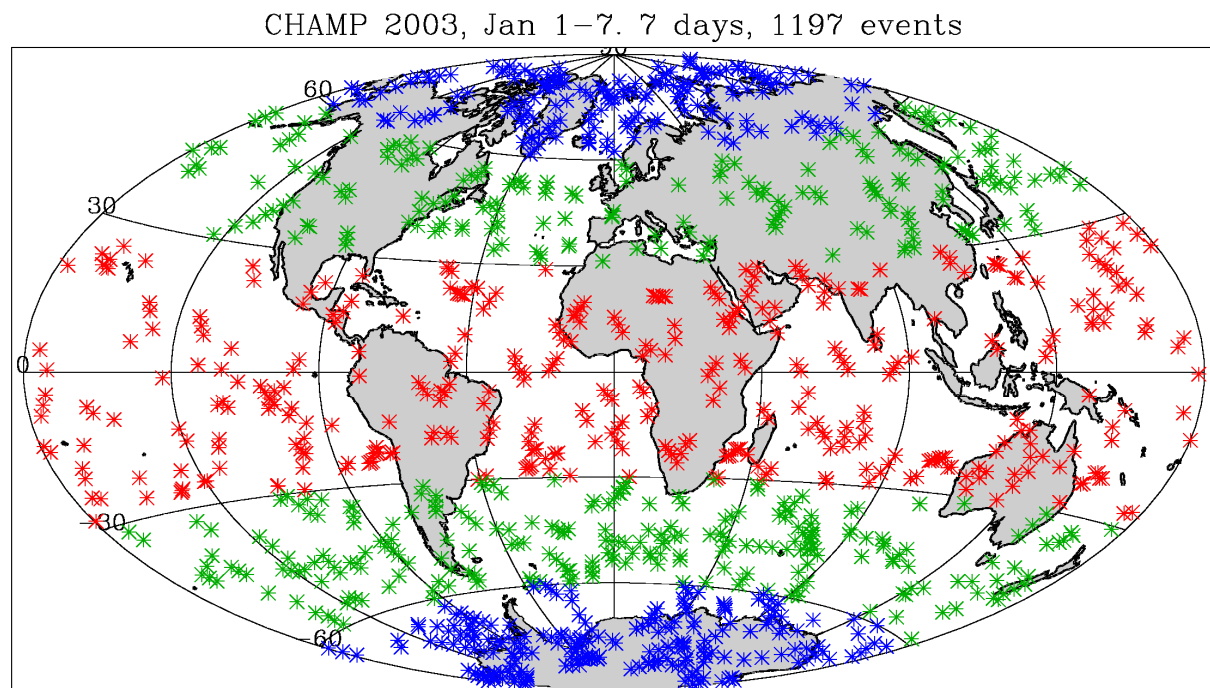


Figure 6.1: CHAMP data retrieved by IGAM for retrieval intercomparison with GFZ with the IGAM/MSIS scheme: Geographical distribution of 1197 atmospheric profiles (Jan 1 – 7, 2003). The whole sample is separated into three latitude bands: low (red,  $-30$  degree to  $+30$  degree, 377 events), middle (green,  $\pm 30$  degree to  $\pm 60$  degree, 436 events), and high (blue,  $\pm 60$  degree to  $\pm 90$  degree, 384 events).

The operational GFZ retrieval yields 1250 atmospheric profiles for the validation period. Due to different data treatment and different quality control schemes at IGAM and GFZ, the IGAM-retrieved profiles do not simply form a sub-set of the GFZ-results, but also contain events that are not available in the GFZ-set and vice versa. As a result, only the intersection of these sets, 1136 events for the IGAM/MSIS retrieval, and 1130 events for the IGAM/ECMWF retrieval, were available for comparison. The results are presented in section 6.2.1.

### 6.1.3. CHAMP Data for Comparison with ECMWF Analyses

For a first comparison of CCR results with operational ECMWF analyses the same CHAMP data sample as described in the previous section was used (Jan 1 – 7, 2003). Since there were no restrictions in the availability of ECMWF-data, all IGAM-retrieved CHAMP profiles of this period were compared to ECMWF analyses (1187 for IGAM/ECMWF and 1197 for IGAM/MSIS, see Figure 6.1). The results of this comparison are presented in section 6.2.2.

Further comparisons with ECMWF analyses focusing on climatologies derived from a large ensemble of CCRv2 results and aiming at finding deficiencies in the ECMWF analyses are available in Chapter 7.

### 6.1.4. CHAMP Data for Comparison with MIPAS and GOMOS

CHAMP 2002, Sep 8,12,14–28, Oct 11–13. 20 days, 3160 events.

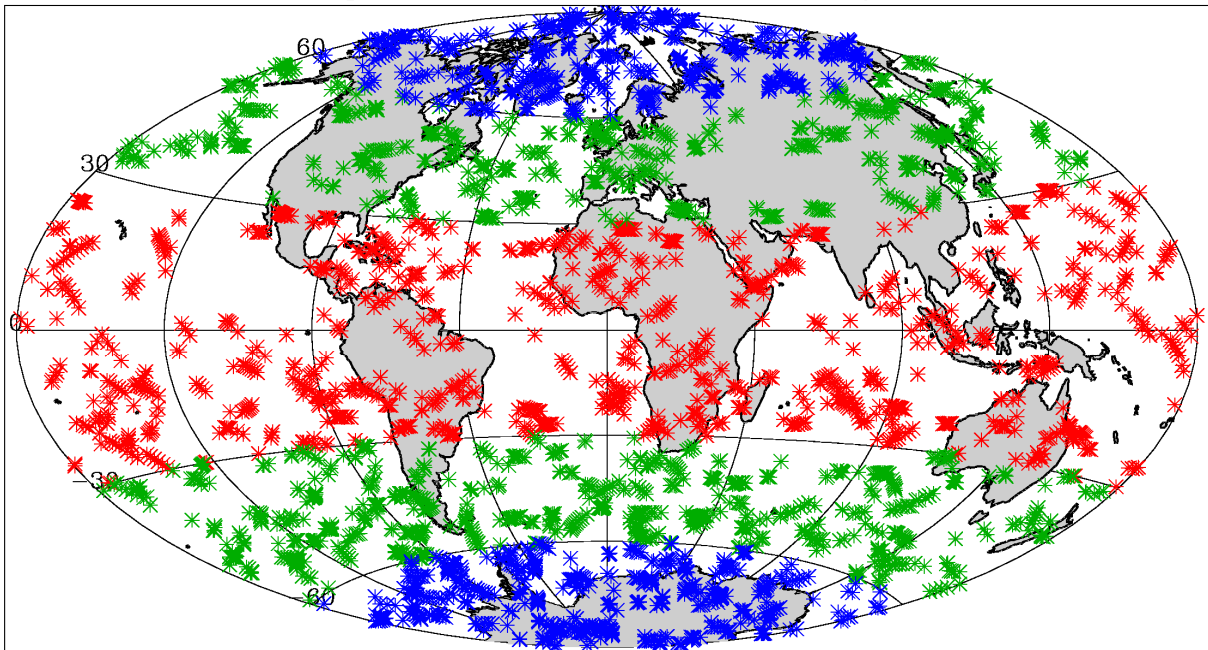


Figure 6.2: CHAMP data retrieved by IGAM with the IGAM/ECMWF retrieval scheme for comparison with MIPAS: Distribution of 3160 temperature profiles (Sep 8, 12, 14 – 28, Oct 11 – 13, 2002). The whole sample is separated into three latitude bands: low (red, – 30 degree to + 30 degree, 984 events), middle (green,  $\pm$  30 degree to  $\pm$  60 degree, 1222 events), and high (blue,  $\pm$  60 degree to  $\pm$  90 degree, 954 events).

The study periods for the CHAMP – MIPAS and CHAMP – GOMOS comparisons were restricted by the availability of data from those two ENVISAT instruments (see section 6.1.6 for a description of the ENVISAT datasets). For the MIPAS-study, a 20-day ensemble of CHAMP data from September and October 2002 (Sep 8, Sep 12, Sep 14 – 28, Oct 11 – 13) was used, which corresponds to the MIPAS data availability in this period. The total ensemble consists of 3161 (IGAM/MSIS) or 3160 CHAMP occultation events (IGAM/ECMWF, see Figure 6.2), respectively, which corresponds to  $\sim 160$  events per day on average.

For the GOMOS-study, an 11-day subset of the ensemble shown in Figure 6.2 was used (Sep 20 – 27, Oct 11 – 13) corresponding to the GOMOS data availability. The ensemble consists of 1689 (IGAM/MSIS) or 1798 CHAMP occultation events (IGAM/ECMWF, see Figure 6.3), respectively which corresponds to  $\sim 160$  events per day on average. The results of both comparison studies are presented in section 6.2.2.

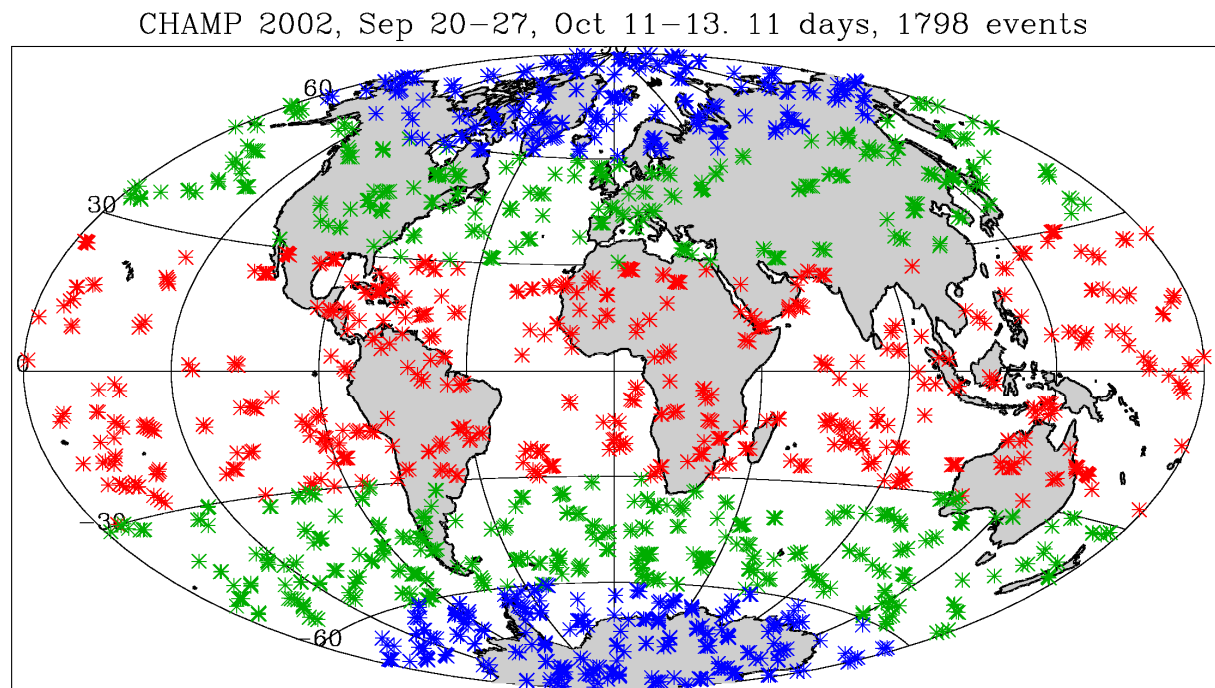


Figure 6.3: CHAMP data retrieved by IGAM with the IGAM/ECMWF retrieval scheme for comparison with GOMOS: Distribution of 1798 temperature profiles (Sep 20 – 28, Oct 11 – 13, 2002). The whole sample is separated into three latitude bands: low (red,  $-30$  degree to  $+30$  degree, 573 events), middle (green,  $\pm 30$  degree to  $\pm 60$  degree, 684 events), and high (blue,  $\pm 60$  degree to  $\pm 90$  degree, 541 events).

### 6.1.5. ECMWF Correlative Data

The first correlative dataset used to validate CCR, the operational CHAMP results from GFZ, has already been described in section 6.1.2. Besides that, a second correlative dataset was extracted from operational ECMWF analyses. Vertical profiles of temperature and refractivity interpolated to the mean tangent point latitude and longitude of the CHAMP occultation event were extracted from the nearest analysis time layer of the 6-hourly operational ECMWF analyses, i.e., the time delay between the CHAMP- and the ECMWF-profile is less than 3 hours in any case. The analysis fields were retrieved from ECMWF on a Gaussian grid corresponding to the T42L60 spectral resolution, i.e., on a grid containing  $128 \times 64$  horizontal grid cells and 60 altitude layers. The horizontal ECMWF-resolution ( $\sim 300$  km) roughly corresponds to the horizontal resolution of RO atmospheric profiles and

the vertical ECMWF-resolution of 60 levels up to 0.1 hPa is coarser than the RO resolution which has to be regarded in the interpretation of the results.

#### 6.1.6. ENVISAT/MIPAS and ENVISAT/GOMOS Correlative Data

In March 2002, the European Space Agency (ESA) launched ENVISAT, a polar-orbiting Earth observation satellite which provides measurements of the atmosphere, ocean, land, and ice. It was put into a sun-synchronous orbit of 98.5 degree inclination which results in a global coverage and higher observational density at the poles than at the equator. The platform carries ten instruments, amongst those GOMOS, MIPAS and SCIAMACHY are dedicated to the observation of the Earth's atmosphere. The main objective of these instruments is to monitor the chemical composition of the atmosphere but they are also capable of measuring fundamental physical parameters like density and temperature.

Temperature profiles from MIPAS and GOMOS are utilized for comparison with CCRv2 results in this thesis. For this purpose, we defined CHAMP and ENVISAT profiles to be coinciding and thus comparable if they are less than 300 km and 3 hours apart from each other using the simplification of fixed mean latitudes and longitudes of the observed profiles.

The Michelson Interferometer for Passive Atmospheric Sounding (MIPAS) is a Fourier transform spectrometer for the measurement of high-resolution gaseous emission spectra at the Earth's limb. Thermal emissions in the infrared are very sensitive to temperature changes and MIPAS is therefore able to measure precise temperature profiles. The MIPAS temperatures used for this study were produced by the Institut für Meteorologie und Klimaforschung (IMK) in Karlsruhe (IMK product version V1.0). Details on the MIPAS retrieval can be found in the articles of *von Clarmann et al.* [2003a] and *von Clarmann et al.* [2003b]. ECMWF analyses are used as an initial guess in the iterative MIPAS retrieval process, but not as background constraint as in the IGAM/ECMWF CHAMP retrieval. MIPAS temperatures can therefore be regarded as largely independent from ECMWF data. Regarding the measurement resolution, MIPAS is dedicated to distribute atmospheric profiles from 6 km – 70 km altitude with a vertical resolution of 3 km and a horizontal resolution between 300 km and 500 km along track. Due to the sensitivity of the measurement principle to clouds, the number of available measurements per day varies from several tens to low hundreds [*Wang et al.*, 2004].

The MIPAS-temperature profiles used for comparison with CHAMP profiles in this study are taken from 20 days in September and October 2002 (Sep 8, 12, 14 – 28, Oct 11 – 13, see Figure 6.4) and are near-equally distributed in space, except for an increased observational density near the poles.

Out of the 3160 CHAMP and 6561 MIPAS profiles, 184 profiles could be identified as coincidences, most of them occurring at high latitudes. The sparser observational density of both, CHAMP and MIPAS, at low latitudes becomes especially obvious when combining both data sets. Only 16 coincidences took place at low latitudes compared to 41 at mid latitudes and 124 at high latitudes (Figure 6.5). The CCRv2 – MIPAS comparison results are presented in Section 6.2.2.

ENVISAT/MIPAS 2002, Sep 8,12,14–28, Oct 11–13. 20 days, 6561 events.

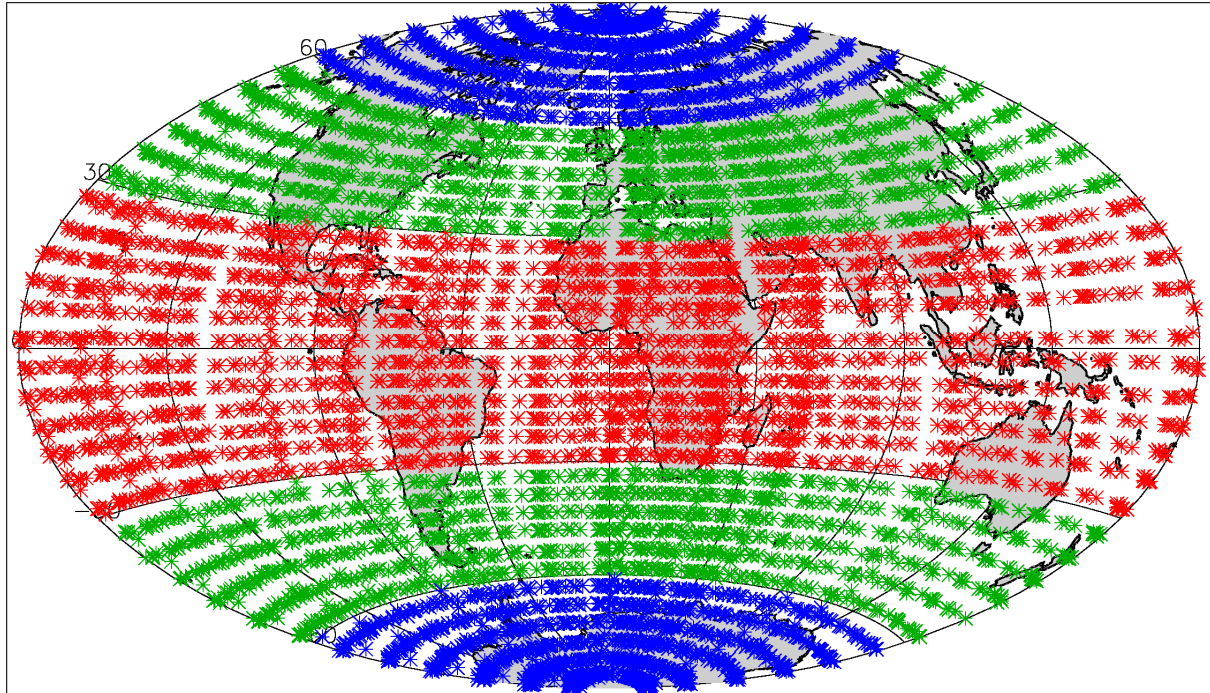


Figure 6.4: Distribution of 6561 temperature profiles retrieved by IMK (product version 1.0) from operational ESA level 1b MIPAS data. Period: Sep 8, 12, 14–28, Oct 11–13, 2002. The whole sample is separated into three latitude bands: low (red,  $-30$  degree to  $+30$  degree, 2118 events), middle (green,  $\pm 30$  degree to  $\pm 60$  degree, 2151 events), and high (blue,  $\pm 60$  degree to  $\pm 90$  degree, 2292 events).

CHAMP–MIPAS coincidences. 2002, Sep 8,12,14–28, Oct 11–13. 184 events

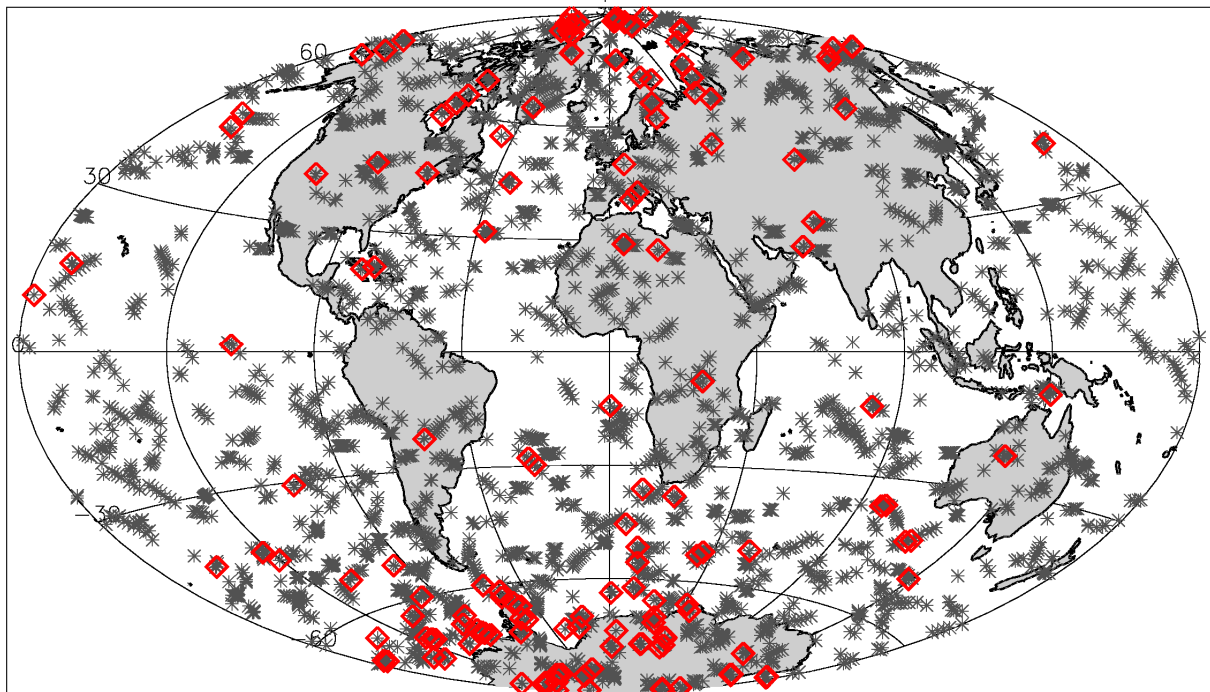


Figure 6.5: Distribution of 3160 CHAMP temperature profiles (grey asterisks) in the period Sep 8, 12, 14–28, Oct 11–13, 2002 and 184 coinciding MIPAS events out of the ensemble 6561 events show in Fig. 3.5 (red diamonds). Coincidence criteria: 300 km / 3 hrs.

The Global Ozone Monitoring by Occultation of Stars instrument (GOMOS) exploits stellar occultation (i.e., the information carried by a star's light when it is modified during its travel through the Earth's atmosphere as the star sets behind the horizon) in the ultraviolet, visible and the near infrared spectral region. The major objective of GOMOS is monitoring of upper tropospheric, stratospheric, and mesospheric ozone, i.e., in the altitude range between 15 km and 120 km. GOMOS is additionally equipped with two fast photometers sampling simultaneously the star flux at two wavelengths (around 490 nm and 675 nm) with a frequency of 1 kHz in order to correct for scintillations in the recorded star spectra. By measuring the time-shift between the "blue" and the "red" photometer, it is possible to determine bending angles caused by density variations of the atmosphere. These bending angles allow for the retrieval of atmospheric temperatures quite similar to the RO retrieval. A preliminary algorithm to derive these "high resolution temperature profiles" (HRTTP) was developed by Service d'Aéronomie du CNRS, France. It has been implemented into the GOMOS processing chain, and will be evaluated by comparison with CHAMP-RO temperature profiles in this study (Section 6.2.2).

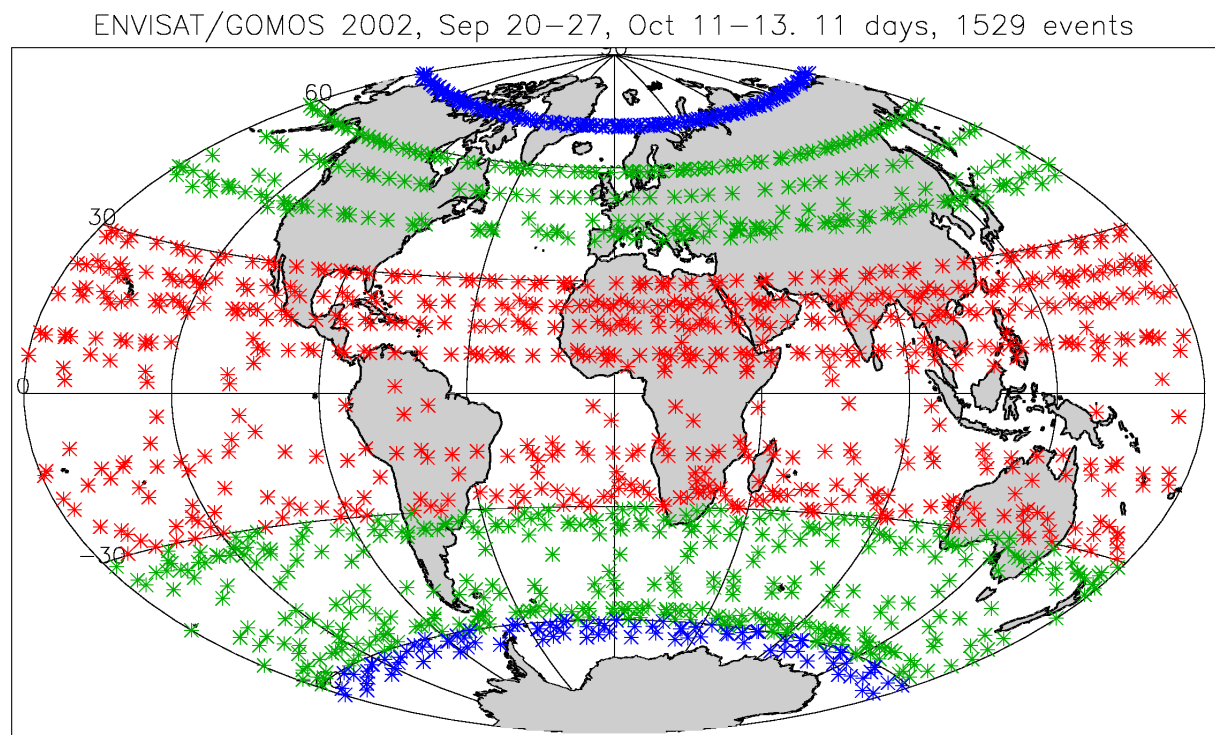


Figure 6.6: Distribution of 1529 high resolution temperature profiles retrieved from GOMOS data. Period: Sep 20 – 27, Oct 11 – 13, 2002. The whole sample is separated into three latitude bands: low (red, - 30 degree to + 30 degree, 644 events), middle (green,  $\pm 30$  degree to  $\pm 60$  degree, 625 events), and high (blue,  $\pm 60$  degree to  $\pm 90$  degree, 260 events).

In addition to the HRTTP-retrieval, a temperature retrieval based on bending angles profiles extracted from GOMOS star tracker data (SFA/SATU) is under development at IGAM [Retscher *et al.*, 2004]. These data products present the movement of the instrument's CCD-detector. The star image is kept inside the CCD with a sampling rate of 100 Hz and errors of 10  $\mu$ rad from the central position. Once the bending angle profile and accompanying impact parameters are available, an inverse Abel transform can be applied in a similar way as in the RO retrieval to retrieve atmospheric parameters. First preliminary results of this retrieval algorithm are evaluated against CCR temperature profiles in Section 6.2.2.

The GOMOS/HRTP and GOMOS/IGAM profiles used for comparison with CHAMP profiles are taken from an 11 days period in September and October 2002 (Sep 24 – 27, Oct 11 – 13, see Figure 6.6). Out of the 1592 GOMOS profiles and 1798 CHAMP RO profiles recorded in this period, 32 and 20 coinciding events for the GOMOS/HRTP- and GOMOS/IGAM-retrieval, respectively, were identified using the same coincidence criteria as in the MIPAS study (300 km/3 hrs). Again, most of the coincidences can be found in the high-latitude region (see Figure 6.7).

CHAMP–GOMOS coincidences. 2002, Sep 20–27, Oct 11–13. 32 events

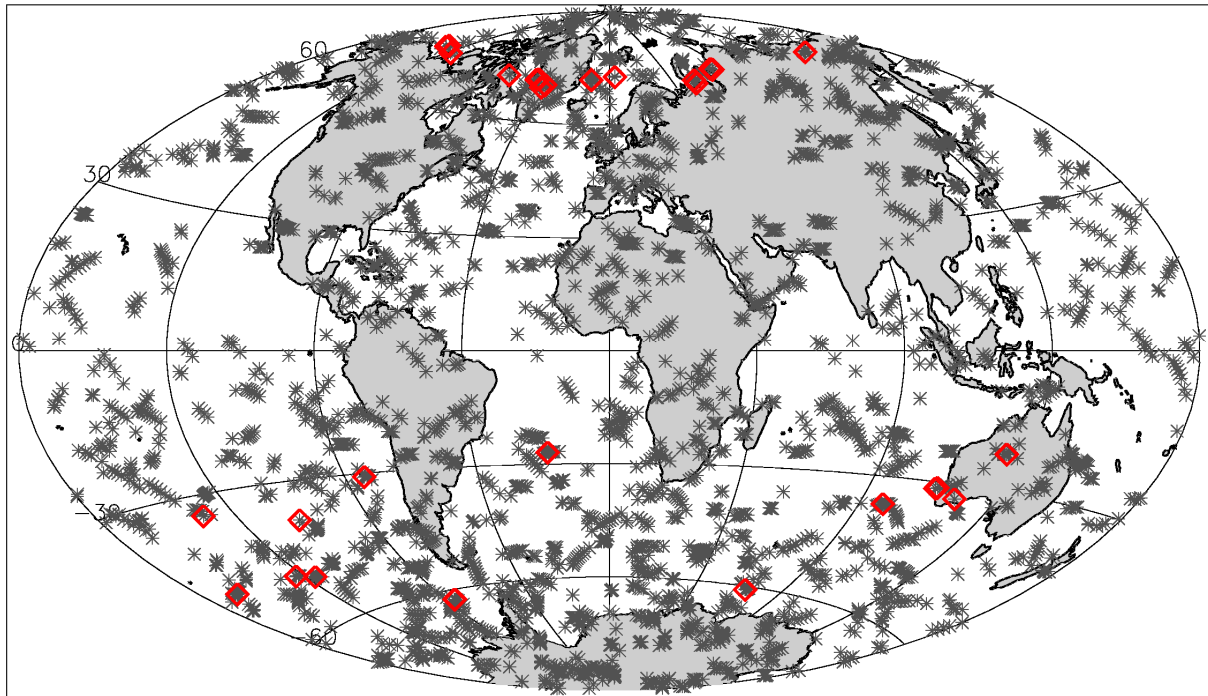


Figure 6.7: Distribution of 1798 CHAMP temperature profiles (grey asterisks) from the period Sep 20 – 27, Oct 11 – 13, 2002 and 32 coinciding GOMOS events out of the ensemble of 1529 events show in Fig. 3.8 (red diamonds). Coincidence criteria: 300 km / 3 hrs.

## 6.2. Validation Results

### 6.2.1. IGAM – GFZ Retrieval Intercomparison

In a retrieval intercomparison study (i.e., the comparison of different retrieval schemes applied to the same set of data), no representation errors occur and no measurement errors occurring in the measurement chain before the retrieval starts can be analyzed, but since the retrieval schemes are applied to real CHAMP, all “real world” noise, even those that could not be simulated in retrieval validation study in section 4.3 like small-scale structures in the ionosphere, are included here. This study is an important consistency-check for CCRv2 under realistic conditions and additionally allows to focus on the differences between the IGAM- and GFZ-retrieval schemes.

Refractivity and temperature profiles from CCR are compared to the GFZ operational results. Since GFZ does not deliver atmospheric profiles from CHAMP above 35 km, the validation could not be performed up to 40 km as in the other comparisons presented in this Chapter.

### Refractivity

Figure 6.8 and Figure 6.9 show the relative bias  $\mathbf{b}_{rel}$  (bold line) and rel. bias  $\pm$  rel. standard deviation profiles  $\mathbf{b}_{rel} \pm \mathbf{s}_{rel}$  (light lines) of refractivity retrieved with the CCRv2 schemes (IGAM/MSIS and IGAM/ECMWF) relative to GFZ operational retrieval results (CCRv2 – GFZ) for the global ensemble (left panel) and for the latitudinal separated ensembles in the three following panels.

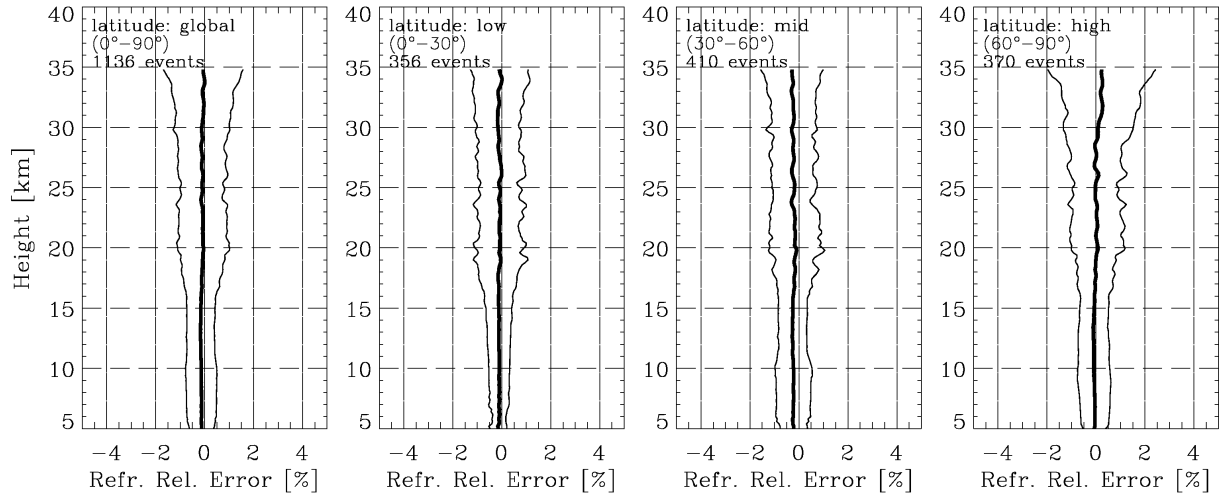


Figure 6.8: Relative bias  $\mathbf{b}_{rel}$  (bold) and rel. bias  $\pm$  rel. standard deviation profiles  $\mathbf{b}_{rel} \pm \mathbf{s}_{rel}$  (light) of refractivity retrieved from CHAMP level 2 data with the IGAM/MSIS scheme relative to operational GFZ (version 4) results. Left panel: global ensemble (1136 occultation events), middle-left panel: low-latitude ensemble (356 events), middle-right panel: mid-latitude ensemble (410 events), right panel: high-latitude ensemble (370 events).

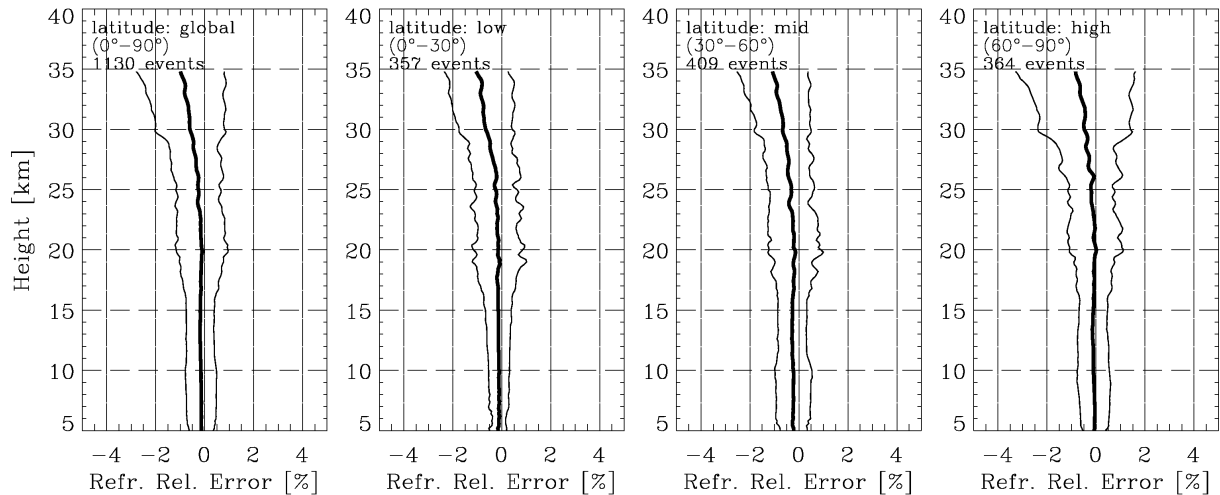


Figure 6.9: Relative bias  $\mathbf{b}_{rel}$  (bold) and rel. bias  $\pm$  rel. standard deviation profiles  $\mathbf{b}_{rel} \pm \mathbf{s}_{rel}$  (light) of refractivity retrieved from CHAMP level 2 data with the IGAM/ECMWF scheme relative to operational GFZ (version 4) results. Left panel: global ensemble (1130 occultation events), middle-left panel: low-latitude ensemble (352 events), middle-right panel: mid-latitude ensemble (409 events), right panel: high-latitude ensemble (364 events).

Both CCR retrieval schemes are, compared to GFZ, virtually bias-free below 25 km in all latitude bands (a slight bias of some  $-0.2\%$  exists in the mid-latitude sample). Above 25 km IGAM/ECMWF shows an increasing negative bias relative to GFZ approaching  $-1\%$  at 35 km. IGAM/MSIS stays in accordance with GFZ even above 25 km.  $s_{rel}$  amounts  $\sim 0.5\%$

below 16 km and  $\sim 1.1\%$  above that up to  $\sim 33$  km in the IGAM/MSIS case and up to  $\sim 30$  km in the IGAM/ECMWF case. An additional increase above 33 (30) km is due to data in the high-latitude sample.

### Temperature

Figure 6.10 and Figure 6.11 show the  $\mathbf{b}$  and  $\mathbf{b} \pm \mathbf{s}$  profiles of dry temperature retrieved with the IGAM/MSIS and the IGAM/ECMWF schemes, respectively, compared to GFZ operational retrieval results.

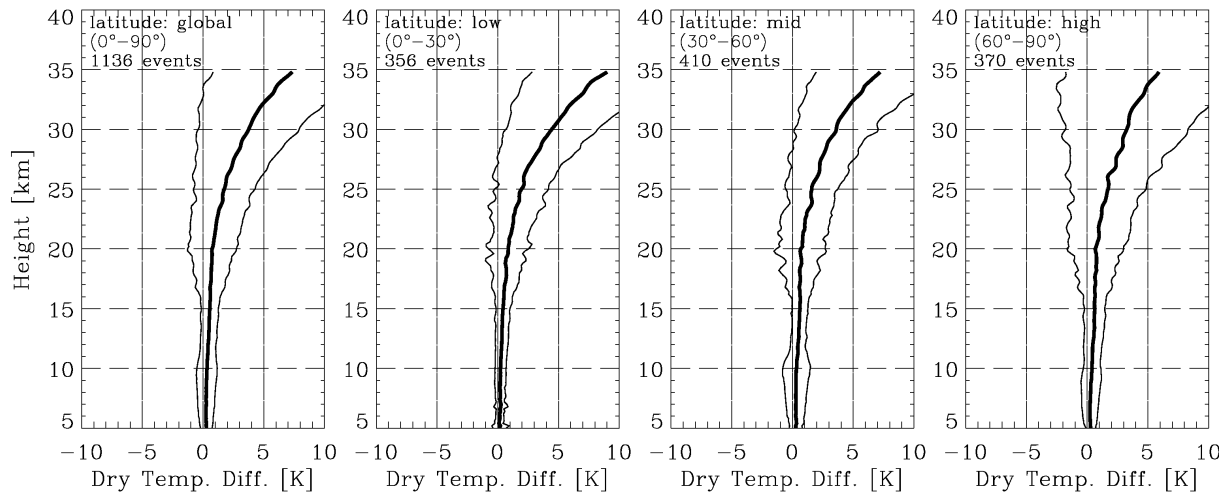


Figure 6.10: Bias  $\mathbf{b}$  (bold) and bias  $\pm$  standard deviation profiles  $\mathbf{b} \pm \mathbf{s}$  (light) of dry temperature retrieved from CHAMP level 2 data with the IGAM/MSIS scheme relative to operational GFZ (version 4) results. Left panel: global ensemble (1136 occultation events), middle-left panel: low-latitude ensemble (356 events), middle-right panel: mid-latitude ensemble (410 events), right panel: high-latitude ensemble (370 events).

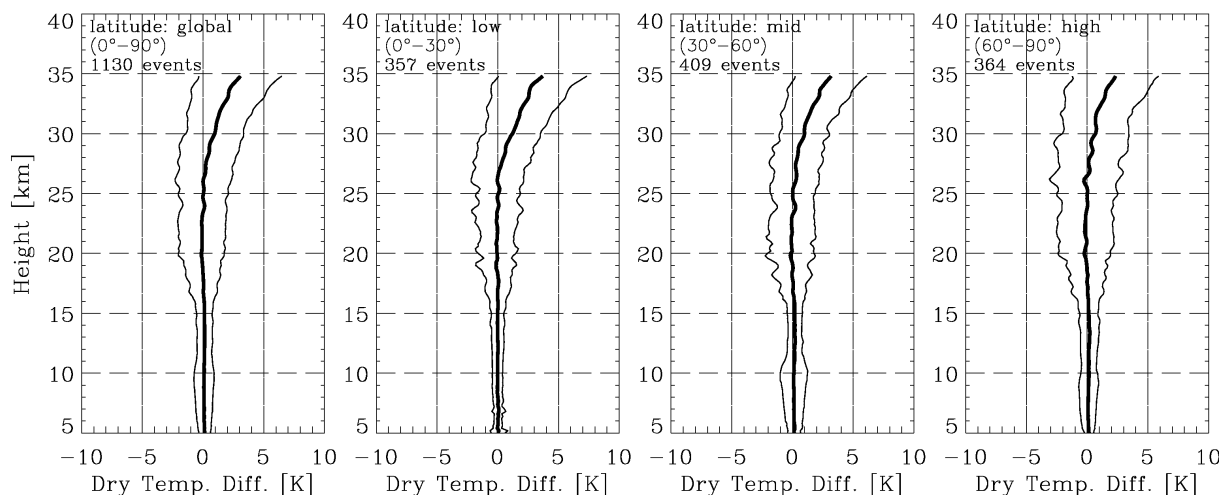


Figure 6.11: Bias  $\mathbf{b}$  (bold) and bias  $\pm$  standard deviation profiles  $\mathbf{b} \pm \mathbf{s}$  (light) of dry temperature retrieved from CHAMP level 2 data with the IGAM/ECMWF scheme relative to operational GFZ (version 4) results. Left panel: global ensemble (1130 occultation events), middle-left panel: low-latitude ensemble (352 events), middle-right panel: mid-latitude ensemble (409 events), right panel: high-latitude ensemble (364 events).

The IGAM/MSIS dry temperatures in the global ensemble are virtually unbiased relative to the GFZ results between 5 and 15 km, slightly positive biased ( $< 1$  K) between 15 and 20 km

and severely positive biased above that, starting with 1 K at  $\sim 21$  km and increasing to 7 K at 35 km. In opposition to that, the IGAM/ECMWF temperatures are unbiased up to 27 km relative to the GFZ dry temperatures. Above 27 km, a positive bias increasing up to 3 K at 35 km occurs. The standard deviations amount to  $\sim 0.5$  K below 16 km in both cases and increase up to 6 K and 3 K at 35 km, respectively. Except from slight variations, the description of the global ensemble applies to the latitudinal separated ensembles as well.

### Interpretation of the IGAM-GFZ Intercomparison Results

The behavior of the IGAM-biases relative to GFZ can be explained by different background information used and by the different methods of integrating these data into the retrieval. Most striking is the fact that the refractivity bias seems to be inconsistent with the temperature bias. While, on refractivity level, the IGAM/MSIS scheme is unbiased at high altitudes and the IGAM/ECMWF scheme is biased, on temperature level IGAM/MSIS scheme is heavily biased and the IGAM/ECMWF scheme only slightly biased.

This seeming inconsistency can be explained when the use of background information in the GFZ retrieval scheme is examined more closely: Similar to IGAM/MSIS GFZ uses MSIS bending angles and a statistical optimization approach to optimize observed bending angle profiles. In the sample analyzed here, both optimization schemes are unbiased relative to each other (which doesn't mean that they are unbiased relative to the atmospheric conditions). Apparently, in this case, the quality of the background dataset is more important than details of the optimization scheme like the bias correction in CCRv2. Since the only difference between IGAM/MSIS and IGAM/ECMWF is the way the bending angles are optimized this is clearly the reason for the bias relative to GFZ (and at the same time to IGAM/MSIS). A major difference between CCR and GFZ retrieval shows up in the temperature comparison where IGAM/MSIS and GFZ are heavily biased relative to each other. The reason for this is that IGAM/MSIS doesn't use any further background information after optimization of bending angles, but GFZ initializes the hydrostatic integral with information extracted from operational ECMWF analyses at 43 km. This also explains why IGAM/ECMWF is closer to GFZ on temperature level.

The double utilization of background information from two different sources in the GFZ scheme clearly overemphasizes background information because in the optimization of bending angles, observed and background information are, according to their error definitions, ideally combined yielding the most likely combination. Any further addition of background information yields less likely and background-biased results. Further on, the use of three sources of information also increases the sources of errors and makes it more difficult to trace back retrieval errors to their origin. The inconsistency described is not a feature that is only found in the GFZ retrieval scheme but the general practice in all RO retrieval schemes the author is aware of. Problems with the application of data from such retrieval schemes can arise when both, temperature and refractivity, are used because these two datasets are not physically consistent with each other.

At this point, no empirical evidence for the absolute quality of the results of any scheme is given (see sections 6.2.2 for such studies) but methodological objections are raised against the "traditional" approach of initializing the hydrostatic integral.

One significant result of this intercomparison is the standard deviation "jump" at 16 km. Other validation studies [e.g., Wickert *et al.*, 2004c] imply that the major part of the variation between 16 km and 30 km is due to increased variance in the CCRv2 data set. Tests showed that stronger removal of vertical fluctuations of bending angles during the ionospheric correction procedure as described by Hocke *et al.* [2003] (see section 5.3) can reduce the standard deviation, but introduces a positive temperature bias above 30 km. Since the IGAM retrieval schemes are aiming to produce high-quality data for climate applications where bias-free data is most important, we decided to accept a more pronounced variance in the data set

in order to avoid biases. If maximum data yield at high altitudes is not the most important issue, the variance can also be reduced using stricter internal quality control as described in section 5.3.

### 6.2.2. Validation with Independent Data Sources

When comparing CHAMP occultation data with independent data sources, the derived error estimates represent a combined estimate of the observation errors of both instruments (or the ECMWF model error, respectively) and of the representation error. The representation error stems from the spatial distance and the time delay between two observations, the limited horizontal resolution of limb-viewing remote sensing methods, and the limited spatial and temporal model resolution in ECMWF analyses.

Additionally, the comparison of differently orientated slant profiles with each other or with vertical ECMWF-derived profiles can cause representation errors. In general, the average zenith angle of the tangent point trajectory of RO profiles near the Earth's surface is about 85 degree. This fact and other representation errors become important in the lower troposphere, below  $\sim 7$  km, where high horizontal variability frequently occurs [Foelsche and Kirchengast, 2004a; 2004b; Syndergaard *et al.* 2003]. Since we will not interpret results in the lower troposphere, this aspect of the representation error is negligible here. The representation error due to different vertical resolution of the compared profiles can not be neglected, however.

#### ECMWF-NWP analyses

The refractivity profile relative error statistics of the CCRv2 schemes, both compared to coinciding ECMWF analyses, are shown in Figure 6.12 and Figure 6.13. In these figures,  $\mathbf{b}_{rel}$  (bold line) and  $\mathbf{b}_{rel} \pm \mathbf{s}_{rel}$  profiles (light lines) are depicted.

It must be noted that for the IGAM/MSIS retrieval ECMWF-analyses can be regarded as independent validation data. The IGAM/ECMWF retrieval is not independent from ECMWF at high altitudes since ECMWF data are used as background information in the statistical optimization process. Therefore, the comparison of IGAM/ECMWF retrieved refractivities with ECMWF analyses can not be regarded as a strict validation. However, the influence of the two very different sources of background information used in a very different way in the retrieval (MSISE-90 climatology as a search library of representative states of the atmosphere, and co-located ECMWF analyses, respectively) can be compared this way.

In the IGAM/MSIS retrieval,  $\mathbf{b}_{rel}$  oscillates around  $-0.4\%$  below 25 km in the global, as well as in the mid- and high latitude ensembles, while it ranges from  $-0.75\%$  to  $0\%$  in low latitudes. In all ensembles, especially in the global mean,  $\mathbf{b}_{rel}$  approaches  $0\%$  in the 25 km – 35 km range and drastically increases to levels  $> 3\%$  above that.  $\mathbf{s}_{rel}$  stays below  $1\%$  at 5 – 20 (18) km height in mid- and high (low) latitudes and in the global mean, varies around  $1.2\%$  up to 32 km and increases above that to levels  $> 3\%$  in all ensembles.

Below 25 km the IGAM/ECMWF scheme performs very similar than IGAM/MSIS but the negative refractivity bias of some  $-0.4\%$  reaches up to 35 km nearly constantly. Since the IGAM/ECMWF retrieval results are optimized towards the ECMWF analyses at high altitudes (the transition height from background-dominated to observation-dominated lies at some 50 km in the refractivity profile), we can not conclude that the IGAM/MSIS retrieval performs better between 25 and 35 km where the bias disappears. Quite contrary, the negative refractivity bias seems to be constant with height (as represented in the IGAM/ECMWF results) and only masked by the declining data quality above 25 km in the case of IGAM/MSIS. This height-constant bias is probably caused by a not yet clearly identified inconsistency in the altitude allocation of either the retrieved, or the reference data. A similar bias compared to ECMWF analyses, at least up to 25 km (above it might be masked by other

errors as well), can be found in the RO-derived refractivities of other leading institutions in the field of RO-retrieval (GFZ, Danish Meteorological Institute (DMI); [Steiner, 2004; Wickert et al., 2004c; Beyerle et al., 2004]).

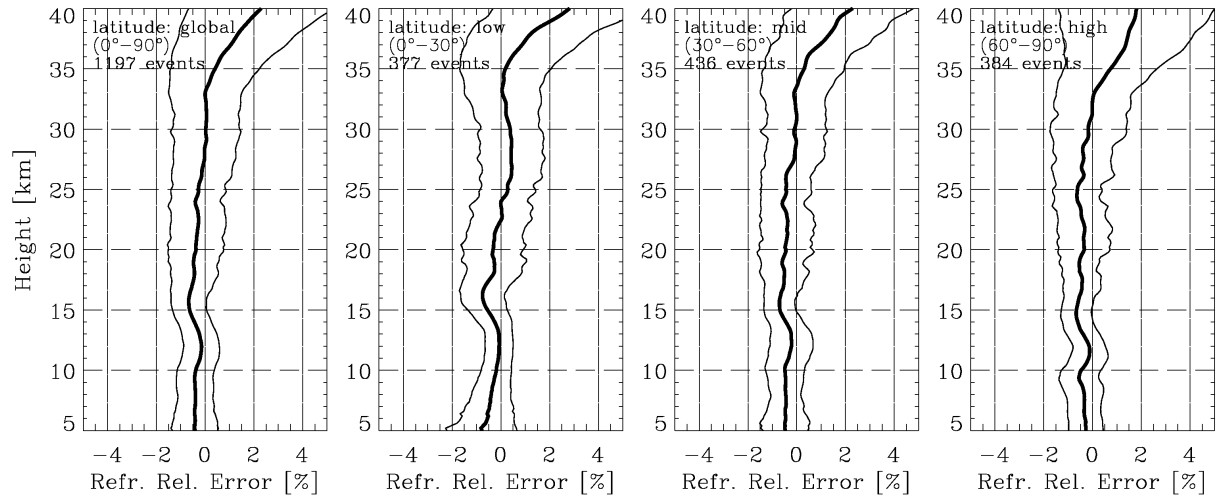


Figure 6.12: Relative bias  $\mathbf{b}_{rel}$  (bold) and rel. bias  $\pm$  rel. standard deviation profiles  $\mathbf{b}_{rel} \pm \mathbf{s}_{rel}$  (light) of refractivity retrieved from CHAMP level 2 data with the IGAM/MSIS scheme relative to data derived from coinciding ECMWF operational analyses. Left panel: global ensemble (1197 occultation events), middle-left panel: low-latitude ensemble (377 events), middle-right panel: mid-latitude ensemble (436 events), right panel: high-latitude ensemble (384 events).

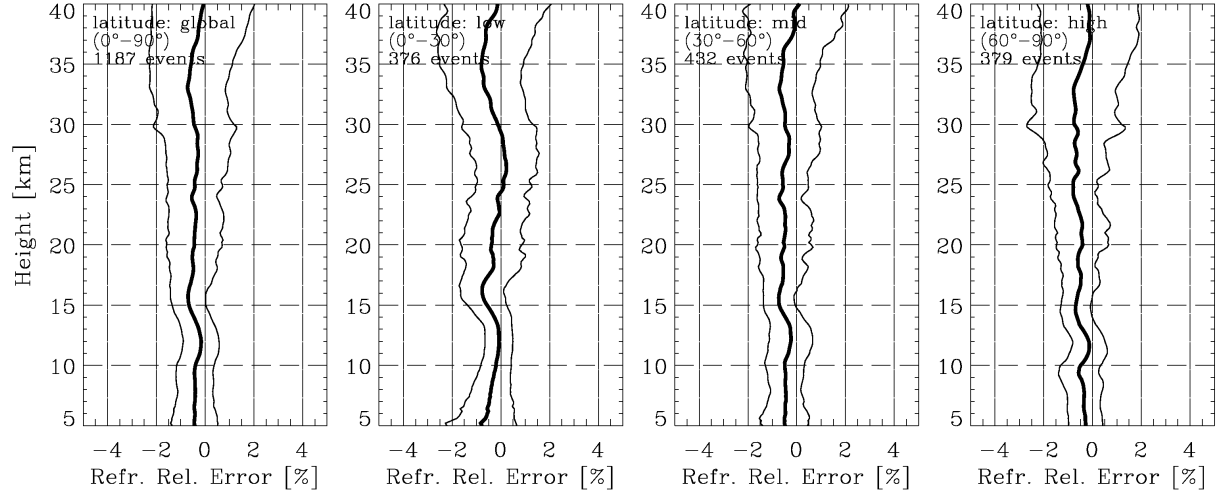


Figure 6.13: Relative bias  $\mathbf{b}_{rel}$  (bold) and rel. bias  $\pm$  rel. standard deviation profiles  $\mathbf{b}_{rel} \pm \mathbf{s}_{rel}$  (light) of refractivity retrieved from CHAMP level 2 data with the IGAM/ECMWF scheme relative to data derived from co-located ECMWF operational analyses. Left panel: global ensemble (1187 occultation events), middle-left panel: low-latitude ensemble (376 events), middle-right panel: mid-latitude ensemble (432 events), right panel: high-latitude ensemble (379 events).

The comparison of the bias profiles of both IGAM retrieval schemes indicates that the refractivity profiles derived by the IGAM/ECMWF scheme are virtually background-independent and, apart from the minor height-constant bias mentioned before, unbiased below 35 km. The same conclusion can be drawn for the IGAM/MSIS results below 25 km and, if biases in the order of 0.1 % are acceptable, below 35 km. Above 35 km, the IGAM/MSIS results can not be regarded to yield useful observed information. The IGAM/ECMWF results

might be useful up to higher altitudes, but no clear conclusions about that can be drawn from this comparison.

A further salient feature in Figure 6.12 and Figure 6.13 is the wave-shaped structure in the bias profile between 10 km and 20 km that is present in all ensembles regardless of the retrieval scheme applied. This structure is clearly not a particular feature of the CCRv2 retrieval schemes (see, e.g., CCRv2 – GFZ comparison), can also be found in the temperature bias profiles the altitude of the tropopause (see next subsection) and is rather related to ECMWF than to RO data retrieval quality as will be discussed in section 7.3.

Figure 6.14 and Figure 6.15 show  $\mathbf{b}$  and  $\mathbf{b} \pm \mathbf{s}$  profiles of dry temperature retrieved with the IGAM/MSIS and the IGAM/ECMWF schemes, respectively, with respect to ECMWF analysis profiles. The IGAM/MSIS temperature error statistics in the global ensemble show qualitatively similar features as the error statistics relative to the GFZ-operational dry temperatures: Virtually no bias between 5 km and 15 km, a positive bias  $< 1$  K between 15 km and 20 km and a positive bias above that height, starting with 1 K at  $\sim 20$  km and increasing to 6 K at 35 km. The IGAM/ECMWF dry temperatures are unbiased up to  $\sim 30$  km. Above, a warm bias of about 1.5 K occurs. The standard deviations amount to 1 K – 2 K below 16 km and increase up to  $\sim 2.5$  K in 25 km in both cases. Above that, the IGAM/MSIS standard deviation increases drastically while the IGAM/ECMWF values stay below 3 K up to 35 km. Except for slight variations, the description of the global ensemble applies to the latitudinal separated ensembles as well.

The strong warm high-altitude bias of the IGAM/MSIS dry temperatures compared to co-located ECMWF temperatures (as well as compared to the GFZ dry temperatures) shows that this retrieval scheme, applied to CHAMP data yields biased results in the order of 1 K and bigger above 20 km. This shows that the background bias correction algorithm involved is not fully effective when applied to CHAMP data. It was demonstrated in the previous section that IGAM/MSIS is, in terms of refractivity biases, equally successful than the GFZ scheme. The obvious worse performance on temperature level shows that this quality on refractivity level is not sufficient for the retrieval of temperatures above 15 km to 20 km without adding additional background information. In the case of GFZ, ECMWF temperatures are added to retain satisfying quality which is not the case in the IGAM/MSIS retrieval.

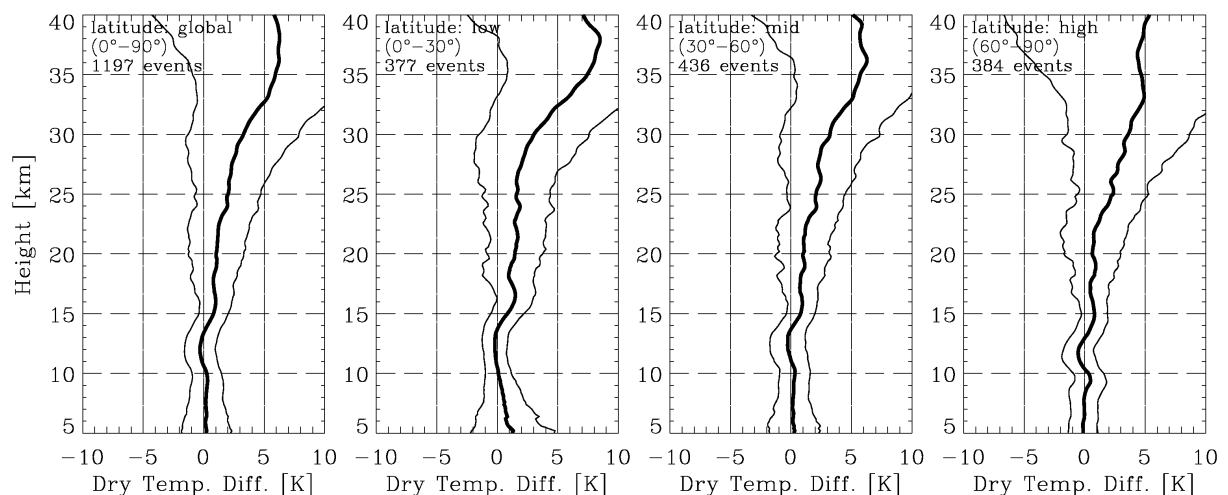


Figure 6.14: Bias  $\mathbf{b}$  (bold) and bias  $\pm$  standard deviation profiles  $\mathbf{b} \pm \mathbf{s}$  (light) of dry temperature retrieved from CHAMP level 2 data with the IGAM/MSIS scheme relative to temperatures derived from co-located ECMWF operational analyses. Left panel: global ensemble (1197 occultation events), middle-left panel: low-latitude ensemble (377 events), middle-right panel: mid-latitude ensemble (436 events), right panel: high-latitude ensemble (384 events).

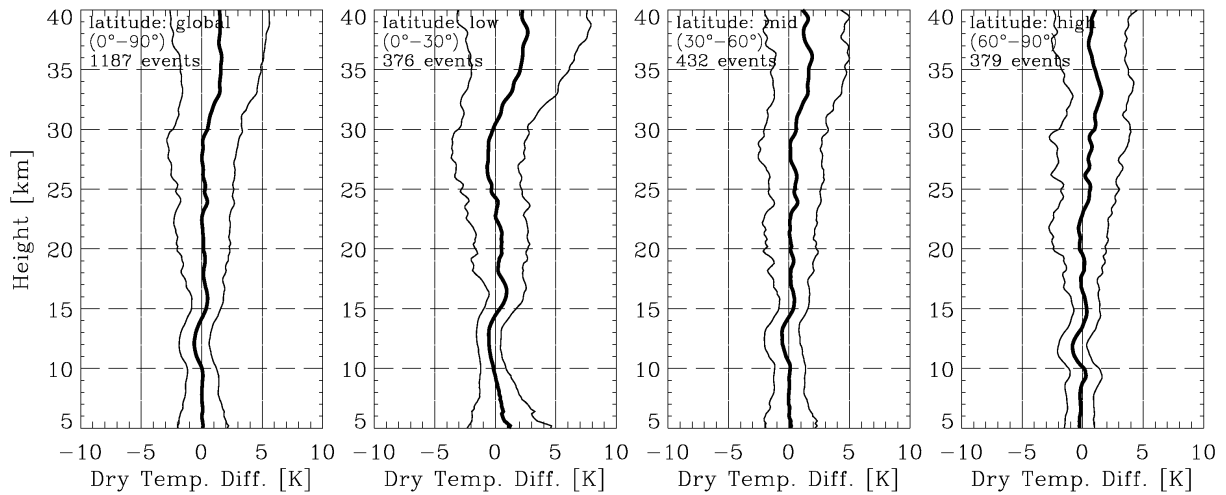


Figure 6.15: Bias  $b$  (bold) and bias  $\pm$  standard deviation profiles  $b \pm s$  (light) of dry temperature retrieved from CHAMP level 2 data with the IGAM/ECMWF scheme relative to temperatures derived from co-located ECMWF operational analyses. Left panel: global ensemble (1187 occultation events), middle-left panel: low-latitude ensemble (376 events), middle-right panel: mid-latitude ensemble (432 events), right panel: high-latitude ensemble (379 events).

Due to the fact that the IGAM/MSIS scheme was successfully evaluated in simulation studies using MetOp-GRAS receiver specifications (section 4.3.4), the lacking performance applied to CHAMP data indicates that worse data quality at high altitudes (higher receiver-noise level, outliers, residual ionospheric noise stemming from small-scale structures in the ionosphere that were not modeled in the simulation study), prevents the scheme, and particularly the bias correction algorithms, from being successful.

In opposition to that, the IGAM/ECMWF dry temperatures are virtually unbiased against ECMWF analyses below 30 km and slightly warm biased above that. The most interesting feature of this comparison is that, though ECMWF temperatures were used as background information in the retrieval, the IGAM/ECMWF retrieval results differ from it at high altitudes (30 km – 40 km). This indicates that the retrieval is not dominated by the background at least down to 40 km which makes it a potentially valuable observation up to this altitude. The discrepancy between IGAM/ECMWF temperatures and ECMWF analysis temperatures is not necessarily a deficiency of the observation since ECMWF is hardly constrained by observations above 30 km and might be cold biased (see also section 7.3).

Wave-shaped structures in the dry temperature bias profiles (between 8 km and 18 km) are found  $\sim 2$  km lower than similar structures in the refractivity bias profiles. This is in accordance with the retrieval procedure, since the involved hydrostatic integration causes downward-propagation of information. It will be shown in section 7.3 that these structures can predominately attributed to the ECMWF analysis and are not discussed in the current section which is focusing on the CCR performance.

## MIPAS

Figure 6.16 and Figure 6.17 show  $b$  and  $b \pm s$  profiles of CCR dry temperature, with respect to ENVISAT/MIPAS temperature profiles. The IGAM/MSIS temperature error statistics are not discussed since the main conclusions drawn above qualitatively apply here as well. Characteristic features according to the MIPAS instrument are discussed by means of the IGAM/ECMWF error statistics (Figure 6.17).

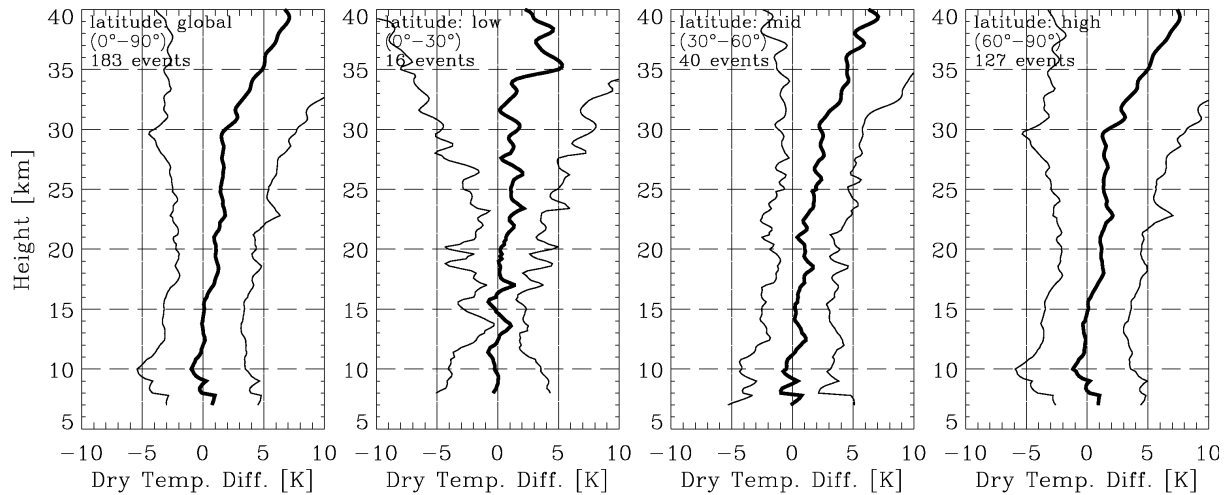


Figure 6.16: Bias **b** (bold) and bias  $\pm$  standard deviation profiles **b**  $\pm$  **s** (light) of dry temperature retrieved from CHAMP level 2 data with the IGAM/MISIS scheme relative to coinciding temperature profiles from ENVISAT/MIPAS. Coincidence-criteria: 300 km/3 hrs. Left panel: global ensemble (183 events), middle-left panel: low-latitude ensemble (16 events), middle-right panel: mid-latitude ensemble (40 events), right panel: high-latitude ensemble (127 events).

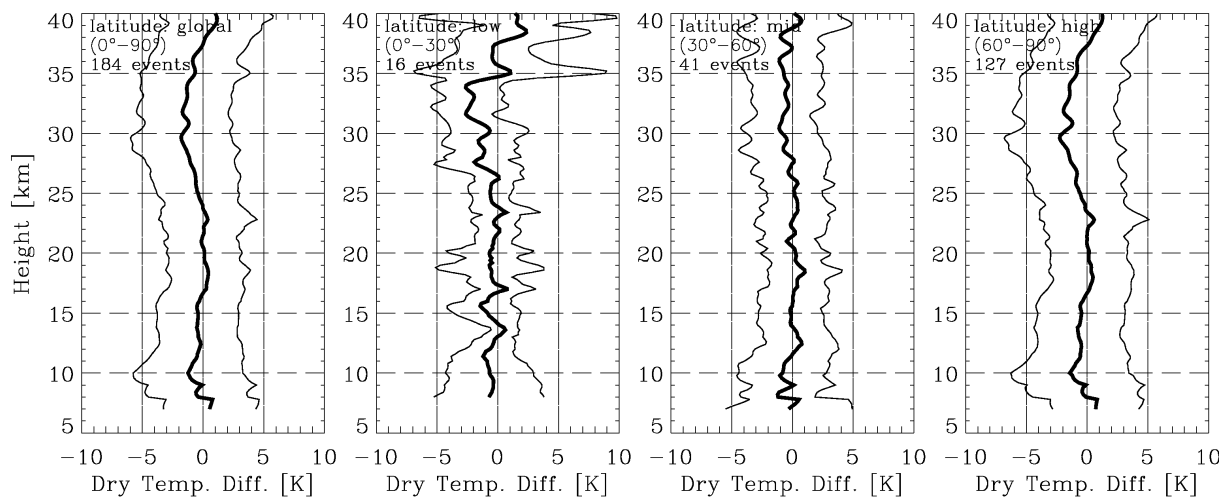


Figure 6.17: Bias **b** (bold) and bias  $\pm$  standard deviation profiles **b**  $\pm$  **s** (light) of dry temperature retrieved from CHAMP level 2 data with the IGAM/ECMWF scheme relative to coinciding temperature profiles from ENVISAT/MIPAS. Coincidence-criteria: 300 km/3 hrs. Left panel: global ensemble (184 events), middle-left panel: low-latitude ensemble (16 events), middle-right panel: mid-latitude ensemble (41 events), right panel: high-latitude ensemble (127 events).

In the global and latitudinal separated ensembles virtually no bias between 6 km and 25 km and a cold bias of about 1 K between 25 km and 35 km exists (peeking at  $\sim 30$  km, 2 K). Between 30 km and 37 km the bias vanishes again. The standard deviation in the global ensemble is height-constant and amounts to  $\sim 3$  K. The low- and mid-latitude ensembles feature smaller standard deviations but this can not be interpreted easily since the sample-size in these ensembles is very small (16 and 41 events, respectively). The major contribution to the global error statistics stems from the high-latitude ensemble comprising 127 events.

The near-height independent standard deviation of  $\sim 3$  K of the IGAM/ECMWF – MIPAS error statistics can be mainly contributed to the variance in the MIPAS data set and representation errors, since in the previous sections and in other studies [e.g. *Hajj et al.*, 2003] it has been shown that the RO technique and the CCRv2 retrieval schemes exhibit a standard

deviation of  $< 2$  K below 25 km. Above that altitude, both data sets may contribute in equal parts.

The most interesting result of this comparison is the fact that the IGAM/ECMWF temperatures are not warm biased against MIPAS temperatures above 30 km as it is the case in the comparisons with ECMWF analyses and the operational GFZ CHAMP results (which are strongly constrained by ECMWF temperatures above 30 km). Since MIPAS is virtually independent from ECMWF (see Section 6.1.6) this is a strong argument for the reliability of the CHAMP derived temperatures of the IGAM/ECMWF-scheme above 30 km.

### GOMOS HRTP

Figure 6.18 and Figure 6.19 show  $\mathbf{b}$  and  $\mathbf{b} \pm \mathbf{s}$  profiles of dry temperature retrieved with the IGAM/MSIS and the IGAM/ECMWF schemes, respectively, with respect to GOMOS/HRTP temperature profiles (see Section 6.1.6). Due to lacking quality of GOMOS data below 20 km, only the height interval from 20 km – 40 km is shown. Apart from GOMOS-characteristic features that will be discussed by means of the IGAM/ECMWF – GOMOS/HRTP error statistics, the IGAM/MSIS – GOMOS/HRTP error statistics roughly feature the main characteristic of the IGAM/MSIS error-statistics relative to other data sources, namely a significant warm bias in the middle stratosphere.

In the global error statistics of IGAM/ECMWF – GOMOS/HRTP, a remarkable, but statistically not significant bias can be found starting from  $\sim 2$  K at 20 km, crossing 0 K at 23 km, negatively peaking with  $-2$  K at 25 km, becoming positive again at 31 km and rising up to  $\sim 3$  K at  $\sim 33$  km. Above that, the bias shows a big variability ranging from  $-2$  K to 7 K. The standard deviation is in the order of 7 K between 20 km and 25 km and 3 K to 4 K between 25 km and 32 km. The sample sizes of the latitudinal separated ensembles are too small to be interpreted separately.

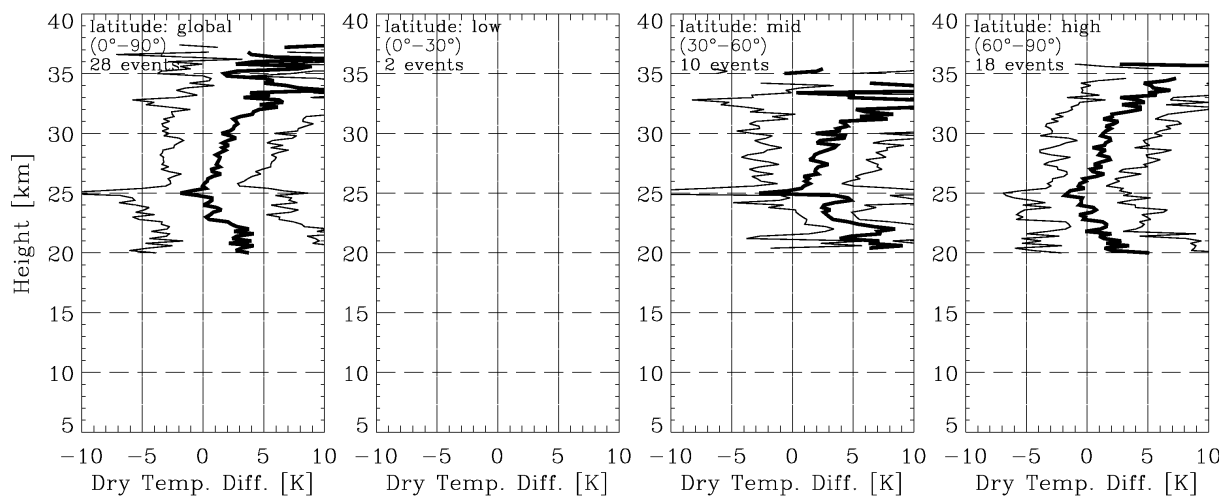


Figure 6.18: Bias  $\mathbf{b}$  (bold) and bias  $\pm$  standard deviation profiles  $\mathbf{b} \pm \mathbf{s}$  (light) of dry temperature retrieved from CHAMP level 2 data with the IGAM/MSIS scheme relative to coinciding GOMOS/HRTP temperature profiles. Coincidence-criteria: 300 km/3 hrs. Left panel: global ensemble (28 events), middle-left panel: low-latitude ensemble (2 events, no error statistics possible), middle-right panel: mid-latitude ensemble (10 events), right panel: high-latitude ensemble (18 events). The discrepancy in the sample sizes is due to the fact that in some GOMOS-profiles only few data-points are available. The number of available profiles is defined as the maximum number of data points at all altitude levels which can be smaller than the sum of the profiles.

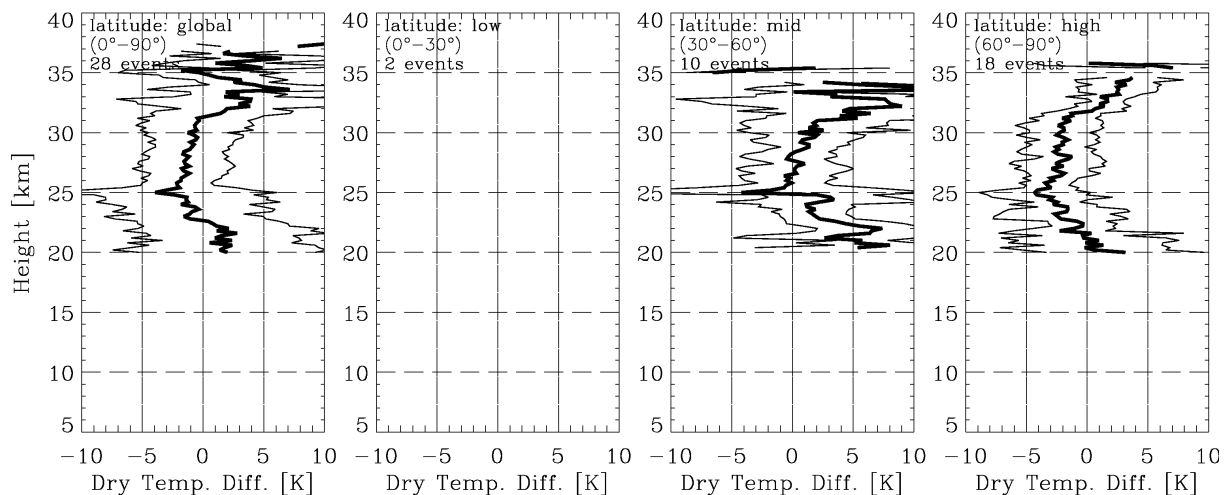


Figure 6.19: Bias **b** (bold) and bias  $\pm$  standard deviation profiles **b**  $\pm$  **s** (light) of dry temperature retrieved from CHAMP level 2 data with the IGAM/ECMWF scheme relative to coinciding GOMOS/HRTP temperature profiles. Coincidence-criteria: 300 km/3 hrs. Left panel: global ensemble (28 events), middle-left panel: low-latitude ensemble (2 events, no error statistics possible), middle-right panel: mid-latitude ensemble (10 events), right panel: high-latitude ensemble (18 events). The discrepancy in the sample sizes is due to the fact that in some GOMOS-profiles only few data-points are available. The number of available profiles is defined as the maximum number of data points at all altitude levels which can be smaller than the sum of the profiles.

The available set of profiles for comparison comprises 32 events (see Sect. 6.1.6), only 28 of them contain data-points on common altitude levels, which makes this study statistically poor-founded. In addition, the GOMOS/HRTP data are preliminary and not yet validated, implying that these results have to be interpreted carefully, but they allow some conclusions about the GOMOS/HRTP retrieval (taking CCRv2 results as reference):

The method basically works and provides atmospheric temperature profiles agreeing with CHAMP-, MIPAS-, and ECMWF-data in the altitude-interval between 20 and  $\sim$  32 km in the range of 5 K. However, many missing data points, and insufficient quality control makes it difficult to use and validate GOMOS/HRTP data. Advancements in this area (reduction of missing data points, quality control), in the reduction of biases, and in the extension of the usable altitude-range are of greatest interest for further HRTP-retrieval algorithm development.

### GOMOS/IGAM

Figure 6.20 shows **b** and **b**  $\pm$  **s** profiles of dry temperature retrieved with the IGAM/ECMWF scheme, with respect to GOMOS/IGAM temperature profiles (see section 6.1.6). Due to lacking quality of GOMOS data below 20 km, only the height interval from 20 km – 40 km is shown. In the global error statistics, a remarkable and statistically significant cold bias (CHAMP colder than GOMOS) can be found starting from  $-8$  K at 20 km and declining to  $-3$  K at 40 km. The standard deviation amounts to some 8 K between 20 km and 25 km, 3 – 6 K between 25 km and 35 km, and drastically increases above that. The sample sizes of the latitudinal separated ensembles are too small to be interpreted separately.

The comparison of CCRv2 results with preliminary GOMOS/IGAM temperature profiles is not consistent with the comparison to other data sources indicating that GOMOS/IGAM features a warm bias of some 5 K. Again, this comparison can be used to evaluate GOMOS results, but not to judge the quality of the CCR retrieval.

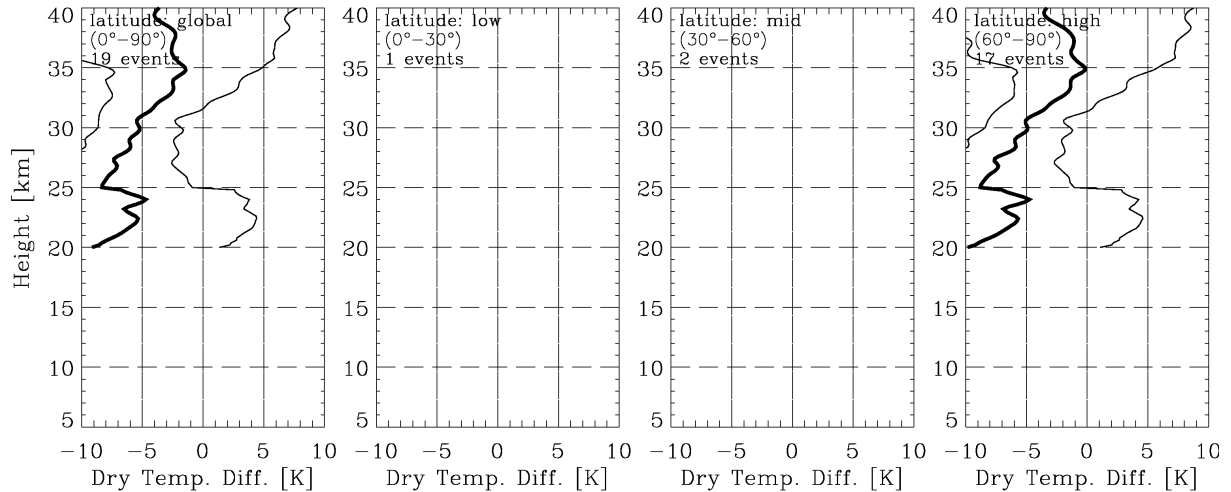


Figure 6.20: Bias  $\mathbf{b}$  (bold) and bias  $\pm$  standard deviation profiles  $\mathbf{b} \pm \mathbf{s}$  (light) of dry temperature retrieved from CHAMP level 2 data with the IGAM/ECMWF scheme relative to coinciding GOMOS/IGAM temperature profiles. Coincidence-criteria: 300 km / 3 hrs. Left panel: global ensemble (19 events), middle-left panel: low-latitude ensemble (1 event, no error statistics possible), middle-right panel: mid-latitude ensemble (2 events, no error statistics possible), right panel: high-latitude ensemble (18 events). The discrepancy in the sample sizes is due to the fact that in some GOMOS-profiles only few data-points are available. The number of available profiles is defined as the maximum number of data points at all altitude levels which can be smaller than the sum of the profiles.

### 6.3. Summary of the CCR Validation

The results of the simulation studies (section 4.3) showed that the newly developed statistical optimization algorithm including background bias correction (IGAM/MSIS) is principally capable to effectively improve the retrieval performance at high altitudes (above 25 km). However, the background bias correction algorithm is not effective when applied to CHAMP data. The degraded performance can be explained by residual ionospheric noise stemming from small-scale structures in the ionosphere that were not modeled in the simulation study, by intermittent errors in the CHAMP high altitude data (e.g., artifacts caused by clock malfunctions), and by the overall noise level of CHAMP.

However, since RO retrievals independent from NWP analyses are highly desirable, especially for their use in combination with models by means of data assimilation techniques, this scheme will be further developed to become more robust against noisy data, and better profile-search libraries than the MSISE-90 climatology are envisaged. Additionally, it could be demonstrated that refractivity profiles retrieved with IGAM/MSIS are of satisfactory quality with a bias in order of 0.1 % up to 35 km, standard deviation below 1 % at 5 km – 20 km, and around 1.2 % up to 32 km and that they are of the same quality as other retrieval schemes from leading institutions in the field of RO retrieval.

The IGAM/ECMWF retrieval scheme demonstrates that, by careful use of background information, relative independency from the background can be maintained up to at least 40 km whilst the retrieval performance, especially for temperature profiles, is drastically improved. Compared to ECMWF analyses, the IGAM/ECMWF temperature profiles are virtually unbiased between 5 km and 30 km and warm biased by  $\sim 1.5$  K between 30 km and 40 km (demonstrating the relative independence from ECMWF). The comparison to coinciding temperature profiles from ENVISAT/MIPAS, an instrument virtually independent from ECMWF background data, showed a very good agreement in this altitude region, and indicates that the encountered bias is probably attributable to the ECMWF data.

Furthermore, the results of the comparison with ECMWF analyses show that, additionally to the well known negative refractivity bias in the lower troposphere [e.g., *Ao et al.*, 2003], a minor, height-independent constant negative refractivity bias of about  $-0.4\%$  exists in the RO retrieval results compared to ECMWF analyses. A similar bias compared to ECMWF analyses, at least up to 25 km, can be found in the RO-derived refractivities of other leading institutions [*Steiner*, 2004; *Wickert et al.*, 2004c; *Beyerle et al.*, 2004], but it was not as clearly identified yet since it is masked by the major refractivity bias in the lower troposphere and by increasing noise and the influence of background information above 25 km. The IGAM/ECMWF retrieval identifies this bias quite clearly as being height-constant, which will help to eliminate it in future algorithm improvements.

Generally, the performance studies show that the CCRv2 schemes are in-line, and in some aspects better performing, than state-of-the-art retrieval schemes of other institutions.

# 7 Radio Occultation Based Climatologies

## 7.1. The CHAMPCLIM Project

The framework for the work presented in this thesis is the CHAMPCLIM project. The major aim of CHAMPCLIM is to help ensure that CHAMP/GPS RO data are exploited in the best possible manner, in particular for the most demanding application of retrieved atmospheric profiles in terms of data quality, which is climate monitoring. The main objectives of the project address three areas, 1) CHAMP RO data and algorithms validation, 2) CHAMP/GPS-based RO data processing advancements in order to optimize the climate utility of the data, and 3) CHAMP/GPS-based monitoring of climate variability and change, respectively [Kirchengast, 2003]. Areas 1 and 2 were addressed in the previous sections of thesis while area 3 is object of ongoing work and partly addressed in this Chapter. For more information on the CHAMPCLIM project the interested reader is referred to the article of *Foelsche et al.* [2004].

## 7.2. First Climatologies from CHAMP

### 7.2.1. Sampling Strategies – Sampling Errors

For the creation of climatologies (i.e., gridded dataset describing the mean and variability of the atmospheric state) suitable spatial and temporal averaging strategies have to be applied. Several facts have to be regarded for this setup:

Most data users claim for high spatial and temporal resolution. This claim is counterbalanced by increasing sampling errors with increasing resolution. Ultimately, the resolution of a single measurement and the measurement density set the limits for the resolution of any gridded dataset derived from measurements.

In the case of RO, the vertical resolution of a single measurement amounts some 1 km and the horizontal resolution (in direction of the ray) 250 km – 300 km. Higher vertical resolution might be achieved by enhanced retrieval techniques in future [e.g., *Jensen et al.*, 2003 and references therein] but higher horizontal resolution can only be reached by combining RO data with higher resolved data from a different source. Though the numbers above are rough estimates and have to be determined separately for each retrieval scheme if exact knowledge of the resolution is required, they give a first idea of the upper bounds for possible resolution of pure RO-derived climatologies. In case of over-sampling (higher measurement density than physical resolution), it can be useful to provide gridded data even at smaller grid spacing than it would correspond to the measurement's physical resolution. In vertical, RO measurements are generally over-

sampled. CHAMP uses a measurement frequency of 50 Hz which roughly corresponds to one measurement each 100 to 200 m altitude. This enables to provide gridded data at full (1 km grid distance) or even slightly higher vertical resolution which can be advantageous for the user of the data to avoid artificial smoothing during interpolation procedures. However, in such a case it must be clearly stated that the resolution of the gridded data is not the physical resolution of the dataset and that neighboring values are not independent from each other.

The second bound for the resolution of a gridded dataset is defined by the measurement density and distribution. Each grid cell has to contain sufficient data to ensure that the representativeness of the data for the mean location and time of the cell is given. Due to the claim for high resolution one will generally accept some representativeness error provided that it is smaller than or at least in the order of the measurement error.

In the horizontal, the spatial measurement density depends on the temporal averaging period and on geometrical properties of the measurement system. In case of CHAMPCLIM, one GPS receiver on a LEO satellite with high orbital inclination (see section 2.9) yields some 150 globally well distributed atmospheric profiles per day with higher density (referred to equal areas) at high latitudes and lower density at low latitudes.

Additionally, it is of interest to evenly sample the diurnal circle. According to the orbit parameters of CHAMP, the local time of the ascending and descending nodes is about the same time as the local time of the corresponding occultation events. With a change rate of  $\sim 1$  hour per 11 days of both nodes [Wickert *et al.*, 2005] the diurnal circle is ideally scanned within  $\sim 130$  days. This implies that even seasonal means (90 – 92 day period) are not ideally sampling the diurnal cycle. However, the effect of this non-ideal diurnal sampling is attenuated by the fact that the ascending node always yields measurements twelve hours after the descending node which automatically accounts for the diurnal range to some degree. More than that, error studies focusing on the diurnal effect show that seasonal and even monthly sampling periods do not notably increase the sampling error due to the diurnal effect (B. Lackner and B. Pirscher, Wegener Center, Graz, Austria, personal communication, 2005).

The above arguments implied a preliminary setup of global seasonal (three month) climatologies on a horizontal grid containing 18 latitude bins  $\times$  24 longitude bins (see Figure 7.1) with one vertical layer each 500 m and a more aggregated version containing zonal means in 18 latitude bands of 10 degree width to reduce the representativeness error. Concerning the vertical range, a very conservative setup extends from 10 km to 30 km, which is the optimal height range of the RO technique, and a setup showing the performance at the edges of the RO vertical measurement range extends from the surface to 40 km.

In Figure 7.2 a global map of all CHAMP occultation events in the prime CHAMPCLIM testbed season, the summer season 2003 (JJA2003, 13 566 events after quality control) is displayed in the meridionally and zonally resolved grid. Figure 7.3 shows the corresponding mean occultation numbers for each latitude band. In the global mean, each bin includes 77 atmospheric profiles which would be clearly sufficient for deriving robust first- and second order statistics as required for the climatologies. However, due to the highly inclined orbit of CHAMP, the measurement density is not even above the globe when referenced to equal areas. At high latitudes more than 150 profiles are collected in each bin while at low latitudes only some 25 events can be found. In extreme cases, the number of profiles per bin is below 10 which can cause severe representativeness errors or entirely prevent the creation of statistics.

## JJA 2003: CHAMP Occultation Event Distribution (Global)

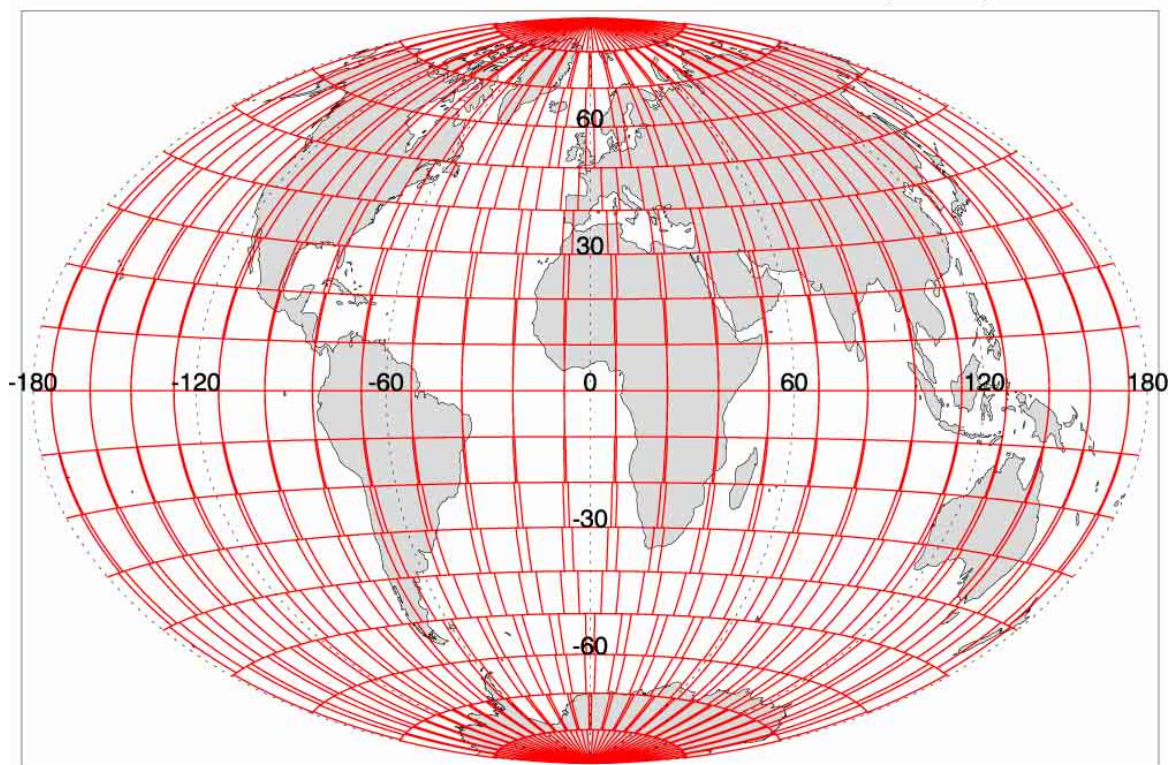


Figure 7.1: Map demonstrating the preliminary horizontal CHAMPCLIM sampling strategy for seasonal climatologies consisting of a regular equal area grid with 18 latitudinal x 24 zonal bins. This corresponds to a grid spacing of 10 degree latitude and 15 degree longitude with zonally overlapping bins a high latitudes. The more aggregated version of the preliminary CHAMPCLIM climatology consists of zonal means in the same 18 latitude bands.

## JJA 2003: CHAMP Occultation Event Distribution (Global)

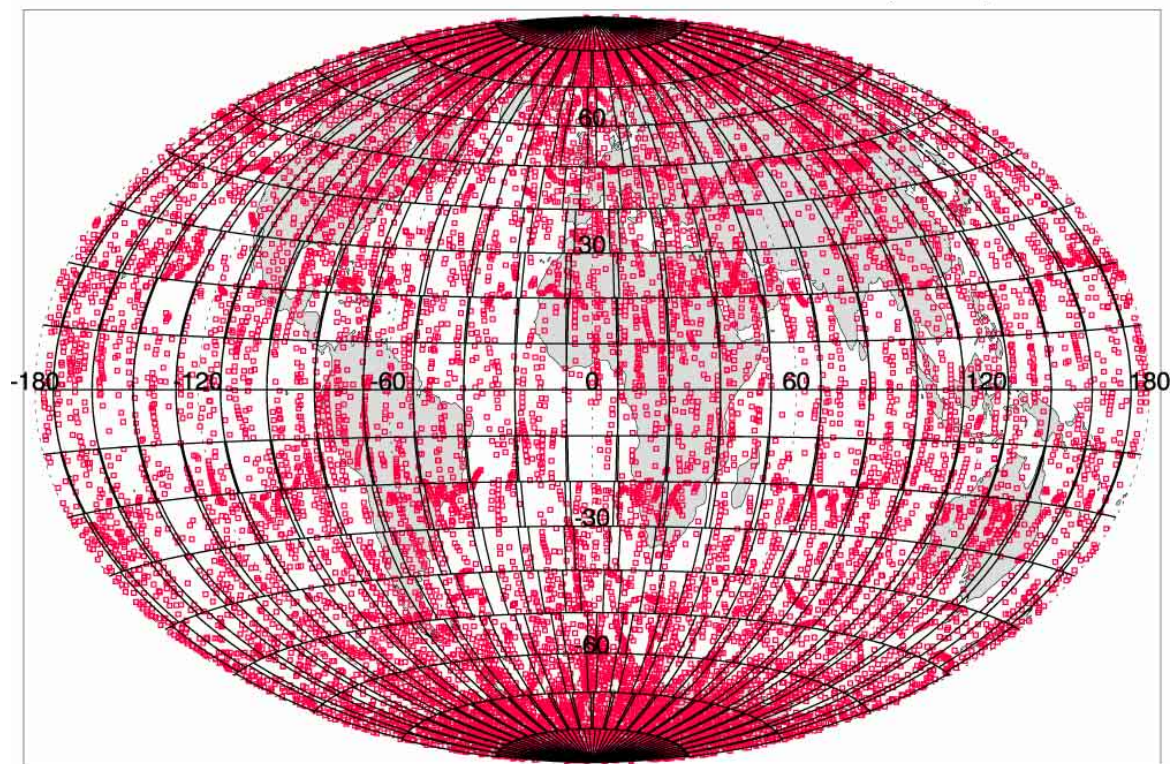


Figure 7.2: Distribution of 13,566 occultation events recorded by CHAMP during the summer season (JJA) 2003 (18 bins x 24 bins setup).

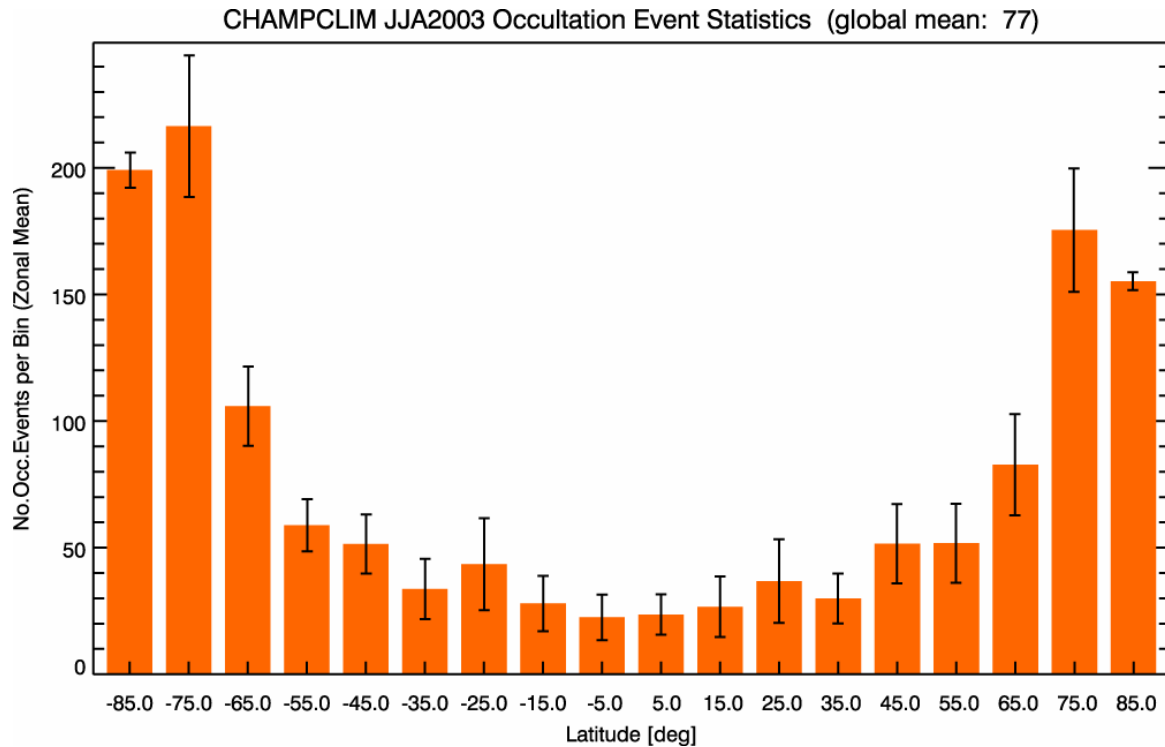


Figure 7.3: Seasonal mean and standard deviation of occultation number per bin in each latitude band in JJA2003.

Generally, the sampling error can easily be determined by pseudo-simulation of the CHAMP measurements using near-realistic atmospheric fields as data source. ECMWF operational analyses represent today's best knowledge of the state of the atmosphere and are ideally suited for such an exercise where seasonal mean temperature profiles in each bin are extracted from ECMWF fields and compared to the mean of the profiles extracted at the times and locations of the actual CHAMP measurements. This method allows for separating the measurement error from the sampling error since only the coordinates of the measurement, but not the measurement itself is involved. The only assumption needed is that the ECMWF analyses represent the spatial and temporal variability of the atmosphere with sufficient precision which is assured in most parts of the analysis by the integration of a massive amount of observations into the analysis [e.g., *ECMWF*, 2004].

For preliminary sampling error studies using the 18 bins x 24 bins grid in the CHAMPCLIM testbed season JJA2003 show that the seasonal climatologies on this grid provide satisfactory results in most bins but as well feature big sampling errors in some cases. Figure 7.4 shows two selected latitude versus height slices of such sampling error analyses. A complete set of 24 slices is presented in the Appendix.

White spots in these figures denote regions where less than 3 measurements are available and no error statistics can be calculated (for the final CHAMPCLIM products more stringent standards for the minimum sample size will be applied). Such situations predominately occur in the lower- to mid-troposphere at low latitudes and are caused by the low measurement density in that region one hand, and by the fact that the moist conditions in the equatorial troposphere represent particularly difficult conditions for RO measurements and retrievals and frequently cause signal loss or retrieval failure at lower altitudes on the other hand.

The left panel of Figure 7.4 represents the 15 degree wide band centered on the  $-80$  degree meridian. It is an example for a good case generally featuring sampling errors below  $\pm 0.3$  K in the RO "core" region between 10 km and 30 km. Only very few spots

feature sampling errors beyond  $\pm 0.9$  K in this region. The right panel represents a bad case which, though generally featuring sampling errors below  $\pm 0.3$  K in most regions as well, shows errors beyond  $\pm 1.8$  K in some parts of the core region.

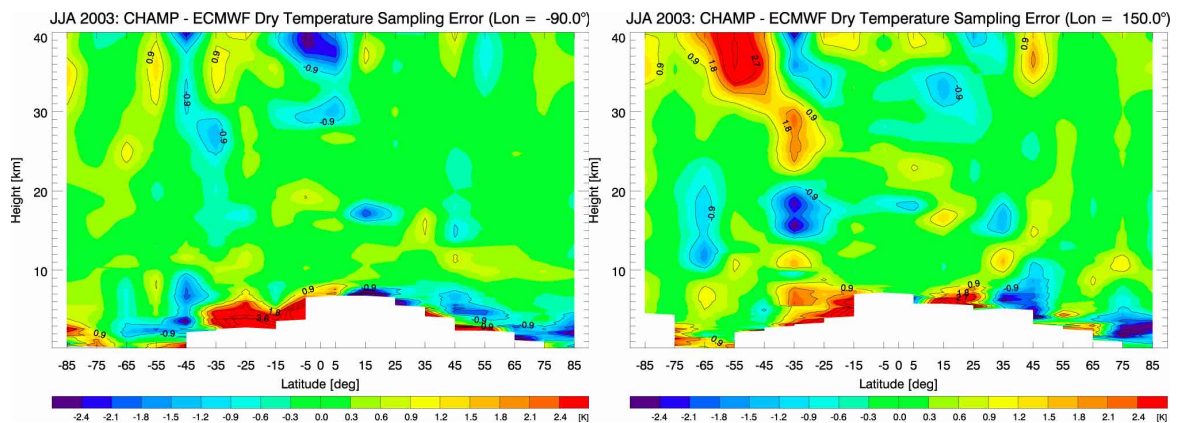


Figure 7.4: CHAMPCLIM (18 bins x 24 bins setup) sampling errors in the  $-90$  degree (left panel) and  $150$  degree (right panel) meridian band in JJA2003.

These examples show that the seasonal 18 bins x 24 bins setup might be, in terms of spatial and temporal resolution, beyond the high-resolution limit for reliable RO climatologies derived from a single satellite like CHAMP. More than that, the inspection of the sampling error for other seasons (not shown) shows that in extreme cases even empty bins occur which clearly calls for a coarser grid.

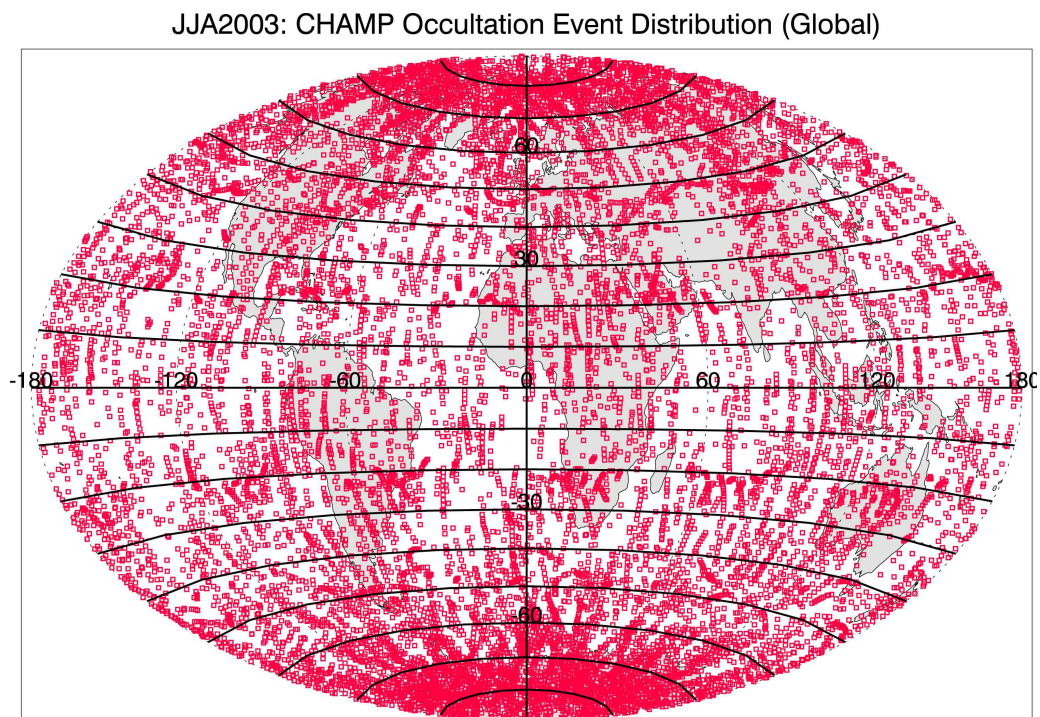


Figure 7.5: Distribution of 13 566 occultation events recorded by CHAMP during the summer season (JJA) 2003 (18 latitude bands, zonal mean setup).

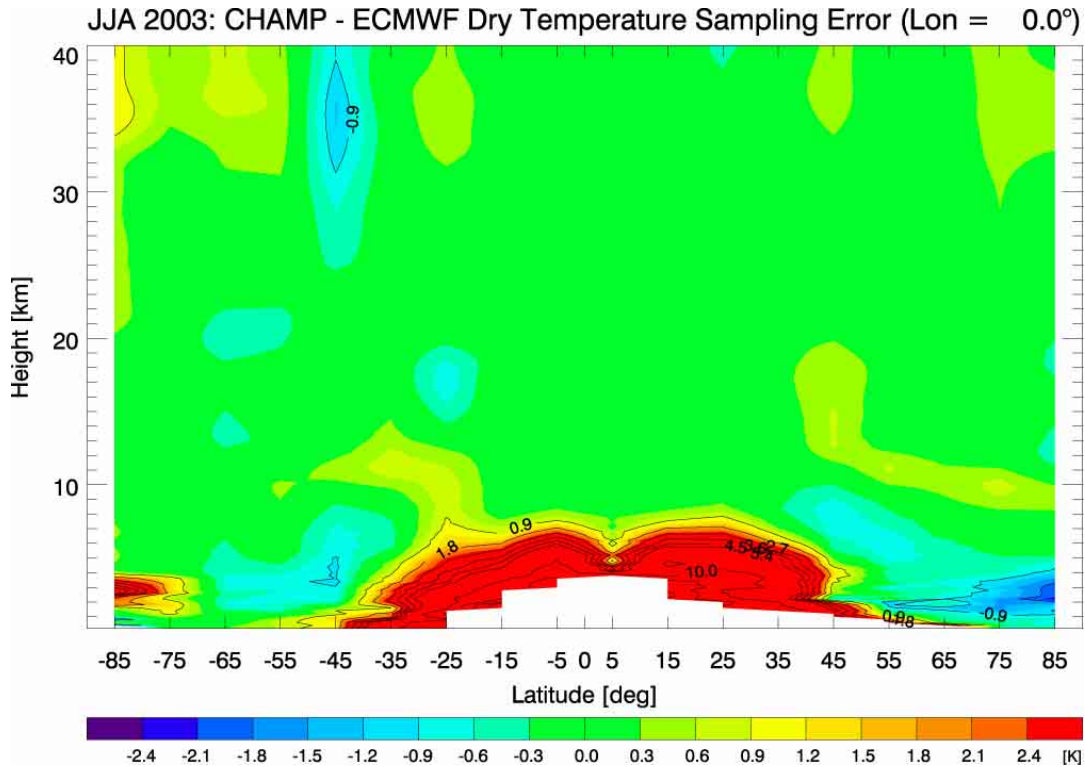


Figure 7.6: CHAMPCLIM 18 latitude bands, zonal means: Sampling errors in JJA2003.

For the creation of reliable climatologies targeted at the general user in the field of climate research sampling errors beyond 2 K are clearly too high. A basic and very robust approach to reduce sampling errors while conserving important spatial structures in the atmosphere is to regard zonal means in 18 ten degree latitude bands. Such a sampling grid, together with the locations of all JJA2003 CHAMP occultation events (after quality control) is displayed in Figure 7.5. The corresponding dry temperature sampling error (Figure 7.6) remains below  $\pm 0.3$  K virtually everywhere in the RO core region and even in most parts of the region between 30 and 40 km.

In the low latitude troposphere a huge positive sampling error occurs. The same is true for the 18 bins x 24 bins setup, but due to sparse data in this region it is less visible in that case. The reason for this bias is clearly related to moist and variable conditions in the low-latitude troposphere that often cause RO receiver to lose the signal or the retrieval to fail. This causes a selective removal of moist data points at the lower end of each measured profile (i.e., profiles recorded under moist conditions generally are generally cut off at higher altitudes than profiles recorded under dry conditions). Since moisture is equivalent to a reduction of the dry temperature (see section 3.2.3), a warm dry temperature bias results from this systematic sampling error.

This bias is a general problem that might be reduced by advanced RO receivers and advanced tropospheric retrieval techniques but cannot be avoided entirely. The implication of this sampling error is on one hand, that data below a certain altitude has to be removed from the climatology before delivering it to the general user. On the other hand, it is important to keep this sampling effect in mind when validating retrieval schemes in order not to mistake it for a defect of the retrieval scheme.

The two preliminary CHAMPCLIM binning strategies described above are used in this thesis. Currently, extensive sampling error studies are performed within the CHAMPCLIM project in order to define the final zonally resolved CHAMPCLIM grid with well balanced and well defined sampling errors. Furthermore, different geometrical configurations are developed [Borsche et al., 2005] since regular (same number of

longitude bins at each latitude) and equal area binning strategy induces overlapping bins at higher latitudes. If non-overlapping bins (and therefore not artificially correlated data points) are desired, which might be the case for studies focusing on the spatial correlation of climate parameters, one has to either reduce the number of bins towards the poles or to drop the claim for equal areas in each bin.

### 7.2.2. Quality of Seasonal RO-Based Climatologies

This section shows different error parameters of the JJA2003 climatology on the 18 bins x 24 bins and the 18 latitude bands, zonal mean sampling grid. All CHAMP data presented here has been retrieved with the IGAM/ECMWF scheme (see section 5.4). The reference data was extracted from ECMWF analyses (i.e., the CHAMPCLIM climatologies are not entirely independent from the reference at high altitudes since ECMWF analyses are used as background information in the retrieval scheme as well).

The CHAMPCLIM zonal mean refractivity and dry temperature fields for JJA2003 are displayed in Figure 7.7. For comparison, the same fields, but extracted from ECMWF operational analyses are displayed in Figure 7.8.

While the refractivity field is dominated by its exponential decrease obscuring other features, the dry temperatures show the typical features of the Boreal summer/Austral winter atmosphere with a cold, well developed polar vortex over Antarctica and the cold equatorial tropopause.

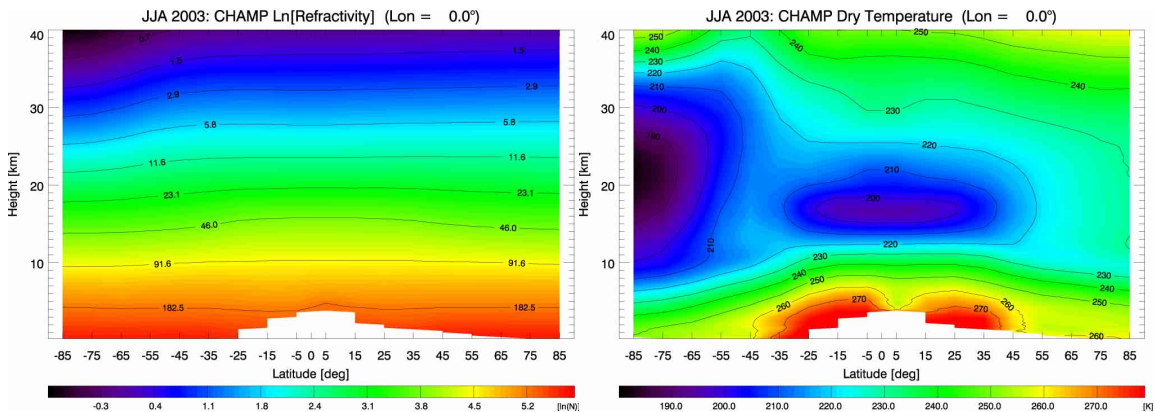


Figure 7.7: CHAMPCLIM zonal mean refractivities (left panel) and dry temperatures (right panel) for JJA2003.

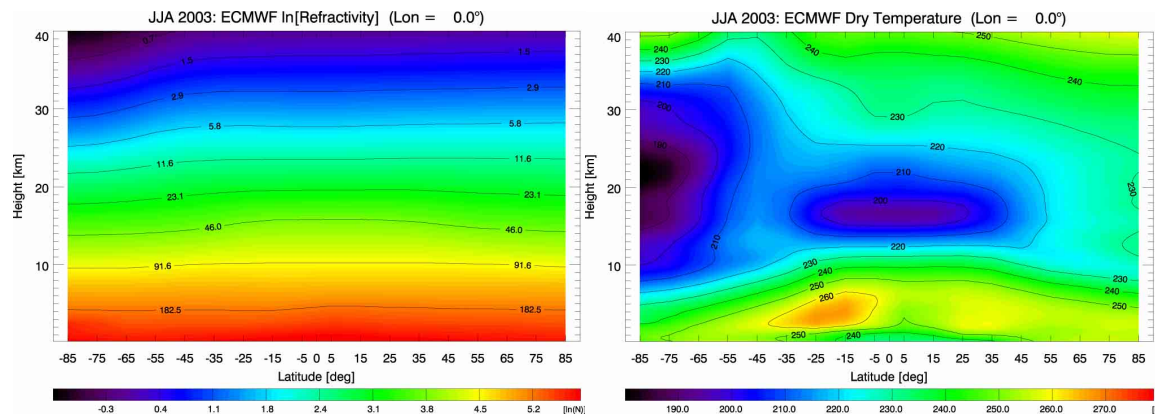


Figure 7.8: Zonal mean refractivities (left panel) and dry temperatures (right panel) for JJA2003 extracted from ECMWF operational analyses.

Figure 7.9 depicts the relative measurement bias of refractivity and the measurement bias of dry temperature (both excluding the sampling error since ECMWF data has been extracted coinciding with the measured profiles). In most of the core region, the refractivity bias stays below  $\pm 0.25\%$  –  $0.5\%$  and dry temperature bias below  $\pm 0.3$  K. Apart from that, several features stand out:

Though the measurement bias is not influenced by the sampling error described in section 7.2.1, a severe negative refractivity bias and warm dry temperature bias occurs in the low latitude troposphere. Since the reference temperatures from ECMWF were extracted as dry temperature and the bias occurs as refractivity bias as well, it is not the discrepancy between dry temperature and temperature either, but a real measurement deficiency in the lowermost 5 km of the atmosphere. In the total climatological error (see Figure 7.10) this measurement error is covered by the higher reaching low-latitude troposphere sampling error and CHAMPCLIM will not deliver data at these altitudes. Therefore, this measurement error will not be discussed here. The interested reader is referred to the articles of *Beyerle et al.* [2004] and *Ao et al.*, [2003] for a discussion of this effect known as the “negative refractivity bias”.

Other outstanding features are a warm bias in the low-latitude tropopause, a wave-like bias structure in the polar-vortex region, and a warm dry temperature bias above 30 km. All of these features turned out to be primarily related to ECMWF analysis and not to CHAMP data and will be discussed in section 7.3.

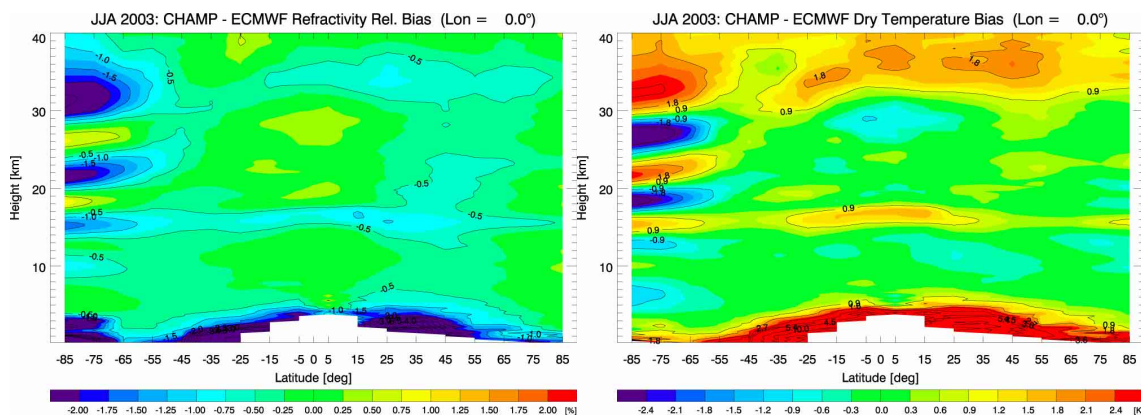


Figure 7.9: Zonal mean refractivity (left panel) and dry temperature (right panel) measurement bias (CHAMP – ECMWF) for JJA2003.

The total climatological error depicted in Figure 7.10 includes the sampling error and shows an accordingly higher low-latitude troposphere bias. Apart from that, the measurement bias and the total error are very similar showing that the sampling error is small in this season.

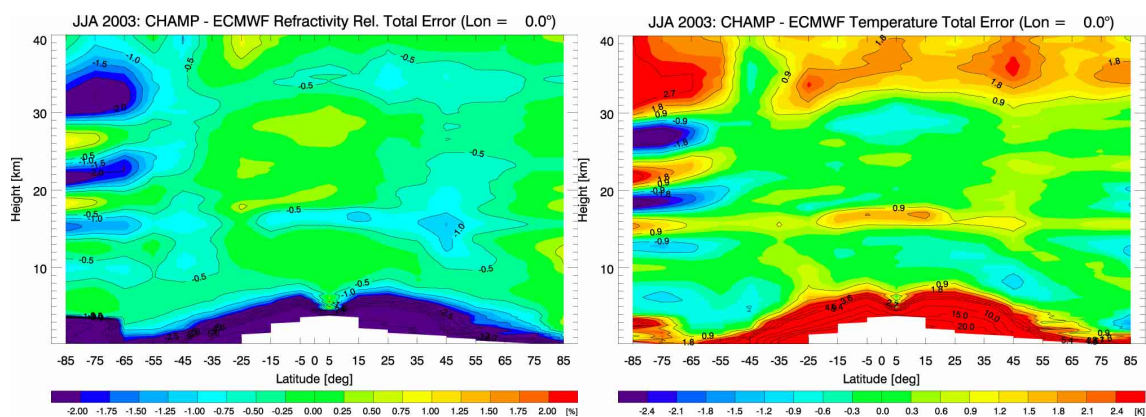


Figure 7.10: Zonal mean refractivity (left panel) and dry temperature (right panel) total error (CHAMP – ECMWF) for JJA2003.

Figure 7.11 shows the zonal mean standard deviation error in JJA2003. In terms of dry temperature, it is below 1.5 K between 10 km and 20 km (for the exception at low latitudes see section 7.3) and between 1.5 K and 3 K between 20 km and 30 km. Above 30 km (a region where the retrieval results are not independent from the reference data) the standard deviation peaks at 4 K – 4.5 K and is converging towards zero above that height where the background data becomes dominant (not shown). At low altitudes (below 3 km – 6 km) the random error is huge indicating the lacking performance of the retrieval scheme in the lower troposphere.

It has to be noted that the random error presented here refers to the variability of the error of single RO profiles. The climatological mean refractivities and dry temperatures as presented in Figure 7.7 feature, due to big samples sizes a very small random error. The 18 latitude bands contain some 750 (ranging from 304 to 1276) occultations each which reduces the random error for the mean by a factor of  $\sim 27$  (ranging from 17 to 36) resulting in standard deviations of climatological mean dry temperature error around 0.1 K.

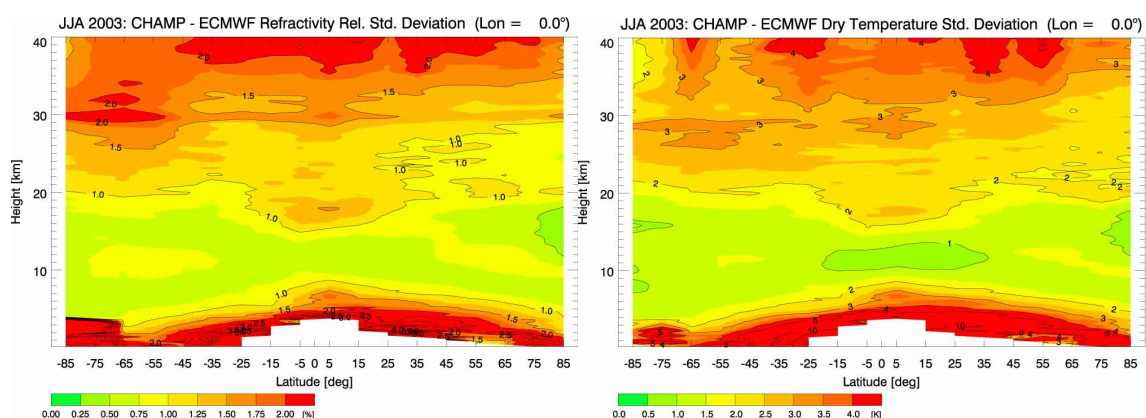


Figure 7.11: CCR measurement random error in JJA2003. Left panel: refractivity, right panel: dry temperature.

As a general conclusion, the systematic error of seasonal mean temperatures from CHAMPCLIM can be estimated to be smaller than  $\pm 0.3$  K in most parts of the core region (10 – 30 km), eventually peaking at  $\pm 0.6$  K. However, it is not easy to judge if these peaks have to be attributed to RO data or to the ECMWF analyses. Below 10 km CHAMPCLIM features a severe warm bias which is related to retrieval deficiencies and sampling problems. Data below 10 km at low latitudes and below 5 km at high latitudes

have to be handled with care and should be removed from datasets aimed at the general user. Due to the robust statistics (big sample sizes) the random error of the climatological results are extremely small in the core region ranging from 0.05 to 0.18 K.

The quality of the climatologies on the 18 bins x 24 bins grid is comparable to the zonal mean errors, but features more scatter. For demonstration the dry temperature measurement bias and total error for some meridional slices as in section 7.2.1 are shown here (Figure 7.12 and Figure 7.13). A comprehensive collection of several error estimates for all meridional bands is presented in the Appendix.

In the left hand panels the  $-90$  degree band (good case) and in the right panels the  $150$  degree band (bad case) is shown. In terms of measurement bias the climatology of both meridional slices perform about similar as expected and are more or less (apart from more scatter due to smaller samples) of similar quality as the zonal mean dry temperatures. In the total error, however, the quality differences become larger, since the sampling error adds to the total error budget. Also, seasonal means are less precise due to smaller statistical samples (see Figure 7.3). The standard deviation of the means amount to 0.15 K to 1 K in the core region.

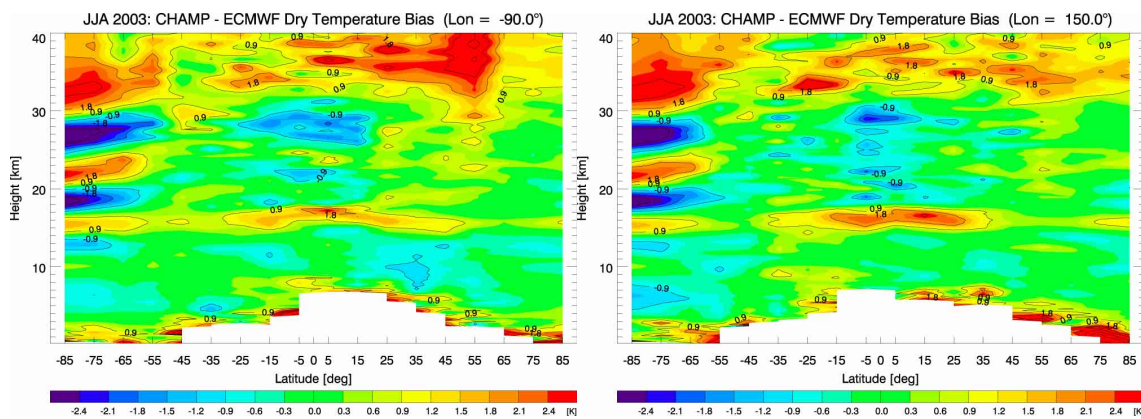


Figure 7.12: JJA2003 measurement bias of dry temperature (18 bins x 24 bins setup) for two selected meridional bands:  $-90$  degree (left panel) and  $150$  degree (right panel)

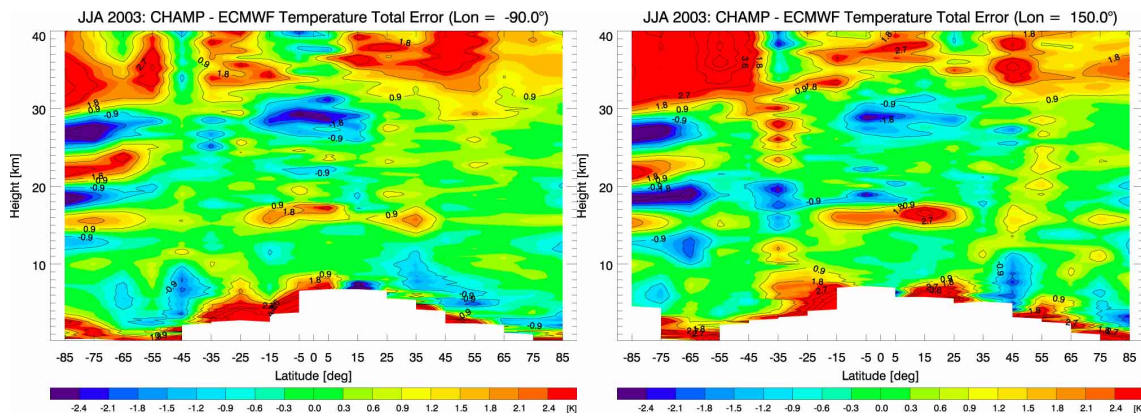


Figure 7.13: JJA2003 total error of dry temperature (18 bins x 24 bins setup) for two selected meridional bands:  $-90$  degree (left panel) and  $150$  degree (right panel).

### 7.3. CHAMP RO Climatologies for Model Validation

#### 7.3.1. Relevance of ECMWF Operational Analysis and its Validation

The results presented in section 7.2.2 and Chapter 6 show good agreement of CHAMPCLIM data with various reference datasets but also, regarding ECMWF analyses, some salient deviations in Austral polar winter region and near the tropical tropopause. This section demonstrates and discusses the latter discrepancies. Many of the results presented here have been published by *Gobiet et al.* [2005].

For this purpose the CHAMPCLIM core data (10 km – 30 km altitude, zonal means in 18 ten degree bands) is used to compare operational global analyses from the Integrated Forecasting System (IFS) of ECMWF against it, focusing on eventual deficiencies in ECMWF data. This is not only a first demonstration of use of CHAMPCLIM data but also of relevance to the broader scientific community since ECMWF analyses are used as initial conditions for the NWP forecast system and in addition for numerous applications in atmospheric sciences such as the validation of new remote sensing systems, as forward model or background information in the simulation or retrieval of remote sensing data, as basis for atmospheric process studies like dynamics of trace gases, troposphere-stratosphere exchange, or stratospheric ozone depletion. This wide field of applications of ECMWF analyses (often as reference dataset) makes it difficult, but at the same time particularly important, to evaluate the analysis itself.

Especially the stratospheric part, which is weakly constrained by observations, is barely validated. Most operational upper air observation systems like radiosondes and the Advanced Microwave Sounding Unit A (AMSU-A) are unsuitable as reference for this purpose since they are part of the analysis itself. One way to cope with this problem is to evaluate short-range forecasts instead of analyses [e.g., *Knudsen*, 2003] but this approach has limited significance for the analyses. Direct comparison of analyses with ground based or airborne research observations provide valuable insights but are rare and provide information only discretely in space and time [e.g., *Hertzog et al.*, 2004]. Intercomparison studies provide insights into relative errors between analyses from different institutions but not into absolute errors. For example, *Manney et al.* [2003] showed that in the Arctic winter stratosphere the area featuring temperatures below the threshold for polar stratospheric cloud formation ( $\sim 195$  K) can vary by up to 50 % between different analyses.

The RO technique in general and CHAMP in particular offer new possibilities for the evaluation of analyses (see *Schröder et al.* [2003] for a first demonstration) by providing globally distributed profiles of temperature and geopotential height ranging from the lower troposphere to the middle/upper stratosphere with high long-term stability.

#### 7.3.2. ECMWF and CHAMPCLIM Data Used

The IFS of ECMWF uses a semi-Lagrangian model with 60 vertical levels (L60) up to 0.1 hPa, spectral representation in the horizontal with triangular truncation at wave number 511 (T511) for upper air fields and horizontal derivatives, and a Gaussian grid in the horizontal for dynamic tendencies and diabatic physical parameterizations. This setup corresponds to horizontal grid spacing of  $\sim 40$  km. IFS provides ten-day forecasts started twice a day from an initial state (i.e., the analysis) produced via four-dimensional variational data assimilation dynamically combining a short-range forecast with observational data [*ECMWF*, 2004]. It operationally generates analyses for 00, 06, 12, and

18 UT every day. As an example, the ECMWF JJA2003 zonal mean temperature is shown in Figure 7.8.

Though a vast amount of observations is assimilated, the analysis is still weakly constrained by observations in some regions like the polar stratosphere where radiosondes are sparse and the main observational information source are AMSU-A radiances with low vertical resolution [e.g., *Thépaut and Andersson, 2003*] and, since October 2003, Advanced Infrared Sounder (AIRS) radiances [*ECMWF, 2003*].

All RO temperature profiles used in this Chapter were retrieved from CHAMP phase delay data using the IGAM/ECMWF retrieval scheme. Since at high altitudes the observed data are optimized by combining them with background information derived from the ECMWF analyses the CHAMP data is not independent from the validated data. In this study, predominantly data between 10 and 30 km are used, a range where no direct background information is used and where the effect of downward propagation of background information from the analysis through the RO retrieval is small to negligible in the differences discussed ( $< 0.2$  K at 30 km, quickly decreasing below 30 km). More than that, any potential contribution of the background to the retrieved CHAMP data can only introduce biases towards the data under evaluation and therefore reduce the differences between the CHAMPCLIM and ECMWF datasets.

The IGAM/ECMWF retrieval scheme generally yields some 130–180 globally distributed temperature profiles per day resulting in  $\sim 12,500$  profiles per season. The study is based on 2.5 years of CHAMP data (March 2002 to August 2004) comprising 124,355 profiles. As an example, the CHAMPCLIM JJA2003 seasonal zonal mean temperatures in 10 degree latitude bands are depicted in Figure 7.7 demonstrating the general features of the Austral winter stratosphere with a well-developed polar vortex (minimum in  $-90$  degree to  $-80$  degree band: 181.7 K at 21.5 km).

### 7.3.3. Validation Methodology

The ECMWF – CHAMP comparison is based on the same statistics of temperature difference profiles as used in the previous Chapter. ECMWF analyses were used on model levels (L60 grid) with reduced horizontal resolution (T42,  $\sim 300$  km grid spacing), roughly corresponding to the horizontal resolution of RO data, in order to avoid spatial representation errors. For each RO profile a coinciding profile was extracted from the analysis, i.e., spatially interpolated to the locations of the RO data using the nearest time layer of the analysis. This approach ensures that potential sampling errors due to non-uniform distribution or limited coverage of RO observations cannot perturb the difference statistics. For this study, the 2.5 years of difference profiles were divided into ten seasons, with each season sampled into the ten degree latitude band grid presented in section 7.2.1.

For each latitude band the ensemble mean (bias) and standard deviation profiles were computed. The discussion below mainly exploits the bias profiles, i.e., the biases of ECMWF vs. CHAMP. This means the RO data were chosen as reference but does not imply they are the “truth”.

### 7.3.4. Results and Discussion

The results are presented in latitude (pole-to-pole) versus height slices in the core CHAMPCLIM altitude range (10–30 km). Figure 7.14 depicts the seasonal zonal mean temperature bias in four seasons from March-April-May (MAM) 2002 to December-

January-February (DJF) 2003-2004. The general agreement between the two datasets has already been discussed in the previous Chapter, but two prominent features not discussed in detail yet stand out: A cold bias at the low-latitude tropopause region and a wave-like bias structure in the Austral winter polar vortex.

### Low Latitude Tropopause Bias

The cold bias of up to  $-2$  K in the low-latitude tropopause is systematically visible in all seasons. The inspection of single profiles (not shown; see also *Hajj et al.* [2004]) indicates that this effect might be related to the different vertical resolution of the analyses and the RO data (RO resolution  $\sim 1$  km at that altitude, resolution of ECMWF analyses  $> 1.3$  km). *Gorbunov and Kornblueh* [2003] suggested the bias to be induced by the lower vertical resolution of the tropopause in ECMWF analyses. Though we as well find indication for this interpretation, we find it complicated by the fact that single difference profiles do not exhibit uniform shapes around the tropopause, i.e., ECMWF profiles cannot simply be described as smoothed versions of the CHAMP RO profiles. Figure 7.15 illustrates this by the enhanced random temperature deviations near the low-latitude tropopause. Differences in representation of atmospheric wave activity and tropopause height variability, both weaker in the analysis, can be expected to play a relevant role though it has to be pointed out that these interpretations are preliminary and subject of ongoing research.

### Antarctic Polar Vortex Bias

The prominent wavelike bias in the JJA2003 polar vortex, with a magnitude of  $-2.5$  K to  $+3.5$  K is resulting from the different representation of the vortex' zonal mean shape in both data sets. Similar, but less pronounced bias-patterns can be found in MAM and SON 2003. In year 2002, a year with a considerably warmer polar vortex (minimum in the  $-90$  degree to  $-80$  degree band:  $185.0$  K at  $20$  km,  $3.3$  K warmer than in 2003) and a vortex split in late September [e.g., *Allen et al.*, 2003], the situation is qualitatively the same, but the bias magnitude is smaller compared to 2003 (maxima in JJA2002:  $-1.9$  K and  $+2.3$  K), suggesting that the bias is related to very low temperatures.

In opposite to the tropopause bias, the vortex bias is not accompanied by any remarkably increased random deviations (see Figure 7.15). Regarding the lessons learned from the validation studies presented in previous sections it can be clearly attributed to the ECMWF analysis since its magnitude is far beyond the error characteristics of the RO method and it cannot be attributed to resolution-induced effects or sampling errors. Furthermore, there is no physical reason why the RO method should perform worse at lower temperatures or southern polar latitudes.

It is remarkable that the nodes of the "bias wave pattern" at  $\sim 20$  km,  $\sim 25$  km, and  $\sim 30$  km are very close to the maxima of the temperature weighting functions of AMSU-A channels 10, 11, and 12 [e.g., *Staelin and Chen*, 2000], indicating that the bias may be related to the assimilation of AMSU-A radiances. However, an oscillatory vertical bias structure has also been found in ECMWF's re-analysis ERA-40 in the 1992 – 1997 January zonal mean temperatures [*Randel et al.*, 2004], a period with AMSU-A not yet available.

Figure 7.16 shows the ECMWF and CHAMP RO seasonal zonal mean temperature and the associated bias for JJA2004. The polar vortex still features a bias but its shape has changed compared to JJA2003: The wave pattern above  $20$  km is reduced in magnitude and the sign of the bias is partly reversed. Below  $20$  km the bias kept its shape and is even more pronounced than in 2002 and 2003. These changes are probably related to the addition of new data to the ECMWF analysis scheme in October 2003 (AIRS radiances)

[ECMWF, 2003] and changes in the assimilation scheme like bias adjustments of satellite data (A. Simmons, ECMWF, pers. communication, 2005).

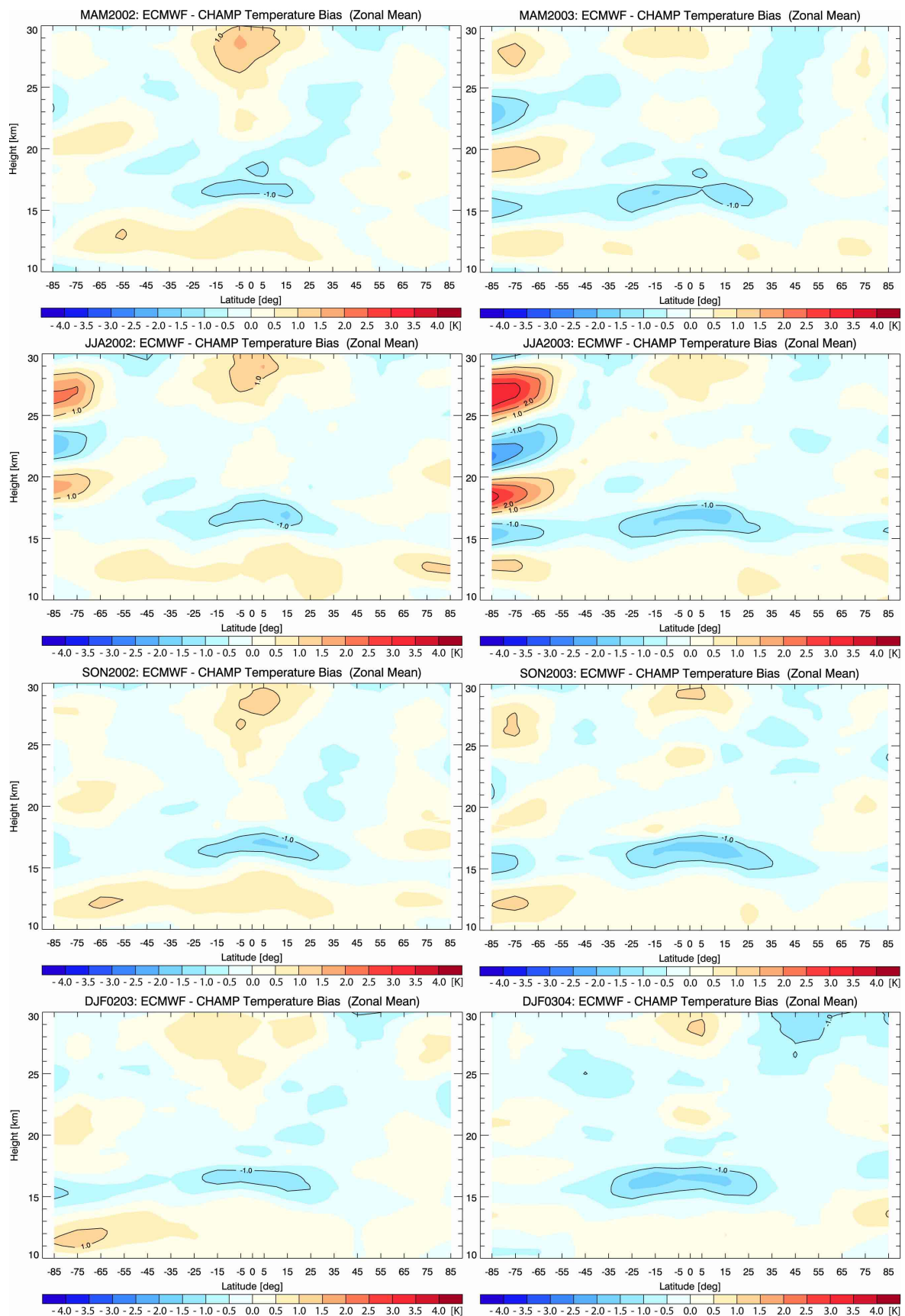


Figure 7.14: Seasonal zonal mean temperature bias (10 degree latitude bands) of ECMWF analyses vs. CHAMP RO data throughout four seasons (MAM2002 – DJF2003/2004).

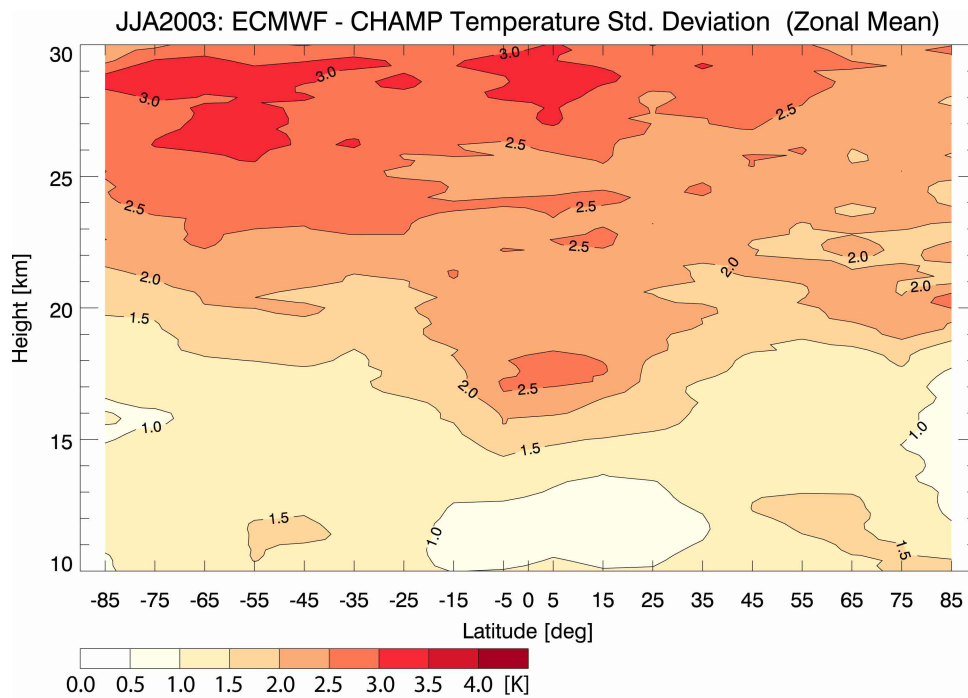


Figure 7.15: JJA2003 random temperature deviations (standard deviation of ECMWF vs. CHAMP differences).

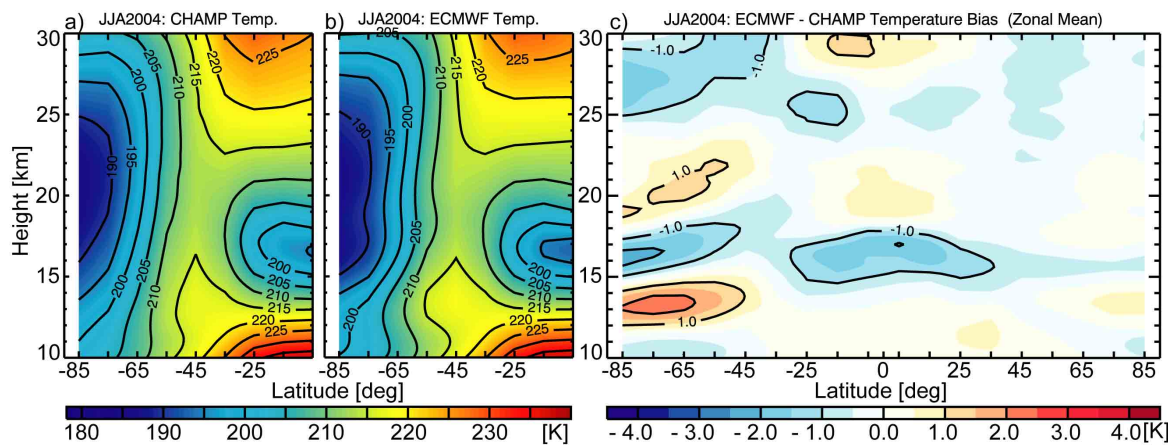


Figure 7.16: JJA2004 seasonal zonal mean CHAMP RO (a) and ECMWF (b) temperatures and ECMWF vs. CHAMP bias (c).

### Upper Stratosphere Bias

A further stable bias can be found when examining the ECMWF vs. CHAMP comparison results at higher altitudes between 30 and 40 km as exemplified in Figure 7.17 for the season DJF2003/2004. In this example, but also generally in all other seasons (not shown), the ECMWF analyses are cold biased by 1 K – 2 K above 30 km. Though CHAMP RO data retrieved with the IGAM/ECMWF scheme cannot be regarded as being entirely independent from background information at these altitudes, the influence of background information, which was extracted from ECMWF analysis, can only reduce the bias of ECMWF relative to IGAM/MSIS retrieval results. This implies that the found bias is related to deficiencies of ECMWF analyses in the upper stratosphere and amounts at least to – 1 K to – 2 K as shown in Figure 7.17.

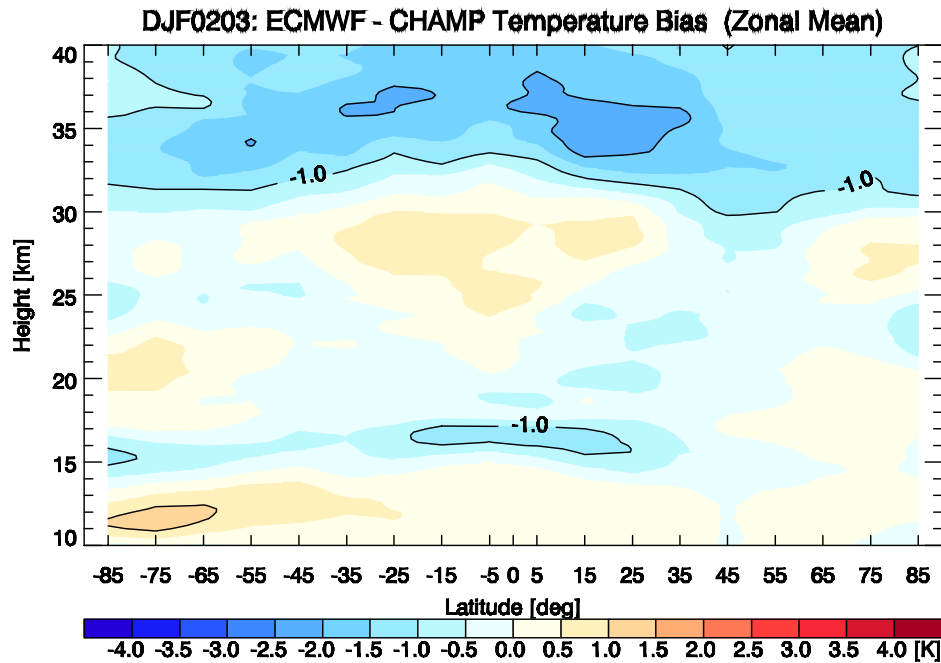


Figure 7.17: DJF2003/2004 seasonal zonal mean ECMWF vs. CHAMP bias.

### 7.3.5. Concluding Remarks

Generally, the results presented in this section show very good agreement between ECMWF analyses and CHAMP RO temperatures retrieved with the IGAM/ECMWF scheme in their seasonal zonal means between 10 km and 30 km (bias < 0.5 K) but also demonstrate deficiencies in the representation of the Austral polar vortex in the analyses (bias up to 3.5 K). Recent changes in the ECMWF assimilation scheme obviously reduced these problems in the 20 km – 30 km region but below 20 km the biases remain or even increase. Further studies including additional data are foreseen to obtain more clear insight. This polar vortex bias can have considerable impact, for example, on stratospheric ozone depletion studies.

Additionally, a systematic cold bias at the low-latitude tropopause was found. Though a minor contribution to this bias may root in the RO data, there is strong indication and independent evidence (A. Simmons, ECMWF, pers. communication, 2005) that it can be mainly attributed to the analyses. It is probably caused by weak representation of atmospheric wave activity and tropopause height variability, which is currently under closer study in the framework of the CHAMPCLIM project.

A cold bias of ECMWF compared to CHAMP in the upper stratosphere (above 30 km) of – 1 K to – 2 K demonstrates the relative independence of the IGAM/ECMWF retrieval scheme of the background information and indicates at the same time severe problems in the representation of upper stratosphere temperatures in ECMWF analyses.

These results reinforce evidence from recent and on-going impact experiments [Healy *et al.*, 2005] (S.B. Healy, ECMWF, pers. communication, 2005), that RO data will have significant positive impact when included in ECMWF's and other operational weather prediction systems.

# Conclusions

The first major objective of this thesis was the creation of a robust and bias-free retrieval scheme for atmospheric profiles from CHAMP RO data with special focus on the retrieval performance in the stratosphere. This work led to several important conclusions:

It has been shown that RO retrieval combined with any statistical optimization approach is superior to the so-called exponential extrapolation technique. Once using statistical optimization, one has to be aware that potential biases in the background information cannot be corrected for by this technique. Several implementations of statistical optimization, some of them including bias-correction steps, have been developed, implemented, and evaluated. The results of evaluation studies using simulated RO data revealed biases in the MSISE-90 climatology (used as background information) and demonstrated that these biases can be corrected for by comparison of background with observed RO data.

The advantage of this approach, which uses profiles of background information from climatology (e.g., MSISE-90) as a catalogue of possible states of the atmosphere from which it selects the most suitable one and additionally adjusts it towards the observation, is not only its better performance compared to other schemes, but also its greater degree of independency from modeled data. A further positive aspect is that high quality bending angle profiles up to 120 km, as can be obtained by this technique, enables to abandon any further background information in later steps of the retrieval, like model information for the initialization of the hydrostatic integral at stratospheric height within 30 km – 50 km.

The application of this scheme (IGAM/MSIS) to data from CHAMP showed similar quality as results from other leading institutions on refractivity level but a significant bias in temperatures above 15 km – 20 km demonstrating that, in this case, initialization of the hydrostatic integral would be necessary (just as it is the case in other schemes). This degraded performance compared to the results from simulated data can be explained by residual ionospheric noise stemming from small-scale structures in the ionosphere that were not modeled in the simulation study, by intermittent errors in the CHAMP high altitude data (e.g., artifacts caused by clock malfunctions), and by the overall noise level of CHAMP. However, since RO retrievals independent from NWP analyses are highly desirable, especially for their use in combination with models by means of data assimilation techniques, this scheme will be further developed to become more robust against noisy data, and better profile-search libraries than the MSISE-90 climatology are envisaged. Additionally, it could be demonstrated that refractivity profiles retrieved with IGAM/MSIS are of satisfactory quality with a bias in order of 0.1% up to 35 km, standard deviation below 1 % at 5 km – 20 km, and around 1.2 % up to 32 km.

To derive an optimal stand-alone temperature product, a second scheme using ECMWF operational analyses as background information has been developed. The IGAM/ECMWF scheme demonstrates that, by careful use of background information, relative independency from the background can be maintained up to 40 km whilst the retrieval performance, especially for temperature profiles, is significantly improved compared to the IGAM/MSIS scheme. Comparisons to various correlative data showed that the

IGAM/EWCMF temperature products are essentially unbiased between 5 km and 30 km. Furthermore, comparisons against ECMWF analyses showed a warm bias by  $\sim 1.5$  K between 30 km and 40 km demonstrating the relative independence from ECMWF and comparison to data from ENVISAT/MIPAS showed a very good agreement in this altitude region, which indicates that the encountered bias is probably attributable to the ECMWF data.

Generally, the performance studies show that the IGAM retrieval schemes are in-line, and in some aspects better performing, than state-of-the-art retrieval schemes of other institutions.

The second major objective was to generate and assess the quality of first global temperature climatologies based on the profiles obtained from the advanced RO retrieval process.

From the atmospheric profiles derived with the IGAM/ECMWF scheme the first RO based seasonal climatologies of refractivity and dry temperature has been derived demonstrating that seasonal zonal mean climatologies in 10 degree latitude bands are feasible with data from only one RO receiver like the one on CHAMP with small sampling errors (generally below 0.3 K). Additionally a severe sampling error in the low latitude troposphere region (additional to the well known measurement error in that region) has been described.

Finally, the validation of ECMWF operational analyses demonstrates the utility of RO data in general and CHAMPCLIM products in particular as climate reference datasets. The results revealed several significant deficiencies in the analyses and reinforce evidence from recent and on-going impact experiments, that RO data will have significant positive impact when included in ECMWF's and other operational weather prediction systems.

The CHAMP GPS receiver is currently the only RO instrument in continuous operation resulting in relatively coarse geographical resolution of RO climatologies. But near-future missions such as the European MetOp and the US/Taiwan COSMIC mission will soon provide a wealth of RO data which will be used to enhance the CHAMPCLIM climatologies and enable to create much finer resolved climatologies.

# References

- Ahmad, B., and G.L. Tyler (1999), Systematic errors in atmospheric profiles obtained from Abelian inversion of radio occultation data: Effects of large-scale horizontal gradients, *J. Geophys. Res.*, 104, D4, 3971-3992.
- Allen, D.R., R.M. Bevilacqua, G.E. Nedoluha, C.E. Randall, and G.L. Manney (2003), Unusual stratospheric transport and mixing during the 2002 Antarctic winter, *Geophys. Res. Lett.*, 30, 1599, doi:10.1029/2003GL017117.
- Andrews, D.G. (2000), *An introduction to atmospheric physics*, Cambridge University Press, Cambridge, United Kingdom.
- Ao, C.O., T.K. Meehan, G.A. Hajj, A.J. Mannucci, and G. Beyerle (2003), Lower-Troposphere Refractivity Bias in GPS Occultation Retrievals, *J. Geophys. Res.*, 108 (D18), 4577, 10.1029/2002JD003216.
- Baede, A.P.M., E. Ahlonsou, Y. Ding, D. Schimel, B. Bolin, and S. Pollonais (2001a), The climate system: An overview, in: *Climate Change 2001: The Scientific Basis. Contribution of Working Group I to the Third Assessment Report of the Intergovernmental Panel on Climate Change*, Houghton, J.T., Y. Ding, D.J. Griggs, M. Noguer, P.J. van der Linden, X. Dai, K. Maskell, and C.A. Johnson (eds.), Cambridge University Press, Cambridge, United Kingdom.
- Bassiri, S., and G.A. Hajj (1993), Higher-order ionospheric effects on the GPS observables and means of modeling them, *Manuscr. Geod.*, 18, 280-289.
- Bevis, M., S. Businger, S. Chiswell, T.H. Herring, R.A. Anthes, C. Rocken, and R.H. Ware (1994), GPS meteorology: Mapping zenith wet delays onto precipitable water, *J. Appl. Met.*, 33, 379-386.
- Beyerle, G., J. Wickert, T. Schmidt, and C. Reigber (2004), Atmospheric sounding by GNSS radio occultation: An analysis of the negative refractivity bias using CHAMP observations, *J. Geophys. Res.*, 109, D01106, doi: 10.1029/2003JD003922.
- Born, M., E. Wolf (1999), *Principles of optics*, 7<sup>th</sup> edition, Cambridge University Press, Cambridge, U.K.
- Borsche, M., A. Gobiet, A.K. Steiner, U. Foelsche, G. Kirchengast, T. Schmidt, and J. Wickert (2005), Pre-operational Retrieval of Radio Occultation Based Climatologies within the CHAMPCLIM Project, in *Occultations for Probing Atmosphere and Climate 2*, edited by U. Foelsche, A.K. Steiner, G. Kirchengast, Springer, Berlin-Heidelberg-New York, submitted.
- Budden, K.W. (1985), *The propagation of radio waves*, Cambridge University Press, Cambridge, U.K.
- Cubasch, U., et al (2001), Projections of Future Climate Change, in: *Climate Change 2001: The Scientific Basis. Contribution of Working Group I to the Third Assessment Report of the Intergovernmental Panel on Climate Change*, Houghton, J.T., Y. Ding, D.J. Griggs, M. Noguer, P.J. van der Linden, X. Dai, K. Maskell, and C.A. Johnson (eds.), Cambridge University Press, Cambridge, United Kingdom.
- ECMWF (2003), Changes to the operational forecasting system, *ECMWF Newsletter*, 99,1-2.
- ECMWF (2004), IFS documentation CY28r1, ECMWF, Reading, U.K.
- ESA (2004), ACE+ – Atmosphere and Climate Explorer, *Reports for Mission Selection. The Six Candidate Earth Explorer Missions*, ESA SP-1279(4), ESA Publications Division c/o ESTEC, Noordwijk, The Netherlands.
- Eyre, J.R. (1994), Assimilation of radio occultation measurements into a numerical weather prediction system, *Technical Memorandum No. 199*, ECMWF Research Department, Reading, U.K.
- Fieldbo, G., A.J. Kilore, R. Eshleman (1971), The neutral atmosphere of Venus as studied with the Mariner V radio occultation experiments, *Astron. J.*, 76, 123-140.

- Finlayson-Pitts, B.J., and J.N. Pitts Jr. (1999), *Chemistry of the upper and lower atmosphere*, 969pp, Academic Press, San Diego, CA, USA.
- Fishbach, F.F., A Satellite Method for Temperature and Pressure Below 24 km (1965), *Bull. Am. Meteorol. Soc.*, 9, 528-532.
- Fleming, E.L., S. Chandra, M.R. Shoeberl, and J.J. Barnett (1988), Monthly mean global climatology of temperature, wind, geopotential height and pressure for 0-120 km, *Tech. Memorandum 100697*, National Aeronautics and Space Administration, Washington, D.C.
- Foelsche, U. (1999), Tropospheric water vapor imaging by combination of spaceborne and ground-based GNSS sounding data, *Ph.D thesis*, Inst. for Geophys., Astrophys., and Meteorol., Univ. of Graz, Austria.
- Foelsche, U., G. Kirchengast, and A.K. Steiner (2003), Global climate monitoring based on CHAMP/GPS radio occultation data, First CHAMP Mission Results, in *First CHAMP Mission Results for Gravity, Magnetic and Atmospheric Studies*, edited by C. Reigber et al., Springer-Verlag, Heidelberg, 397-407.
- Foelsche, U., and G. Kirchengast, Sensitivity of GNSS occultation profiles to horizontal variability in the troposphere: A simulation study (2004a), in *Occultations for Probing Atmosphere and Climate*, edited by G. Kirchengast, U. Foelsche, A.K. Steiner, Springer, Berlin-Heidelberg-New York, 127-136.
- Foelsche, U., and G. Kirchengast (2004b), Sensitivity of GNSS radio occultation data to horizontal variability in the troposphere, *Phys. Chem. Earth*, 29(2-3), 225-240, doi:10.1016/j.pce.2004.01.007.
- Foelsche, U., A. Gobiet, A. Löscher, G. Kirchengast, A.K. Steiner, J. Wickert, and T. Schmidt (2005), The CHAMPCLIM project: An overview, in *Earth observation with CHAMP - Results from three years in orbit*, edited by C. Reigber, H. Lühr, P. Schwintzer, and J. Wickert, Springer, Berlin-Heidelberg-New York, 615-620.
- Folland, C.K., T.R. Karl, J.R. Christy, R.A. Clarke, G.V. Gruza, J. Jouzel, M.E. Mann, J. Oerlemans, M.J. Salinger and S.-W. Wang (2001), Observed Climate Variability and Change, in: *Climate Change 2001: The Scientific Basis. Contribution of Working Group I to the Third Assessment Report of the Intergovernmental Panel on Climate Change*, Houghton, J.T., Y. Ding, D.J. Griggs, M. Noguer, P.J. van der Linden, X. Dai, K. Maskell, and C.A. Johnson (eds.), Cambridge University Press, Cambridge, United Kingdom.
- Forster, P.M.D., and K.P. Shine (2002), Assessing the climate impact of trends in stratospheric water vapor, *Geophys. Res. Lett.*, 29, 1086, 10.1029/2001GL013909.
- Gates, W.L., J. Boyle, C. Covey, C. Dease, C. Doutriaux, R. Drach, M. Fiorino, P. Gleckler, J. Hnilo, S. Marlais, T. Phillips, G. Potter, B.D. Santer, K.R. Sperber, K. Taylor, D. Williams (1999), An overview of the results of the Atmospheric Model Intercomparison Project (AMIP I). *Bull. Am. Met. Soc.*, 80, 29-55.
- Giorgi, F., et al (2001), Regional Climate Information – Evaluation and Projections, in: *Climate Change 2001: The Scientific Basis. Contribution of Working Group I to the Third Assessment Report of the Intergovernmental Panel on Climate Change*, Houghton, J.T., Y. Ding, D.J. Griggs, M. Noguer, P.J. van der Linden, X. Dai, K. Maskell, and C.A. Johnson (eds.), Cambridge University Press, Cambridge, United Kingdom.
- Gobiet A. and G. Kirchengast (2002), Sensitivity of atmospheric profiles retrieved from GNSS occultation data to ionospheric residual and high-altitude initialization errors. *Tech. Rep. ESA/ESTEC-1/2002*, Inst. for Geophys., Astrophys., and Meteorol., Univ. of Graz, Austria.
- Gobiet, A., and G. Kirchengast (2004), Advancements of GNSS radio occultation retrieval in the upper stratosphere for optimal climate monitoring utility, *J. Geophys. Res.* 109, D24110, doi:10.1029/2004JD005117.
- Gobiet, A., A.K. Steiner, C. Retscher, U. Foelsche, and G. Kirchengast (2004), Radio Occultation Data and Algorithms Validation Based on CHAMP/GPS Data, *Tech. Report for ASA No. 1/2004*, 50 p., Inst. for Geophys., Astrophys., and Meteorol., Univ. of Graz, Austria.
- Gobiet, A., U. Foelsche, A.K. Steiner, M. Borsche, G. Kirchengast, and J. Wickert (2005), Climatological validation of stratospheric temperatures in ECMWF operational analyses with CHAMP radio occultation data, *Geophys. Res. Lett.*, 32, L12806, doi:10.1029/2005GL022617.
- Goody, R., J. Anderson, T. Karl, R. Balstad Miller, G. North, J. Simpson, G. Stephens, and W. Washington (2002), Why monitor climate change?, *Bull. Amer. Met. Soc.*, 83, 6, 873-878.
- Goody, R., J. Anderson, and G. North (1998), Testing climate models: An approach, *Bull. Amer. Met. Soc.*, 79, 11, 2541-2554.

- Gorbunov, M.E., S.V. Sokolovskiy, and L. Bengtsson (1996), Space refractive tomography of the atmosphere: modeling of direct and inverse problems, *Tech. Rep. No. 210*, Max-Planck Institute for Meteorology, Hamburg, Germany.
- Gorbunov, M.E., and A.S. Gurvich (1998), Algorithms of inversion of Microlab-1 satellite data including the effects of multipath propagation, *Int. J. Remote Sensing*, 19, 2283-2300.
- Gorbunov, M.E., A.S. Gurvich, and L. Kornblueh (2000), Comparative analysis of radioholographic methods of processing radio occultation data, *Radio Sci.*, 35(4), 1025– 1034.
- Gorbunov, M.E. (2002a), Canonical transform method for processing radio occultation data in the lower troposphere, *Radio Sci.*, 37(5), 1076, doi:10.1029/2000RS002592.
- Gorbunov, M.E. (2002b), Radio-holographic analysis of Microlab-1 radio occultation data in the lower troposphere, *J. Geophys. Res.*, 107(D12), 4156, doi:10.1029/2001JD000889.
- Gorbunov, M.E. (2002c), Ionospheric correction and statistical optimization of radio occultation data, *Radio Sci.*, 37, 1084, doi: 10.1029/2000RS002370.
- Gorbunov, M.E. (2002d), Radioholographic analysis of radio occultation data in multipath zones, *Radio Sci.*, 37(1), 1014, doi:10.1029/2000RS002577.
- Gorbunov, M.E., and L. Kornblueh (2003), Analysis and validation of Challenging Minisatellite Payload (CHAMP) radio occultation data, *J. Geophys. Res.*, 108, 4584, doi:10.1029/2002JD003175.
- GRAS-SAG (1998), The GRAS instrument on MetOp, *ESA/EUMETSAT Rep.* (ESA No. VR/3021/PI, EUMETSAT No. EPS/MIS/IN/9), ESA/ESTEC, Noordwijk, Netherlands.
- Gurvich, A.S. and T.G. Krasil'nikova (1987, 1990), Navigation Satellites for Radio Sensing of the Earth's Atmosphere. *Sov. J. Remote Sensing*, 6, 89-93, 1987 (in Russian), 6, 1124-1131, 1990 (in English).
- Hajj, G.A., E.R. Kursinski, L.J. Romans, W.I. Bertinger, S.S. Leroy (2002), A technical description of atmospheric sounding by GPS occultation, *J. Atmos. Sol.-Terr. Phys.*, 64, 451-469.
- Hajj, G.A., C.O. Ao, B.A. Iijima, D. Kuang, E.R. Kursinski, A.J. Mannucci, T.K. Meehan, L.J. Romans, M. de la Torre Juarez, and T.P. Yunck (2004), CHAMP and SAC-C atmospheric occultation results and intercomparisons, *J. Geophys. Res.*, 109, D06109, doi:10.1029/2003JD003909.
- Hajj, G.A., et al. (2004)
- Hardy, K.R., G.A. Hajj, and E.R. Kursinski (1994), Accuracies of atmospheric profiles obtained from GPS occultations, *Int. J. Satell. Commun.*, 12, 463-473.
- Hare, S. H. E., L. J. Gray, W. A. Lahoz, A. O'Neill, and L. Steenman-Clark (2004), Can stratospheric temperature trends be attributed to ozone depletion?, *J. Geophys. Res.*, 109, D05111, doi:10.1029/2003JD003897.
- Healy, S.B. and J.R. Eyre (2000), Retrieving temperature, water vapour and surface pressure information from refractive-index profiles derived by radio occultation data: A simulation study, *Q. J. R. Meteorol. Soc.*, 126, 1661-1683.
- Healy, S. B., A. M. Jupp, and C. Marquardt (2005), Forecast impact experiment with GPS radio occultation measurements, *Geophys. Res. Lett.*, 32, L03804, doi:10.1029/2004GL020806.
- Hedin, A.E. (1991), Extension of the MSIS thermosphere model into the middle and lower atmosphere, *J. Geophys. Res.*, 96, 1159-1172.
- Hertzog, A., C. Basdevant, F. Vial, C.R. Mechoso (2004), The accuracy of stratospheric analyses in the northern hemisphere inferred from long-duration balloon flights, *QJRM*, 130, 597, 607-626.
- Hocke, K. (1997), Inversion of GPS meteorology data, *Ann. Geophysicae*, 15, 443-450.
- Hocke, K., K. Igarashi, and T. Tsuda (2003), High-resolution profiling of layered structures in the lower stratosphere by GPS occultation, *Geophys. Res. Lett.*, 30(8), 1426, doi:10.1029/2002GL016566.
- Hofman-Wellenhof, B., H. Lichtenegger, and J. Collins (1992), *GPS: Theory and Practice*, Springer, Berlin.
- IPCC (2000), *IPCC Special Report Emission Scenarios. Summary for Policy Makers*, N. Nakicenovic and R. Swart (eds.), Cambridge University Press, Cambridge, UK.
- IPCC (2001a), *Climate Change 2001: The Scientific Basis. Contribution of Working Group I to the Third Assessment Report of the Intergovernmental Panel on Climate Change*, J.T. Houghton, Y. Ding, D.J. Griggs,

- M. Noguer, P.J. van der Linden, X. Dai, K. Maskell, and C.A. Johnson (eds.), Cambridge University Press, Cambridge, United Kingdom.
- IPCC (2001b), *Climate Change 2001: Impacts, Adaptation, and Vulnerability. Contribution of Working Group II to the Third Assessment Report of the Intergovernmental Panel on Climate Change*, J.J. McCarthy, O.F. Canziani, N.A. Leary, D.J. Dokken, K.S. White (eds.), Cambridge University Press, Cambridge, United Kingdom.
- International Climate Change Taskforce (2005), *Meeting the climate challenge*, The Institute for Public Policy Research, London, UK; The Center for American Progress, Washington, D.C., U.S.A.; The Australian Institute, Canberra, Australia.
- Jackson, J.D. (1983), *Klassische Elektrodynamik*, Walter de Gruyter, Berlin-New York.
- Jensen, A.S., M.S. Lohmann, H.-H. Benzon, and A.S. Nielsen (2003), Full Spectrum Inversion of radio occultation signals, *Radio Sci.*, 38(3), 1040, doi:10.1029/2002RS002763.
- Kiehl, J.T., and Kevin E. Trenberth (1997), Earth's annual global mean energy budget, *Bull. Amer. Meteor. Soc.*, 78, 2, 197-208.
- Kirchengast, G., A.K. Steiner, U. Foelsche, L. Kornblueh, E. Manzini, and L. Bengtsson (2000), Spaceborne climate change monitoring by GNSS occultation sensors, *Proc. 11th Symp. on Global Change Studies*, Amer. Met. Soc. Annual Meeting 2000, Long Beach/CA, U.S.A., 62-65.
- Kirchengast, G., J. Fritzer, and J. Ramsauer (2002), End-to-end GNSS Occultation Performance Simulator Version 4 (EGOPS4) Software User Manual (Overview and Reference Manual), *Techn. Report for ESA/ESTEC No. 3/2002*, Inst. for Geophys., Astrophys., and Meteorol., Univ. of Graz.
- Kirchengast, G. (2003), CHAMPCLIM. Radio Occultation Data Analysis Advancement and Climate Change Monitoring based on the CHAMP/GPS Experiment – Part I, Updated CHAMPCLIM Proposal to ASA, University of Graz, Austria.
- Kirchengast, G. and P. Høeg (2004), The ACE+ Mission: An Atmosphere and Climate Explorer based on GPS, GALILEO, and LEO-LEO Radio Occultation, in *Occultation for Probing Atmosphere and Climate*, G. Kirchengast, U. Foelsche, A.K. Steiner (Eds.), Springer, Berlin-Heidelberg-New York, 201-220.
- Knudsen, B.M. (2003), On the accuracy of analysed low temperatures in the stratosphere, *Atmos. Chem. Phys.*, 3, 1759-1768.
- König, R., S. Zhu, C. Reigber, K.-H. Neumayer, H. Meixner, R. Galas, G. Baustert, and P. Schwintzer (2002), CHAMP rapid orbit determination for GPS atmospheric limb sounding, *Adv. Space Res.*, 30, 2, 289-293.
- Kuo, Y.-H., T.-K. Wee, S. Sokolovskiy, C. Rocken, W. Schreiner, D. Hunt, and R.A. Anthes (2004), Inversion and Error Estimation of GPS Radio Occultation Data, *J. Meteor. Soc. Japan*, 82, 1B, 507-531.
- Kursinski, E.R., G.A. Hajj, K.R. Hardy, L.J. Romans and L.T. Schofield (1995), Observing tropospheric water vapor by radio occultation using the Global Positioning System, *Geophys. Res. Lett.*, 22, 2 365-2 368, 1995.
- Kursinski, E.R., et al., (1996), Initial Results of Radio Occultation of Earth's Atmosphere Using the Global Positioning System. *Science*, 271, 1107-1110.
- Kursinski, E.R., G.A. Hajj, J.T. Schofield, R.P. Linfield, and K.R. Hardy (1997), Observing Earth's Atmosphere with Radio Occultation Measurements Using the Global Positioning System, *J. Geophys. Res.*, 102, 23429-23465.
- Kursinski, E.R., and G.A. Hajj (2001), A comparison of water vapor derived from GPS occultations and global weather analyses, *J. Geophys. Res.*, 106, 1113-1138.
- Ladreiter, H.P., G. Kirchengast (1996), GPS/GLONASS sensing of the neutral atmosphere: Model-independent correction of ionospheric influences, *Radio Sci.*, 31, 4, 877-891.
- Lee, L.-C., C. Rocken, and E.R. Kursinski (eds.) (2001), *Applications of Constellation Observing System for Meteorology, Ionosphere, and Climate*, Springer Verlag, Hong Kong, China.
- Leitinger, R., and G. Kirchengast (1997a), Easy to use global and regional models – a report on approaches used in Graz, *Acta Geod. Geophys. Hung.*, 32, 329-342.
- Leitinger, R., and G. Kirchengast (1997b), Inversion of the plasma signal in GNSS occultations – simulation studies and sample results, *Acta Geod. Geophys. Hung.*, 32, 379-394.
- Lusignan, B., G. Modrell, A. Morrison, J. Pomalaza, and S.G. Ungar (1969), Sensing the Earth's Atmosphere with Occultation Satellites, *Proc. IEEE*, 4, 458-467.

- Mann, M.E., R.S. Bradley, and M.K. Hughes (1999), Northern Hemisphere temperature during the past millennium: Inferences, uncertainties, and limitations, *Geophys. Res. Lett.*, 26, 6, 759-762.
- Mann, M.E., R.S. Bradley, and M.K. Hughes (1998), Global-scale temperature patterns and climate forcing over the past six centuries, *Nature*, 392, 779-787.
- Manney, G.L., et al. (2003), Lower stratospheric temperature differences between meteorological analyses in two cold Arctic winters and their impact on polar processing studies, *J. Geophys. Res.*, 108, 8328, doi:10.1029/2001JD001149.
- Melbourne, W.G., E.S. Davies, C.D. Duncan, G.A. Hajj, K.R. Hardy, E.R. Kursinski, T.E. Meehan, L.E. Young, and T.P. Yunck (1994), The application of spaceborne GPS to atmospheric limb sounding and global change monitoring, JPL Publication 94-18, Jet Propulsion Laboratory, Pasadena, CA, U.S.A.
- Mitchell, J.F.B et al. (2001), Detection of climate change and attribution of causes, in: *Climate Change 2001: The Scientific Basis. Contribution of Working Group I to the Third Assessment Report of the Intergovernmental Panel on Climate Change*, Houghton, J.T., Y. Ding, D.J. Griggs, M. Noguer, P.J. van der Linden, X. Dai, K. Maskell, and C.A. Johnson (eds.), Cambridge University Press, Cambridge, United Kingdom.
- Moberg, A., D.M. Sonechkin, K. Holmgren, N.M. Datsenko, W. Karlén (2005), High variable Northern Hemisphere temperatures reconstructed from low- and high-resolution proxy data, *Nature*, 433, 613-617.
- Moritz, H. (1980), Geodetic reference system 1980, *Bulletin Géodésique*, 54, 395-405.
- Palmer, P.I., J.J. Barnett, J.R. Eyre, S.B. Healy (2000), A nonlinear optimal estimation method for radio occultation measurements of temperature, humidity, and surface pressure, *J. Geophys. Res.*, 105(D13), 17513-17525.
- Peixoto, J.P. and A.H. Oort (1992), *Physics of climate*, 520pp, American Institute of Physics, Woodbury, NY.
- Peixoto, J.P. and A.H. Oort (1996), The climatology of relative humidity in the atmosphere, *J. Climate*, 9, 3443-3463.
- Prentice, I.C. et al. (2001), The carbon cycle and atmospheric carbon dioxide, in: *Climate Change 2001: The Scientific Basis. Contribution of Working Group I to the Third Assessment Report of the Intergovernmental Panel on Climate Change*, Houghton, J.T., Y. Ding, D.J. Griggs, M. Noguer, P.J. van der Linden, X. Dai, K. Maskell, and C.A. Johnson (eds.), Cambridge University Press, Cambridge, United Kingdom.
- Ramaswamy, V., et al. (2001), Radiative forcing of climate change, in: *Climate Change 2001: The Scientific Basis. Contribution of Working Group I to the Third Assessment Report of the Intergovernmental Panel on Climate Change*, Houghton, J.T., Y. Ding, D.J. Griggs, M. Noguer, P.J. van der Linden, X. Dai, K. Maskell, and C.A. Johnson (eds.), Cambridge University Press, Cambridge, United Kingdom.
- Randel, W., E. Fleming, N. Geller, M. Gelman, K. Hamilton, D. Karoly, D. Ortland, S. Pawson, R. Swinbank, P. Udelhofen, F. Wu, M. Baldwin, M.-L. Chanin, P. Keckhut, A. Simmons, D. Wu (2003), The SPARC intercomparison of middle atmosphere climatologies, *SPARC Newsletter*, 20, 10-15.
- Randel, W., et al. (2004), The SPARC intercomparison of middle-atmosphere climatologies, *J. Climate*, 17, 986-1003.
- Reigber, C., P. Schwintzer, and A. Kohlhasse (1995), CHAMP – A challenging micro-satellite payload for geophysical research and application, Feasibility study for DARA, *Final report*, GFZ Potsdam, Germany.
- Retscher, C., A. Gobiet, and G. Kirchengast, Stratospheric temperature and ozone sounding with ENVISAT/GOMOS stellar occultation (2004), in *Occultation for Probing Atmosphere and Climate*, G. Kirchengast, U. Foelsche, A.K. Steiner (Eds.), Springer, Berlin-Heidelberg-New York, 299-308.
- Rieder, M.J., and G. Kirchengast (2001), Error analysis and characterization of atmospheric profiles retrieved from GNSS occultation data, *J. Geophys. Res.*, 106(D23), 31755-31770.
- Rocken C., et al. (1997), Analysis and Validation of GPS/MET Data in the Neutral Atmosphere, *J. Geophys. Res.*, 102(D25), 29849-29866.
- Rodgers, C.D. (2000), *Inverse Methods for Atmospheric Sounding: Theory and Practice*, World Scientific Publ., Singapore.
- Roeckner E, L. Bengtsson, J. Feichter, J. Lelieveld, H. Rodhe (1999), Transient climate change simulations with a coupled atmosphere-ocean gcm including the tropospheric sulfur cycle, *J. Climate*, 12, 3004-3032.

- Santer, B. D., et al. (2003), Behavior of tropopause height and atmospheric temperature in models, reanalyses and observations: Decadal changes, *J. Geophys. Res.*, 108(D1), 4002, doi:10.1029/2002JD002258.
- Schröder, T., S. Leroy, M. Stendel, and E. Kaas (2003), Validating the microwave sounding unit stratospheric record using GPS occultation, *Geophys. Res. Lett.*, 30, 1734, doi:10.1029/2003GL017588.
- Schweitzer, S. (2004), Atmosphere and Climate Explorer Mission ACE+: Humidity and Temperature Retrieval Performance Analysis, *Master Thesis*, Institute for Geophysics, Astrophysics, and Meteorology, University of Graz, Austria.
- Solheim, F.S., J. Vivekanandan, R.H. Ware, C. Rocken (1999), Propagation delays induced in GPS signals by dry air, water vapor, hydrometeors, and other particulates, *J. Geophys. Res.*, 104, 9663-9670.
- Smith, E.K., and S. Weintraub (1953), The constants in the equation for atmospheric refractive index at radio frequencies, *Proceedings of the I.R.E.*, 41, 1035-1037.
- Sokolovskiy, S., and D. Hunt (1996), Statistical optimization approach for GPS/Met data inversions, paper presented at URSI GPS/Met Workshop, Tucson, Arizona.
- Spilker, J.J. (1980), Signal Structure and Performance Characteristics, in: Janiczek, P.M. (ed.), *Global Positioning System: Papers Published in NAVIGATION*, Vol.1, Institute of Navigation, Washington, DC, U.S.A., 29-54.
- Stainforth, D.A., et al. (2005), Uncertainty in predictions of the climate response to rising levels of greenhouse gases, *Nature*, 433, 403-406.
- Staelin, D.H., and F.W. Chen (2000), Precipitation Observations Near 54 and 183 GHz Using the NOAA-15 Satellite, *IEEE Trans. Geosci. Remote Sensing*, 38, 2322-2332.
- Steiner, A.K., (1998), High resolution sounding of key climate variables using the radio occultation technique, *Ph.D. thesis*, Institute for Meteorology and Geophysics, University of Graz, Austria.
- Steiner, A.K. (2004), Error Analyses of Refractivity Profiles Retrieved from CHAMP Radio Occultation Data, Danish Meteorological Institute (DMI) Scientific Report, 04-02, Copenhagen, Denmark.
- Steiner, A.K., G. Kirchengast, and H.P. Ladreiter (1999), Inversion, Error Analysis and Validation of GPS/MET Occultation Data, *Ann. Geophys.*, 17, 22-138.
- Steiner, A.K., G. Kirchengast, U. Foelsche, L. Kornblueh, E. Manzini, and L. Bengtsson (2001), GNSS occultation sounding for climate monitoring, *Phys. Chem. Earth A*, 26, 13-124.
- Steiner, A. K., and G. Kirchengast (2004), Ensemble-based analysis of errors in atmospheric profiles retrieved from GNSS occultation data, *Occultations for Probing Atmosphere and Climate*, G. Kirchengast, U. Foelsche, A.K. Steiner (Eds.), Springer, Berlin-Heidelberg-New York, 149-160, 2004.
- Steiner, A.K., A. Gobiet, U. Foelsche, and G. Kirchengast (2004), Radio occultation data processing advancements for optimizing climate utility, *Tech. Report for ASA No. 3/2004*, 87p., Inst. f. Geophys., Astrophys., and Meteorol., Univ. Graz, Austria.
- Syndergaard, S. (2000), On the ionosphere calibration in GPS radio occultation measurements, *Radio Sci.*, 35, 865-883.
- Syndergaard, S. (1999), Retrieval analysis and methodologies in atmospheric limb sounding using the GNSS radio occultation technique, *Scientific Report*, 99-6, Danish Meteorological Institute, Copenhagen, Denmark.
- Syndergaard, S. (1998), Modeling the impact of the Earth's oblateness on the retrieval of temperature and pressure profiles from limb sounding, *J. Atmos. Sol.-Terr. Phys.*, 60, 2, 171-180.
- Syndergaard, S., D. Flittner, R. Kursinski, D. Feng, B. Herman, and D. Ward (2003), Simulating the influence of horizontal gradients on retrieved profiles from ATOMS occultation measurements – a promising approach for data assimilation, , in *Occultations for Probing Atmosphere and Climate*, edited by G. Kirchengast, U. Foelsche, A.K. Steiner, Springer, Berlin-Heidelberg-New York, 221-232.
- Thayer, G.D. (1974), An improved equation for the radio refractive index of air, *Radio Sci.*, 9, 803-807.
- Thépaut, J.-N., and E. Andersson (2003), Assimilation of high-resolution satellite data, *ECMWF Newsletter*, 97, 6-12.
- Turchin, V.F., and V.Z. Nozik (1969), Statistical regularization of the solution of incorrectly posed problems, *Phys. Atmos. Ocean*, 5(1), 14-18.

- von Clarmann, T., N. Glatthor, U. Grabowski, M. Höpfner, S. Kellmann, M. Kiefer, A. Linden, G. Mengistu Tsidu, M. Milz, T. Steck, G. P. Stiller, D. Y. Wang, H. Fischer, B. Funke, S. Gil-López, and M. López-Puertas (2003a), Retrieval of temperature and tangent altitude pointing from limb emission spectra recorded from space by the Michelson Interferometer for Passive Atmospheric Sounding (MIPAS), *J. Geophys. Res.*, 108, D23, 4736, doi:10.1029/2003JD003602.
- von Clarmann, T., S. Ceccherini, A. Doicu, A. Dudhia, B. Funke, U. Grabowski, S. Hilgers, V. Jay, A. Linden, M. López-Puertas, F.-J. Martín-Torres, V. Payne, J. Reburn, M. Ridolfi, F. Schreier, G. Schwarz, R. Siddans, and T. Steck, A blind test retrieval experiment for infrared limb emission spectrometry, *J. Geophys. Res.*, 108, D23, 4746, doi:10.1029/2003JD003835.
- von Engeln A., G. Nedoluha, G. Kirchengast, and S. Bühler (2003), One-dimensional variational (1-D Var) retrieval of temperature, water vapor, and a reference pressure from radio occultation measurements: A sensitivity analysis, *J. Geophys. Res.*, 108(D11), 4337, doi:10.1029/2002JD002908.
- Vorob'ev, V.V. and T.G. Krasnil'nikova (1994), Estimation of the accuracy of the atmospheric refractive index recovery from Doppler shift measurements at frequencies used in the NAVSTAR system, *Phys. Atmos. Ocean*, 29, 602-609.
- Wang, D.Y., J. Wickert, G. Stiller, T. Clarmann, G. Beyerle, T. Schmidt, M.L. Puertas, B. Funke, S. Gil-López, N. Glatthor, U. Grabowski, M. Höpfner, S. Kellmann, M. Kiefer, A. Linden, G.M. Tsidu, M. Milz, T. Steck, H. Fischer, and Ch. Reigber (2004), Comparisons of MIPAS/ENVISAT and GPS-RO/CHAMP Temperature Profiles, in *Earth Observation with CHAMP. Results from Three Years in Orbit*, edited by C. Reigber et al., Springer-Verlag, Heidelberg, 567-572.
- Ware, R., et al., GPS Sounding of the atmosphere from low Earth orbit: Preliminary results, *Bull. Am. Meteorol. Soc.*, 77, 19-40, 1996.
- WGS (1998), *WGS 84 Implementation Manual*, prepared by the European Organization for the Safety of Air Navigation (EUROCONTROL), Brussels, Belgium, and Institute of Geodesy and Navigation (IfEN), University Munich, Germany.
- Wickert, J., C. Reigber, G. Beyerle, R. König, C. Marquardt, T. Schmidt, L. Grunwaldt, R. Galas, T.K. Meehan, W.G. Melbourne, and K. Hocke (2001), Atmosphere sounding by GPS radio occultation: first results from CHAMP, *Geophys. Res. Lett.*, 28, 3263-3266.
- Wickert, J. (2002), Das CHAMP-Radiokkultationsexperiment: Algorithmen, Prozessierungssystem und erste Ergebnisse, *Ph.D. thesis, Scientific Technical Report STR02/07*, GeoForschungZentrum Potsdam, Germany.
- Wickert, J., R. Galas, T. Schmidt, G. Beyerle, C. Reigber, C. Förste, and M. Ramatschi (2004a), Atmospheric sounding with CHAMP: GPS ground station data for occultation processing, *Phys. Chem. Earth.*, 29, 267-275.
- Wickert, J., T. Schmidt, G. Beyerle, R. König, C. Reigber, and N. Jakowski (2004b), The radio occultation experiment aboard CHAMP: Operational data analysis and validation of vertical atmospheric profiles, *J. Meteorol. Soc. Jpn*, 82, 381-395.
- Wickert, J., A. Gobiet, G. Beyerle, A. Steiner, G. Kirchengast, U. Foelsche, T. Schmidt (2004c), GPS radio occultation with CHAMP: Comparison of atmospheric profiles from GFZ Potsdam and IGAM Graz, in *Earth Observation with CHAMP. Results from Three Years in Orbit*, edited by C. Reigber et al., Springer-Verlag, Heidelberg, 525-530.
- Wickert, J., G. Beyerle, R. König, S. Heise, L. Grunwaldt, G. Michalak, Ch. Reigber, and T. Schmidt (2005), GPS radio occultation with CHAMP and GRACE: A first look at a new and promising satellite configuration for global atmospheric sounding, *Ann. Geophys.*, 653-658.
- WMO (2003), *The second report on the adequacy of the global observing systems for climate in support of the UNFCCC, GCOS-82*, WMO, Geneva, Switzerland.
- Yunck, T.P., G.F. Lindal, and C.H. Liu (1988), The Role of GPS in Precise Earth Observation. *Proc. IEEE Position, Location and Navigation Symposium (PLANS 88)*, Orlando, FL., Nov. 29-Dec. 2.
- Yunck, T.P., C.H. Liu, and R. Ware (2000), A history of GPS sounding, *Terr. Atmos. Oceanic Sci.*, 11, 1, 1-20.



# List of Symbols

$^{\circ}\text{C}$	degree Celsius
$\nabla$	gradient operator
$\nabla \cdot$	divergence operator
$\Delta \cdot$	Laplace operator
$\nabla \times$	rotation operator
$\nabla_{\perp \mathbf{s}}$	gradient perpendicular to the direction of vector $\mathbf{s}$
$\alpha$	total bending angle of an GNSS ray passing the atmosphere in limb sounding geometry [rad]
$\bar{\alpha}_k$	low-pass filtered bending angle of signal $Lk$ [rad]
$\alpha_C$	ionosphere corrected angle [rad]
$\alpha_k$	total bending angle of signal $Lk$ [rad]
$\gamma$	angle between the two lines connecting the center of refraction with the satellites
$\gamma_k^I$	extra optical path of a received GPS signal caused by the ionosphere [m]
$\gamma^N$	extra optical path of a received GPS signal caused by neutral atmosphere [m]
$\gamma^V$	optical path of a received GPS signal corresponding to the signal travel time in vacuum [m]
$\gamma_k$	extra optical path of a received GPS signal caused by neutral atmospheric and ionospheric refraction [m]
$\delta\alpha_1, \delta\alpha_2$	high-pass fractions of bending angles
$\varepsilon$	electric permittivity [ $\text{AsV}^{-1}\text{m}^{-1}$ ]
$\varepsilon_r$	electric permittivity of a medium [1]
$\varepsilon_0$	dielectric constant: $8.854\,188 \dots \cdot 10^{-12} \text{ AsV}^{-1}\text{m}^{-1}$
$\theta_L$	angel between the center to LEO-satellite line and the ray direction
$\theta_G$	angel between the center to GPS-satellite line and the ray direction
$\lambda$	wavelength [m]
$\mu_0$	magnetic constant: $4\pi \cdot 10^{-7} \text{ VsA}^{-1}\text{m}^{-1}$
$\nu_k$	extra optical path of a received GPS signal caused by receiver noise (thermal noise and local multi-path effects) [m]
$\pi$	Pi: 3.141593
$\rho$	charge density [ $\text{C m}^{-3}$ ]
$\vec{\sigma}$	conductivity tensor [ $\Omega \text{ m}^{-1}$ ]
$\varphi$	angle between $\mathbf{r}$ and the tangent of the ray at point $\mathbf{r}$
$\phi$	latitude [deg]
$\Phi_k$	recorded phase in number of cycles of signal $Lk$ [1]
$\vec{\chi}_e$	electric susceptibility tensor [1]
$\vec{\chi}_m$	magnetic susceptibility tensor [1]
$a$	impact parameter [m]

<b>B</b>	magnetic induction [T]
$B_{par}$	absolute value of Earth's magnetic field parallel to EM wave propagation [T]
$C$	constant in the reduced Appelton-Hartree formula: $40.3 \text{ m}^3 \text{ s}^{-2}$
$C^G, C^L$	extra optical path of a received GPS signal caused by transmitter and receiver clock errors [m]
$C_{CA}, C_{P1}$	Power of the $CA$ and $L1 P$ components of $L1$
$C_{P2}$	Power of $L2$
$c$	EM wave's phase velocity in a refractive medium [ $\text{ms}^{-1}$ ]
$c_0$	EM wave's phase velocity in vacuum: $299\,792\,458 \text{ ms}^{-1}$
$ds$	arc element
<b>D</b>	dielectric displacement [ $\text{C m}^{-2}$ ]
$D(t)$	Amplitude modulation on GPS signals containing navigation data
<b>E</b>	electric field strength [ $\text{V m}^{-1}$ ]
$e$	pressure of water vapor [hPa]
$f$	frequency [ $\text{s}^{-1}$ ]
$f_D$	Doppler shift [ $\text{s}^{-1}$ ]
$f_k$	transmitted carrier frequency of signal $Lk$ [ $\text{s}^{-1}$ ]
$f_L$	received carrier frequency [ $\text{s}^{-1}$ ]
$f_G$	transmitted carrier frequency [ $\text{s}^{-1}$ ]
$g(\phi, z)$	normal gravity as a function of latitude $\phi$ and height $z$ [ $\text{ms}^{-2}$ ]
$g(\phi)$	normal gravity at the surface according to the international gravity formula [ $\text{ms}^{-2}$ ]
$g_{45}$	normal gravity at the surface and $\phi = 45^\circ$ ( $9.80665 \text{ ms}^{-2}$ )
<b>H</b>	magnetic field strength [ $\text{A m}^{-1}$ ]
<b>J</b>	current density [ $\text{A m}^{-2}$ ]
$K$	constant n the reduced Appelton-Hartree formula: $1.13 \cdot 10^{-12} \text{ m}^3 \text{ T}^{-1} \text{ s}^{-3}$
$k_1, k_2, k_3$	constants in the Smith-Weintraub refractivity formula
$k$	index denoting the GPS signal ( $k = 1$ for $L1$ , $k = 2$ for $L2$ )
$L$	optical path [m]
$L1, L2$	the two GPS signals (generally written as $Lk$ )
$L_C$	ionosphere corrected optical path [m]
$L_k$	optical path of signal $Lk$ [km]
$N$	refractivity, $N = (n - 1) \cdot 10^6$
$N_e$	electron density [ $\text{m}^{-3}$ ]
$N^{IO_k}$	ionospheric refractivity for signal $Lk$
$N^{NE}$	neutral atmospheric refractivity
<b>n</b>	unit vector in direction of wave propagation
$n$	refractive index
$P(t)$	PNR sequence of $\pm 1$ containing $P$ -code (amplitude modulation on GPS signals)
$p$	RO retrieved pressure of air [hPa]
$p_{dry}$	RO retrieved pressure of air using the "dry air assumption" [hPa]
$p_d$	pressure of dry air [hPa]
$q$	specific humidity [g/kg]
$R_C$	local radius of curvature [m]
<b>r</b>	position vector (relative to center of refraction)
$r$	radius (distance to center of refraction)
$r_L$	distance of the LEO satellite to center of refraction
$r_G$	distance of the GPS satellite to center of refraction
<b>s</b>	unit vector in ray direction
$S_k$	ray path of signal $Lk$

$S_{L1}, S_{L2}$	scalar electric or magnetic field of the $L1$ and $L2$ signal at a fixed position
$T$	temperature [K]
$T_{dry}$	RO retrieved temperature using the “dry air assumption” [K]
$t$	time [s]
$v'_L$	radial velocity of the satellite in LEO [ $\text{ms}^{-1}$ ]
$v^{\prime\prime}_L$	tangential velocity of the satellite in LEO [ $\text{ms}^{-1}$ ]
$v'_G$	radial velocity of the GPS satellite [ $\text{ms}^{-1}$ ]
$v^{\prime\prime}_G$	tangential velocity of the GPS satellite [ $\text{ms}^{-1}$ ]
$X(t)$	PRN sequence of $\pm 1$ containing $CA$ -code (amplitude modulation on GPS signals)
$Y(t)$	PNR sequence of $\pm 1$ containing encrypted $P$ -code (amplitude modulation on GPS signals)
$Z$	geopotential height [gpm]
$z$	height above the Earth's surface approximated by the WGS-84 ellipsoid [m]



# List of Acronyms

1DVar	One-dimensional variational data assimilation
A/S	Anti-spoofing
ACE+	Atmosphere and Climate Explorer, Proposed European climate monitoring satellite mission
AMSU-A	Advanced Microwave Sounding Unit A
CA-code	Coarse acquisition code
CHAMP	CHALLENGING Minisatellite Payload, German-U.S. LEO satellite in orbit 2000-2005/6 carrying the TRSR-2 RO receiver
CIRA-86	climatology of the middle atmosphere [ <i>Fleming</i> , 1986]
COSMIC	Constellation Observing System for Meteorology, Taiwan-U.S. RO constellation carrying the IGOR RO receiver, launch scheduled 2005
DJF	December, January, and February
DLR	German Aerospace Center,
DoD	U.S. Department of Defense
EGOPS	End-to-end GNSS Occultation Performance Simulator
EM	electromagnetic
ENVISAT	Polar-orbiting Earth observation satellite of ESA
ESA	European Space Agency
EUMETSAT	Europe's Meteorological Satellite Organisation
EQUARS	Brazilian EQUatorial Atmosphere Research Satellite in low-inclined LEO, carrying the IGOR RO receiver, launch scheduled 2007
GALILEO	European GNSS scheduled to be operational in 2008
GCM	General Circulation model
GCOS	Global climate observing system
GFZ	GeoForschungsZentrum Potsdam, Germany
GLONASS	Global Navigation Satellite System, Russian GNSS
GNSS	Global Navigation Satellite System
GO	geometrical optic
GOMOS	Global Ozone Monitoring by Occultation of Stars stellar occultation instrument onboard ENVISAT
GPS	Global Navigation System, U.S. GNSS
GPS/MET	GPS/Meteorology, first satellite experiment applying the RO method to the Earth's atmosphere, 1995-1997
GRACE	Gravity Recovery and Climate Experiment, U.S.-German LEO twin-satellites carrying the TRSR-2 RO receiver, in orbit 2002--2007.
GRAS	GNSS Receiver for Atmospheric Sounding, RO receiver onboard MetOp
IFS	Integrated Forecasting System of ECMWF.
IGAM	Institute of Geophysics, Astrophysics, and Meteorology, University of Graz, Austria
IPCC	Intergovernmental Panel of Climate Change
JJA	June, July, and August

JPL	Jet Propulsion Laboratory, Pasadena, California, U.S.A.
L1, L2	Link-1, Link-2, the two GPS signals
MAM	March, April, May
MetOp	Europe's operational polar-orbiting weather satellite series (~ 2006-2020), first launch scheduled 2005
MIPAS	Michelson Interferometer for Passive Atmospheric Sounding. Fourier transform spectrometer onboard ENVISAT
MSISE-90	climatology of the middle atmosphere [ <i>Hedin</i> , 1991]
NASA	National Aeronautics and Space Administration, U.S.A.
NWP	Numerical weather prediction
Ørsted	Danish LEO satellite carrying the TRSR-1 receiver, in orbit 1999-2000
<i>P</i> -code	Precise code
PNR	Pseudo random noise
RMS	Root mean square
RO	Radio occultation
SNR	Signal-to-noise ratio
SON	September, October, and November
SI	International system of units.
S/A	Selective Availability
SAC-C	Satélite de Aplicaciones Científicas-C, Argentinean LEO satellite in orbit 2000-~2005 carrying the TRSR-3 RO receiver.
SCIAMACHI	Scanning Imaging Absorption Spectrometer for Atmospheric Chartography. A instrument sounding the chemical composition of the atmosphere onboard ENVISAT
SUNSAT	Stellenbosh University Satellite, South African LEO satellite carrying the TRSR-1 RO receiver, in orbit 1999-~2005
TAR	IPCC Third Assessment Report – Climate Change 2001
TRSR-1	GPS RO receiver developed by JPL.
TRSR-2	GPS RO receiver developed by JPL.
TRSR-3	GPS RO receiver developed by JPL.
UBH	Upper boundary height.
UCAR	University Cooperation for Atmospheric Research, Boulder, Colorado, U.S.A
UNFCCC	United Nations Framework Convention on Climate Change
WMO	World Meteorological Organization
<i>Y</i> -code	Encrypted <i>P</i> -code when n A/S is on

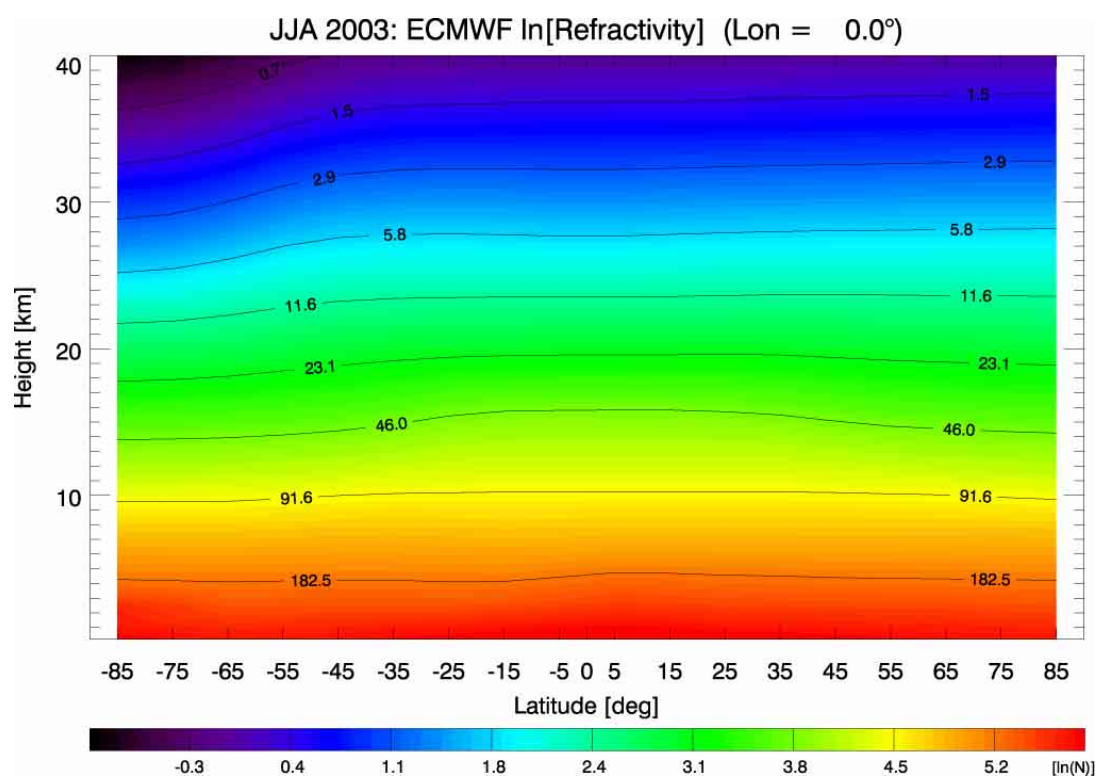
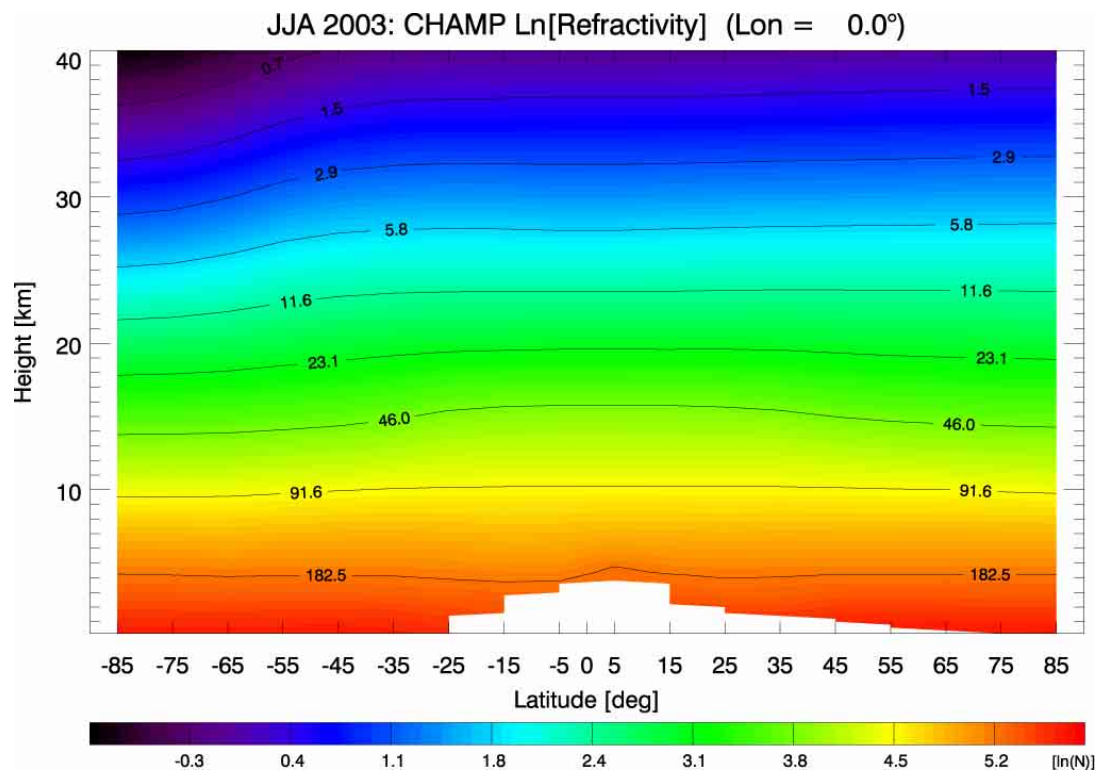
# Appendix

## JJA2003 CHAMPCLIM Results

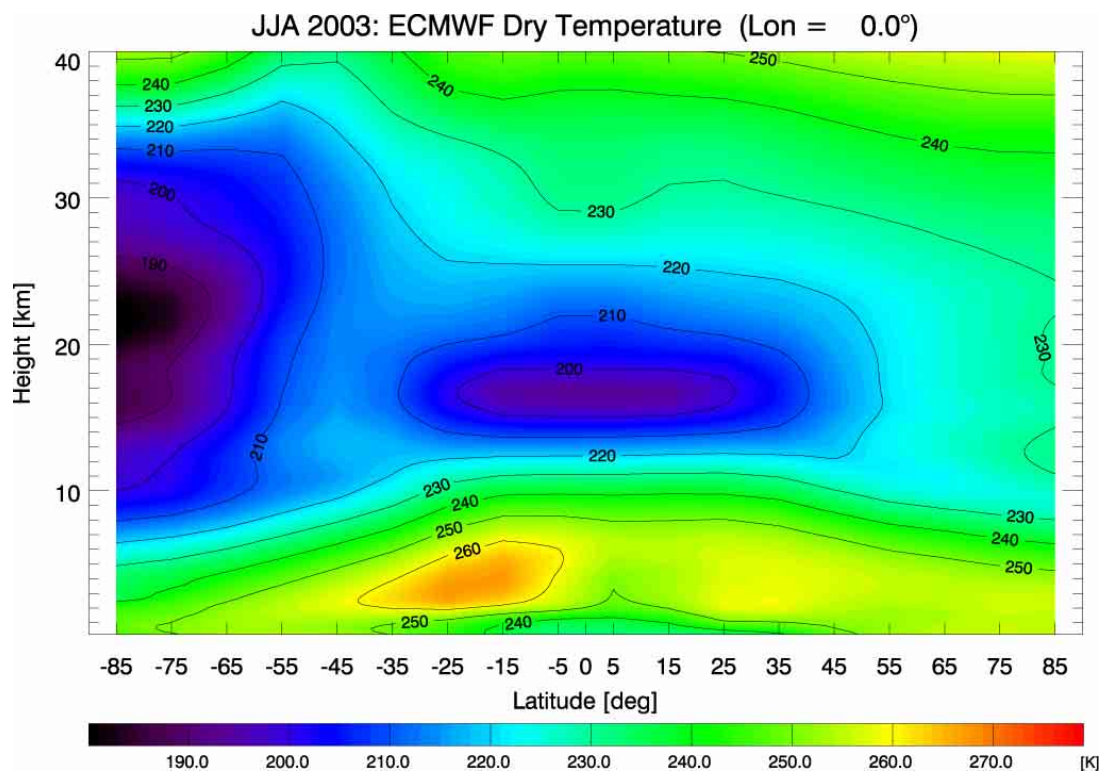
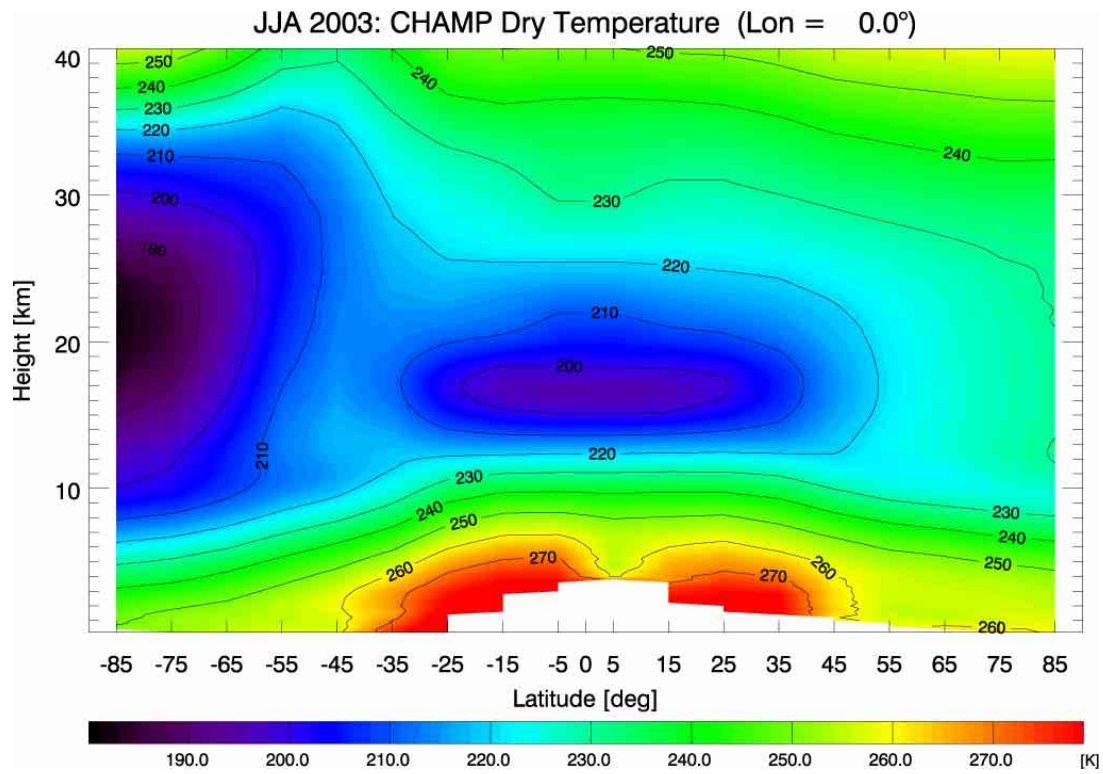
This Appendix gives a detailed overview on the preliminary CHAMPCLIM results for JJA 2003 as well as on the correlative data extracted from ECMWF operational analyses. All CHAMPCLIM data presented here were retrieved from operational CHAMP phase delays provided by GFZ Potsdam with the IGAM/ECMWF retrieval scheme as described in Chapter 5 and sampled on the preliminary CHAMPCLIM grids as described in section 7.2.1.

## A.1 CAMPCLIM and ECMWF Refractivity and Dry Temperature

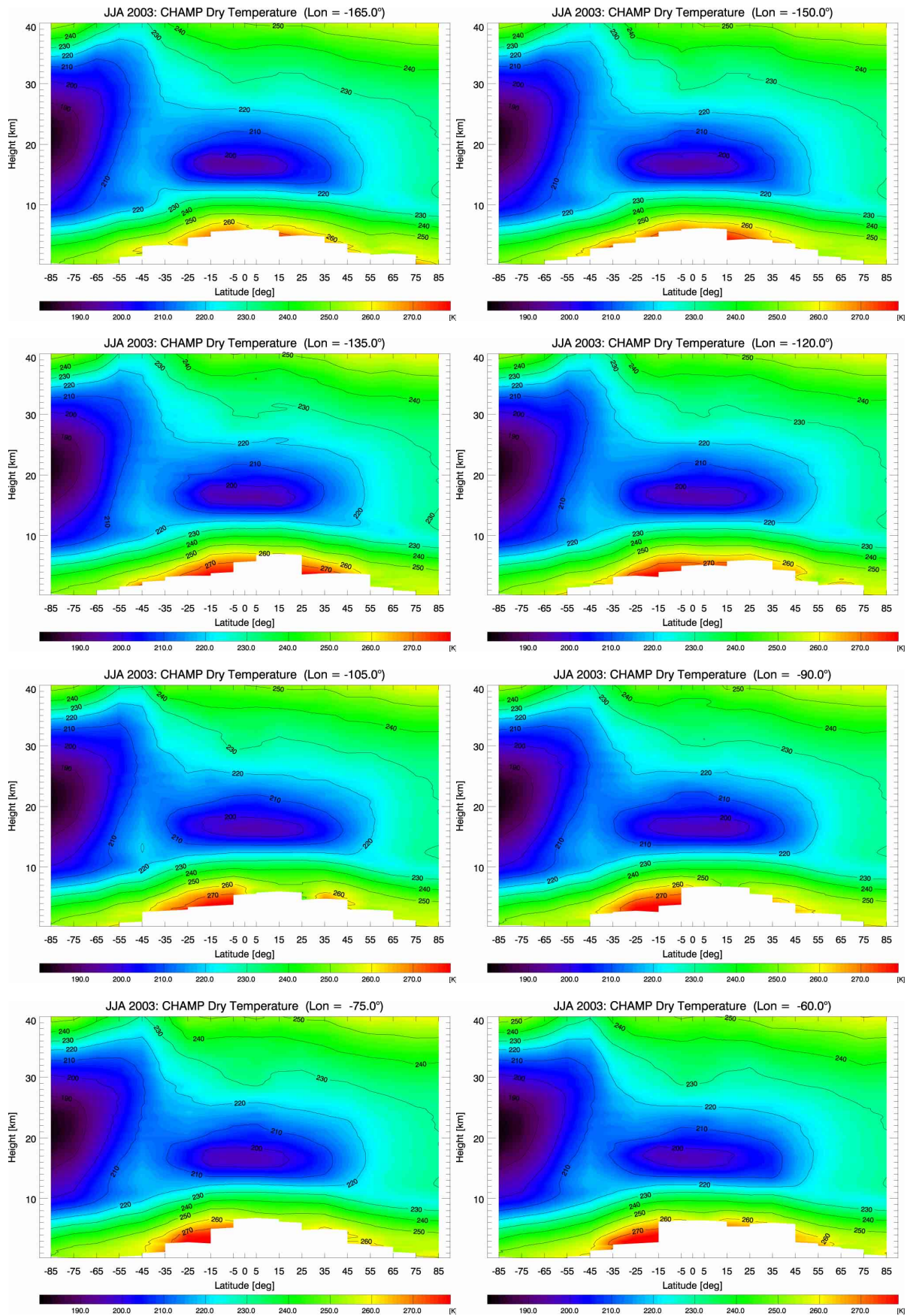
## A.1.1 Refractivity: 18 Latitude Bands (10 Degree Zonal Means)

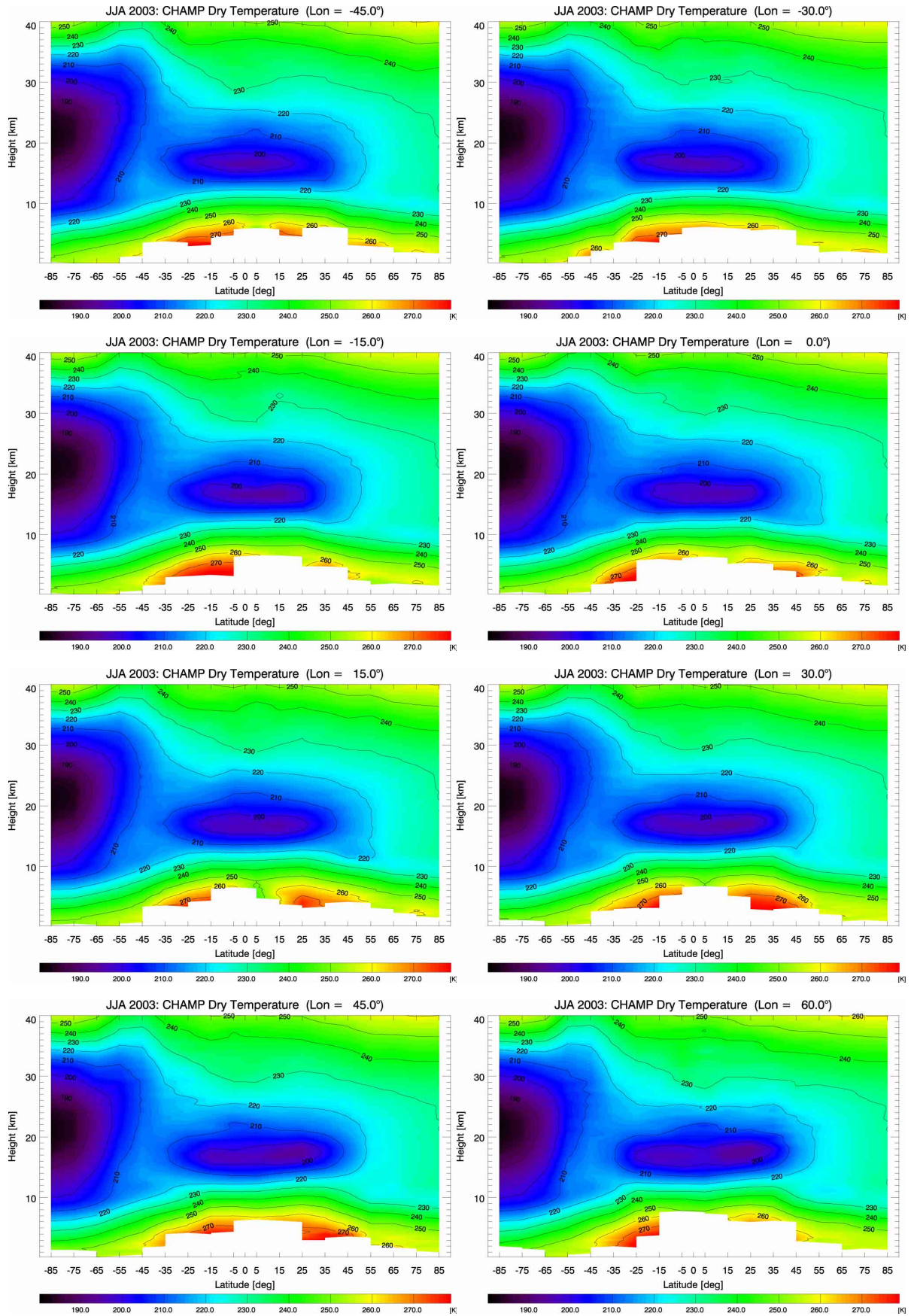


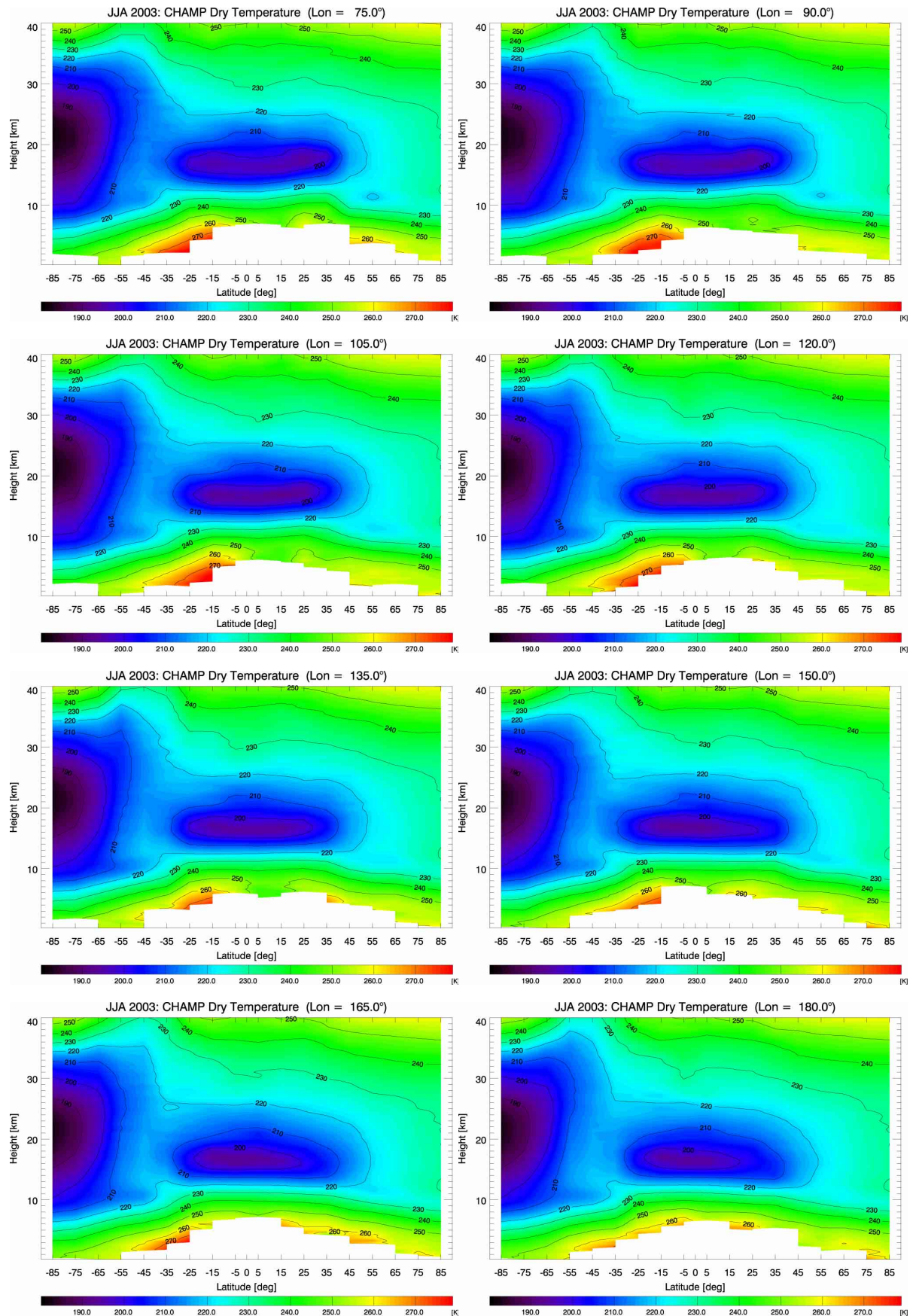
## A.1.2 Dry Temperature: 18 Latitude Bands (10 Degree Zonal Means)



### A.1.3 Dry Temperature: 18 Latitude x 24 Longitude Bins

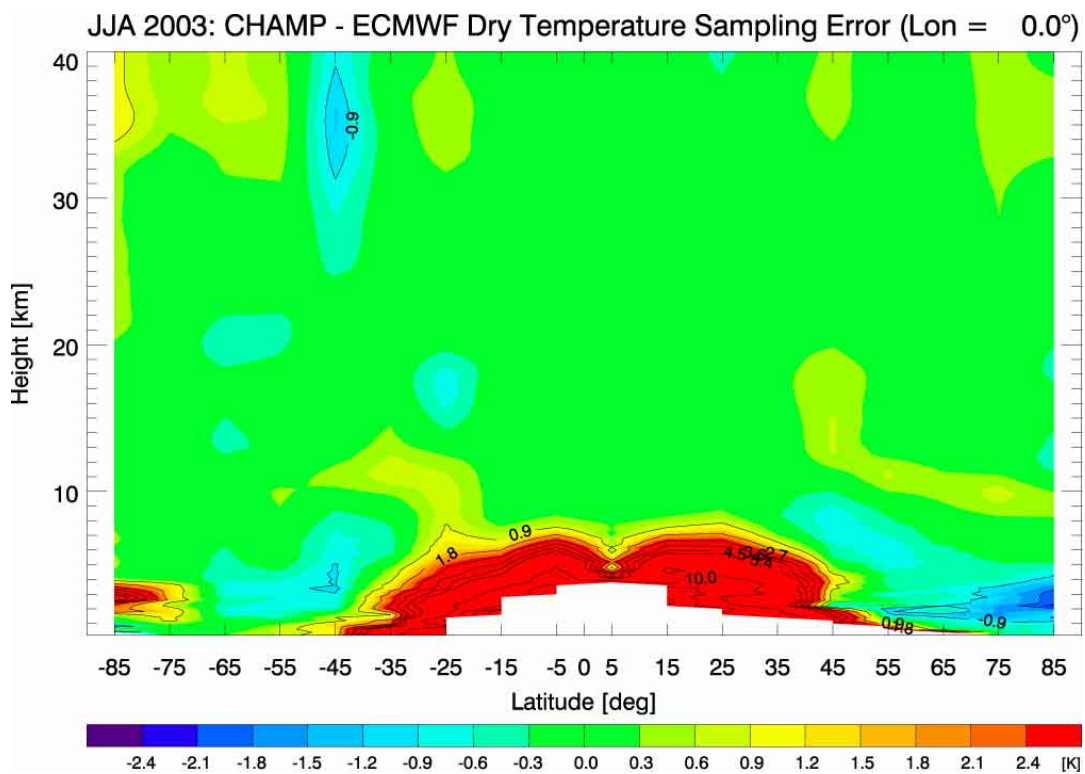
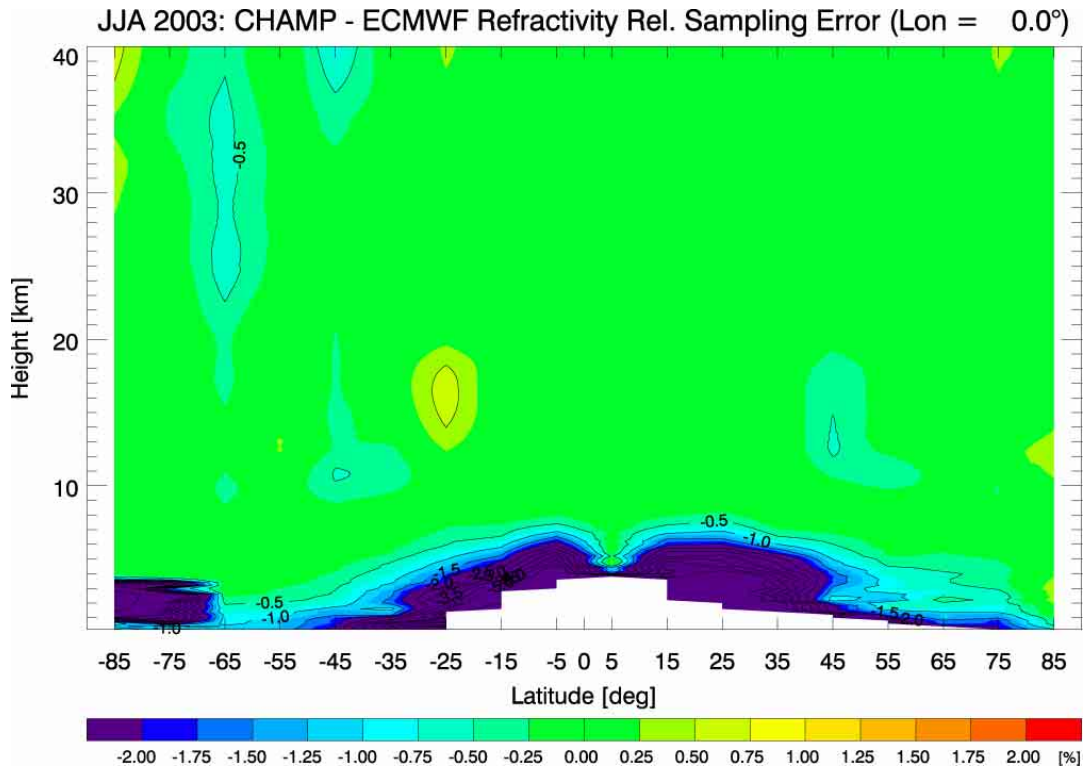




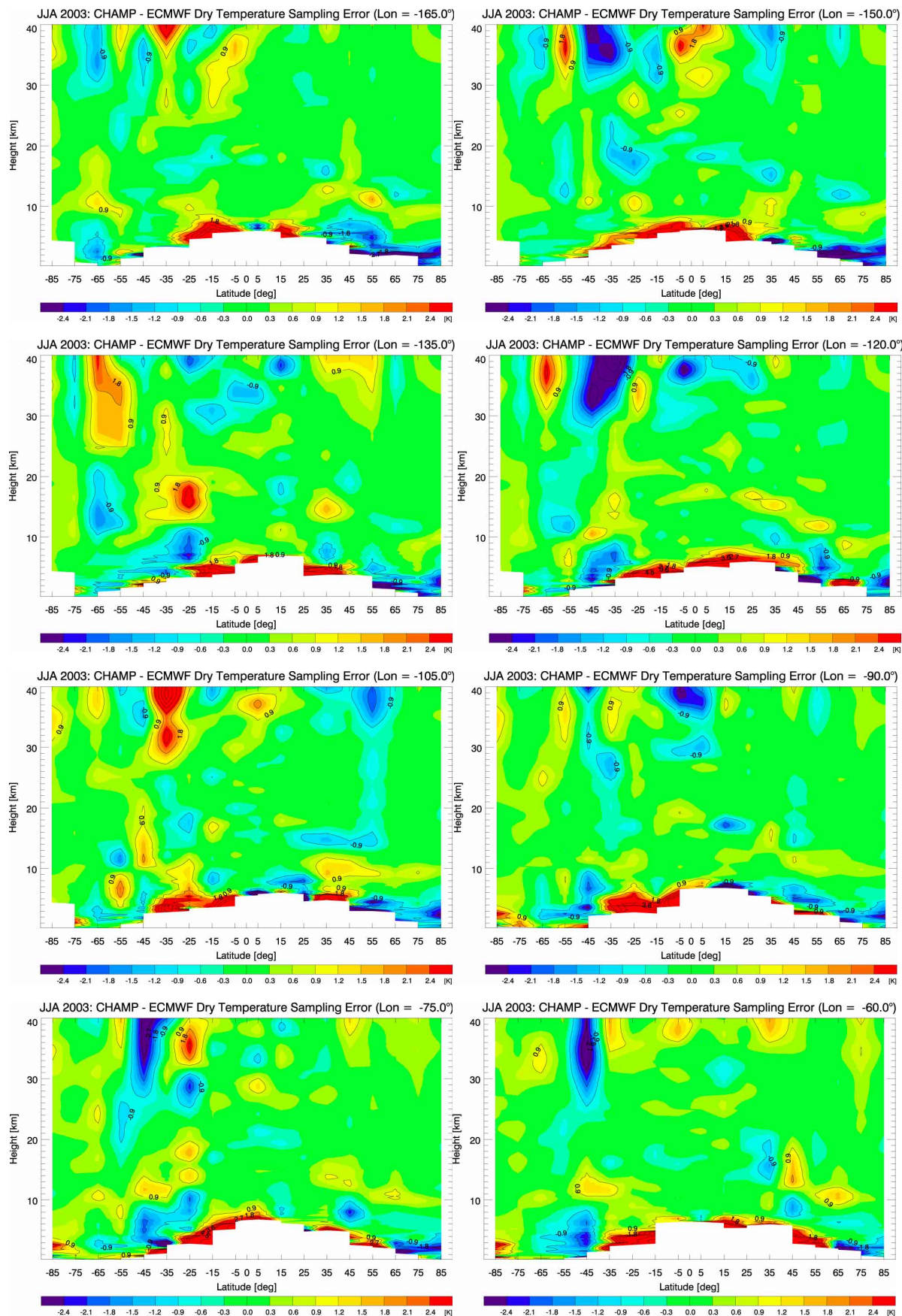


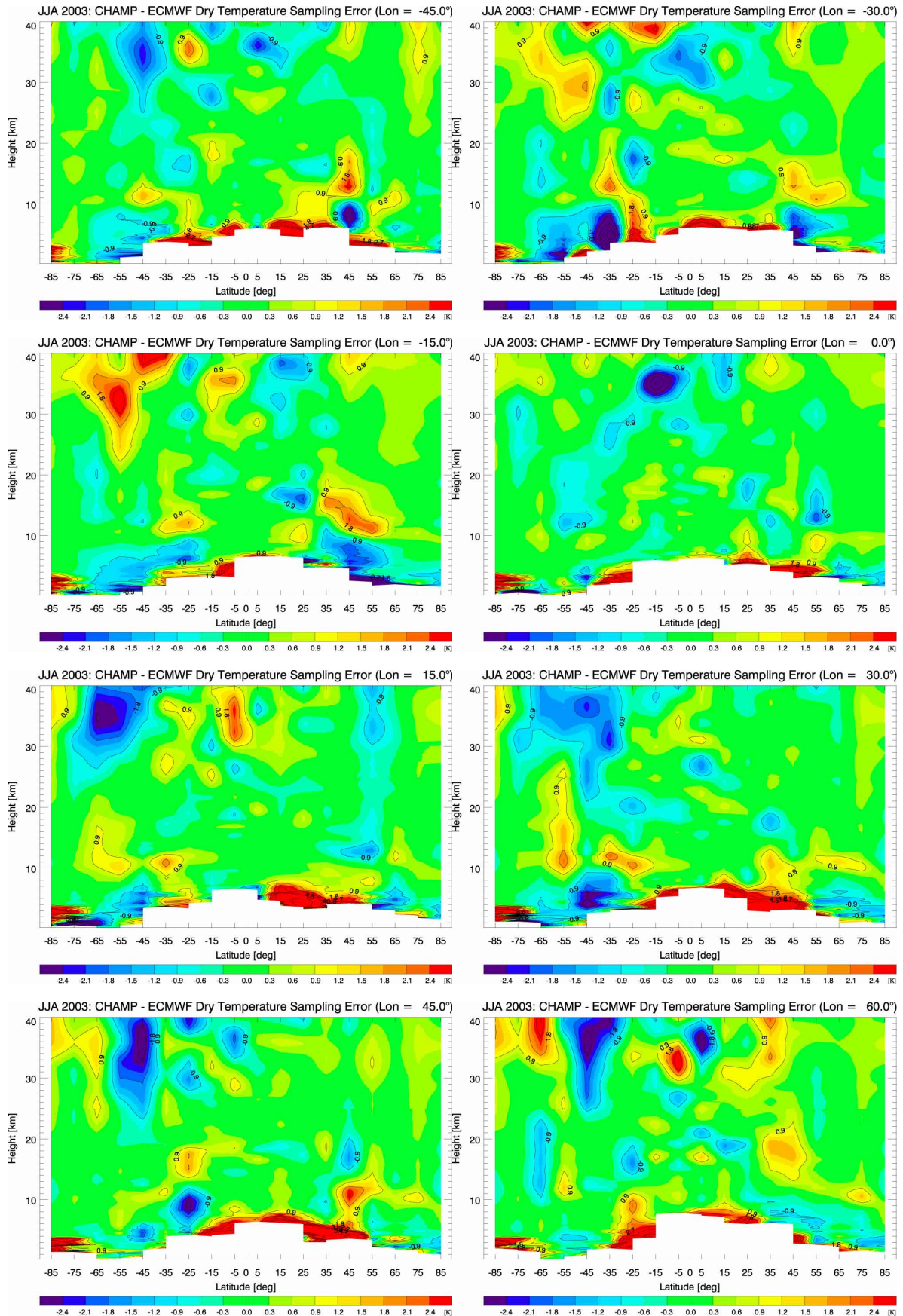
## A.2. Refractivity and Dry Temperature Sampling Error Estimate

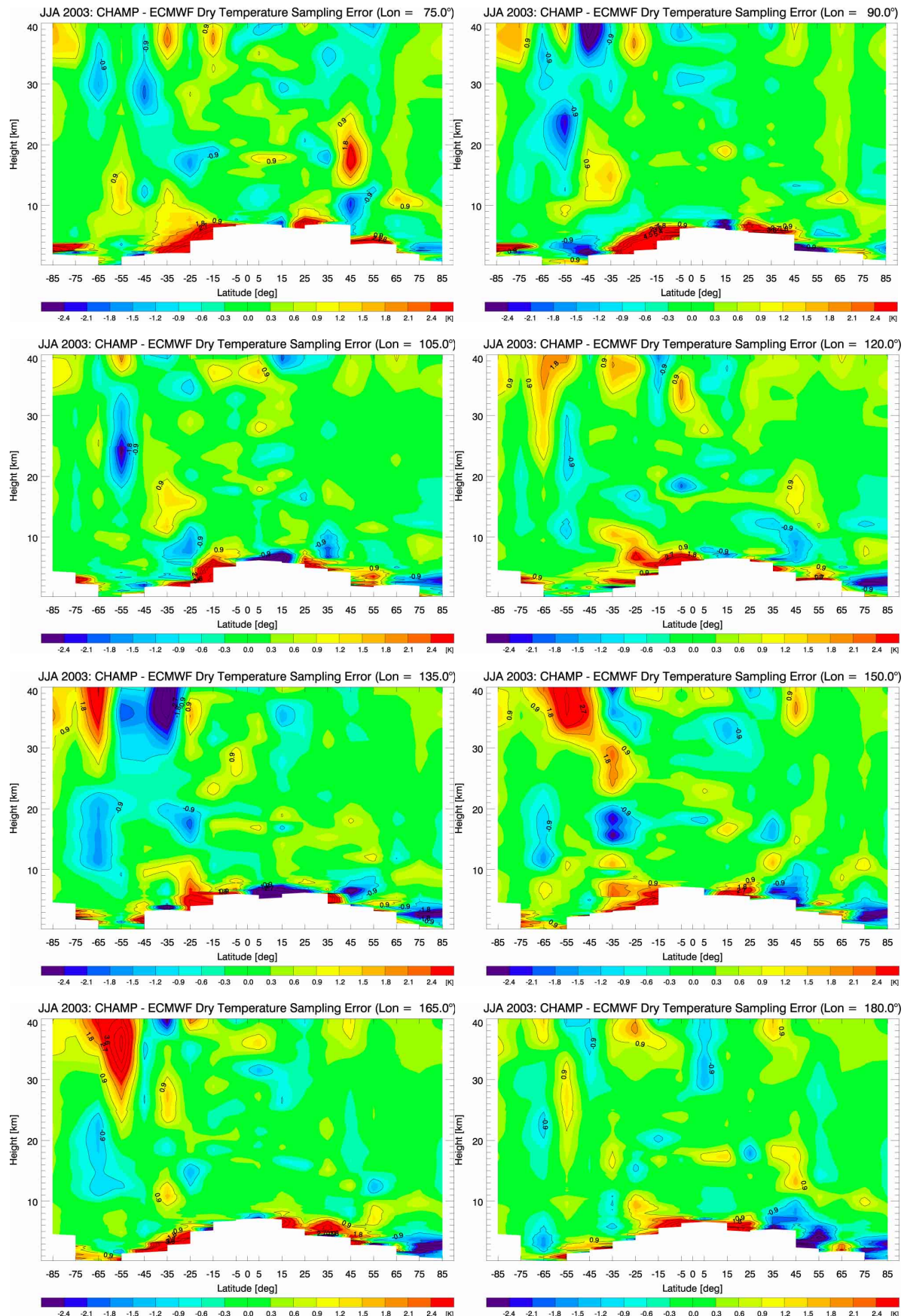
### A.2.1 18 Latitude Bands (10 Degree Zonal Means)



### A.2.2 18 Latitude x 24 Longitude Bins

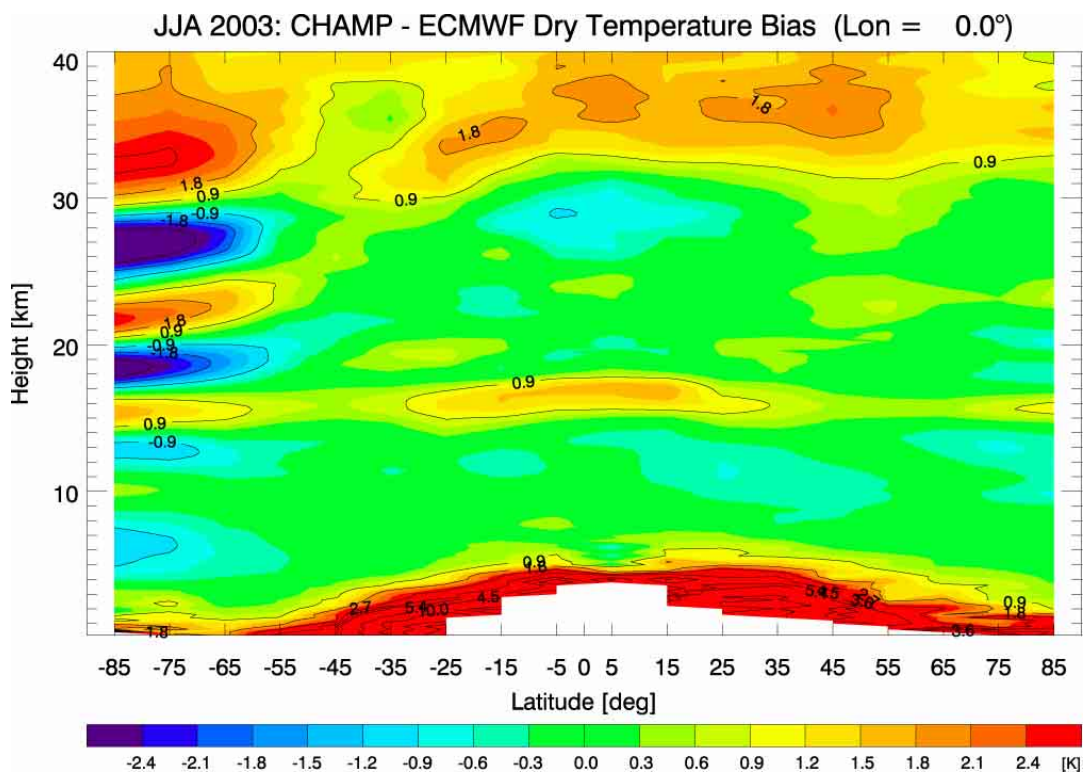
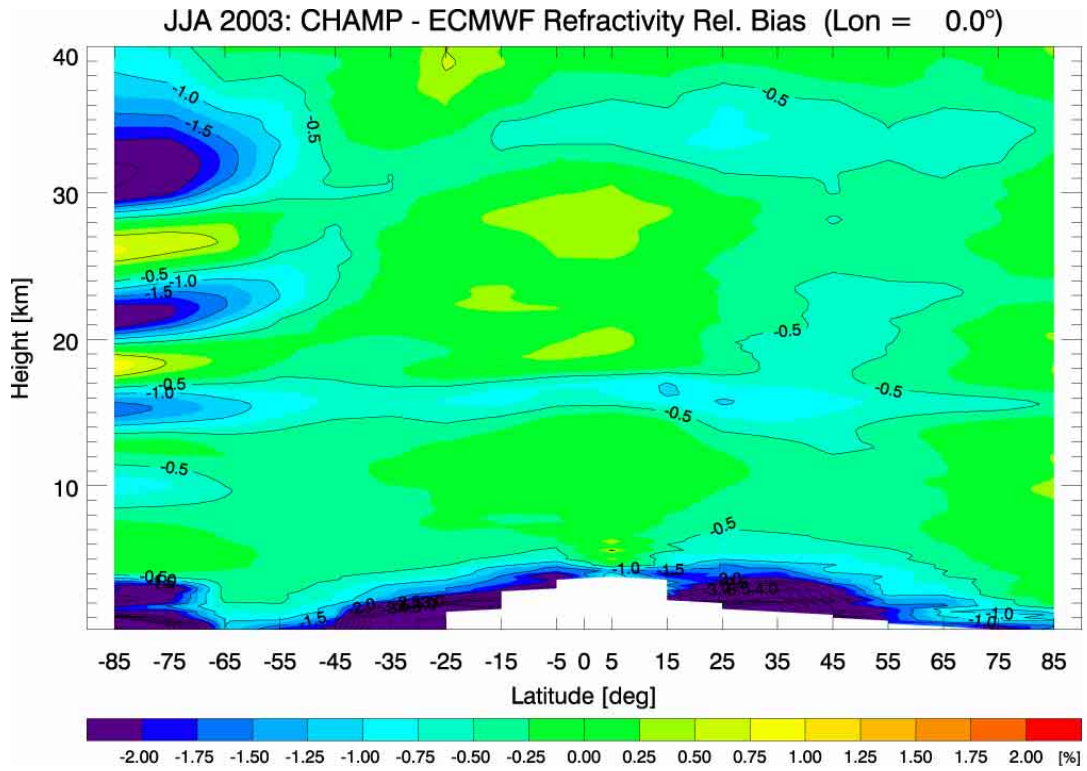




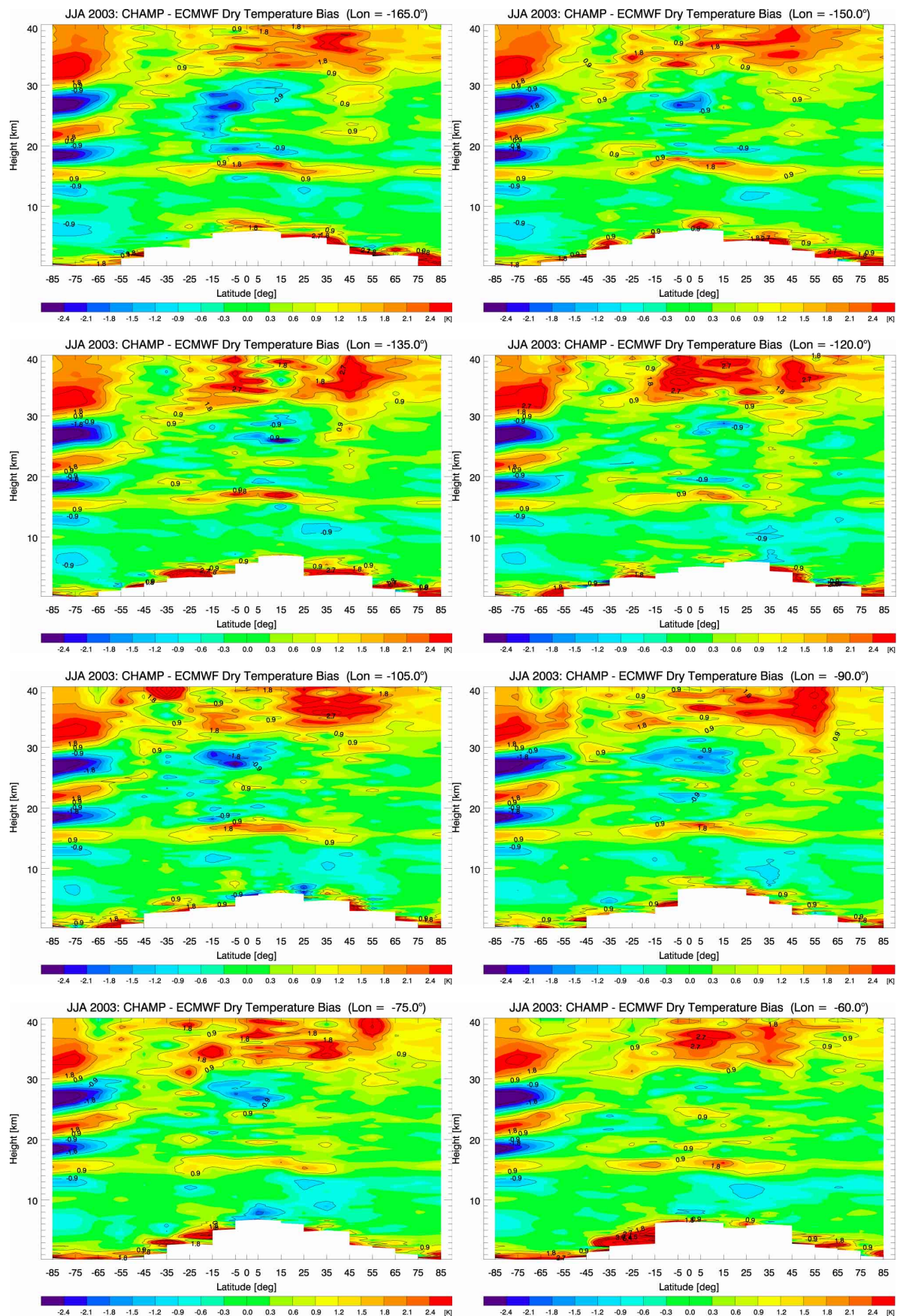


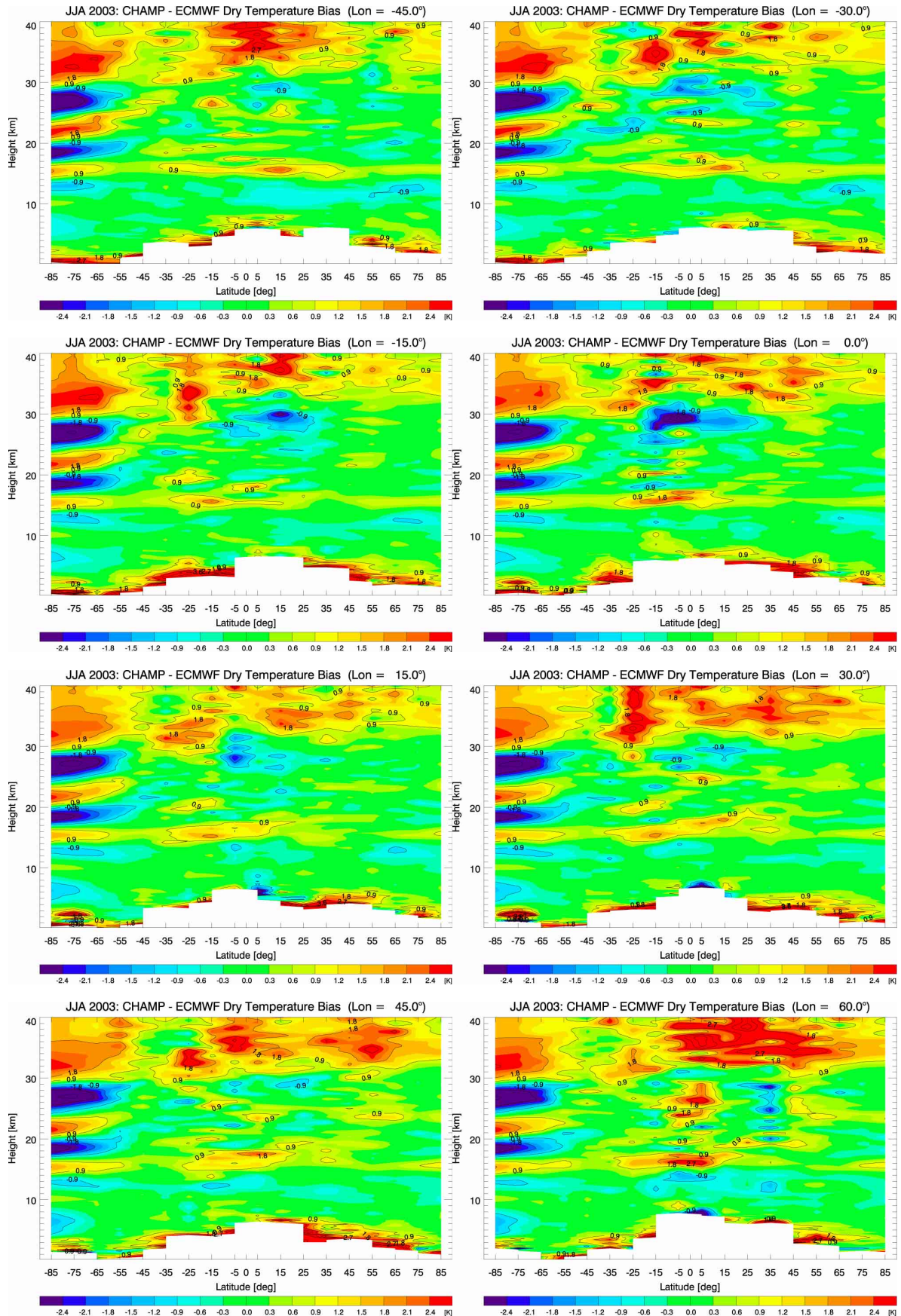
### A.3 Refractivity and Dry Temperature Measurement Bias (vs. ECMWF)

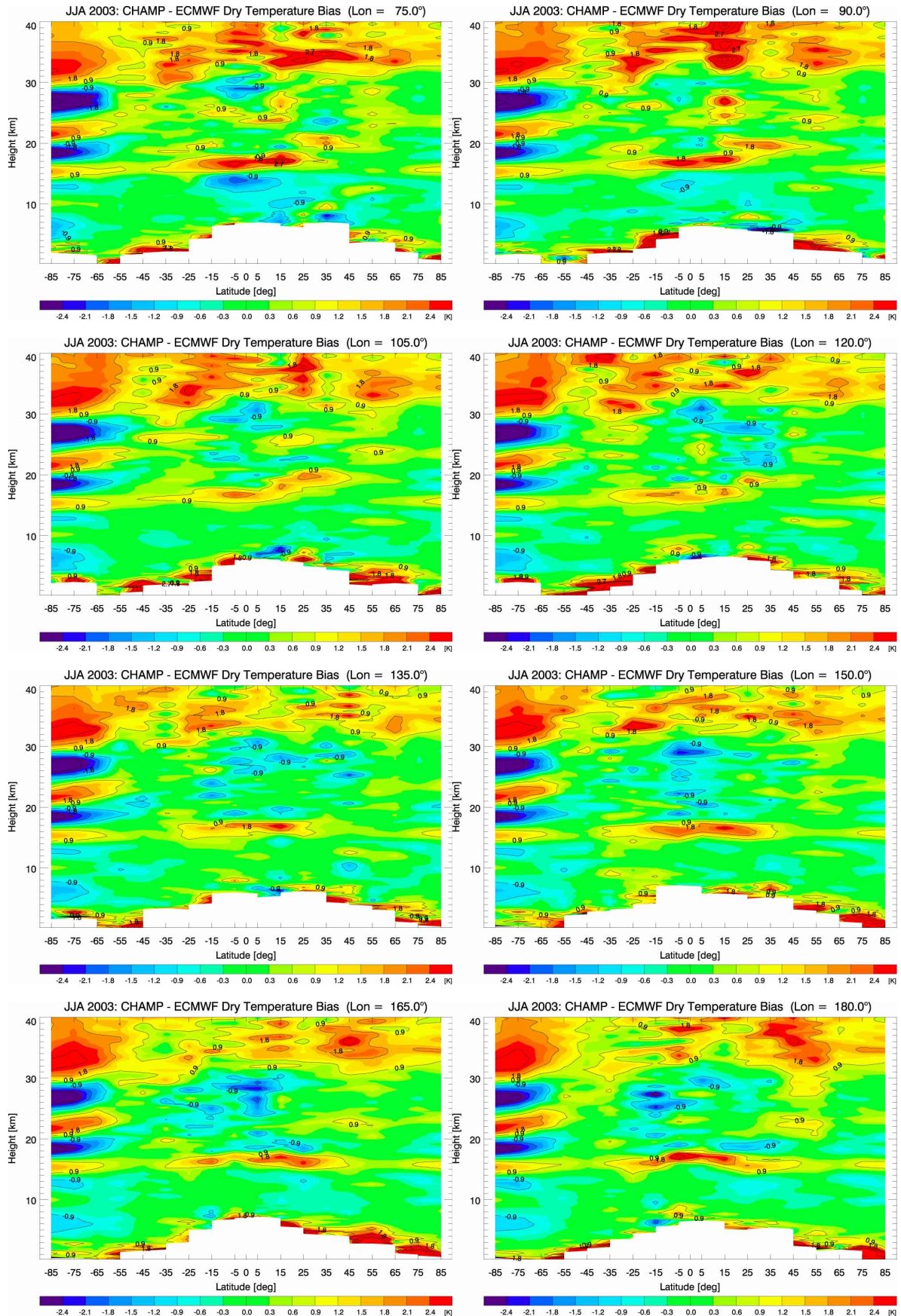
#### A.3.1 18 Latitude Bands (10 Degree Zonal Means)



### A.3.2 18 Latitude x 24 Longitude Bins

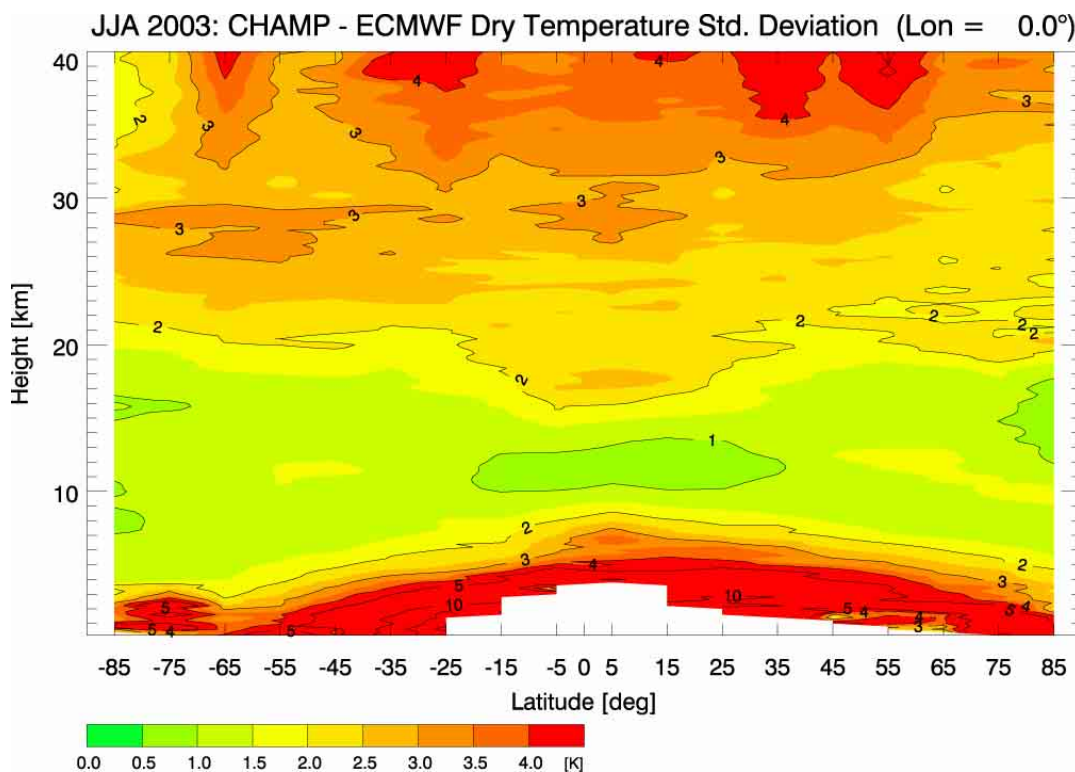
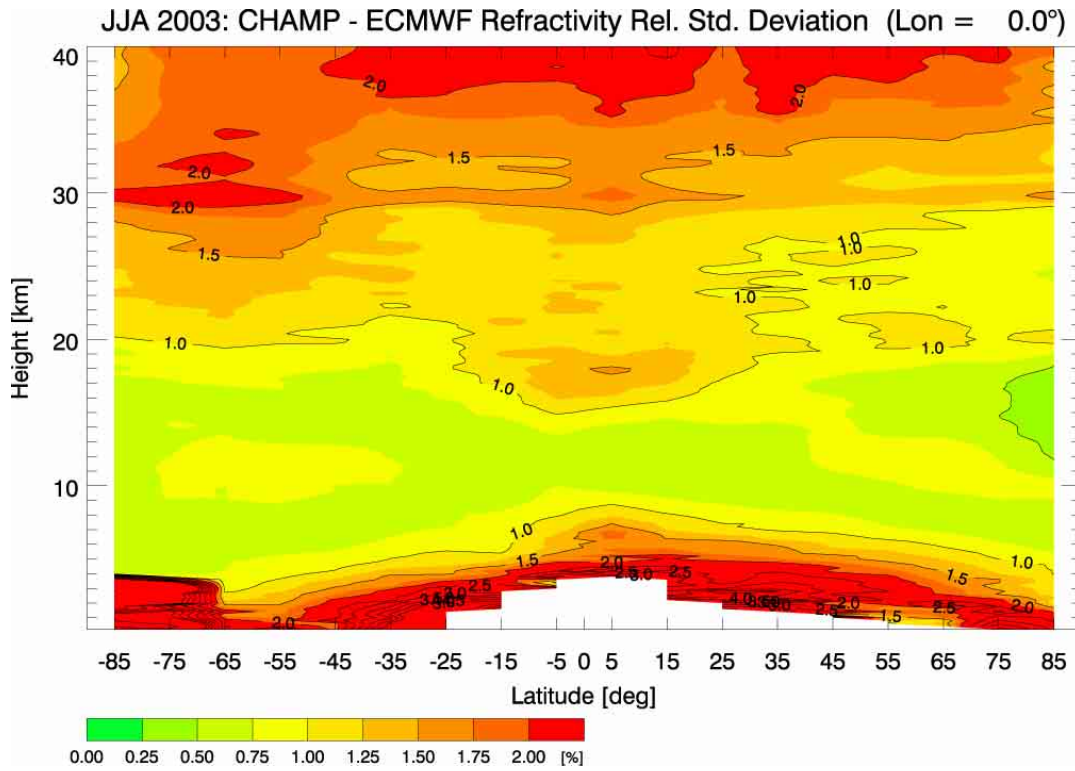




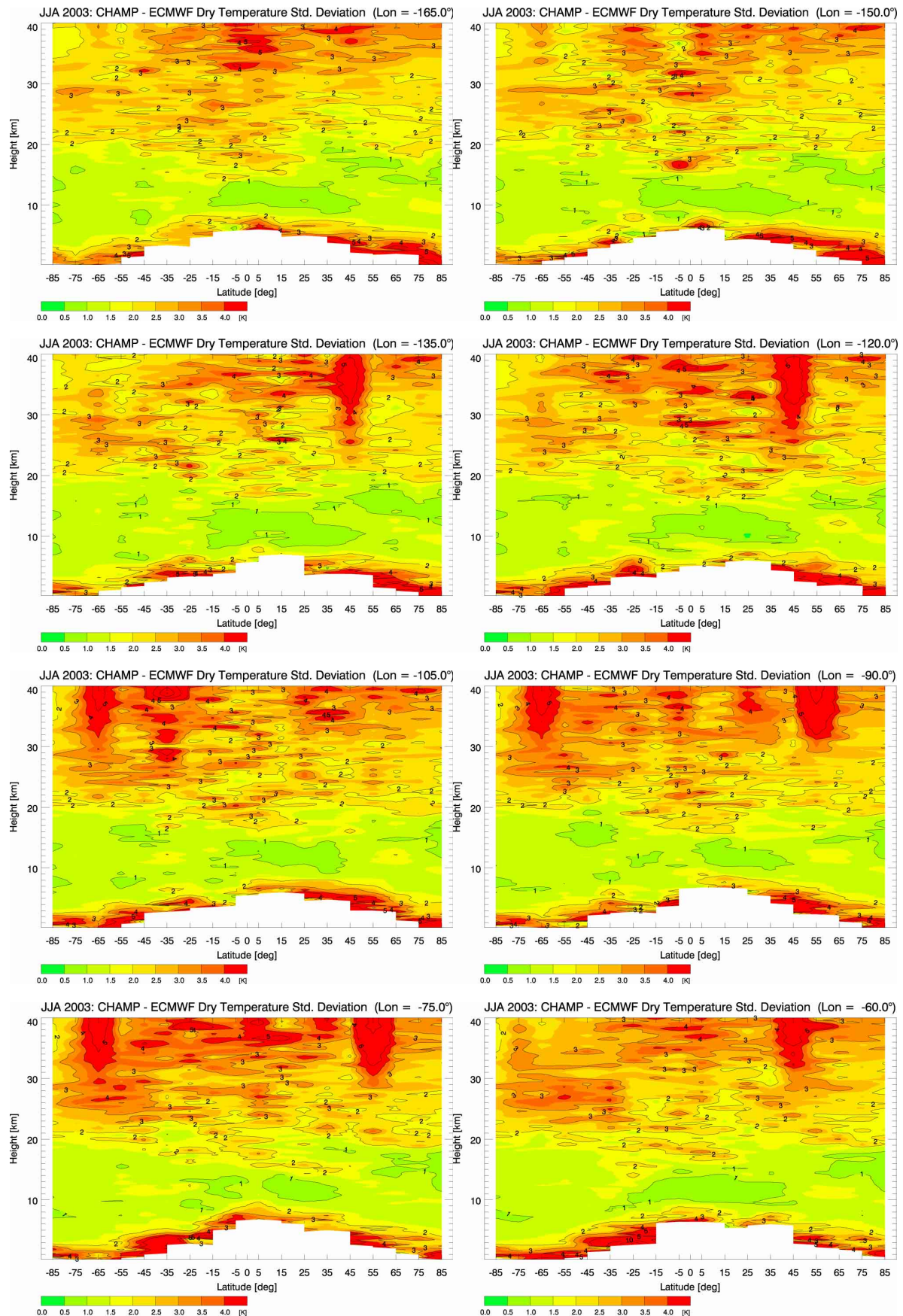


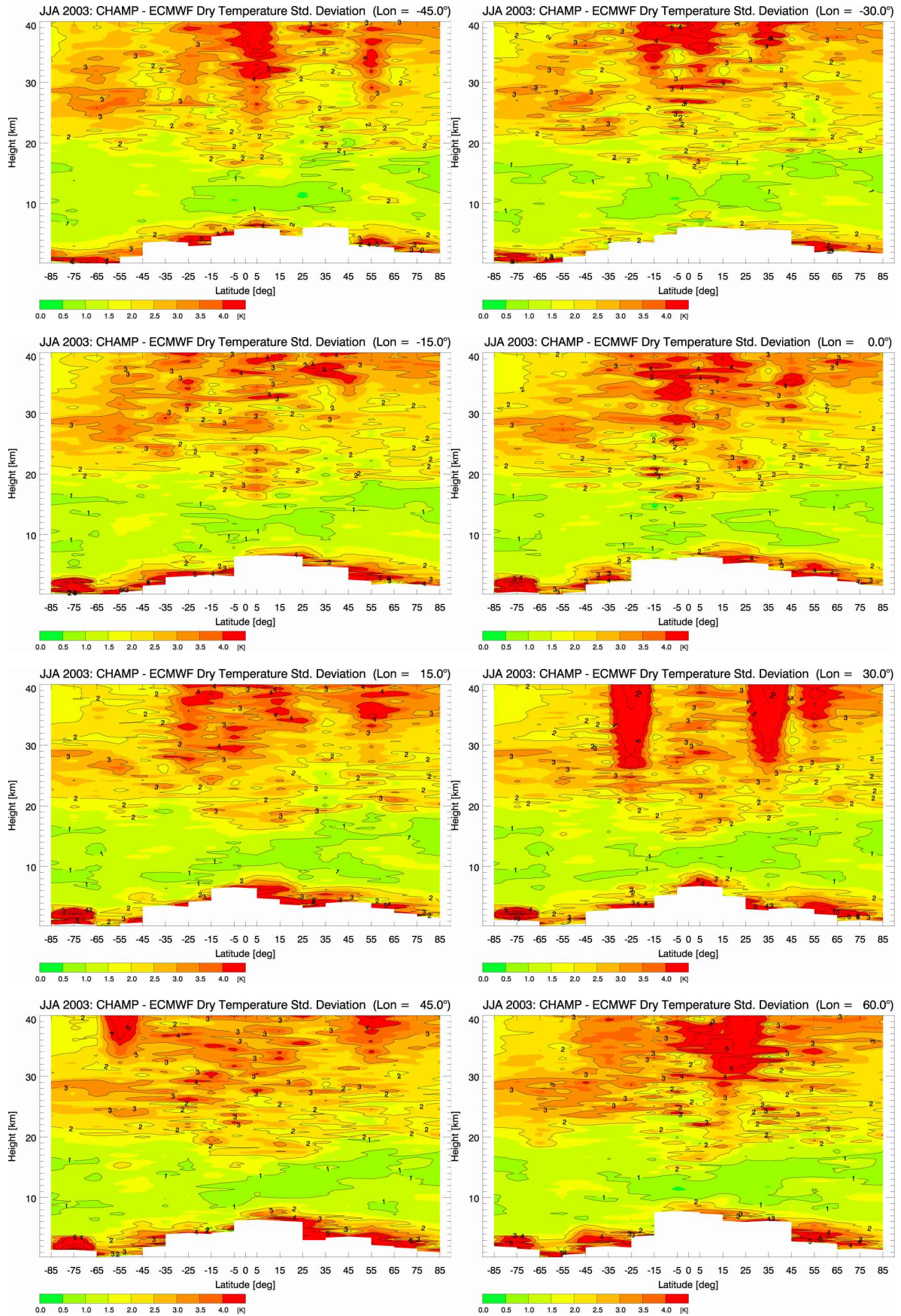
## A.4 Refractivity and Dry Temperature Measurement Random Error (vs. ECMWF)

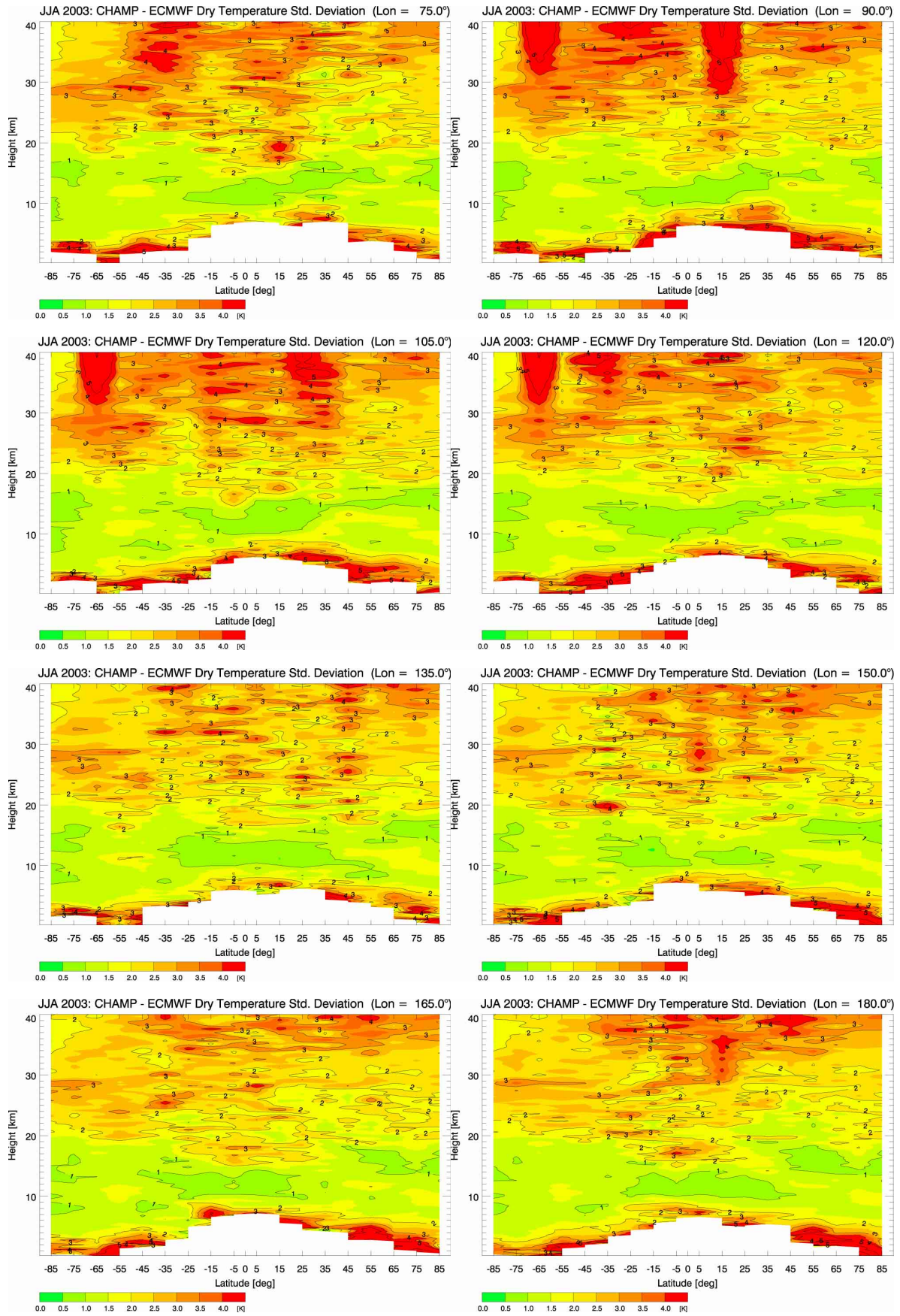
### A.4.1 18 Latitude Bands (10 Degree Zonal Means)



### A.4.2 18 Latitude x 24 Longitude Bins

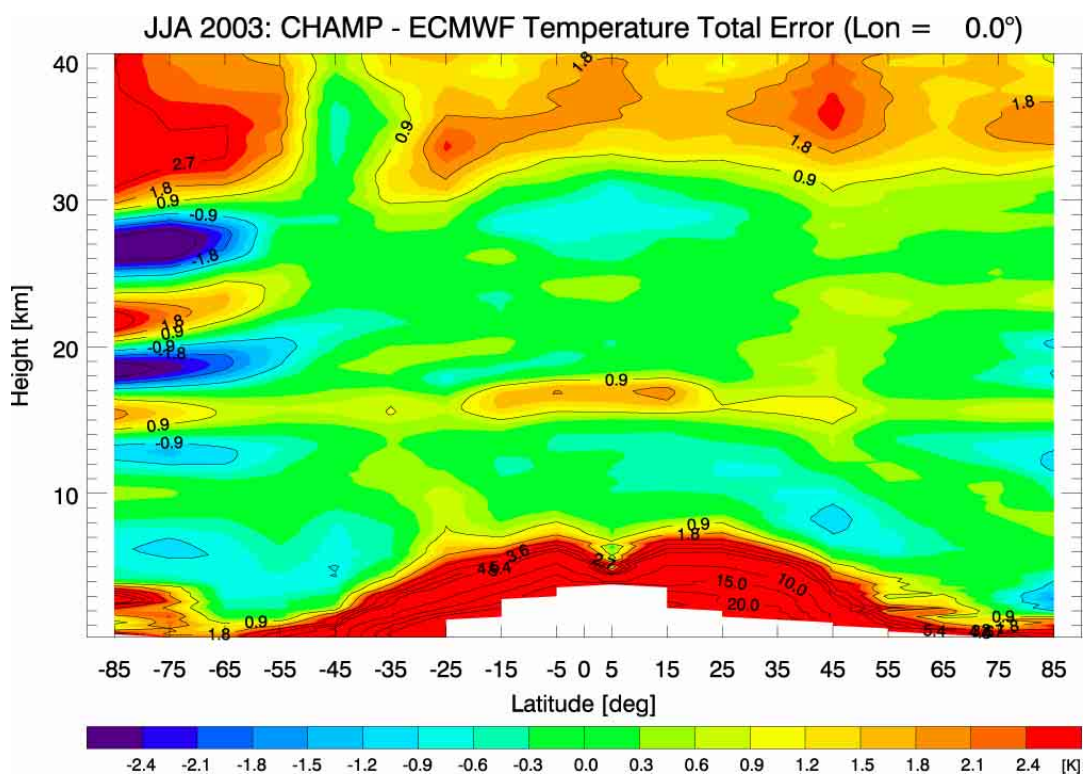
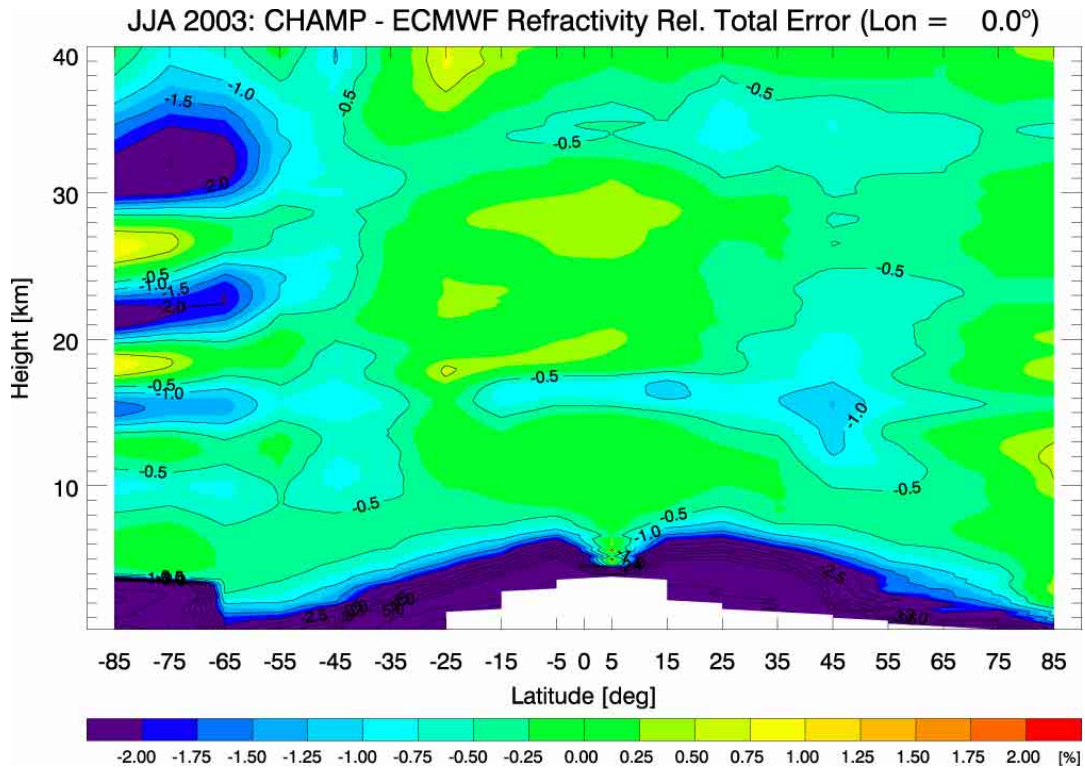




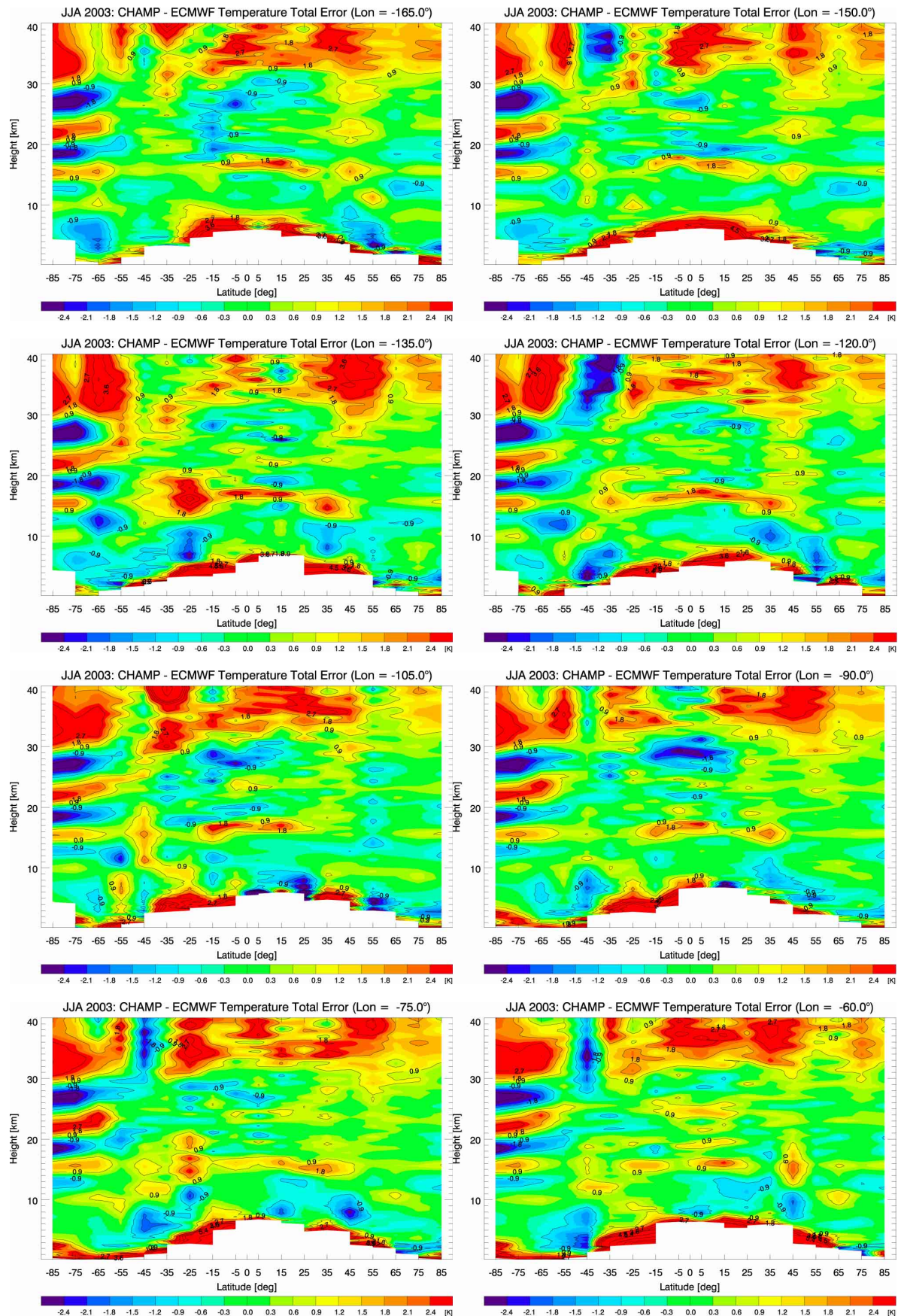


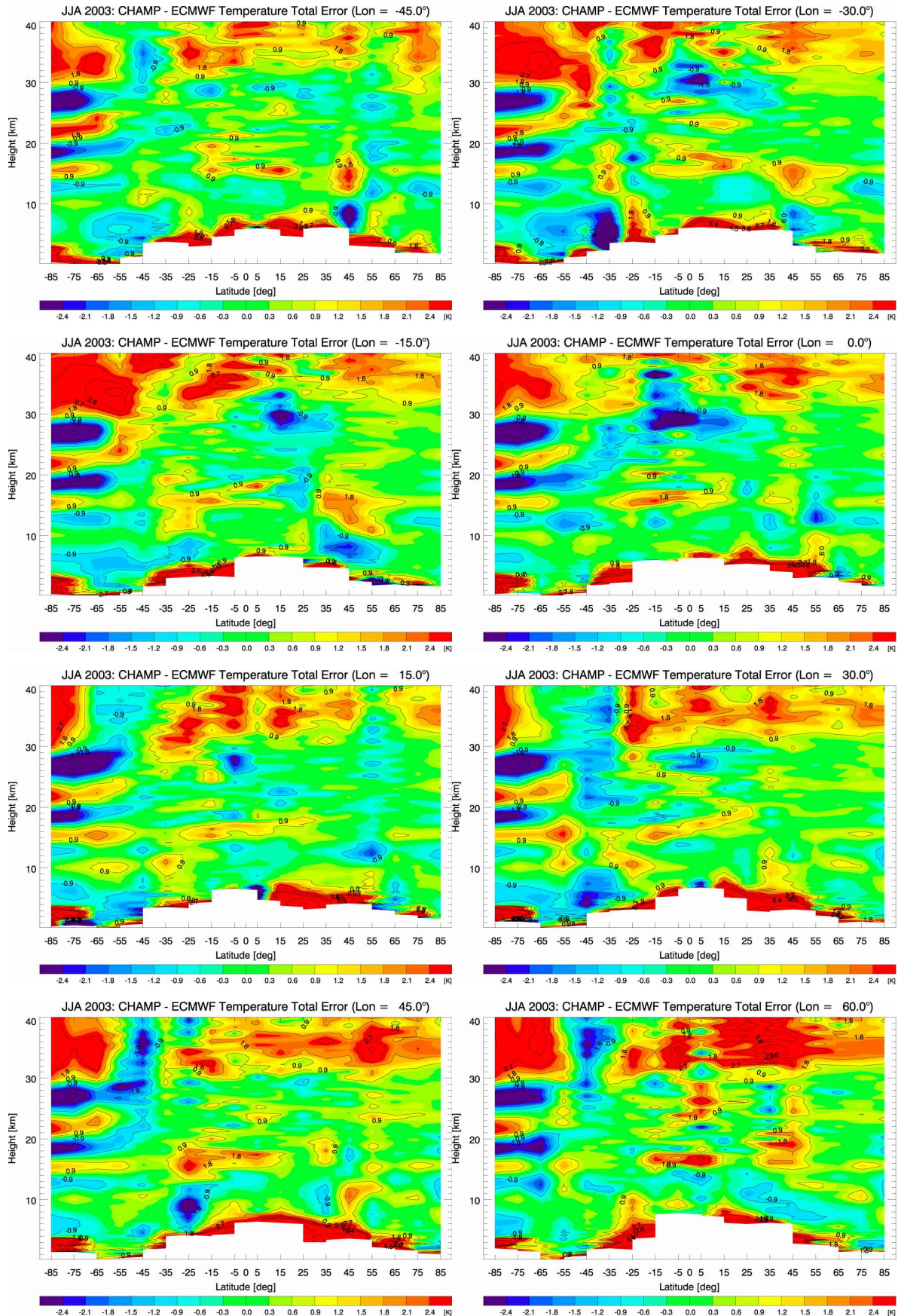
## A.5 Refractivity and Dry Temperature Climatological Total Error (vs. ECMWF)

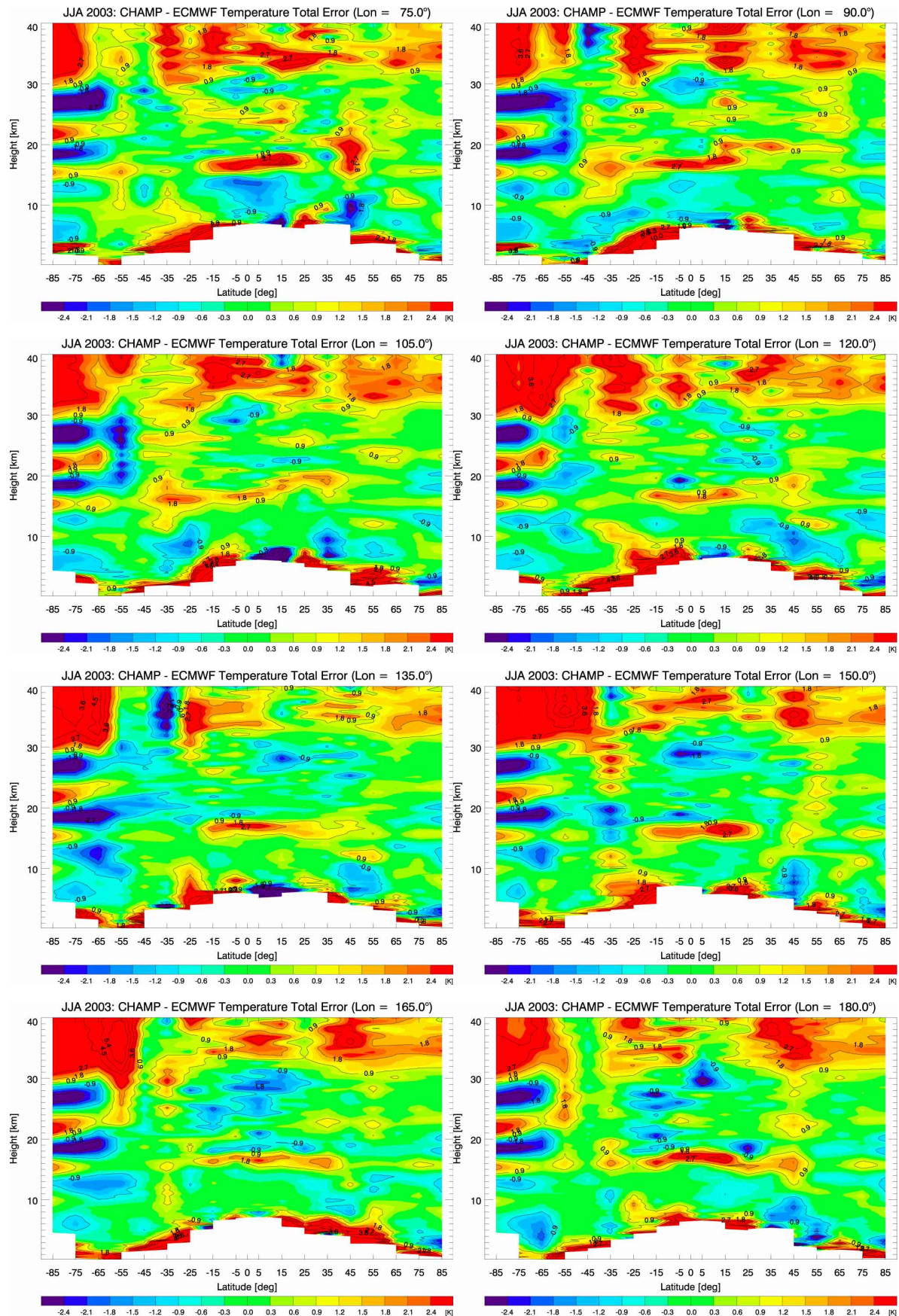
### A.5.1 18 Latitude Bands (10 Degree Zonal Means)



### A.5.2 18 Latitude x 24 Longitude Bins







*Abstract:*

The satellite-based radio occultation (RO) technique provides vertical profiles of, e.g., atmospheric temperature, geopotential height, or, if background information is added, water vapor. RO can contribute to global climate monitoring in a unique way due to its characteristics such as absolute calibration and long term stability, global coverage, all-weather capability, high accuracy, high vertical resolution, and cost effectiveness.

This report gives an overview of the basic technical characteristics of the RO technique, of its state of implementation with focus on the first satellite mission providing RO data on a longer term (CHAMP), and of the state-of-the-art of RO retrieval techniques. In addition, the enhancement of retrieval schemes by sensible inclusion of background information using the statistical optimization method is described and it is shown that RO retrieval combined with the statistical optimization approach is superior to other state-of-the-art techniques. Furthermore, the development of semi-operational retrieval schemes that are capable to cope with RO data from CHAMP in a stable way is described and, based on these schemes, the first RO-based global climatologies are generated. It is demonstrated that seasonal-zonal mean temperature climatologies between 10 km and 30 km altitude with a bias  $< 0.3$  K are feasible with data from one single satellite. Finally, as a first application, the results are used to evaluate operational meteorological analyses from the European Centre for Medium-range Weather Forecasts (ECMWF) showing a very good agreement in general, but also demonstrating systematic deficiencies of the ECMWF analyses in the tropical tropopause and the Antarctic polar vortex region.

*Zum Inhalt:*

Mit Hilfe der satellitengestützten Radiookkultationsmethode (RO) können vertikale Profile der Temperatur und anderer atmosphärischer Grundparameter gemessen werden. Durch ihre einzigartigen Eigenschaften wie „absolute“ Kalibrierung und hohe Langzeitstabilität, hohe Genauigkeit, globale Bedeckung, die Fähigkeit unabhängig vom Bewölkungsgrad Daten zu liefern und hohe Kosteneffizienz hat die Methode das Potenzial die globale Klimaüberwachung in naher Zukunft grundlegend zu verbessern.

Dieser Bericht gibt einen Überblick über die RO Methode und beschreibt inwieweit sie derzeit implementiert ist, wobei besonderes Augenmerk auf die erste längerfristige RO-Mission (CHAMP) gelegt wird. In Folge wird die Verbesserung der Auswertung von RO-Daten durch statistische Optimierung unter Nutzung von Hintergrundinformation über den Zustand der Atmosphäre beschrieben und gezeigt, dass statistische Optimierung anderen gängigen Methoden überlegen ist. Weiters wird die Entwicklung eines stabilen semi-operationellen Auswerteschemas für RO Daten von CHAMP beschrieben. Darauf basierend werden erstmals globale Klimatologien der Temperatur zwischen 10 und 30 km Höhe aus RO-Daten erzeugt, die im saisonal-zonalen Mittel einen systematischen Fehler von  $< 0.3$  K aufweisen. Als erste Anwendung werden diese Klimatologien genutzt um die Qualität der operationellen meteorologischen Analysen des Europäischen Zentrums für Mittelfristige Wettervorhersage (EZMW) zu überprüfen. Generell zeigt der Vergleich einen hohen Grad an Übereinstimmung, allerdings werden auch systematische Abweichungen in der Region der tropischen Tropopause und des Antarktischen Polar-Vortex festgestellt, die auf Mängel in den EZMW-Analysen hinweisen.